Development of the efficient calculation of polarized radiative transfer based on the correlated *k*-distribution method and forward peak truncation approximation

相関 k 分布法と前方散乱の切断近似による

偏光放射伝達の効率的計算法の開発

February 2022

Masahiro Momoi

Graduate School of

Science and Engineering

CHIBA UNIVERSITY

(千葉大学審査学位論文)

Development of the efficient calculation of polarized radiative transfer based on the correlated *k*-distribution method and forward peak truncation approximation

相関 *k* 分布法と前方散乱の切断近似による

偏光放射伝達の効率的計算法の開発

February 2022

Masahiro Momoi

Graduate School of

Science and Engineering

CHIBA UNIVERSITY

Abstract

The surface temperature of the Earth has considerably risen within the range of 0.8 to 1.3°C over the past century (IPCC [2021]). This global warming has been driven by atmospheric components, including aerosols, clouds, and gases; substantial uncertainty remains regarding their impacts on the Earth's climate. Additional information is needed regarding the influence of atmospheric components on global warming. Sky radiance observation by ground-based photometers is a rapidly progressing remote sensing technology. It can provide useful information regarding the atmospheric aerosol and its associated radiative effects. Recently, polarized radiance has become the focus of observational studies.

In this work, to enable ground-based radiometer data analysis, we developed an efficient computation method (Improved Multiple and Single scattering approximation (IMS) by *n*-th order multiple scattering correction of the forward Peak; P^n-IMS) for sky radiance, including the polarization effects. We also conducted a survey of the information contained in the sky radiance in the water vapor absorption region using a newly developed gas absorption table (WV-CKD).

Firstly, we developed a novel calculation method for polarized radiation. The P^1- and P^2-IMS methods are extended versions of the Truncated Multiple and Single scattering approximation (TMS) and IMS methods established by Nakajima and Tanaka [1988], which were formulated using a scalar approximation of the radiation field. We extended these methods to include the polarization effect based on the vector radiative transfer theory. We also developed an *n*-th order scattering correction. A series of numerical tests revealed that the P^1-IMS method was sufficiently accurate to reconstruct the Stokes parameters within 0.2%, except for total radiance. The total radiance in the solar aureole region requires a higher order scattering correction by the P^2- and P^3-IMS methods. Numerical tests indicated that the P^3-IMS method reconstructed sky radiance with ≤ 1% error using a low hemispheric quadrature stream ($N = 10$) in the 340–1020 nm spectral region within a moderately thick atmosphere at an aerosol optical thickness of 1 at 500 nm. Thus, the P^3-IMS method is more efficient than the P^1-IMS method, which requires $N > 20$.

A later study investigated the information content of the sky radiance at 940 nm, which is a water vapor absorption region in the near-infrared wavelength. To rapidly compute the narrow-band sky radiance at 940 nm, we developed the WV-CKD while maintaining a suitable accuracy (< 0.3%). Numerical tests indicated that sky radiance in the almucantar plane contains information regarding precipitable water vapor (PWV). In contrast, sky radiance in the principal plane contains information regarding both PWV and the aerosol vertical profile. We developed a procedure to obtain PWV from the sky-radiometer without pre/post calibration. We applied the method to actual SKYNET observations and compared the PWV with the microwave radiometer. The results indicated that the PWV derived from the sky-radiometer was in good agreement with the PWV obtained from the microwave radiometer.

要旨

地球温暖化に伴って過去 1 世紀で 0.8～1.3℃の大幅な地表面温度の上昇がある（IPCC [2021]）。これは、エアロゾル、雲、ガスなどの大気成分によって引き起こされていることが知られているが、地球の気候に対するこれらの影響については依然としてかなりの不確実性がある。したがって、大気成分に関するより多くの情報が求められている。急速な進歩を遂げているリモートセンシング技術の一つに地上での分光放射計観測がある。分光放射計は天空輝度観測により、大気中のエアロゾル量とそれに関連する放射効果に関する情報を得ることができる。また近年は、より多くの観測情報を得るために天空輝度の偏光成分の観測に注目が集まっている。

本研究では、SKYNET 観測網のスカイラジオメーターや AERONET 観測網のサンスカイラジオメーターなどの地上観測型の天空観測分光放射計の分析に必要な精度を維持しながら、放射伝達モデルを高速化する手法を二つ開発した。一つは偏光効果を含む空の放射輝度の効率的な計算手法（Improved Multiple and Single scattering approximation (IMS) by any *n*-th order multiple scattering correction of the forward Peak; P^n-IMS）の開発である。もう一つは 940 nm の水蒸気吸収領域を効率計算する k 分布テーブルの作成と、それを利用した 940 nm の天空輝度に含まれるエアロゾルおよび水蒸気に関する情報の調査である。

前者の研究で新たに開発した、P^1-IMS および P^2-IMS は、スカラー近似大気に対して定式化された、Nakajima and Tanaka [1988] の TMS（Truncated Multiple and Single scattering approximation）および IMS の拡張である。TMS と IMS はそれぞれ、前方ピークの 1 次と 2 次の散乱補正である。これらの方法を拡張して、ベクトル放射伝達理論に基づく偏光効果を考慮した。また、3 次以上の散乱を定式化し、n 次の散乱補正を導出した。一連の数値実験によると、全放射輝度以外のストークスパラメータは P^1-IMS により 0.2%以内で計算できることを示した。太陽光輪領域の全放射輝度の計算には、より高次の補正である P^2-IMS および P^3-IMS が必要であることがわかった。また P^3-IMS を用いると、エアロゾルの光学的厚さが 1 の比較的厚い大気であってもストリーム数を少なく抑えた（10 程度）上で 1%以内の精度が得られた。計算時間はストリーム数の 2～3 乗に比例し、P^1-IMS では同じ精度を得るには 20 以上のストリーム数を必要とするため、P^3-IMS は非常に効率的な計算方法であることがわかった。

後者の研究では、近赤外波長の水蒸気吸収領域の 1 つである 940nm での天空放射輝度の情報を調査した。調査にあたり、狭帯域の天空輝度を 0.3%の精度で計算可能な気体吸収テーブルを新たに開発した。数値実験により、太陽等高度面の天空輝度には可降水量（PWV）に関する情報があり、子午面の天空輝度には PWV に加えてエアロゾルの鉛直プロファイルに関する情報があることがわかった。これらの調査に基づいて、事前/事後校正なしでスカイラジオメーターから PWV を取得する手法（SKYNET/DSRAD）を開発した。実際の SKYNET のスカイラジオメータ観測に適用したところ、マイクロ波放射計と比較してよく一致していることが確認された。

Table of Contents

Chapter 6: Application to the ground-based angular-scanning radiometer observation

Abbreviation

AAOT	Absorption Aerosol Optical Thickness
AERONET	AErosol RObotic NETwork
AFGL	Air Force Geophysics Laboratory
AOT	Aerosol Optical Thickness
AOT500	Aerosol Optical Thickness at 500 nm
CEReS	Center for Environmental Remote Sensing
CKD	Correlated *k*-distribution
CR	Complex Refractive index
ESR	European SKYNET radiometers network
FSTAR	System for Transfer of Atmospheric Radiation for Flux calculation
GNSS/GPS	Global Navigation Satellite System/Global Positioning System
GRASP	Generalized Retrieval of Aerosol and Surface Properties
IL	Improved Langley
IMS	Improved Multiple and Single scattering approximation
IPOL1	scalar mode of PSTAR version 4
IPOL4	full-vector mode of PSTAR version 4
ISDC	International SKYNET Data Center
LBL	Line-By-Line
LUT	Look-Up Table
NEIS	National Institute for Environmental Studies
NS-ratio	Non-Spherical ratio
P^n-IMS	Improved Multiples and Single scattering approximation by *n*-th order multiple scattering correction of the forward Peak
PSTAR	System for Transfer of Atmospheric Radiation for Polarized radiance calculations
PWV	Precipitable Water Vapor
RI	Imaginary part of Refractive index
RR	Real part of Refractive index
RSTAR	System for Transfer of Atmospheric Radiation for Radiance calculations
RTM	Radiative Transfer Model
SDF	Size distribution function
SK2P	SKYMAP version 2.0 with a full-vector mode
SK2R	SKYMAP version 2.0 with a scalar mode

SL	Standard Langley-plot
SN-CKD	StaNdard look-up table of correlated *k*-distribution method implemented in RSTAR
SORD	Successive ORDers of scattering
SSA	Single scattering albedo
STAR	System for Transfer of Atmospheric Radiation
SZA	Solar Zenith Angle
TMS	Truncated Multiple and Single scattering approximation
UV	UltraViolet
V42	SKYRAD.pack Version 4.2
V50	SKYRAD.pack Version 5.0
WV-CKD	look-up table of correlated *k*-distribution method in Water Vapor absorption band
XIL	cross (X) Improved Langley

Nomenclature

Alphabet

$\mathbf{A}^{(m)}$	matrix defined in Eq. (2.14d)
$\mathbf{A}_{\pm}^{(m)}$	$\mathbf{A}^{(m)}$ term defined in Eq. (2.27f)
$\mathbf{A}_{\mathrm{l},\pm}^{(m)}$	$\mathbf{A}^{(m)}$ term in scalar approximation defined in Eq. (2.31f)
$\mathbf{B}_l$	coefficient matrix for $\mathbf{A}^{(m)}$, which contains the Greek constants
$\widehat{\mathbf{B}}_l, \mathbf{B}_l^*$	forward peak and truncated coefficient matrix for $\mathbf{A}^{(m)}$ defined in Eq. (4.2)
$\mathbf{C}_n^{(m)}$	matrix defined in Eq. (4.8d)
C_k	amplitude for size spectrum in the sky-radiometer analysis program defined in Eq. (6.4)
$\mathbf{D}$	diagonal matrix for the relation of mirror symmetry defined in Eq. (2.15a)
D	standard deviation of transmittance of H_2O absorption in sub-band defined in Eq. (5.9a)
$\widehat{\mathbf{D}}$	$\mathbf{D}$ matrix for all discrete ordinate directions defined in Eq. (2.27c)
$\mathbf{D}_k$	auxiliary matrices defined in Eqs. (2.21a) and (2.21b)
$\boldsymbol{D}_1$	vector defined in Eq. (2.34b)
d	distance between Earth and the sun
E	function defined in Eq. (2.59b)
$\mathbf{E}_4$	4×4 unit matrix
$\mathcal{F}$	forward model defined in Eq. (3.1)
F_0	calibration constant
$\tilde{F}_0, \tilde{F}_{\mathrm{ds}}, \tilde{F}_{\mathrm{df}}$	convolved F_0, F_{ds}, and F_{df} by ψ defined in Eq. (2.60)
$\bar{F}_0, \bar{F}_{\mathrm{ds}}, \bar{F}_{\mathrm{df}}$	band-average of F_0, F_{ds}, and F_{df}
$F_{\mathrm{ds}}, F_{\mathrm{df}}$	sensor output current of the direct solar irradiance and diffuse irradiance integrated in the SVA
$F_{\mathrm{df}}^{\downarrow}$	downward horizontal radiative flux
$\boldsymbol{F}_{\mathrm{sol}}$	solar irradiance vector
F_{sol}	extra-terrestrial solar irradiance
$\bar{F}_{\mathrm{sol}}$	band averaged F_{sol} defined in Eq. (2.64c)
f	delta-M truncation fraction defined in Eq. (2.42c)
f_{p}	aerosol/cloud delta-M truncation fraction defined in Eq. (4.20c)
G	cost function defined in Eq. (3.3)
g, h	function defined in Eqs. (2.48c) and (2.56)

h_n	function defined in Eq. (4.17b)
i	imaginary unit defined as $i = \sqrt{-1}$
$\boldsymbol{J}$	source function defined in Eq. (2.8b)
$\boldsymbol{J}_1, \boldsymbol{J}_2, \boldsymbol{J}_3, \boldsymbol{J}_4$	source function of perturb vector radiative transfer defined in Eq. (4.4)
$\boldsymbol{J}_5, \boldsymbol{J}_6$	source function of perturb vector radiative transfer defined in Eq. (4.11)
J_1, J_2, J_3, J_4	source function of perturb scalar radiative transfer defined in Eq. (2.50)
$\mathbf{K}_j, \mathbf{K}_\mathrm{o}, \mathbf{K}_\mathrm{a}$	Jacobian matrix defined in Eq. (3.4)
$\mathbf{K}^\mathrm{S}, \mathbf{K}^\mathrm{NS}$	scattering kernels for spherical and non-spherical particles
$K_\mathrm{ext}^\mathrm{S}, K_\mathrm{ext}^\mathrm{NS}$	kernels of extinction properties for spherical and non-spherical particles
K	temperature
$\mathbf{L}$	rotation matrix defined in Eqs. (2.3-4)
L	diffuse relative radiance defined in Eq. (2.59a)
$\tilde{L}, \tilde{T}$	convolved L and T by ψ defined in Eq. (2.61)
$\bar{L}, \bar{T}$	band-average of L and T defined in Eq. (2.62)
$\hat{L}, \hat{T}$	convolved $\bar{L}$ and $\bar{T}$ by $\bar{\psi}\bar{F}_\mathrm{sol}$ defined in Eqs. (2.64)
$\acute{L}, \acute{T}$	convolved L and T by $\bar{F}_\mathrm{sol}$ defined in Eqs. (5.12a-b)
$\mathbf{M}$	matrix of quadrature points defined in Eq. (2.27a)
$\mathbf{M}_\mathrm{I}$	matrix of quadrature points in scalar approximation defined in Eq. (2.31a)
M_max	maximum order of the expansion by generalized spherical function
M^*	truncation order of the expansion by generalized spherical function
$m_\mathrm{Re}, m_\mathrm{Im}$	real and imaginary parts of the refractive index
$m_{0,j}$	optical air mass of aerosol extinction, Rayleigh scattering, water vapor absorption, and ozone absorption ($j = \mathrm{p}, \mathrm{R}, \mathrm{H2O}, \mathrm{O3}$)
N	number of quadrature points (discrete ordinate directions)
N_band	number of sub-bands
N_ch	number of quadrature points (k distribution)
N_Ω	number of computation direction (Chapter 4)
$\mathbf{P}$	phase matrix defined in Eq. (2.2)
$\hat{\mathbf{P}}, \mathbf{P}^*$	forward peak and truncated phase matrix of $\mathbf{P}$ defined in Eq. (4.1)
P_{11}	phase function
$\hat{P}_{11}, P_{11}^*$	forward peak and truncated phase function of P_{11}
$\mathbf{P}_\mathrm{c}^{(m)}, \mathbf{P}_\mathrm{s}^{(m)}$	cosine and sine series of phase matrix defined in Eqs. (2.14b-c)
$\mathbf{P}_l^m$	expansion matrix for $\mathbf{A}^{(m)}$ defined in Eq. (2.15c)
P_l^j	associated Legendre function
P_l	Legendre function
$P_{m,n}^l$	generalized spherical function

p	pressure
p_0	standard pressure
Q	multiple scattering term of total radiance
R	normalized radiance defined in Eq. (2.58b)
$\tilde{R}$	ratio of $\tilde{L}$ to $\tilde{T}$ defined in Eq. (2.61b)
$\hat{R}$	ratio of $\hat{L}$ to $\hat{T}$ defined in Eq. (5.10a)
R_l^j, T_l^j	auxiliary functions defined in Eqs. (2.16b-c)
$\mathbf{S}_j, \mathbf{S}_\mathrm{o}, \mathbf{S}_\mathrm{a}$	covariance matrix
$\mathbf{S}_\mathrm{o}^{(j)}$	covariance matrix of $\mathbf{S}_\mathrm{o}$ defined in Eq. (6.11b)
$\mathbf{S}_\mathrm{Re}, \mathbf{S}_\mathrm{Im}, \mathbf{S}_\mathrm{Vol}$	covariance matrix of $\mathbf{S}_\mathrm{a}$ defined in Eq. (6.15b)
$\mathbf{S}_{k,\pm}^{(m)}$	source terms defined in Eq. (2.27d)
$\mathbf{S}_{\mathrm{I},\pm}^{(m)}$	source terms in scalar approximation defined in Eq. (2.31c)
T	transmittance
$T_\mathrm{A}, T_\mathrm{R}$	transmittances of aerosol extinction and Rayleigh scattering
$\bar{T}_\mathrm{A}, \bar{T}_\mathrm{R}, \bar{T}_\mathrm{cont}$	band-averaged values of T_A, T_R, and $\bar{T}_\mathrm{cont}$
T_H2O	monochromatic transmittance of H_2O absorption (line and self-continuum)
$\tilde{T}_\mathrm{H20}$	convolved transmittance of H_2O absorption (line and self-continuum)
T_cont	monochromatic transmittance of the O_2 and O_3 continuum absorption
$\tilde{T}_\mathrm{O3}$	convolved transmittance of the O_3 absorption
$T_\mathrm{c}^\mathrm{IMS}, T_\mathrm{c}^\mathrm{TMS}$	CPU time of radiance computation with the IMS and TMS methods defined in Eq. (4.23)
$T_\mathrm{ckd}^{(j)}, R_\mathrm{ckd}^{(j)}$	transmittance and normalized radiance at *j*-th quadrature point of the *k* distribution defined in Eq. (2.62)
$T_\mathrm{H2O,ckd}^{(j)}$	transmittance at *j*-th quadrature point of the H_2O *k* distribution defined in Eq. (5.5b)
t^*	scaled optical thickness defined in Eq. (2.38)
t_Ω	computational time of the IMS correction in each direction defined in Eq. (4.23)
$\mathbf{U}_{k,\pm}^{(m)}$	Stokes term defined in Eq. (2.27e)
$\boldsymbol{u}$	Stokes vector
$\hat{\boldsymbol{u}}$	additional Stokes vector
$\hat{\boldsymbol{u}}_n$	*n*-th order scattering Stokes vector
$\boldsymbol{u}^*$	Stokes vector in truncation space
$\boldsymbol{u}_\mathrm{m}^*$	multiple scattering term of truncated Stokes vector
$\boldsymbol{u}'$	Stokes vector with the P^1-IMS method defined in Eq. (4.3a)
$\boldsymbol{u}_k^{(m)}$	azimuthally separated Stokes vector defined in Eq. (2.23)

$\widetilde{\boldsymbol{u}}$	corrected Stokes vector defined in Eq. (4.19)
$u_{\mathrm{I}}, u_{\mathrm{Q}}, u_{\mathrm{U}}, u_{\mathrm{V}}$	Stokes parameters
u'_{I}	total sky radiance with the TMS method defined
$\hat{u}_{\mathrm{I}}$	additional sky radiance defined in Eq. (2.46)
$\hat{u}_{\mathrm{I},1}, \hat{u}_{\mathrm{I},2}$	first and second scattering radiance defined in Eqs. (2.47) and (2.55)
u^*_{I}	sky radiance in truncation space
$u^*_{\mathrm{I,s}}, u^*_{\mathrm{I,m}}$	single and multiple scattering term of truncated sky radiance
$u'_{\mathrm{I,s}}$	scattering solution with the scaled original phase function
$\mathbf{W}$	matrix of quadrature weights defined in Eq. (2.27b)
$\mathbf{W}_{\mathrm{I}}$	matrix of quadrature weights in scalar approximation defined in Eq. (2.31b)
w	precipitable water vapor
$\boldsymbol{X}, \boldsymbol{Y}$	independent (or explanatory) and dependent variable vector
$\mathbf{Z}_n$	n-th order scattering term of phase matrix defined in Eq. (4.8)
$\hat{\mathbf{Z}}_n$	secondary scattering term of forward peak function
Z_{11}	secondary scattering term of phase function defined in Eq. (2.40)
$\hat{Z}_{11}$	secondary scattering term of forward peak function
$\mathbf{Z}^{(m)}_{\mathrm{c},n}, \mathbf{Z}^{(m)}_{\mathrm{s},n}$	cosine and sine series of $\mathbf{Z}_n$ defined in Eqs. (4.8b-c)

Greek alphabet

α^l_k, β^l_k	Greek constants, which are expansion coefficients of $\mathbf{P}(\Theta)$
$\hat{\alpha}^l_1, \alpha^{*l}_1$	Legendre coefficient of $\hat{P}_{11}$ and P^*_{11} defined in Eqs. (2.43d-e)
γ	correlation coefficient
δ	Delta function
δ_{jk}	Kronecker's delta
η	parameter for size spectrum in the sky-radiometer analysis program defined in Eq. (6.4)
κ	wavenumber
λ	wavelength
$\bar{\lambda}$	central wavelength in sub-band
$\tilde{\lambda}$	effective wavelength with convolved by ψF_{sol}
μ	cosine of polar angle defined in Eq. (2.9)
μ^*	scaled cosine of polar angle defined in Eq. (2.48a)
μ_j, w_j	double-Gaussian quadrature points and weights for discrete ordinate method
ξ_j	quadrature weights of the k-distribution
$\sigma_{\mathrm{ext}}, \sigma_{\mathrm{sca}}, \sigma_{\mathrm{abs}}$	extinction, scattering, and absorption coefficient

$\sigma_{\mathrm{H2O,line}}, \sigma_{\mathrm{H2O,cont}}$	absorption coefficients of the H_2O line and self-continuum absorption
σ_{F_0}	standard deviation of the sky-radiometer calibration constant
$\sigma_{F_{\mathrm{ds}}}, \sigma_{F_{\mathrm{df}}}$	standard deviation of $\tilde{F}_{\mathrm{ds}}$ and $\tilde{F}_{\mathrm{df}}$ in the sky-radiometer measurement
σ_{M}	extra uncertainty defined in Chapter 6
τ	optical thickness
$\tau_{\mathrm{ext}}, \tau_{\mathrm{sca}}$	optical thickness of extinction and scattering defined in Eq. (6.8)
$\tau_{\mathrm{p}}, \omega_{\mathrm{p}}$	aerosol/cloud optical thickness and single scattering albedo
τ_{R}	Rayleigh scattering optical thickness
$\mathbf{\Phi}_k^{(m)}$	base function of Fourier series defined in Eq. (2.22)
Φ	effective bandwidth of filter response function defined in Eq. (5.9b)
ϕ	azimuth angle defined in Eq. (2.9) and Fig. 2.2
$\mathbf{\Psi}_{k,\pm}^{(m)}$	Stokes term defined in Eq. (2.29b)
ψ	filter response function
$\bar{\psi}$	band averaged ψ defined in Eq. (2.64d)
Δ_κ	sub-band interval in wavenumber space
Δ_Ω	field of view or solid view angle
ω	single scattering albedo defined in Eq. (2.7b)
$\hat{\omega}$	peak-scaled single scattering albedo defined in Eq. (2.48b)
ω^*	truncated single scattering albedo defined in Eq. (2.38b)
$\mathbf{\Omega}$	direction vector defined in Eq. (2.9)

Superscript

-1	Inverse matrix
m	Fourier order
T	transpose operation
CKD	correlated *k*-distribution method
LBL	line-by-line approach
R	retrieval variable
M	measurement variable

Subscript

0	solar quantities

Chapter 1: Scientific Background

The information provided in this chapter is based on the papers listed at the end of the chapter. The surface temperature of the Earth has considerably risen within the range of 0.8 to 1.3°C over the past century (IPCC [2021]). The temperature increase has been predicted to reach 1.5°C between 2030 and 2052 if it continues at the current rate (IPCC [2018]); the higher temperatures will be accompanied by increases in extreme weather and natural disasters. This global warming has been driven by atmospheric components, including aerosols, clouds, and gases; substantial uncertainty remains regarding their impacts on the Earth's climate.

For example, black carbon aerosols generated by biomass burning and vehicles have strong light absorption characteristics and cause positive feedback with respect to global warming. In contrast, the sulfate aerosols generated from gases generate negative feedback, although they have an anthropogenic origin (*e.g.*, Nakajima et al. [2020a]). These feedback characteristics have been revealed by the outcomes of laboratory-based experiments, actual observations, and global climate models. There has been increasing information regarding the effects of atmospheric components on global warming since the 5th assessment report (IPCC [2013]) because of an increasing number of atmospheric observations and the development of global climate models. However, considerable estimation uncertainty remains, even in the 6th assessment report (IPCC [2021]). Thus, more information is needed regarding atmospheric components. One such component involves the influence of the various chemical states and particle shapes of atmospheric aerosols, which vary because of their interactions with each other and surrounding gases (*e.g.*, Adachi and Buseck [2015] and Yoshizue et al. [2019]). It is difficult to gather such information from satellite observations with current technology; in situ observations using an electronic microscope are generally required. Recently, an estimation of particle shape from satellite and ground-based radiance observations was attempted, as discussed in Section 1.2. To study the impact of aerosols on the climate, there is rapid progress underway in the measurement of sky radiance by ground-based photometers (*i.e.*, a remote sensing technology). This technique can provide an abundance of information regarding the atmospheric aerosol content and its associated radiative effects (*e.g.*, Nakajima et al. [1983], Dubovik and King [2000], Hashimoto et al. [2012], Sinyuk et al. [2020], and Kudo et al. [2021]).

Atmospheric water vapor, another key factor driving Earth's climate, absorbs near-infrared and visible radiations; it also absorbs and emits infrared radiation to heat and cool the Earth and its atmosphere. Atmospheric heating drives the evaporation of seawater, causing

an increase in temperature via positive feedback (IPCC [2013]). In addition, the distribution of water vapor controls precipitation amounts and aerosol-cloud interactions (Twomey [1990]). Precipitable water vapor (PWV; the column integrated water vapor amount) has been measured using many techniques (*e.g.*, Pérez-Ramírez et al. [2014] and Fragkos et al. [2019]), including radiosondes (*e.g.*, Reber and Swope [1972]), the Global Navigation Satellite System/Global Positioning System receiver (*e.g.*, Bevis et al. [1992] and Shoji [2013]), a microwave radiometer (*e.g.*, Lönert et al. [2009] and Cadeddu et al. [2013]), the Raman lidar system (*e.g.*, Whiteman [2010; 2012]), and a spectroradiometer (*e.g.*, Fowle [1912; 1913; 1915]). The advantages and disadvantages of these instruments are summarized in Table 1.1.

Therefore, it is essential to continuously study atmospheric components, including aerosol and atmospheric water vapor. This chapter provides the historical background to our understanding of the atmospheric radiation process (Section 1.1), details concerning recent progress made with measurement techniques using the ground-based radiometer (Section 1.2.1), and the radiative transfer theory used to calculate the sky radiance distribution (Section 1.2.2).

Table 1.1: Various PWV measurement techniques.

	Temporal resolution	Methodology	Characteristic (○: advantage, ●: disadvantage)
Radiosonde	Twice a day	Temperature, humidity, and pressure are measured by firect measurement sensor with balloon.	●Measurements are conducted at GAW/WMO specific sites. ●long observational time by ascending (~1 h) ●"dry bias" during daytime (*e.g.* , Turner et al. [2003])
Microwave radiometer	High (~ 1-min)	PWV are estimated from brightness temperature in the 22-30 GHz region at 1-min temporal resolution.	●It is limited to distribute worldwide because of high cost. ○High accuracy (*e.g.* , Lönert et al. [2009])
GNSS/GPS receiver	High (~ 5-min)	PWV is estimated from the signal delay with respect to the permanent dipole moment of the water vapor molecule.	○Significant receiver can be available (*e.g.* , GEONET, SOUMINET). ●Complicated postprocessing are required (*e.g.* , Box and Doerflinger [2001]).
Sun-photometer	High (~ 1-min)	PWV is estimated from the atmospheric transmittance around 940 nm.	○Widely distributed by AERONET and SKYNET, but SKYNET does not provide the products. ●Only the data in daytime which is no clouds shading the sun ●Relationship between transmittance and PWV is different for each instruments and each observational site.

1.1. Previous studies of radiative transfer

Earth's climate system is driven by its atmospheric components. Therefore, determination of the net radiative flux is essential to fully understand the Earth's climate (*e.g.*, Manabe and Stricker [1964]). There has been a long history of studies related to radiative transfer (Fig. 1.1). Although there were some attempts to understand the transfer of light before 1666, this section describes the period after 1666 when Isaac Newton discovered "color" (spectrum) in the solar beam using a triangle prism (Shaw [2006]).

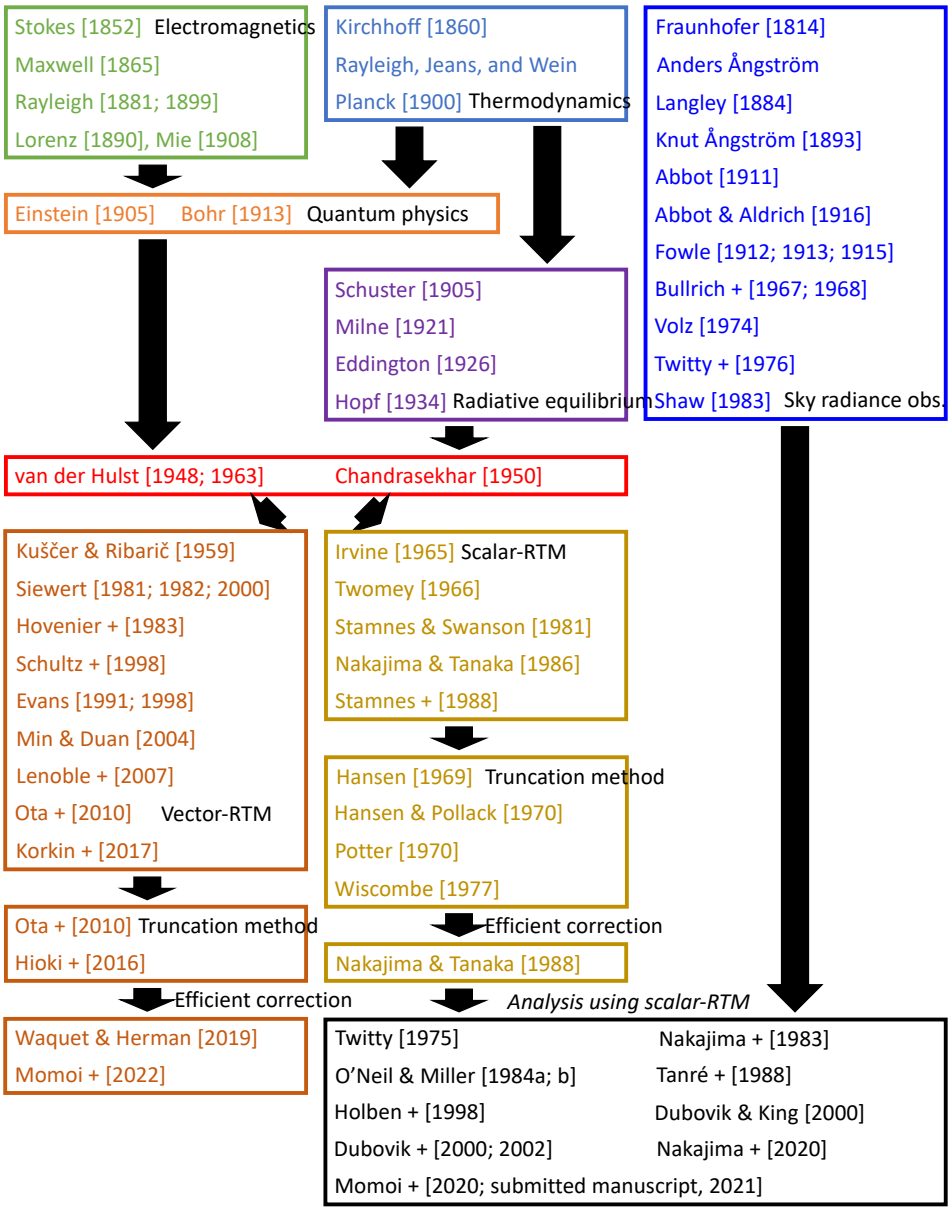

Figure 1.1: Overview of the historical background to our understanding of the radiation process in the atmosphere.

1.1.1. Before the 1950s: studies of relevant fundamental matter

Radiative transfer problems were studied in various fields such as physics, astrophysics, and mathematics. A few decades after Newton's discovery, Christiaan Huygens discovered the polarization phenomena of "double refraction" (birefringence) of calcite crystal, although he could not explain the mechanism (Huygens [1690]).

1.1.1.1. Fundamental studies of radiative transfer theory

After 1850, rapid progress was made in the understanding of particle matter and electromagnetic waves. Stokes [1852] developed a useful expression of the polarization state using observable elements (I, Q, U, and V; see also Chapter 2), which have become known as Stokes parameters. These parameters are commonly used to formulate the vector radiative transfer theory, including polarization effects, which was introduced by Chandrasekhar [1960]. Maxwell systematized the fundamental nature of light in 1865 based on observations by Gauss, Faraday, and Ampere (Griffiths [2013]; Young [2012]). The behavior of electromagnetic waves, which constitute a time-dependent relationship between electric and magnetic fields in a steady-state, can be understood using Maxwell's equations. For example, Lorenz [1890] and Mie [1908] formulated the light scattering of a single spherical particle using Maxwell's equations (Lorenz-Mie theory). For small particles, such as a molecule, Lord Rayleigh explained the radiation scattering behavior that results in the blue color of sky (Rayleigh scattering) (*e.g.*, Rayleigh [1881; 1899]).

During the industrial revolution, thermodynamics was established as a discipline to understand the state of blast-furnaces at high temperatures. The industrial revolution had the harmful side effect of generating air pollution and causing climate issues in future decades. On the basis of thermodynamics investigations, Kirchhoff [1860] proposed the energy conservation law between emission and absorption under a thermodynamic equilibrium (Kirchhoff's law). Subsequently, Wilhelm Wein, Lord Rayleigh, and James Jeans proposed a relationship among wavelength, temperature, and radiative intensity for a black body (known as Wien's radiation law and the Rayleigh-Jeans law). However, they were unable to formulate a specific equation that could be satisfied for any wavelengths (Young [2012]). In 1900, Max Planck proposed a relationship that would hold under any wavelengths (Planck's law), satisfying the Rayleigh-Jeans law and Wien's radiation law at the long and short wavelength limit, respectively.

The concepts (fundamental theories) of particle matter and energy conservation used in modern radiative transfer were established in the early 1990s. However, there were divisions of opinion among researchers (including Christiaan Huygens and Isaac Newton) regarding the question of whether light behaved as a wave or particle; these differences

persisted until 1905, when Albert Einstein introduced the concept of small packages of energy (photons or quanta) (Young [2012]). Max Planck had already proposed a similar treatment to derive Planck's law in 1900. This concept of wave-particle duality was essential for the explanation of gas line absorptions, such as Fraunhofer lines. The mechanism of the line absorptions of hydrogen was studied by Anders Ångström (1814–1874), but he was unable to explain it. Using a simple atomic model of one proton and electron, Niels Bohr explained the emission at a specific wavelength from the atom using classical physics in 1913. This idea was almost equivalent to the Schrödinger equation, as a fundamental equation of modern physics (quantum mechanics) (Griffiths [2014]). The gas line absorption database HITRAN (HIgh resolution TRANsmission; *e.g.*, Rothman et al. [2005]), which is widely used in atmospheric radiation research, was created from experimental data obtained by spectrometers and an understanding of their physics.

Transfer theory was also developed in the 1900s from energy transformations. Arthur Schuster introduced the "scattering process" that occurred during the light transfer process in a "foggy" atmosphere (Schuster [1905]). He formulated the phenomena of isolated scattering by simply treating upward and downward radiation (radiative flux) through a gray atmosphere (including the scattering and absorption processes); this is the fundamental basis of the "two-stream approximation." After several key studies (*e.g.*, Milne [1921], Eddington [1926], and Hopf [1934]), Subrahmanyan Chandrasekhar systematized the theoretical problems related to atmospheric radiative transfer, including particle scattering, in a series of formulas in 1950 (Chandrasekhar [1960]); the concepts underpinning several numerical solution techniques that are used in current radiative transfer models (RTMs) (*e.g.*, the successive order of scattering (van der Hulst [1948]) and discrete ordinate with Gaussian quadrature (Chandrasekhar [1950]) were proposed at that time. Most researchers working at this time treated the azimuth integral radiative transfer (*e.g.*, K-integral (Eddington [1926]) under an unpolarized atmosphere (scalar approximation) because a high computational burden was required to solve radiative transfer using the integrodifferential equation. According to Irvine [1965], even when calculating the n-th order scattering of the source function of the azimuth integral radiative transfer equation by the successive order of scattering concept, there was a time cost of 0.1–0.6 min using a computer in the 1960s (IBM 7094 Model 1). Because of the rapid calculation time, azimuth integral radiative transfers have been used in global climate models (or general circulation models). In summary, these early researchers developed the zeroth order approximation of the Fourier-decomposed azimuth-dependent radiative transfer equation.

1.1.1.2. Measurement of direct solar and diffuse radiation intensities

William Wollaston discovered dark gaps (Fraunhofer lines) in the solar spectrum in 1802, with more than 1000 gaps subsequently identified by Joseph Fraunhofer in 1814 (Shaw [2006]). Anders Ångström (1814–1874) studied the gas absorption lines in the solar spectrum and found "spectral lines" using the unit of 10^{-10} m, which was termed Å after he died (Shaw [2006]). Knut Ångström, Anders Ångström's son, reported the first confirmation that Earth's atmosphere affects sun photometer measurements in 1893; he measured the solar energy at ground level using a pyrheliometer that he had developed (Shaw [2006]). Around that time, Samuel Langley attempted to measure the solar constant using a bolometer (Langley [1884]). Notably, these researchers studied the sun, rather than the Earth's atmosphere and its aerosols and greenhouse gases. After these experiments, the Smithsonian Astronomical Observatory carried out measurements of direct solar and diffuse sky intensities using a pyrheliometer (Abbot [1911]; Abbot and Aldrich [1916]) over 10 years at Montezuma (Chile), Table Mountain (California), and Mount Wilson (California) during the period from 1908 to 1950 in an attempt to determine the solar constant (Roosen et al. [1973]). They measured diffuse radiation for the correction of solar constant monitoring in an approach that was also adopted by Kalitin [1930], Fesenkov [1933], and Pyaskovskaya-Fesenkova [1957] (Terez and Terez [2003]). Also around that time, Fowle [1912; 1913] estimated the PWV using the relationship between PWV and the transmittance of water vapor absorption bands around 1.13 and 1.47 μm at Mount Wilson, California. A few years later, Fowle [1915] conducted observations at multi-elevational sites (Mount Wilson (1730 m), Mount Whitney (4420 m), and Washington (76 m)) using the major water vapor bands. In these monitoring studies, quantities were estimated from a log-log plot between optical air masses and transmittance during the morning or afternoon (Fowle [1913]). This log-log plot is known as a Langley-plot and is currently used for sensor calibration.

1.1.2. After the 1950s: the radiative transfer problem in Earth's atmosphere

1.1.2.1. The radiative transfer problem

The radiative transfer problem has been treated (and recognized) both in the stellar atmosphere and in Earth's atmosphere. Henyey and Greenstein [1941] introduced the "scattering probability" (scattering phase function) of actual observations in astrophysics, which expresses both an isotropic and anisotropic phase function using an asymmetry factor. This phase function has often been used in simulations.

Based on scalar radiative transfer theory (unpolarized radiance), Chandrasekhar [1960] proposed the discrete ordinate method using Gaussian quadrature. According to this formulation, the previous attempts to calculate the radiative flux (*e.g.*, Schuster [1905] and Milne [1921]) could be interpreted as a particular case of 1 hemispheric Gaussian quadrature stream (in total, 2 Gaussian quadrature streams are present in the zenith and nadir directions). Therefore, this technique has been described as a "two-stream approximation." The accuracy of the radiative flux has since been improved using more substantial quadrature streams (*e.g.*, four-stream approximation), but the calculation becomes complicated with increasing stream numbers. In accordance with his numerical solution, Irvine [1965] proposed the successive order of scattering technique for the azimuth-dependent radiative transfer equation, which treats the *n*-th order of scattering. Van der Hulst [1963] and Twomey et al. [1966] proposed the doubling method (or the "adding-doubling" method). Stamnes and Swanson [1981], Nakajima and Tanaka [1986], and Stamnes et al. [1988] proposed discrete ordinate and matrix operator methods for a vertically inhomogeneous atmosphere. Many RTMs have been developed (see also "*Atmospheric radiative transfer codes*" in Wikipedia).

For vector radiative transfer, including polarization effects, Kuščer and Ribarič [1959] developed a formulation using the Stokes parameters (I, Q, U, and V) in a plane-parallel atmosphere based on the work of Chandrasekhar [1960]. For simplification, this theory was re-formulated by Siewert [1981; 1982]. Schultz et al. [1998] and Siewert [2000] proposed the discrete ordinate method. Ota et al. [2010] developed a vector RTM using discrete ordinate and matrix operator methods expanded from works by Nakajima and Tanaka [1983; 1986]. Other techniques (*e.g.*, spherical harmonics discrete ordinate (Evans [1998]), successive order of scattering (Min and Duan [2004]; Lenoble et al. [2007]; Korkin et al. [2017]), and adding-doubling (Hovenier and van der Mee [1983]; de Haan et al. [1987]; Evans [1991]) for the vector radiative transfer equation have also been developed. These vector RTMs were evaluated by several intercomparison projects (*e.g.*, Kokhanovsky et al. [2010] and Emde et al. [2015]), as well as comparisons with various benchmark datasets for

a Rayleigh atmosphere (Coulson et al. [1960]; Nataraj et al. [2009]) and aerosol-laden atmosphere (de Haan et al. [1987]; Wauben et al. [1994]; Garcia and Siewert [1989]; Kokhanovsky et al. [2010]).

Although the diffuse intensity and radiative flux can be calculated by developing solvers (*e.g.*, the discrete ordinate and matrix operator method or the successive order of scattering) for both scalar and vector radiative transfer equations, they have proven it difficult to calculate under aerosol-laden and cloud atmospheres because of anisotropic phase functions (see Figs. 2.3–5). This problem was initially studied by Hansen [1969], Hansen and Pollack [1970], and Potter [1970]. They proposed the scaling method as "truncating" forward scattering energy from the anisotropic phase function under a scalar approximation (see Section 2.5). These techniques have produced accurate estimates of the radiative flux and diffuse intensities, except in the aureole regions. By analyzing the perturbation radiative equation between the exact and truncated radiative transfer equation of the delta-M method (Wiscombe [1977]), Nakajima and Tanaka [1988] proposed the optimal post-processing correction methods (*i.e.*, the Truncated Multiple and Single scattering approximation (TMS) and Improved Multiple and Single scattering approximation (IMS)) for accurate calculations even in the aureole region; the calculations were useful for treatments of the first and second order of scattering, respectively (see Section 2.6). These truncation methods progressed well under a scalar approximation (see the following section). After the 2010s, truncation methods under a scalar approximation were expanded for the vector radiative transfer theory (*e.g.*, Ota et al. [2010] and Hioki et al. [2016]). For accurate calculations in the aureole region under vector radiative transfer, Waquet and Herman [2019] and Momoi et al. [2022] proposed full-vector correction methods for any *n*-th order scattering formulated using a successive order of scattering approach.

1.1.2.2. Monitoring of atmospheric components

By the 1970s, the measurement of multi-wavelength atmospheric transmittance was widely used to monitor air pollution through the development of the sun photometer, using silicon photodiode as a detector (*e.g.*, Volz [1974] and Shaw [1983]). Using such instruments, the diffuse sky radiances of total radiance and the depolarization ratio were measured from the ground and aircraft (*e.g.*, Bullrich et al. [1967; 1968] and Twitty et al. [1976]). In the 1980s, a combined analysis of the direct solar irradiance and angular distribution of the diffuse radiance became available through the development of the rapid but accurate radiative transfer calculation described in the previous section (*e.g.*, O'Neil and Miller [1984a] and Tanré et al. [1988]). It was then possible to estimate aerosol size distributions and the complex refractive index (*e.g.*, Twitty [1975], Nakajima et al. [1983], O'Neil and Miller [1984b], Tanré

et al. [1988], Tonna et al. [1995], Dubovik and King [2000], and Dubovik et al. [2000; 2002]). In the early 2000s, international automatic angular-scanning radiometer networks, such as the AErosol RObotic NETwork (AERONET; http://aeronet.gsfc.nasa.gov; Holben et al. [1998]) and SKYNET (https://www.skynet-isdc.org; Nakajima et al. [2020b]) were established. They mainly measure the direct solar and diffuse irradiances with a finite field of view for estimating aerosol optical (complex refractive index) and the microphysical (volume size distribution) properties in standard operation, rather than polarized radiance; these measurements include the depolarization ratio. Recently, Z. Li et al. [2009] and L. Li et al. [2014] measured the depolarization ratio using the polarized sun-sky photometer CE318-DP, which is an improved version of the AERONET standard instrument. However, no operational analyses have been performed using either AERONET and SKYNET. The Sun-sky radiometer Observation NETwork (SONET) (http://www.sonet.ac.cn), which deploys the CE318-DP, is processing the polarization data, but there remain challenges regarding instrument calibration.

1.2. Overview of recent progress and challenges

As mentioned in the previous section, there are two major international observation networks: SKYNET (Nakajima et al. [2020b]) and AERONET (Holben et al. [1998]). This section describes recent progress and challenges for the ground-based radiometers and data analysis with RTM in AERONET and SKYNET (Table 1.2).

Table 1.2: Previous work that is relevant to this study.

	Ground-based observation using sun-sky radiometer	Radiative transfer modeling with plane-parallel atmosphere (red: scalar, blue: vector, black: other)
Before 1970	Sky radiance observation : e.g., Abbot [1911] Precipitable water vapor were estimated from direct solar irradiance : Fowle [1912; 1913; 1915]	Scattering kernel of spherical particles was developed : Lorenz [1890]; Mie [1908] Systematized radiative transfer problems : Chandrasekhar [1950]
1970s		Efficient calculation for radiative intensity **excluding** aureole region : Hansen [1969]; Hansen+1970]; Potter [1970]; Weinman+ [1975]; Tanaka+ [1977] δ-M method: efficient calculation for radiative **flux** with momentum conservation : Joseph+ [1976]; Wiscombe [1977]
1980s	On-site self-calibration method (IL method) for weak gas absorption band were developed : Tanaka+ [1983]; Nakajima+ [1996]; Campanelli+ [2004; 2007] Aerosol properties were estimated from direct and diffuse radiance using RSTAR : Twitty [1975]; O'Neil+ [1984ab], Nakajima+ [1983; 1996], Tanré+ [1988]; Tonna [1995]	Discrete ordinate method for solving radiative transfer : Stamnes+ [1981]; Nakajima+ [1986]; Stamnes+ [1988] IMS theory: efficient calculation for radiative **intensity including** aureole region : Nakajima+ [1988] RSTAR code including IMS theory (1988) Pcor: correction method of polarization effect on total radiance : Ogawa+ [1989]
1990s	Precipitable water vapor were estimated from transmittance with emprical equation : Bruegge+ [1992] AERONET and SKYNET deployed angular-scanning radiometer analyzed using RSTAR : Holben+ [1998]; Nakajima+ [2020b]	Scattering kernel of spheroidal particles was developed : Mischenko+ [1994]; Yang+ [1996]; Dubovik+ [2006] Correlated k-distribution method: efficient calculation of gas absorption : Lacis+ [1991]; Fu+ [1992] δ-fit method: efficient calculation for radiative **excluding** aureole region : Hu+ [2000]
2000s	Spheroid fraction in aerosols were estimated : Dubovik+ [2006]; Kobayashi+ [2012]; Kudo+ [2021]	PSTAR code for vector RT : Ota+ [2010]
2010s	Polarized radiance distribution on principal plane were measured with an AERONET instrument : Z. Li+ [2009]; L. Li+ [2014] Ozone was estimated from sky-radiometer : Khatri+ [2014]; Kudo+ [2021] Cloud optical properties were estimated from sky-radiometer : Khatri+ [2019] Calibration method at water vapor channel using (modified) Langley-plot method for sky-radiometer : Uchiyama+ [2014; 2018; 2019]; Campanelli+ [2014; 2018]	DOMAS method: efficient calculation for radiative **intensity** : Korkin+ [2011] Vector δ-fit: Extended from δ-fit of Hu et al. (2000) : Hioki+ [2016] SORD code (w/o efficient calculation scheme) : Korkin+ [2017] δ-M+ method: Subspecies of δ-M : Lin+ [2018] Aureole correction method for the intensity derived by Potter-like solution : Waquet+ [2019]
2020s	AERONET data were analyzed using SORD on NASA supercomputer : Sinyuk+ [2020] On-site self-calibration method (IL method) for water vapor band of sky-radiometer were developed : **This study (Momoi+ [2020])** Study of polarization effect on analysis using total radiance (w/o polarized radiance) using RpSTAR : **This study**	P^nIMS theory: extended and generalized from IMS theory for vector RT : **This study (Momoi+ [2022a])** WVCKD: efficient calculation table for water vapor channel of sky-radiometer using CKD method : **This study (Momoi+ [2022b])** RpSTAR code including P^nIMS theory (2022)
Future?	*SKYNET data will be analyzed using vector RTM* *Analysis using polarized radiance will be studied*	

1.2.1. Monitoring by ground-based remote sensing using an angular-scanning radiometer

In SKYNET, the main sky-radiometer models used are POM-01 and POM-02 (Prede, Japan); they both measure the direct solar and diffuse irradiances in the ultraviolet, visible, and near-infrared wavelengths. These measurements are used for the remote sensing of aerosols, cloud, water vapor, and ozone (Table 1.3). Table 1.3 shows the relationships between the wavelengths and the main targets of remote sensing. The aerosol channels are 340, 380, 400, 500, 675, 870, and 1020 nm; the water vapor channel is 940 nm; the ozone channel is 315 nm; and the cloud channels are 1225, 1627, and 2200 nm. Through the on-site self-calibration of the aerosol channels by the Improved Langley (IL) method (Tanaka et al. [1986]; Nakajima et al. [1996]; Campanelli et al. [2004; 2007]) or cross Improved Langley (XIL) method (Nakajima et al. [2020b]), using the unique observational protocol of measuring the direct solar and diffuse irradiances by the same detector, the SKYNET system is capable of long-term and continuous aerosol observation (Fig. 1.2). In AERONET, the sun-sky radiometer model CE-318 (Cimel, France) is mainly used to study objects similar to those measured; however, different detectors measure direct solar irradiance and diffuse irradiances. AERONET conducts replacements and calibration through an annual side-by-side comparison with a reference instrument or a Langley-plot under stable conditions (low aerosol optical thickness (AOT)) (Holben et al. [1998]) because the on-site self-calibration (*i.e.*, IL and XIL) methods are unavailable. The atmospheric transmittances and angular distribution of the diffuse radiances obtained by these instruments contain large amounts of information regarding aerosols (Nakajima et al. [1983]; Nakajima et al. [1996]; Dubovik et al. [2000]), clouds (Khatri et al. [2019]), water vapor (Holben et al. [1998]; Campanelli et al. [2014; 2018]; Uchiyama et al. [2014; 2018; 2019]), and ozone (Khatri et al. [2014]). These physical quantities are estimated by programs using the multi-term least square method (Dubovik and King [2000]; Rogers [2000]) and an RTM as a forward model.

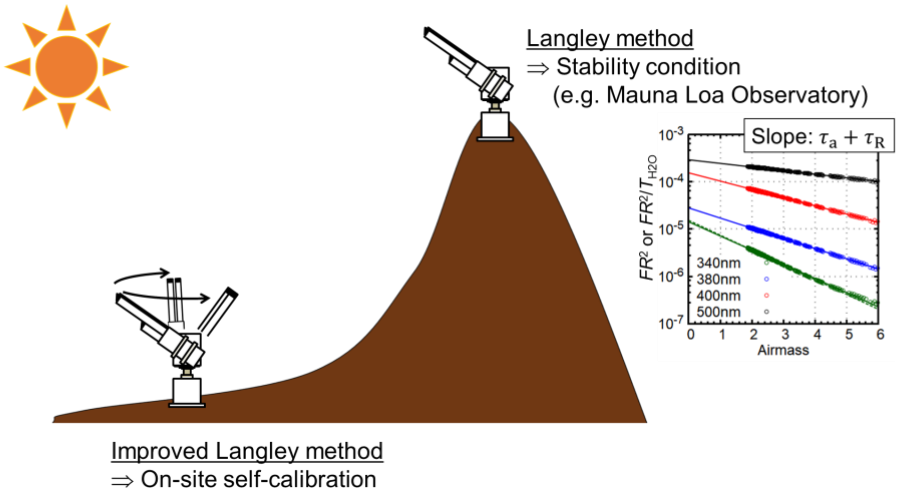

Figure 1.2: Calibration concepts in SKYNET and AERONET.

Table 1.3: SKYNET and AERONET angular-scanning radiometer specifications. Each sky radiometer is equipped with a filter indicated by a circle.

Wavelength [nm]	Gas absorption	Main target substance	POM-01 Standard	POM-02 Standard	CE318-TS9 Standard
315	O_3	Ozone	○	○	—
340	—	Aerosol	—	○	○
380	—	Aerosol	—	○	○
400	—	Aerosol	○	○	—
440	—	Aerosol	—	—	○
500	—	Aerosol	○	○	○
675	—	Aerosol	○	○	○
870	—	Aerosol	○	○	○
937	H_2O	Water vapor	—	—	○
940	H_2O	Water vapor	○	○	—
1020	—	Aerosol	○	○	○
1627	CH_4, CO_2	Cloud	—	○	—
1640	—	Cloud	—	—	○
2200	CH_4, H_2O	Cloud	—	○	—

1.2.1.1. Aerosols

Estimation of physical quantities, particularly aerosol optical and microphysical properties, has developed alongside advances in computational technology and RTM developments. In the 1980s, the combined analysis of the direct solar irradiance and angular distribution of the diffuse radiances became possible through the establishment of a rapid but accurate radiative transfer calculation (*e.g.*, O'Neil and Miller [1984a] and Tanré et al. [1988]). It was then possible to estimate aerosol size distributions and the complex refractive index (*e.g.*, Twitty [1975], Nakajima et al. [1983], O'Neil and Miller [1984b], Tanré et al. [1988], Tonna et al. [1995], Dubovik and King [2000], and Dubovik et al. [2000; 2002]). In the early 2000s, because of developments concerning the scattering kernels of non-spherical particles (Mischenko and Travis [1994]; Yang and Liou [1996]; Dubovik et al. [2006]), the estimation of aerosol sphericity was attempted (Dubovik et al. [2006]; Kobayashi et al. [2010]; Kudo et al. [2021]). A dataset containing the scattering kernels of various particle shapes (Core-gray shell; Voronoi dust; Voronoi soot) was recently developed (Kahnert et al. [2013]; Ishimoto et al. [2010; 2019]). However, the angular distribution of the diffuse polarized radiances contains information regarding particle shapes, rather than the diffuse total radiance measured by traditional SKYNET and AERONET instruments (Li et al. [2009]). Therefore, in recent years, the observance of polarized radiances by ground- and satellite-based photometers has attracted attention but remains difficult to use effectively (Dubovik et al. [2019]).

1.2.1.2. Water vapor

Despite robust progress in aerosol estimation from the angular distribution of the diffuse radiances in aerosol channels, the angular distribution in the gas absorption band has not been used; it remains difficult to calculate the sky radiances for operational analysis because of the extensive computational burden. Therefore, based on estimation of the PWV (*i.e.*, the total atmospheric water vapor contained in a vertical column) using a ground-based sun photometer, the direct solar irradiance has been used in calculations (Fowle [1912; 1913; 1915]; Bruegge et al. [1992]; Schmid et al. [1996; 2001]; Halthore et al. [1997]; Holben et al. [1998]; Campanelli et al. [2014; 2018]; Uchiyama et al. [2014; 2018; 2019]). In SKYNET and AERONET, Campanelli et al. [2014; 2018], Uchiyama et al. [2014; 2018; 2019], and Giles et al. [2019] used the empirical equation $\ln \tilde{T}_{\mathrm{H2O}} = -a(mw)^b$ (Bruegge et al. [1992]) to describe the relationship between the band-averaged transmittance of atmospheric water vapor $\tilde{T}_{\mathrm{H2O}}$ and PWV w. In this equation, a and b are adjustment parameters, which are affected by the filter response function of the radiometer. These parameters are determined using various approaches, including a comparison with other instruments (*e.g.*, Global Navigation Satellite System/Global Positioning System receivers or surface humidity

observations (Campanelli et al. [2014; 2018])) and atmospheric transmittance simulations (Uchiyama et al. [2014]; Giles et al. [2019]). In the later methods, Giles et al. [2019] used the line-by-line (LBL) method (*e.g.*, Rothman et al. [2005; 2013]) under a US standard atmosphere, while Uchiyama et al. [2014] used the correlated *k*-distribution (CKD) method (Lacis and Oinas [1991]; Fu and Liou [1992]) under six Air Force Geophysics Laboratory (AFGL) standard atmospheres. However, Campanelli et al. [2014; 2018] reported that the parameters a and b vary seasonally and spatially because of differences in the vertical profiles of water vapor, temperature, and pressure. Therefore, parameters should be estimated seasonally and spatially, but the implementation of this approach using the LBL method carries a high computational cost. Moreover, to obtain the band-averaged transmittance of atmospheric water vapor, the water vapor channel must be calibrated. The calibration constant (*i.e.*, the sensor output current of the extra-terrestrial solar irradiance at the mean distance between the Earth and the sun) in the water vapor channel can be determined by the Langley method. For example, Uchiyama et al. [2014] calibrated the water vapor channel of a sky-radiometer with a high level of accuracy using observations from the Mauna Loa Observatory (3400 m a.s.l.). The AERONET photometer is calibrated annually by lamp calibration and a side-by-side comparison with a reference spectroradiometer (Holben et al. [1998]). Dedicated effort and expenses are required to maintain accurate long-term calibrations using these methods.

Momoi et al. [2020] report that the angular distribution of diffuse radiances for the water vapor absorption band in the almucantar plane is affected by PWV; they propose another PWV retrieval method based on this relationship using the CKD method. This method is suitable for use with long-term observations because, using the SKYMAP algorithm, a calibration constant can be determined from the PWV data derived from the on-site angular distribution of diffuse radiance. However, this approach requires accurate calculations of sky radiances in the water vapor absorption band by the RTM. Furthermore, new algorithms for the simultaneous retrieval of water vapor and aerosols, as well as an assessment of the retrieval using the water vapor absorption band, are needed because the diffuse radiances at 940 nm in parts of the sky other than the almucantar plane contain information regarding aerosol vertical inhomogeneity (Momoi et al. [2020]). Despite the progress described above, a detailed assessment of the information content of the water vapor and aerosols included in the direct solar irradiance and diffuse radiance is impossible because of the large computational burden. Momoi et al. [2022b] (Chapter 5) report an issue with the CKD method used by Momoi et al. [2020], which is a standard look-up table of the OpenCLASTR project (see next section). After their improvement, an accurate PWV can be attained (Chapter 6).

1.2.2. The calculation of radiative transfer

For the measurement of physical quantities through angular-scanning radiometer observations, RTMs have an essential role. The accurate calculation of sky radiances is more complicated in an aerosol-laden atmosphere than in a molecular atmosphere (or Rayleigh atmosphere) because of the aerosol forward scattering required to treat the high order of the Fourier-decomposed radiative transfer equation. Pioneering studies were conducted by Hansen [1969], Hansen and Pollack [1970], and Potter [1970]. These early methods used a simple angularly smooth function to truncate the forward peak of the original phase function, such as a log-linear function (Potter [1970]; see Section 2.5), Gaussian function sum for a Hankel transformation solution of multiple scattering (Weinman et al. [1975]), and Lorentzian function (Tanaka and Nakajima [1977]). Joseph et al. [1976] and Wiscombe [1977] proposed the delta-M truncation method that conserves the angular moment of the phase function. By comparison of error propagation among the truncation methods mentioned above, Nakajima and Tanaka [1988] determined that the delta-M method (Wiscombe [1977]) was the optimal algorithm for reconstructing whole sky radiances and radiative fluxes. Rozanov and Lyapustin [2010] also reached a similar conclusion on the basis of a comparison with the newer truncation methods of the delta-fit (Hu et al. [2000]) and delta-function (Potter [1970]; Mitrescu and Stephens [2004]). These reports suggested that truncating the phase function with momentum conservation would be a suitable procedure for reconstructing the radiances of the exact angular moment in the whole sky. In this respect, the earlier methods could cause extreme errors distributed throughout the sky. These errors are mainly caused by non-modification of the original phase function at scattering angles larger than the truncation angle. However, compensation of this all-angle modification of the truncated phase function in the delta-M method generates Gibbs type angular fluctuations in the truncated phase function; hence, it generates fluctuations in the calculated radiance (see Fig. 4.3). By solving the perturbed radiative transfer equation, Nakajima and Tanaka [1988] proposed the TMS and IMS correction methods. The TMS and IMS methods suppress the fluctuation by treating the first and second order scattering of the forward peak of the original phase function in the truncation space, respectively (Section 2.4). In addition to the method proposed by Nakajima and Tanaka [1988], several other approaches have been proposed for calculation of forward scattering in a scalar approximation. Korkin et al. [2011] proposed two methods (DOMAS and DOM2+) based on a small-angle modification (*e.g.*, Irvine [1968]). In the aureole region, the DOMAS method is more suitable than the TMS method for coarse aerosol and cloud particles at hemispheric angular integration quadrature streams of 16 and 32 (Korkin et al. [2012]). These methods adopt a smooth truncated phase function and can reconstruct an optimal angular distribution of radiance for large stream numbers. In contrast, the TMS and

IMS methods based on the delta-M method can reconstruct whole sky radiances, including the aureole region, even in the presence of lower hemispheric stream numbers. This includes six streams with errors less than 1% in the aerosol models proposed by Nakajima and Tanaka [1988]. This aspect of the TMS and IMS methods is beneficial for the analysis of large-volumes of data, such as satellite imagery data.

Waquet and Herman [2019] developed a new correction method for the vector RTM truncated by a Gaussian function within a scattering angle of 16°; it was used in the RTM for successive order scattering approximation in the Generalized Retrieval of Aerosol and Surface Properties algorithm (Dubovik et al. [2011]). This method considers high order scatterings in a manner similar to the IMS method. However, it assumes multiple scattering of the forward peak of the original phase function treated by the successive order scattering approximation. Similar to the problem in the DOMAS method with the scalar approximation, this assumption violates the moment conservation of the phase matrix and hence the conservation of polarization radiances at low stream numbers.

The TMS and IMS methods were developed using the System for Transfer of Atmospheric Radiation (STAR) series developed and managed by the OpenCLASTR project (http://157.82.240.167/~clastr/). It includes various RTMs, such as a scalar RTM known as STAR for Radiance calculations (RSTAR; Nakajima and Tanaka [1986; 1988]), a vector RTM known as STAR for Polarized radiance calculations (PSTAR; Ota et al. [2010]), and a flux calculation code known as STAR for Flux calculations (FSTAR; Nakajima et al. [2000]). The RSTAR and PSTAR adopt a combined discrete ordinate and matrix operator method (Stamnes and Swanson [1981]; Nakajima and Tanaka [1986]; Stamnes et al. [1988]) with the delta-M decomposition (Wiscombe [1977]). The RSTAR and PSTAR models with the TMS method can reconstruct the radiance of the aureole regions within 1% error, with low stream numbers of 6–10 in the hemisphere. This is a strong advantage for analyses of large-volume satellite observational data (*e.g.*, Hashimoto and Nakajima [2017], Sekiguchi et al. [2018], and Shi et al. [2019]). The RSTAR model is suitable for analyses of downward sky radiance data from a ground-based angular-scanning radiometer observation led by AERONET and SKYNET using the IMS method, which is an improved version of TMS that can be used to reconstruct sky radiances in the aureole regions.

In AERONET, the RSTAR was used until the AERONET inversion algorithm version 2 (Dubovik and King [2000]); subsequently, it was replaced with a vector RTM (Successive ORDers of scattering (SORD); Korkin et al. [2017]) in the AERONET inversion algorithm version 3 to treat the polarization effect (Sinyuk et al. [2020]). The polarization effect was mainly derived from Rayleigh scattering and enhances the sky radiance by approximately 8%, particularly at small aerosol optical thicknesses and ultraviolet

wavelengths (Fig. 1.3). Therefore, the AERONET inversion algorithm version 3 can accurately calculate sky radiances at ultraviolet wavelengths. However, the computational load for calculations in the aureole region is larger for SORD than for RSTAR; therefore, a supercomputer ("Discover" cluster at the NASA Center for Climate Simulation) is required for operational analysis (Sinyuk et al. [2020]) because SORD has no truncation. An inversion system known as SKYRAD.pack is used in SKYNET, which is based on the RSTAR code (Nakajima et al. [1996]; Kobayashi et al. [2006]; Hashimoto et al. [2012]). The code equips a semi-empirical correction of the polarization effect on the total radiance by Ogawa et al. [1989]. However, this correction method assumes a single homogeneous layer and thus limits aerosol models to the generation of errors ≥ 1% (Fig. 1.4). Although the recent SKYRAD.pack MRI version 2 developed by Kudo et al. [2021] can select a scalar RTM (RSTAR) or full-vector RTM (PSTAR), the PSTAR selection requires a large computational load with a stream number of more than $N = 20$ to calculate the sky radiances in the aureole regions (Chapter 4). Therefore, an improved algorithm based on a full-vector RTM is needed to reconstruct the Stokes vector field. Momoi et al. [2022a] develop IMS by n-th order multiple scattering correction of the forward Peak (P^n-IMS) using PSTAR. Both P^1- and P^2-IMS are formulated for the full-vector radiative transfer theory extended from TMS and IMS, respectively. Additionally, P^n-IMS ($n > 2$) is any n-th order of forward scattering (see Chapter 4). Using this efficient RTM, we determine the difference in the volume size distribution estimated from sky radiance observations between scalar and vector RTMs (Chapter 6).

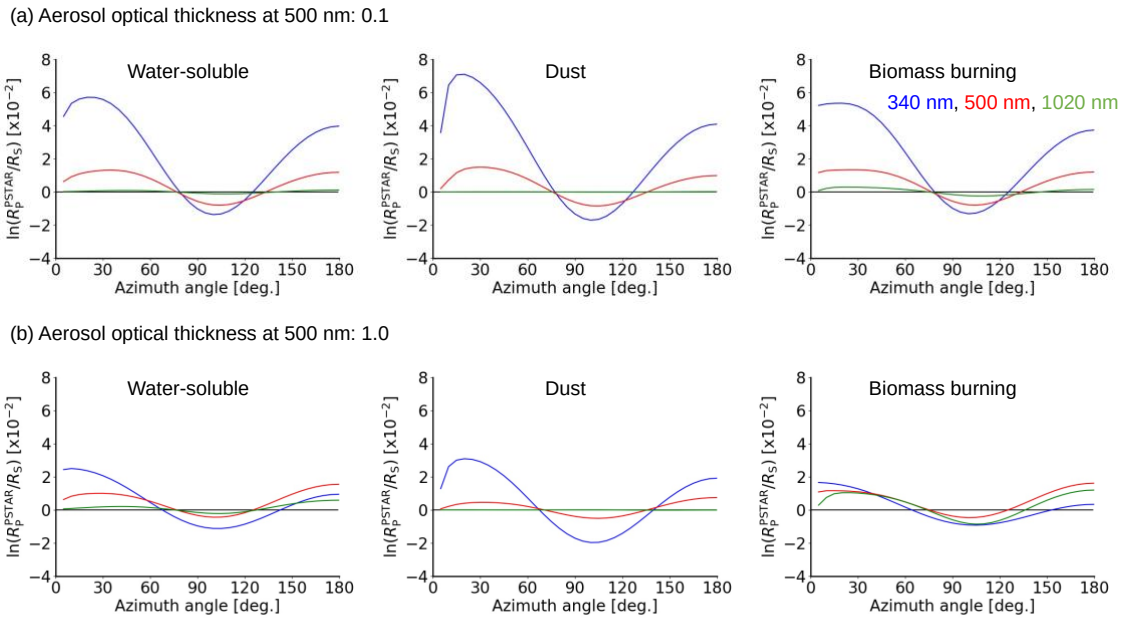

Figure 1.3: Comparison between the intensity with (R_S) and without (R_P^{PSTAR}) the polarized effect computed by PSTAR2/TMS. The aerosol models refer to Dubovik et al. [2000].

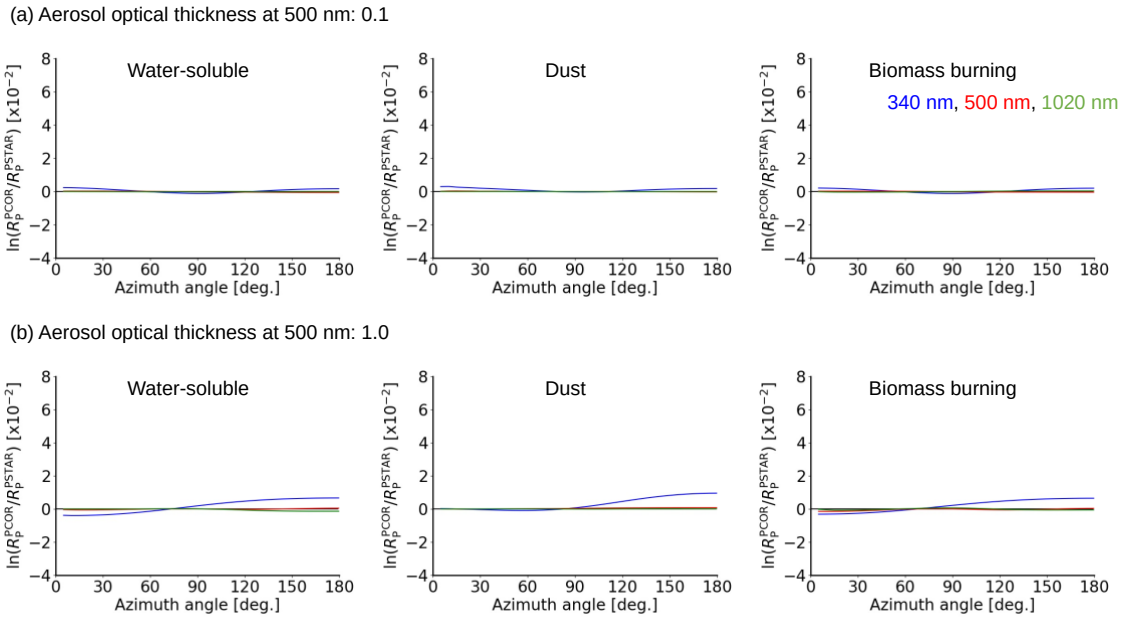

Figure 1.4: As described in Fig. 1.3, but comparing the intensity, including the polarization effect, computed by PSTAR2/TMS (R_P^{PSTAR}) and RSTAR7/TMS, with the polarization correction method proposed by Ogawa et al. [1989] (R_P^{PCOR}). The aerosol models refer to Dubovik et al. [2000].

1.3. Main scopes and purposes

In this study, we develop two efficient radiative transfer computation methods for ground-based radiometer data analysis: first, the development of an efficient computation method (P^n-IMS) of the sky radiances, including the polarization effects; and second, a survey of the information content in the sky radiance in the water vapor absorption region using a newly developed gas absorption table: look-up tables for the CKD method in the 940 nm water vapor absorption region (WV-CKD). This thesis is based on the papers of Momoi et al. [2020; 2022a; 2022b].

References

[1] Abbot, C. G., 1911: The silver disk pyrheliometer, Smithson. Misc. Collect., 56, 11 pp., Smithsonian Institution, Washington, D.C., USA.

[2] Abbot, C. G. and L. B. Aldrich, 1916: The pyranometer- An instrument for measuring sky radiation, Smithson. Misc. Collect., 66, 9 pp., Smithsonian Institution, Washington, D.C., USA.

[3] Adachi K, P. R. Buseck, 2015: Changes in shape and composition of seasalt particles upon aging in an urban atmosphere, Atmos Chem, 100:1–9. doi.org/10.1016/j.atmos env.2014.10.036

[4] Bevis, M., S. Businger, T. A. Herring, C. Rocken, R. A. Anthes, and R. H. Ware, 1992: GPS meteorology: Remote sensing of atmospheric water vapor using the Global Positioning System, J. Geophys. Res., 97, 15787-15801

[5] Bock, O. and Doerflinger, E.: Atmospheric modelling in GPS data analysis for high accuracy positioning, Phys. Chem. Earth, 26, 373–383, 2001.

[6] Bruegge, C. J., J. E. Conel, R. O. Green, J. S. Margolis, R. G. Holm, and G. Roon, 1992: Water vapor column abundance retrievals during FIFE, J. Geophys. Res., 97, 18759-18768

[7] Bullrich, K., Eiden, R., and Nowak,W.: Sky Radiation, polarization and twilight radiation in Greenland, Pure Appl. Geophys., 64, 220–242, 1967.

[8] Bullrich, K., Eiden, R., Jaenicke, R., and Nowak, W.: Solar radiation extinction, sky radiation, sky light polarization and aerosol particle total number and size distribution on the Island Maui (Hawaii), Pure Appl. Geophys., 69, 280–319, 1968.

[9] Cadeddu, M. P., Liljegren, J. C., and Turner, D. D.: The Atmospheric radiation measurement (ARM) program network of microwave radiometers: instrumentation, data, and retrievals, Atmos. Meas. Tech., 6, 2359–2372, https://doi.org/10.5194/amt-6-2359-2013, 2013.

[10] Campanelli, M., Nakajima, T., and Olivieri, B.: Determination of the solar calibration constant for a sun-sky radiometer: proposal of an in-situ procedure, Appl. Opt., 43, 651-659, 2004

[11] Campanelli, M., Estellés, V., Tomasi, C., Nakajima, T., Malvestuto, V., and Martínez-Lozano, J. A.: Application of the SKYRAD Improved Langley plot method for the in situ calibration of CIMEL Sun-sky photometers, Appl. Opt., 46, 2688-2702, 2007

[12] Campanelli, M., T. Nakajima, P. Khatri, T. Takamura, A. Uchiyama, V. Estelles, G. L. Liberti, and V. Malvestuto, 2014: Retrieval of characteristic parameters for water vapour transmittance in the development of ground-based sun-sky radiometric measurements of columnar water vapour, Atmos. Meas. Tech., 7, 1075-1087

[13] Chandrasekhar, S., 1960: Radiative transfer. Dover publications, Inc., New York., ISBN 0-486-60590-6.

[14] Coulson K. L., J. V. Dave, Z. Sekera, 1960: Tables related to radiation emerging from a planetary atmosphere with Rayleigh scattering, Berkely, US: University of California Press.

[15] de Haan, J. F., Bosma, P. B. and Hovenier, J. W., The adding method for multiple scattering calculations of polarized light. Astron. Astrophys. 1987, 183, 371-391

[16] Dubovik, O., Smirnov, A., Holben, B. N., King, M. D., Kaufman, Y. J., Eck, T. F., and Slutsker, I.: Accuracy assessments of aerosol optical properties retrieved from Aerosol Robotic Network (AERONET) Sun and sky radiance measurements, J. Geophys. Res., 105, 9791–9806, 2000

[17] Dubovik, O. and M. D. King, 2000: A flexible inversion algorithm for retrieval of aerosol optical properties from sun and sky radiance measurements, *J. Geophys. Res.*, **105**, 20673–20696

[18] Dubovik, O., Holben, B., Eck, T. F., Smirnov, A., Kaufman, Y. J., King, M. D., Tanré, D., and Slutsker, I.: Variability of absorption and optical properties of key aerosol types observed in worldwide locations, J. Geophys. Res., 59, 590–608, 2002.

[19] Dubovik, O., Sinyuk, A., Lapyonok, T., Holben, B. N., Mishchenko, M., Yang, P., Eck, T. F., Volte, H., Muñoz, O., Veihelmann, B., van der Zande, W. J., Leon, J.-F., Sorokin, M., and Slutsker, I.: Application of spheroid models to account for aerosol particle nonsphericity in remote sensing of desert dust, J. Geophys. Res., 111, D11208, doi:10.1029/2005JD006619, 2006

[20] Dubovik O., M. Herman, A. Holdak, T. Lapyonok, D. Tanré, J. L. Deuzé, F. Ducos, A. Sinyuk, A. Lopatin, 2011: Statistically optimized inversion algorithm for enhanced retrieval of aerosol properties from spectral multi-angle polarimetric satellite observations, Atmos. Meas. Tech., 4, 975-1018.

[21] Dubovik, O., Z. Li, M. I. Mishchenko, D. Tanréa, Y. Karol, B. Bojkov, B. Cairns, D. J. Diner, W. R. Espinosa, P. Goloub, X. Gu, O. Hasekamp, J. Hong, W. Hou, K. D. Knobelspiesse, J. Landgraf, L. Li, P. Litvinov, Y. Liu, A. Lopatin, T. Marbach, H. Maring, V. Martins, Y. Meijer, G. Milinevsky, S. Mukai, F. Parol, Y. Qiao, L. Remer, J. Rietjens, I. Sano, P. Stammes, S. Stamnes, X. Sun, P. Tabary, L. D. Travis, F. Waquet, F. Xu, C. Yan, D. Yin, 2019: Polarimetric remote sensing of atmospheric aerosols: Instruments, methodologies, results, and perspectives, *J. Quant. Spectrosc. Radiat. Transfer*, 224, 474-511

[22] Eddington, A., 1926: The internal constitution of the stars, Cambridge, England, p321

[23] Emde, C., C. Barlakas, C. Cornet, F. Evans, S. Korkin, Y. Ota, L. C. Labonnote, A.

Lyapustin, A. Macke, B. Mayer, and M. Wendisch, 2015: IPRT polarized radiative transfer model intercomparison project – Phase A, *J. Quant. Spectrosc. Radiat. Transfer*, 164, 8-36

[24] Evans, K.F., 1991: A new polarized atmospheric radiative transfer model, *J. Quant. Spectrosc. Radiat. Transfer*, 46(5), 413-423

[25] Evans K.F., 1998: The spherical harmonics discrete ordinate method for three-dimensional atmospheric radiative transfer. J. Atmos. Sci., 55, 429–446

[26] Fesenkov, V. G., 1933: To the question of solar constant determination, Sov. Astron. J., 10, 249–266.

[27] Fowle, F. E.: The spectroscopic determination of aqueous vapor, Astrophys. J., 35, 149-162, 1912

[28] Fowle, F. E.: The determination of aqueous vapor above Mount Wilson, Astrophys. J., 37, 359-372, 1912

[29] Fowle, F. E.: The transparency of aqueous vapor, Astrophys. J., 42, 394-411, 1915

[30] Fragkos, K., Antonescu, B., Giles, D. M., Ene, D., Boldeanu, M., Efstathiou, G. A., Belegante, L., and Nicolae, D.: Assessment of the total precipitable water from a sun photometer, microwave radiometer and radiosondes at a continental site in southeastern Europe, Atmos. Meas. Tech., 12, 1979–1997, https://doi.org/10.5194/amt-12-1979-2019, 2019.

[31] Fu, Q., and K. N. Liou, 1992: On the correlated k-distribution method for radiative transfer in nonhomogeneous atmospheres, *J. Atmos. Sci.*, **49**, 2139–2156.

[32] Garcia R. D. M. ,C. E. Siewert, 1989: The FN method for radiative transfer models that include polarization effects, J. Quant. Spectrosc. Radiat. Transfer., 41(2), 117–45.

[33] Giles, D. M., Sinyuk, A., Sorokin, M. G., Schafer, J. S., Smirnov, A., Slutsker, I., Eck, T. F., Holben, B. N., Lewis, J. R., Campbell, J. R., Welton, E. J., Korkin, S. V., and Lyapustin, A. I.: Advancements in the Aerosol Robotic Network (AERONET) Version 3 database – automated near-real-time quality control algorithm with improved cloud screening for Sun photometer aerosol optical depth (AOD) measurements, Atmos. Meas. Tech., 12, 169-209, https://doi.org/10.5194/amt-12-169-2019, 2019

[34] Griffiths, D. J., 2013: Introduction to Electrodynamics Fourth Edition, PEARSON, 599p

[35] Griffiths, D. J., 2014: Introduction to Quantum Mechanics Second Edition, PEARSON, 427p

[36] Halthore, R. N., T. F. Eck, B. N. Holben, and B. L. Markham, 1997: Sun photometric measurements of atmospheric water vapor column abundance in the 940-nm band, J. Geophys. Res., 102, 4343-4352

[37] Hansen, J. E., 1969: Exact and approximate solutions for multiple scattering by cloudy

and hazy planetary atmospheres, J. Atmos. Sci., 26, 478-487.

[38] Hansen, J. E., and J. B. Pollack, 1970: Near-infrared light scattering by terrestrial clouds, J. Atmos. Sci., 27, 265-281.

[39] Hashimoto, M., Nakajima, T., Dubovik, O., Campanelli, M., Che, H., Khatri, P., Takamura, T., and Pandithurai, G.: Development of a new data-processing method for SKYNET sky radiometer observations, *Atmos. Meas. Tech.*, **5**, 2723-2737, 2012

[40] Hashimoto, M., and T. Nakajima, 2017: Development of a remote sensing algorithm to retrieve atmospheric aerosol properties using multiwavelength and multipixel information, *J. Geophys. Res. Atmos.*, **122**, doi:10.1002/2016JD025698

[41] Henyey, L. G., and J. L. Greenstein, 1941: Diffuse radiation in the galaxy, Astrophys.J., 93, 70-83

[42] Hioki, S., P. Yang, G. W. Kattawar, and Y. Hu, 2016: Truncation of the scattering phase matrix for vector radiative transfer simulation, *J. Quant. Spectrosc. Radiat. Transfer*, **183**, 70–77

[43] Holben, B. N., T. F. Eck, I. Slutsker, D. Tanré, J. P. Buis, A. Setzer, E. Vermote, J. A. Reagan, Y. J. Kaufman, T. Nakajima, F. Lavenu, I. Jankowiak and A. Smirnov, 1998: AERONET-A federated instrument network and data archive for aerosol characterization, *Remote Sens. Environ.*, **66**, 1-16

[44] Hopf, E., 1934: Mathematical problems of radiative equilibrium, Cambridge Mathematical Tracts, No. 31, Cambridge.

[45] Hovenier, J. W., and C. V. M. van der Mee, Fundamental relationships relevant to the transfer of polarized light in a scattering atmosphere. Astron. Astrophys., 1983, 128, 1-16.

[46] Hu Y. X., B. Wielicki, B. Lin, G. Gibson, S. C. Tsay, K. Stamnes, and T. Wong, 2000: δ-fit: a fast and accurate treatment of particle scattering phase functions with weighted singular-value decomposition least-squares fitting, J. Quant. Spectrosc. Radiat. Transfer, 65, 681–690

[47] van der Hulst, H. C., 1948: Scattering in a planetary atmosphere, Astrophys. J., 107, 220–246

[48] van der Hulst, H. C., 1963: A new look at multiple scattering, Tech. Rept, Goddard Institute for Space Studies, New York, p81

[49] Huygens, C., 1690: Traité de la Lumière, (Treatise on Light translated by S.P. Thompson, S.P., University of Chicago Press, 2005).

[50] IPCC, Summary for Policymakers. In: Climate Change 2013: The Physical Science Basis. 5 Contribution of Working Group I to the Fifth Assessment Report of the Intergovernmental 6 Panel on Climate Change [Stocker, T.F., Qin, D., Plattner, G.-K.,

Tignor, M., Allen, S.K., Boschung, J., Nauels, A., Xia, Y., Bex, V., and Midgley, P.M. (eds.)], Cambridge University Press, 8 Cambridge, United Kingdom and New York, NY, USA., 2013

[51] IPCC, 2018: Summary for Policymakers. In: Global Warming of 1.5°C. An IPCC Special Report on the impacts of global warming of 1.5°C above pre-industrial levels and related global greenhouse gas emission pathways, in the context of strengthening the global response to the threat of climate change, sustainable development, and efforts to eradicate poverty [Masson-Delmotte, V., P. Zhai, H.-O. Pörtner, D. Roberts, J. Skea, P.R. Shukla, A. Pirani, W. Moufouma-Okia, C. Péan, R. Pidcock, S. Connors, J.B.R. Matthews, Y. Chen, X. Zhou, M.I. Gomis, E. Lonnoy, T. Maycock, M. Tignor, and T. Waterfield (eds.)]. In Press.

[52] IPCC, 2021: Summary for Policymakers. In: Climate Change 2021: The Physical Science Basis. Contribution of Working Group I to the Sixth Assessment Report of the Intergovernmental Panel on Climate Change [Masson-Delmotte, V., P. Zhai, A. Pirani, S. L. Connors, C. Péan, S. Berger, N. Caud, Y. Chen, L. Goldfarb, M. I. Gomis, M. Huang, K. Leitzell, E. Lonnoy, J.B.R. Matthews, T. K. Maycock, T. Waterfield, O. Yelekçi, R. Yu and B. Zhou (eds.)]. Cambridge University Press. In Press.

[53] Irvine, W. M., 1965: Multiple scattering by large particles, Astrophys. J., 142, 1563–1575.

[54] Irvine, W. M., 1968: Diffuse reflection and transmission by cloud and dust layers, J. Quant. Spectrosc. Radiat. Transfer, 8, 471–485.

[55] Ishimoto, H., Zaizen, Y., Uchiyama, A., Masuda, K., and Mano, Y.: Shape modeling of mineral dust particles for light-scattering calculations using the spatial Poisson-Voronoi tessellation, J. Quant. Spectrosc. Ra., 111, 2434–2443, https://doi.org/10.1016/j.jqsrt.2010.06.018, 2010.

[56] Ishimoto, H., Kudo, R., and Adachi, K.: A shape model of internally mixed soot particles derived from artificial surface tension, Atmos. Meas. Tech., 12, 107–118, https://doi.org/10.5194/amt-12-107-2019, 2019

[57] Joseph, J. H., W. J. Wiscombe, and J. A. Weinman, 1976: The delta-Eddington approximation for radiative flux transfer, *J. Atmos. Sci.*, **33**, 2452-2459

[58] Kahnert, M., Nousiainen, T., and Lindqvist, H.: Models for integrated and differential scattering optical properties of encapsulated light absorbing carbon aggregates, Opt. Express, 21, 7974–7993, 2013.

[59] Kalitin, N. N., 1930: To the question of studying sky radiation intensity around the Sun, Bulletin of Constant Actinometric Commission of Main Geophysical Observatory, 1, 51–56 (in Russian).

[60] Khatri, P., Takamura, T., Yamazaki, A., and Uchiyama, A.: Use of 315 nm channel data

of the sky radiometer to estimate the columnar ozone concentration: A preliminary study, J. Meteorol. Soc. Jpn., 92A, 185–194, https://doi.org/10.2151/jmsj.2014-A12, 2014.

[61] Khatri, P., Iwabuchi, H., Hayasaka, T., Irie, H., Takamura, T., Yamazaki, A., Damiani, A., Letu, H., and Kai, Q.: Retrieval of cloud properties from spectral zenith radiances observed by sky radiometers, Atmos. Meas. Tech., 12, 6037–6047, https://doi.org/10.5194/amt-12-6037-2019, 2019.

[62] Kirchhoff, G., 1860: Ueber das Verhältniss zwischen dem Emissionsvermögen und dem Absorptionsvermögen der Körper für Wärme and Licht, Annalen der Physik und Chemie, 109(2), 275–301. (On the relation between the radiating and absorbing powers of different bodies for light and heat, The London, Edinburgh, and Dublin Philosophical Magazine and Journal of Science, 20, 130, 1-21, Translated by Guthrie, G.)

[63] Kobayashi, E., Uchiyama, A., Yamazaki, A., and Matsuse, K.: Application of the Statistical Optimization Method to the Inversion Algorithm for Analyzing Aerosol Optical Properties from Sun and Sky Radiance Measurements, J. Meteor. Soc. Japan, 84, 1047-1062, 2006

[64] Kobayashi, E., Uchiyama, A., Yamazaki, A., and Kudo, R.: Retrieval of aerosol optical properties based on the spheroid model, J. Meteorol. Soc. Jpn., 88, 847–856, 2010

[65] Kokhanovsky, A., V. P. Budak, C. Cornet, M. Duan, C. Emde, I. L. Katsev, D. A. Klyukov, S. V. Korkin, L. C-Labonnote, B. Mayer, Q. Min, T. Nakajima, Y. Ota, A. S. Prikhach, V. V. Razanov, T. Yokota, E. P. Zege, 2010: Benchmark results in vector atmospheric radiative transfer, J. Quant. Spectrosc. Radiat. Transfer, 111, 1931-1946

[66] Korkin, S. V., A. I. Lyapustin, and V. V. Rozanov, 2011: Analysis of the radiative transfer equation with highly assymetric phase function, J. Quant. Spectrosc. Radiat. Transfer, 112, 1595–1608.

[67] Korkin, S. V., A. I. Lyapustin, and V. V. Rozanov, 2012: Modifications of discrete ordinate method for computations with high scattering anisotropy: Comparative analysis, J. Quant. Spectrosc. Radiat. Transfer, 113, 2040–2048.

[68] Korkin, S., A. Lyapustin, A. Sinyuk, B. N. Holben, and A. Kokhanovsky, 2017: Vector radiative transfer code SORD: Performance analysis and quick start guide, J. Quant. Spectrosc. Radiat. Transfer, 200, 295–310.

[69] Kudo, R., H. Diémoz, V. Estellé, M. Campanelli, M. Momoi, F. Marenco, C. Ryder, O. Ijima, A. Uchiyama, K. Nakashima, A. Yamazaki, R. Nagawasa, N. Ohkawara, and H. Ishida, 2021: Optimal use of the Prede POM sky radiometer for aerosol, water vapor, and ozone retrievals, *Atmos. Meas. Tech.*, **14**, 3395-3426, https://doi.org/10.5194/amt-14-3395-2021

[70] Kuščer, I., and M. Ribarič, 1959: Matrix Formalism in the Theory of Diffusion of Light,

Optica Acta: International Journal of Optics, 6:1, 42-51, DOI: 10.1080/713826264

[71] Lacis, A. A., and V. A. Oinas, 1991: Description if the correlated k-distribution method for modeling nongray gaseous absorption, thermal emission, and multiple scattering in vertically inhomogeneous atmospheres, *J. Geophys. Res.*, **96**, 9027–9063.

[72] Lenoble, J., M. Herman, J. L. Deuzé, B. Lafrance, R. Santer, and D.Tanré, 2007: A successive order of scattering code for solving the vector equation of transfer in the earth's atmosphere with aerosols, J. Quant. Spectrosc. Radiat. Transfer, 107, 479–507.

[73] Li, L., K. Li, L. Blarel, and M. Wendisch, 2014: A method to calculate Stokes parameters and angle of polarization of skylight from polarized CIMEL sun/sky radiometers, J. Quant. Spectrosc. Radiat. Transfer, 149, 334–346.

[74] Li, Z., P. Goloub, O. Dubovik, L. Blarel, W. Zhang, T. Podvin, A. Sinyuk, M. Sorokin, H. Chen, B. Holben, D. Tanré, M. Canini, J-P. Buisc, 2009: Improvements for ground-based remote sensing of atmospheric aerosol properties by additional polarimetric measurements, J. Quant. Spectrosc. Radiat. Transfer, 110(17), 1954–1961.

[75] Löhnert, U., D. D. Turner, and S. Crewell, 2009: Ground-based temperature and humidity profiling using spectral infrared and microwave observations. Part I: Simulated retrieval performance in clear-sky conditions, J. Appl. Meteorol. Climatol., 48, 1017–1032.

[76] Lorenz, L., 1890: Lysbevægelser i og uden for en af plane Lysbølger belyst Kugle. Det kongelige danske Videnskabernes Selskabs Skrifter, 6. Række, naturvidenskabelig og mathematisk Afdeling VI. 1-62.

[77] Manabe, S. and F. Stricker, 1964: Thermal Equilibrium of the Atmosphere with a Convective Adjustment, J. Atmos. Sci., 21, 361-385.

[78] Mie G. Beiträge, 1908: zur Optik trüber Medien speziell kolloidaler Goldlösungen (contributions to the optics of diffuse media, particular colloid metal solutions). Ann Phys, 25, 377–445.

[79] Milne, E.A., 1921: Radiative equilibrium in the outer layers of a star, Monthly Notices of the Royal Astronomical Society, Vol. 81, p.361-375

[80] Min, Q.-L., and M. Duan, 2004: A successive order of scattering model for solving vector radiative transfer in the atmosphere, J. Quant. Spectrosc. Radiat. Transfer, 87, 243–259.

[81] Mishchenko, M. I., and L. D. Travis, 1994: T-matrix computations of light scattering by large spheroidal particles, Opt. Commun., 109, 16– 21.

[82] Mitrescu, C., and G. L. Stephens, 2004: On similarity and scaling of the radiative transfer equation, *J. Quant. Spectrosc. Radiat. Transfer*, **86**, 387–394

[83] Momoi, M., R. Kudo, K. Aoki, T. Mori, K. Miura, H. Okamoto, H. Irie, Y. Shoji, A. Uchiyama, O. Ijima, M. Takano, and T. Nakajima, Development of on-site self-

calibration and retrieval methods for sky-radiometer observations of precipitable water vapor, Atmos. Meas. Tech., 13, 2635–2658, https://doi.org/10.5194/amt-13-2635-2020, 2020.

[84] Momoi, M., H. Irie, T. Nakajima, and M. Sekiguchi, Efficient calculation of radiative intensity including the polarization effect in moderately thick atmospheres using a truncation approximation, J. Quant. Spectrosc. Radiat. Transfer, 2022a, 277, 107976, https://doi.org/10.1016/j.jqsrt.2021.107976.

[85] Momoi, M., H. Irie, M. Sekiguchi, T. Nakajima, H. Takenaka, K. Miura, and K. Aoki, Rapid, accurate computation of narrow-band sky radiance in the 940 nm gas absorption region using the correlated *k*-distribution method for sun-photometer observations, Prog. Earth Planet. Sci., 9, 10, https://doi.org/10.1186/s40645-022-00467-6, 2022b.

[86] Nakajima, T., M. Tanaka, and T. Yamauchi, 1983: Retrieval of the optical properties of aerosols from aureole and extinction data. Appl. Opt., 22, 2951-2959.

[87] Nakajima, T., and M. Tanaka, 1986: Matrix formulations for the transfer of solar radiation in a plane-parallel scattering atmosphere. J. Quant. Spectrosc. Radiat. Transfer, 35, 13–21

[88] Nakajima, T., and M. Tanaka, 1988: Algorithms for radiative intensity calculations in moderately thick atmospheres using a truncation approximation. J. Quant. Spectrosc. Radiat. Transfer, 40, 51–69

[89] Nakajima, T., Tonna, G., Rao, R., Boi, P., Kaufman, Y., and Holben, B.: Use of Sky brightness measurements from ground for remote sensing of particulate polydispersions, Appl. Opt., 35, 2672-2686, 1996

[90] Nakajima, T., M. Tsukamoto, Y. Tsushima, A. Numaguti, and T. Kimura, 2000: Modeling of the radiative process in an atmospheric general circulation model. Appl. Opt., 39, 4869-4878, doi:10.1364/AO.39.004869.

[91] Nakajima, T., T. Ohara, T. Masui, T. Takemura, K. Yoshimura, D. Goto, T. Hanaoka, S. Itahashi, G. Kurata, J. Kurokawa, T. Maki, Y. Masutomi, M. Nakata, T. Nitta, X. Seposo, K. Sudo, C. Suzuki, K. Suzuki, H. Tsuruta, K. Ueda, S. Watanabe, Y. Yu, K. Yumimoto, S. Zhao, 2020a: A development of reduction scenarios of the short-lived climate pollutants (SLCPs) for mitigating global warming and environmental problems, Prog. Earth Planet. Sci., doi:10.1186/s40645-020-00351-1

[92] Nakajima, T., M. Campanelli, H. Che, V. Estellés, H. Irie, S. Kim, J. Kim, D. Liu, T. Nishizawa, G. Pandithurai, V. K. Soni, B. Thana, N. Tugjsurn, K. Aoki, S. Go, M. Hashimoto, A. Higurashi, S. Kazadzis, P. Khatri, N. Kouremeti, R. Kudo, F. Marenco, M. Momoi, S.S. Ningombam, C. L. Royder, A. Uchiyama, and A. Yamazaki, 2020b: An overview of and issues with sky radiometer technology and SKYNET, *Atmos. Meas.*

Tech., **13**, 4195-4218, https://doi.org/10.5194/amt-13-4195-2020.

[93] Nataraj V., K-F. Li, Y. I. Young, 2009: Rayleigh scattering in planetary atmospheres: corrected tables through accurate computation of X and Y functions, Astrophys J., 691, 1909–20.

[94] Ogawa, H., M. Tanaka, and T. Nakajima, 1989: A Simple Expression for the Additional Sky Radiance Produced by Polarization Effects, *J. Meteorol. Soc. Jpn.*, **67** (5), 877–888.

[95] O'Neill, N. T. and Miller, J. R.: Combined solar aureole and solar beam extinction measurements. 1: Calibration considerations, Appl. Optics, 23, 3691–3696, 1984a.

[96] O'Neill, N. T. and Miller, J. R.: Combined solar aureole and solar beam extinction measurements. 2: Studies of the inferred aerosol size distribution, Appl. Optics, 23, 3697–3703, 1984b

[97] Ota, Y., A. Higurashi, T. Nakajima, and T. Yokota, 2010: Matrix formulations of radiative transfer including the polarization effect in a coupled atmosphere–ocean system. *J. Quant. Spectrosc. Radiat. Transfer*, **111**, 878–894

[98] Pérez-Ramírez, D., D. N. Whiteman, A. Smirnov, H. Lyamani, B. N. Holben, R. Pinker, M. Andrade, and L. Alados-Arboledas (2014), Evaluation of AERONET precipitable water vapor versus microwave radiometry, GPS, and radiosondes at ARM sites, J. Geophys. Res. Atmos., 119, 9596–9613, doi:10.1002/2014JD021730.

[99] Planck, M., 1900: Zur Theorie des Gesetzes der Energieverteilung im Normalspectrum, Deutsche Physikalische Gesellschaft, 2, 237–245.

[100] Potter, J. F., 1970: The delta function approximation in radiative transfer theory, *J. Atmos. Sci.*, **27**, 943–949.

[101] Pyaskovskaya-Fesenkova, E. V., 1957: Investigations of atmospheric scattering light, Acad. Sci. USSR, Moscow, Russia, 218 pp.

[102] Rayleigh, Load, 1881: X. On the electromagnetic theory of light, The London, Edinburgh, and Dublin Philosophical Magazine and Journal of Science, 12:73, 81-101, DOI: 10.1080/14786448108627074

[103] Rayleigh, Load, 1899: XXXIV. On the transmission of light through an atmosphere containing small particles in suspension, and on the origin of the blue of the sky, The London, Edinburgh, and Dublin Philosophical Magazine and Journal of Science, 47:287, 375-384, DOI: 10.1080/14786449908621276.

[104] Reber, E. E. and Swope, J. R.: On the Correlation of the Total Precipitable Water in a Vertical Column and Absolute Humidity at the Surface, J. Appl. Meteorol., 11, 1322–1325, https://doi.org/10.1175/1520-0450(1972)011<1322:OTCOTT>2.0.CO;2, 1972.

[105] Rodgers, C. D., 2000: Inverse Method for Atmospheric Sounding, World Sci., Singapore, 256 pp

[106] Rothman, L.S. D. Jacquemart, A. Barbe, D. Chris Benner, M. Birk L. R. Brown, M. R. Carleer, C. Chackerian Jr., K. Chance, L. H. Coudert, V. Dana, V. M. Devi, J.-M. Flaud, R. R. Gamache, A. Goldman, J.-M. Hartmann, K. W. Jucks, A. G. Maki, J.-Y. Mandin, S. T. Massie, J. Orphal, A. Perrin, C. P. Rinsland, M. A. H. Smith, J. Tennyson, R. N. Tolchenov, R. A. Toth, J. Vander Auwera, P. Varanasi, and G. Wagner, 2005: The HITRAN 2004 molecular spectroscopic database, J. Quant. Spectrosc. Radiat. Transfer, 96(2), 139–204, https://doi.org/10.1016/j.jqsrt.2004.10.008

[107] Rothman, L.S., I.E. Gordon, Y. Babikov, A. Barbe, D. Chris Benner, P.F. Bernath, M. Birk, L. Bizzocchi, V. Boudon, L.R. Brown, A. Campargue, K. Chance, E.A. Cohen, L.H. Coudert, V.M. Devi, B.J. Drouin, A. Fayt, J.-M. Flaud, R.R. Gamache, J.J. Harrison, J.-M. Hartmann, C. Hill, J.T. Hodges, D. Jacquemart, A. Jolly, J. Lamouroux, R.J. Le Roy, G. Li, D.A. Long, O.M. Lyulin, C.J. Mackie, S.T. Massie, S. Mikhailenko, H.S.P. Müller, O.V. Naumenko, A.V. Nikitin, J. Orphal, V. Perevalov, A. Perrin, E.R. Polovtseva, C. Richard, M.A.H. Smith, E. Starikova, K. Sung, S. Tashkun, J. Tennyson, G.C. Toon, Vl.G. Tyuterev, G. Wagner, 2013: The HITRAN2012 molecular spectroscopic database, J. Quant. Spectrosc. Radiat. Transfer, 130, 4 –50, https://doi.org/10.1016/j.jqsrt.2013.07.002

[108] Rozanov, V. V., and A. I. Lyapustin, 2010: Similarity of radiative transfer equation: error anal- ysis of phase function truncation techniques. *J. Quant. Spectrosc. Radiat. Transfer*, **111**, 1964–1979

[109] Schmid, B., K. J. Thome, P. Demoulin, R. Peter, C. Matzler, and J. Sekler, 1996: Comparison of modeled and empirical approaches for retrieving columnar water vapor from solar transmittance measurements in the 0.94-mm region, J. Geophys. Res., 101, 9345-9358

[110] Schmid, B., J. J. Michalsky, D. W. Slater, J. C. Barnard, R. N. Halthore, J. C. Liljegren, B. N. Holben, T. F. Eck, J. M. Livingston, P. B. Russell, T. Ingold, and I. Slutsker, 2001: Comparison of columnar water-vapor measurements from solar transmittance methods, Appl. Opt., 40, 1886-1896

[111] Shaw, G. E., 1983: Sun photometry. Bull. Amer. Meteor. Soc., 64, 4–10.

[112] Shaw, G. E., 2006: Genesis of sun photometry, Proc. SPIE 6362, Remote Sensing of Clouds and the Atmosphere, XI, 636201, https://doi.org/10.1117/12.692771

[113] Shoji, Y., 2013: Retrieval of Water Vapor Inhomogeneity Using the Japanese Nationwide GPS Array and its Potential for Prediction of Convective Precipitation, J. Meteor. Soc. Japan, 91, 43-62

[114] Siewert CE, 1981: On the equation of transfer relevant to the scattering of polarized light. *Astrophys J*, 245, 1080–6

[115] Siewert CE, 1982: On the phase matrix basic to the scattering of polarized light, *Astron Astrophys*, 109, 195–200

[116] Siewert CE, 2000: A discrete-ordinates solution for radiative-transfer models that include polarization e!ects, *J. Quant. Spectrosc. Radiat. Transfer*, 64, 227–254.

[117] Sekiguchi, M., H. Iwabuchi, T. M. Nagao, and T. Nakajima, 2018: Development of Gas Absorption Tables and an Atmospheric Radiative Transfer Package for Applications Using the Advanced Himawari Imager, *J. Meteorol. Soc. Japan*, **96B**, 77-89, https://doi.org/10.2151/jmsj.2018-007

[118] Shaw, G., 2006: Genesis of sun photometry, Proc. SPIE 6362, Remote Sensing of Clouds and the Atmosphere XI, 636201, doi:10.1117/12.692771

[119] Shi, C., M. Hashimoto, and T. Nakajima, 2019: Remote sensing of aerosol properties from multi-wavelength and multi-pixel information over the ocean, *Atmos. Chem. Phys.*, **19**, 2461–2475

[120] Sinyuk, A., B. N. Holben, T. F. Eck, D. M. Giles, I. Slutsker, S. Korkin, J. S. Schafer, A. Smirnov, M. Sorokin, and A. Lyapustin, 2020: The AERONET Version 3 aerosol retrieval algorithm, associated uncertainties and comparisons to Version 2, *Atmos. Meas. Tech.*, **13**, 3375–3411, https://doi.org/10.5194/amt-13-3375-2020.

[121] Stamnes, K., and R. Swanson, 1981: A new look at the discrete ordinate method. for radiative transfer calculations in anisotropically scattering atmospheres. J. Atmos. Sci., 38, 387-398.

[122] Stamnes, K., S.-C. Tsay, W. Wiscombe, and K. Jayaweera, 1988: Numerically stable algorithm for discrete-ordinate-method radiative transfer in multiple scattering and emitting layered media. Appl. Opt., 27, 2502-2509.

[123] Stokes, G. G., 1852: On the composition and resolution of streams of polarized light from different sources. Transactions of the Cambridge Philosophical Society, 9, 399.

[124] Tanaka, M., and T. Nakajima, 1977: Effects of oceanic turbidity and index of refraction of hydrosols of the flux of solar radiation in the atmosphere-ocean system, *J. Quant. Spectrosc. Radiat. Transfer*, **18**, 93-111.

[125] Tanaka, M., Nakajima, T., and Shiobara, M.: Calibration of a sunphotometer by simultaneous measurements of direct-solar and circumsolar radiances, Appl. Opt., 25, 1170-1176, 1986

[126] Tanré, D., Devaux, C., Herman, M. and Santer, R.: Radiative properties of desert aerosols by optical ground-based measurements at solar wavelengths, J. Geophys. Res., 93, 14223–14231, 1988.

[127] Terez, E. I., and G. A. Terez, G. A., 2003: A method to determine atmospheric optical depth using observations of direct solar radiation, J. Geophys. Res., 108, 4704,

https://doi.org/10.1029/2003JD003829.

[128] Tonna, G., Nakajima, T., and Rao, R.: Aerosol features retrieved from solar aureole data: A simulation study concerning a turbid atmosphere, Appl. Optics, 34, 4486–4499, 1995.

[129] Turner, D. D., B. M. Lesht, S. A. Clough, J. C. Liljegren, H. E. Revercomb, and D. C. Tobin, 2003: Dry bias and variability in Vaisala RS80-H radiosondes: The ARM experience, J. Atmos. Oceanic Technol., 20, 117–132.

[130] Twitty, J. T.: The inversion of aureole measurements to derive aerosol size distributions. J. Atmos. Sci., 32, 584–591, 1975.

[131] Twitty, J. T., R. J. Parent, J. A. Weinman, and E. W. Eloranta, 1976: Aerosol size distribution: remote determination from airborne measurements of the solar aureole, Appl. Optics, 15, 980–989.

[132] Twomey, S., H. Jacobowitz, and H. B. Howell, 1966: Matrix methods for multiple-scattering problems, J. Atmos. Sci., 23, 289-296.

[133] Twomey, S.A.: Aerosol cloud physics and radiation, in Seventh Conf. on Atm. Rad., AMS, San Francisco, CA, pp. j25-j28, 1990

[134] Uchiyama, A., Yamazaki, A., and Kudo, R., 2014: Column Water Vapor Retrievals from Sky Radiometer (POM-02) 940 nm Data, J. Meteorol. Soc. Jpn., 92A, 195–203

[135] Uchiyama A., Matsunaga, T., and Yamazaki, A., 2018: The instrument constant of sky radiometers (POM-02) – Part 1: Calibration constant, Atmos. Meas. Tech., 11, 5363-5388

[136] Uchiyama, A., M. Shiobara, H. Kobayashi, T. Matsunaga, A. Yamazaki, K. Inei, K. Kawai, and Y. Watanabe, 2019: Nocturnal aerosol optical depth measurements with modified sky radiometer POM-02 using the moon as a light source, Atmos. Meas. Tech., 12, 6465–6488, https://doi.org/10.5194/amt-12-6465-2019.

[137] Volz, F. E., 1974: Economical Multispectral Sun Photometer for Measurements of Aerosol Extinction from 0.44 μm to 1.6 μm and Precipitable Water, Appl. Optics, 13, 1732–1733.

[138] Waquet, F., and M. Herman, 2019: The truncation problem, *J. Quant. Spectrosc. Radiat. Transfer*, **229**, 80-91

[139] Wauben W. M. F. , J. F. deHaan, J. W. Hovenier, 1994: A method for computing visible and infrared polarized monochromatic radiation in planetary atmospheres, Astron. Astrophys., 282, 277–90.

[140] Weinman, J. A., J. T. Twitty, S. R. Browning, and B. M. Herman, 1975: Derivation of phase functions from multiply scattered sunlight transmitted through a hazy atmosphere, *J. Atmos. Sci.*, **32**, 577-583.

[141] Whiteman, D. N., Rush, K., Rabenhorst, S., Welch, W., Cadirola, M., McIntire, G., Russo,

F., Adam, M., Venable, D., Connell, R., Veselovskii, I., Forno, R., Mielke, B., Stein, B., Leblanc, T., Mc- Dermid, S., and Vo¨mel, H.: Airborne and Ground-based measurements using a High-Performance Raman Lidar, 27, 1781– 1801, doi:10.1175/2010JTECHA1391, 2010.

[142] Whiteman, D. N., Cadirola, M., Venable, D., Calhoun, M., Miloshevich, L., Vermeesch, K., Twigg, L., Dirisu, A., Hurst, D., Hall, E., Jordan, A., and Vömel, H.: Correction technique for Raman water vapor lidar signal-dependent bias and suitability for water vapor trend monitoring in the upper troposphere, Atmos. Meas. Tech., 5, 2893–2916, https://doi.org/10.5194/amt-5-2893-2012, 2012.

[143] Wiscombe W., 1977: The delta-M method: rapid yet accurate radiative flux calculations for strongly asymmetric phase functions, *J Atmos Sci*, 34, 1408–22.

[144] Yang, P., and K. N. Liou, 1996: Geometric-optics-integral-equation method for light scattering by nonspherical ice crystals, Appl. Opt., 35, 6568– 6584.

[145] Young F., 2012: University Physics with Modern Physics Thirteenth Edition, PEARSON, 1521p

[146] Yoshizue, M., Y. Iwamoto, K. Adachi, S. Kato, K. Miura, M. Uematsu, 2019: Individual particle analysis of marine aerosols collected during the North–South transect cruise in the Pacific Ocean and its marginal seas, Journal of Oceanography, doi.org/10.1007/s10872-019-00519-4

Chapter 2: Atmospheric radiative transfer

This section provides the radiative transfer theory in the Earth atmosphere with assumptions of non-refraction and plane-parallel atmosphere based on the textbooks by Chandrasekhar [1960], Asano [2010], and Hovenier et al. [2004]. Sections 2.7 and 2.8 are based on the theoretical discussion in Momoi et al. [2022]. These assumptions are valid under the clear sky in the aerosol-laden atmosphere in the range of the wavelength of < 4 μm. They are often used to analyze the ground-based angular-scanning radiometer (AERONET and SKYNET) measuring the ultraviolet to near-infrared radiances.

2.1. Polarized radiation

Light (electromagnetic radiation), a transverse wave, consists of the wave of electromagnetic field. The electric and magnetic fields are perpendicular (Fig. 2.1; Young [2012]). Thus, light has a propagating plane known as "polarization." Conventionally, the state of the polarization is expressed by the electric field. Figure 2.2 shows two polarized radiances (linear and circular polarizations) with different superpositions. Such state can be expressed by Stokes parameters (I, Q, U, and V) which consists of observable radiances (Stokes [1852]). Using these parameters, we can express the polarization state as follows:

1) Linear polarized radiance (parallel): $\boldsymbol{u} \equiv [\,\mathrm{I, Q, U, V}]^{\mathrm{T}} = [\,1,1,0,0]^{\mathrm{T}}$
2) Linear polarized radiance (perpendicular): $\boldsymbol{u} \equiv [\,\mathrm{I, Q, U, V}]^{\mathrm{T}} = [\,1,-1,0,0]^{\mathrm{T}}$
3) Linear polarized radiance (+ 45°): $\boldsymbol{u} \equiv [\,\mathrm{I, Q, U, V}]^{\mathrm{T}} = [\,1,0,1,0]^{\mathrm{T}}$
4) Linear polarized radiance (- 45°): $\boldsymbol{u} \equiv [\,\mathrm{I, Q, U, V}]^{\mathrm{T}} = [\,1,0,-1,0]^{\mathrm{T}}$
5) Right-hand circular polarized radiance: $\boldsymbol{u} \equiv [\,\mathrm{I, Q, U, V}]^{\mathrm{T}} = [\,1,0,0,1]^{\mathrm{T}}$
6) Right-hand circular polarized radiance: $\boldsymbol{u} \equiv [\,\mathrm{I, Q, U, V}]^{\mathrm{T}} = [\,1,0,0,-1]^{\mathrm{T}}$
7) Unpolarized radiance: $\boldsymbol{u} \equiv [\,\mathrm{I, Q, U, V}]^{\mathrm{T}} = [\,1,0,0,0]^{\mathrm{T}}$

The radiative transfer equation is extended to a pseudo-vector equation of the Stokes radiance vector $\boldsymbol{u} = \left[u_{\mathrm{I}}, u_{\mathrm{Q}}, u_{\mathrm{U}}, u_{\mathrm{V}}\right]^{\mathrm{T}}$, including the polarization effects (Chandrasekhar [1960]). Then, because the solar beam is unpolarized, $\boldsymbol{F}_{\mathrm{sol}}$ is given as

$$\boldsymbol{F}_{\mathrm{sol}} \equiv [F_{\mathrm{sol}}, 0,0,0]^{\mathrm{T}}. \tag{2.1}$$

The phase matrix (Figs. 2.3-5) related to the Stokes vector is written in the following form (Hovenier et al. [2004]):

$$\mathbf{P}(\Theta) = \begin{pmatrix} P_{11}(\Theta) & P_{12}(\Theta) & 0 & 0 \\ P_{12}(\Theta) & P_{22}(\Theta) & 0 & 0 \\ 0 & 0 & P_{33}(\Theta) & P_{34}(\Theta) \\ 0 & 0 & -P_{34}(\Theta) & P_{44}(\Theta) \end{pmatrix}, \tag{2.2}$$

where $\mathbf{P}(\Theta)$ is the phase matrix in the scattering plane. The phase matrix is transformed to the local median plane, which is defined as a principal plane (*e.g.*, Li et al. [2014]), by a rotation matrix as follows:

$$\mathbf{P}(\Omega, \Omega_0) = \mathbf{L}(\pi - \chi_1)\mathbf{P}(\Theta)\mathbf{L}(-\chi_2), \tag{2.3}$$

$$\mathbf{L}(\chi) \equiv \begin{pmatrix} 1 & 0 & 0 & 0 \\ 0 & \cos 2\chi & \sin 2\chi & 0 \\ 0 & -\sin 2\chi & \cos 2\chi & 0 \\ 0 & 0 & 0 & 1 \end{pmatrix}. \tag{2.4}$$

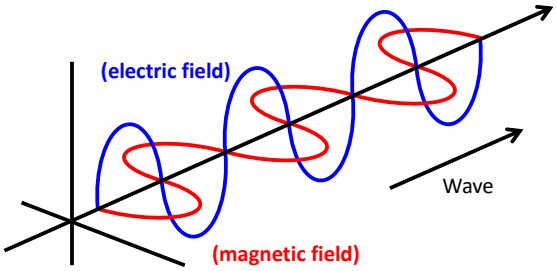

Figure 2.1: Electromagnetic wave.

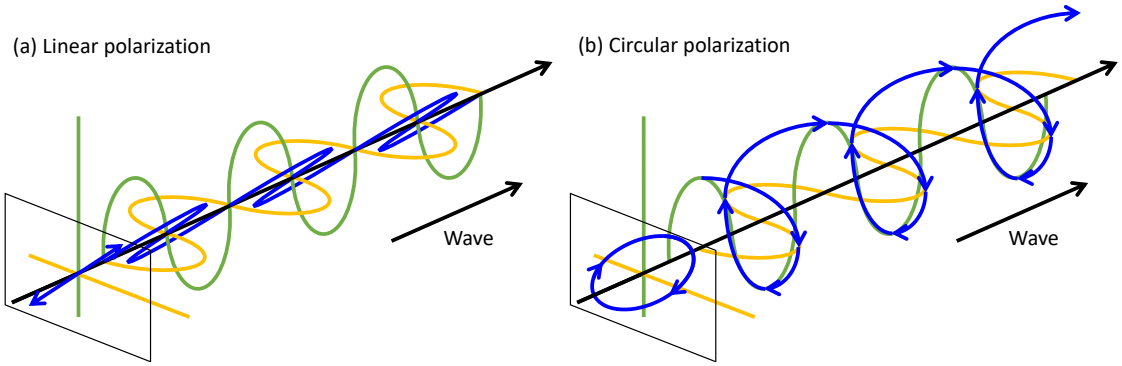

Figure 2.2: Superposed polarized radiation shown by the electric field.

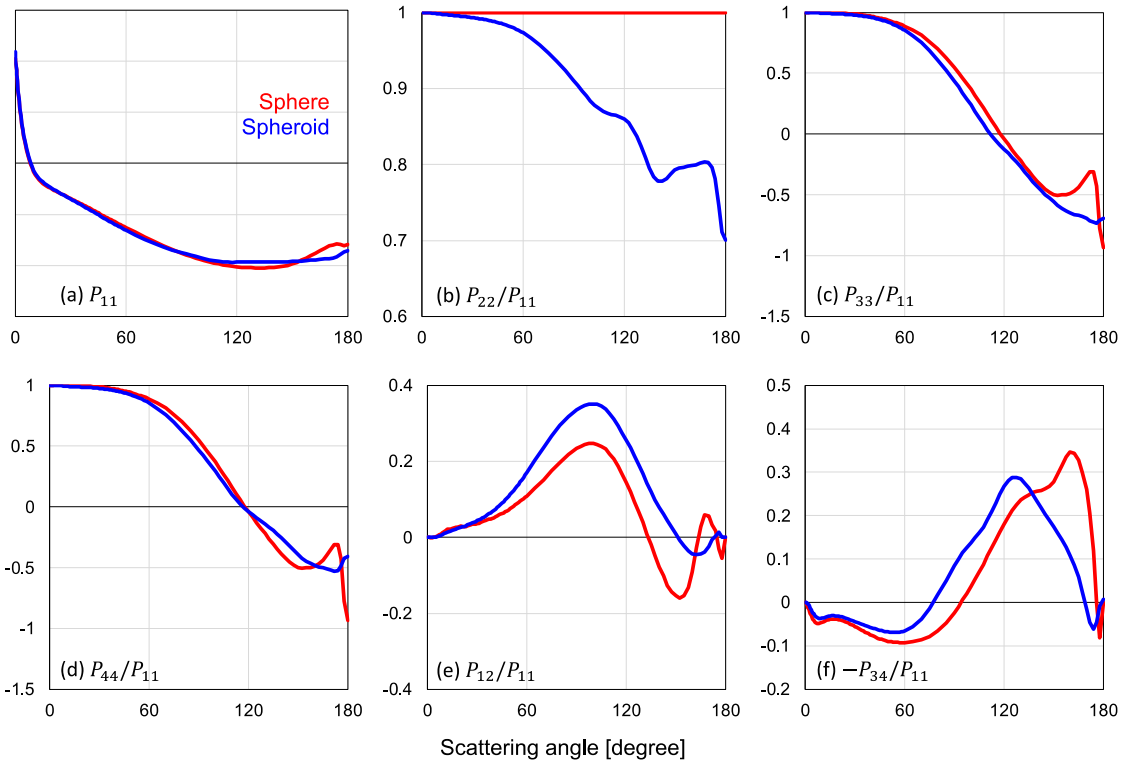

Figure 2.3: Phase matrix of dust1 aerosol (Dubovik et al. [2000]) at 340 nm assumed to be spherical (red) and spheroidal (blue) particles. Axis ratio of spheroidal particles assumes to be 0.6 representing Asian dust reported by Nakajima et al. [1989]. Scattering kernels were developed by Dubovik et al. [2006].

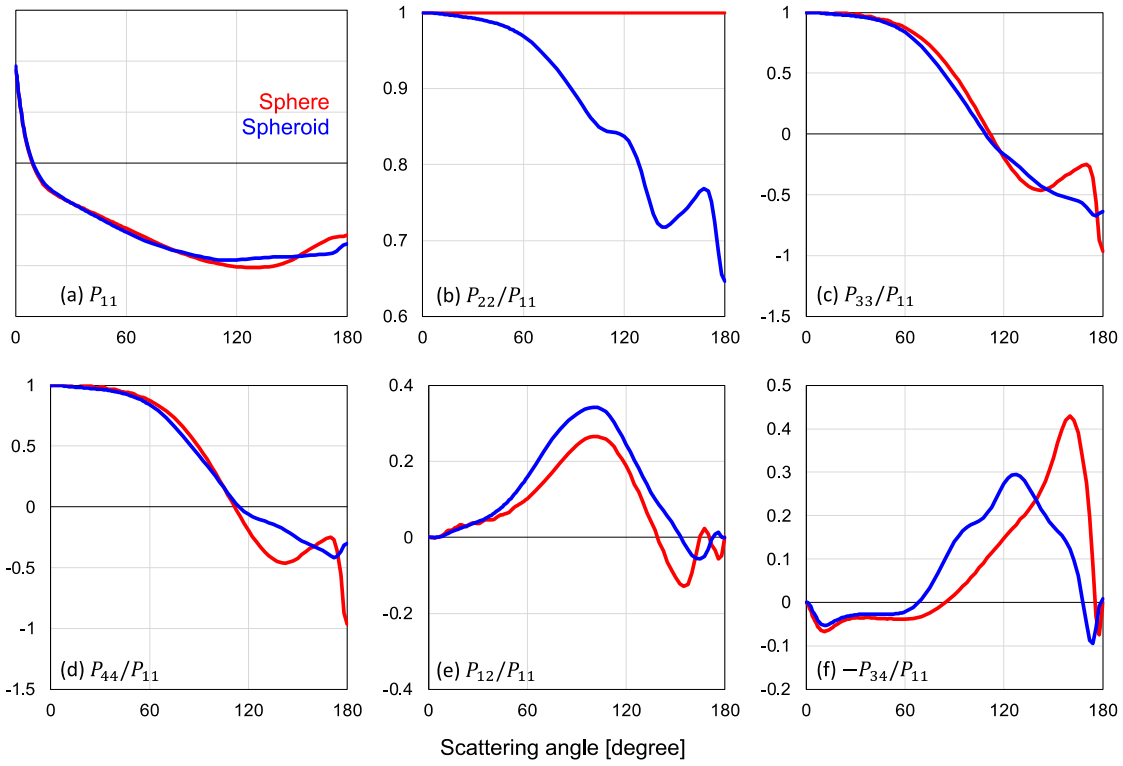

Figure 2.4: Same as Fig. 2.3, but for 500 nm.

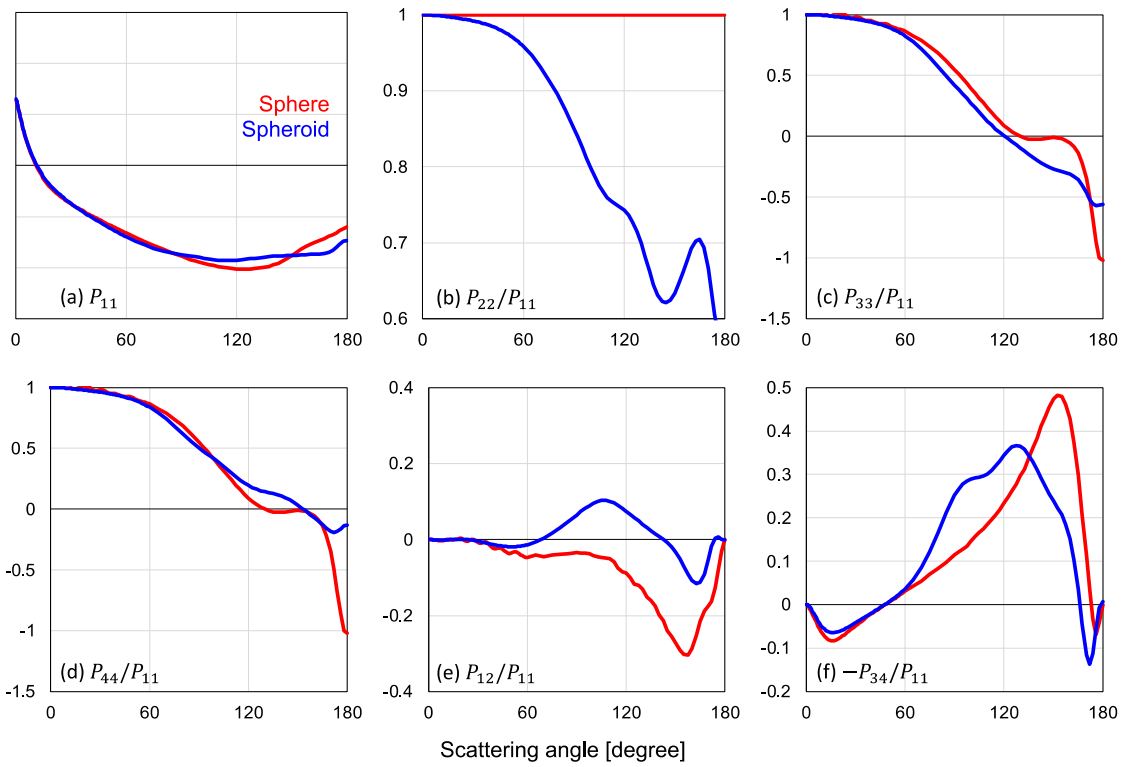

Figure 2.5: Same as Fig. 2.3, but for 1020 nm

2.2. Radiative transfer equation

Radiation is transmitted, absorbed, and scattered by a medium. Figure 2.6 shows the simplest 1-dimensional transfer case, and the radiative transfer equation is obtained as follows:

$$\boldsymbol{u}(x + \mathrm{d}s) - \boldsymbol{u}(x, \lambda) = -\sigma_{\mathrm{ext}}(\lambda)\boldsymbol{u}(x, \lambda)\mathrm{d}s, \tag{2.5}$$

where $\boldsymbol{u}$ is the radiance vector [W/m^2/sr/μm]; x is the position [m]; λ is wavelength [μm]; and σ_{ext} is the extinction coefficient [/m]. By Eq. (2.5), $\boldsymbol{u}(x + \mathrm{d}s)$ is expressed as

$$\boldsymbol{u}(x + \mathrm{d}s, \lambda) = \boldsymbol{u}(x, \lambda) \exp\left[-\int \sigma_{\mathrm{ext}}(\lambda)\mathrm{d}s\right] = \boldsymbol{u}(x, \lambda) \times T(\lambda), \tag{2.6}$$

where $\tau \equiv \int \sigma_{\mathrm{ext}}\mathrm{d}s$ and T are the optical thickness and transmittance, respectively. Eq. (2.6) is known as Beer-Lambert's Law and approximately expresses the transportation of solar incident beam to the incident direction in the atmosphere. Here, σ_{ext} consists of the absorption σ_{abs} and scattering σ_{sca} to the other medium as follows:

$$\sigma_{\mathrm{ext}} = \sigma_{\mathrm{sca}} + \sigma_{\mathrm{abs}}, \tag{2.7a}$$

$$\omega = \frac{\sigma_{\mathrm{sca}}}{\sigma_{\mathrm{ext}}} = \frac{\sigma_{\mathrm{sca}}}{\sigma_{\mathrm{sca}} + \sigma_{\mathrm{abs}}}, \tag{2.7b}$$

where ω is the single scattering albedo (SSA). By scattering light j from next to the medium, radiation is enhanced as follows:

$$\mathrm{d}\boldsymbol{u} = (-\sigma_{\mathrm{ext}}\boldsymbol{u} + \omega\boldsymbol{j})\mathrm{d}s, \tag{2.8a}$$

$$\frac{\mathrm{d}\boldsymbol{u}}{\sigma_{\mathrm{ext}}\mathrm{d}s} = -\boldsymbol{u} + \omega\boldsymbol{J}, \tag{2.8b}$$

where J is the source function. Since $\boldsymbol{J}$ is also extinction in the medium, ω is multiplied in the second term of the right-side hand.

In the Earth's atmosphere, polar coordinates (Fig. 2.7) are useful. Eq. (2.8b) is expanded as

$$\mu \frac{\mathrm{d}\boldsymbol{u}(t;\boldsymbol{\Omega})}{\mathrm{d}t} = -\boldsymbol{u}(t;\ \boldsymbol{\Omega}) + \omega \boldsymbol{J}(t;\ \boldsymbol{\Omega}), \tag{2.9a}$$

$$\cos\Theta = \boldsymbol{\Omega}\cdot\boldsymbol{\Omega}' = \mu\mu' + \sqrt{1-\mu^2}\sqrt{1-\mu'^2}\cos(\phi-\phi'), \tag{2.9b}$$

where u is the sky radiance at t along the unit vector $\boldsymbol{\Omega}$ in the direction (μ,ϕ); μ and ϕ are the cosine of the solar zenith angle (SZA) and the azimuth angle, respectively; $\boldsymbol{\Omega_0}$ is the unit vector in the solar insolation direction (μ_0,ϕ_0); and Θ is the scattering angle between the two direction vectors $\boldsymbol{\Omega}$ and $\boldsymbol{\Omega}'$. In this formulation, τ is used for zenith coordinate instead of z of the standard polar coordinates (Fig. 2.8). Since $\boldsymbol{J}$ is the scattering radiation from next to the medium, it can be expressed by probability distribution matrix $\mathbf{P}$ as follows:

$$\boldsymbol{J}(t;\ \boldsymbol{\Omega},\boldsymbol{\Omega}_0) = \int \mathrm{d}\boldsymbol{\Omega}\,\mathbf{P}(t;\boldsymbol{\Omega},\boldsymbol{\Omega}')\boldsymbol{u}(t;\boldsymbol{\Omega}), \tag{2.10}$$

and $\mathbf{P}$ is called phase matrix normalized to $\int P_{11}(\Theta)\mathrm{d}\cos\Theta = 2\pi$. Including the solar incident beam, $\boldsymbol{J}$ is expressed as

$$\boldsymbol{J}(t;\Omega,\Omega_0) = \int \mathrm{d}\boldsymbol{\Omega}\,\mathbf{P}(t;\Omega,\Omega')\left[\boldsymbol{u}(t;\Omega) + \boldsymbol{F}_{\mathrm{sol}}\exp\left(-\frac{t}{\mu_0}\right)\delta(\mu-\mu_0)\delta(\phi-\phi_0)\right], \tag{2.11}$$

where $\boldsymbol{F}_0$ is the extra-terrestrial solar irradiance. Hence,

$$\boldsymbol{J}(t;\ \boldsymbol{\Omega},\boldsymbol{\Omega}_0) = \mathbf{P}(t;\boldsymbol{\Omega},\boldsymbol{\Omega}_0)\boldsymbol{F}_{\mathrm{sol}}\exp\left(-\frac{t}{\mu_0}\right) + \int \mathrm{d}\boldsymbol{\Omega}\,\mathbf{P}(t;\boldsymbol{\Omega},\boldsymbol{\Omega}')\boldsymbol{u}(t;\boldsymbol{\Omega}). \tag{2.12}$$

First and second terms of the right-side hand in Eq. (2.8) are single and multiple scattering parts, respectively. By using Eps. (2.5a) and (2.8), the radiative transfer equation in the Earth atmosphere is obtained as

$$\mu \frac{\mathrm{d}\boldsymbol{u}(t;\boldsymbol{\Omega})}{\mathrm{d}t} = -\boldsymbol{u}(t;\ \boldsymbol{\Omega}) + \omega\mathbf{P}(t;\boldsymbol{\Omega},\boldsymbol{\Omega}_0)\boldsymbol{F}_{\mathrm{sol}}\exp\left(-\frac{t}{\mu_0}\right) + \omega\int \mathrm{d}\boldsymbol{\Omega}\,\mathbf{P}(t;\boldsymbol{\Omega},\boldsymbol{\Omega}')\boldsymbol{u}(t;\boldsymbol{\Omega}). \tag{2.13}$$

It is impossible to solve the Eq. (2.13) mathematically and requires numerical solutions (*e.g.*,

discrete ordinate, spherical harmonics, adding-doubling, and successive order of scattering methods).

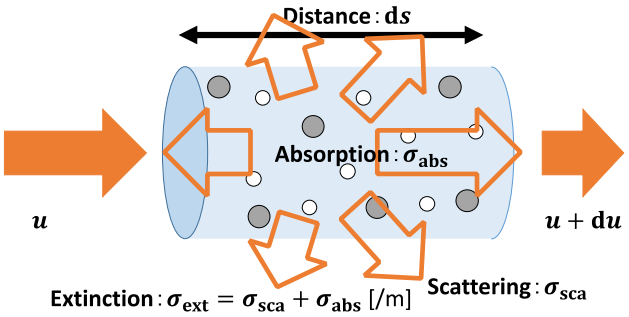

Figure 2.6: Phenomena when light passes through the medium.

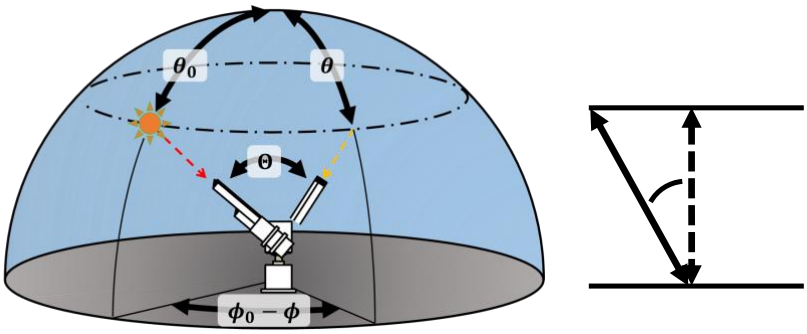

Figure 2.7: Polar coordinates.

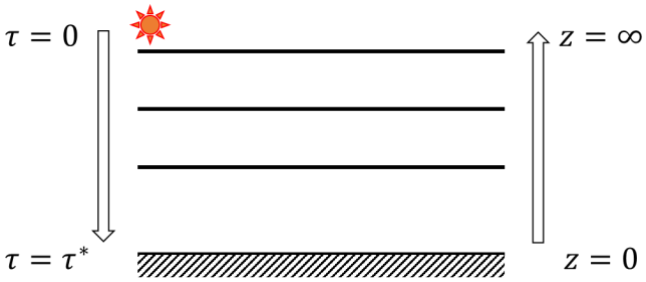

Figure 2.8: Coordinate of the optical thickness in the plane parallel atmosphere.

2.3. Solution of the radiative transfer equation with discrete ordinate method

Several numerical techniques were proposed for sky radiance computation (*e.g.*, successive order of scattering (Min and Duan [2004]), discrete ordinate (Stamnes and Swanson [1981]), spherical harmonics discrete ordinate (Evans [1998]) methods). The RSTAR (Nakajima and Tanaka [1986]) and PSTAR (Ota et al. [2010]) used in the present study solve Eq. (2.9) by the discrete ordinate and matrix operator method (Stamnes and Swanson [1981]; Nakajima and Tanaka [1986]; Stamnes et al. [1988]). In this section, we follow Ota et al. [2010] for the formulation in the vector radiative transfer and Nakajima and Tanaka [1988] in the scalar radiative transfer. In this procedure, the phase matrix in the local median plane $\mathbf{P}$ was decomposed by generalized spherical functions (Siewert [1981; 1982]; Hovenier et al. [2004]) as follows:

$$\mathbf{P}(\Omega,\Omega') = \frac{1}{4\pi}\sum_{m=0}^{\infty}(2-\delta_{0m})\left[\mathbf{P}_{\mathrm{c}}^{(m)}(\mu,\mu')\cos m(\phi-\phi') + \mathbf{P}_{\mathrm{s}}^{(m)}(\mu,\mu')\sin m(\phi-\phi')\right], \quad (2.14a)$$

$$\mathbf{P}_{\mathrm{c}}^{(m)}(\mu,\mu') \equiv \frac{1}{2}\left[\mathbf{A}^{(m)}(\mu,\mu') + \mathbf{D}\mathbf{A}^{(m)}(\mu,\mu')\mathbf{D}\right], \quad (2.14b)$$

$$\mathbf{P}_{\mathrm{s}}^{(m)}(\mu,\mu') \equiv \frac{1}{2}\left[\mathbf{A}^{(m)}(\mu,\mu')\mathbf{D} - \mathbf{D}\mathbf{A}^{(m)}(\mu,\mu')\right], \quad (2.14c)$$

$$\mathbf{A}^{(m)}(\mu,\mu') \equiv \sum_{l=m}^{\infty}(2l+1)\frac{(l-m)!}{(l+m)!}\mathbf{P}_l^m(\mu)\mathbf{B}_l\mathbf{P}_l^m(\mu'), \quad (2.14d)$$

$$\mathbf{D} \equiv \begin{pmatrix} 1 & 0 & 0 & 0 \\ 0 & 1 & 0 & 0 \\ 0 & 0 & -1 & 0 \\ 0 & 0 & 0 & -1 \end{pmatrix}, \quad (2.15a)$$

$$\mathbf{B}_l \equiv \begin{pmatrix} \alpha_1^l & -\beta_1^l & 0 & 0 \\ -\beta_1^l & \alpha_2^l & 0 & 0 \\ 0 & 0 & \alpha_3^l & -\beta_2^l \\ 0 & 0 & \beta_2^l & \alpha_4^l \end{pmatrix}, \quad (2.15b)$$

where δ_{jk} denotes Kronecker's delta; the elements of $\mathbf{B}_l$ are known as Greek constants; and

$$\mathbf{P}_l^m(\mu) \equiv \begin{pmatrix} P_l^m(\mu) & 0 & 0 & 0 \\ 0 & R_l^m(\mu) & -T_l^m(\mu) & 0 \\ 0 & -T_l^m(\mu) & R_l^m(\mu) & 0 \\ 0 & 0 & 0 & P_l^m(\mu) \end{pmatrix}, \tag{2.15c}$$

is the matrix of spherical functions. The elements of $\mathbf{P}_l^m$ are defined as follows:

$$P_l^j(x) = (1-x^2)^{j/2}\frac{d^j}{dx^j}P_l(x) = i^j\left[\frac{(l+j)!}{(l-j)!}\right]^{1/2}P_{0,j}^l(x), \tag{2.16a}$$

$$R_l^j(x) = -\frac{1}{2}i^j\left[\frac{(l+j)!}{(l-j)!}\right]^{1/2}\left[P_{2,j}^l(x) + P_{-2,j}^l(x)\right], \tag{2.16b}$$

$$T_l^j(x) = -\frac{1}{2}i^j\left[\frac{(l+j)!}{(l-j)!}\right]^{1/2}\left[P_{2,j}^l(x) - P_{-2,j}^l(x)\right], \tag{2.16c}$$

where P_l^j is the associated Legendre function, and i is an imaginary unit defined as $i = \sqrt{-1}$. The Greek constants (Eq. (2.15b)) were obtained by the following equations:

$$a_1^l \equiv 2\pi\int_{-1}^{1}P_{11}(x)P_{0,0}^l(x)\mathrm{d}x\,, \tag{2.17a}$$

$$a_2^l + a_3^l \equiv 2\pi\int_{-1}^{1}[P_{22}(x) + P_{33}(x)]P_{2,2}^l(x)\mathrm{d}x\,, \tag{2.17b}$$

$$a_2^l - a_3^l \equiv 2\pi\int_{-1}^{1}[P_{22}(x) - P_{33}(x)]P_{2,-2}^l(x)\mathrm{d}x\,, \tag{2.17c}$$

$$a_4^l \equiv 2\pi\int_{-1}^{1}P_{44}(x)P_{0,0}^l(x)\mathrm{d}x\,, \tag{2.17d}$$

$$\beta_1^l \equiv 2\pi\int_{-1}^{1}P_{12}(x)P_{0,2}^l(x)\mathrm{d}x\,, \tag{2.17e}$$

$$\beta_2^l \equiv 2\pi \int_{-1}^{1} P_{34}(x) P_{0,2}^l(x) \mathrm{d}x\,, \tag{2.17f}$$

where $P_{m,n}^l$ is a generalized spherical function, defined using Rodrigues' formula as:

$$P_{m,n}^l(x) = A_{m,n}^l i^{n-m} \sqrt{\frac{(1-x)^{m-n}}{(1+x)^{m+n}}} \frac{\mathrm{d}^{l-n}}{\mathrm{d}x^{l-n}} [(1-x)^{l-m}(1+x)^{l+m}], \tag{2.18a}$$

with

$$A_{m,n}^l \equiv \frac{(-1)^{l-m}}{2^l} \sqrt{\frac{(l+n)!}{(l-m)!\,(l+m)!\,(l-n)!}}, \tag{2.18b}$$

for $l \in \mathbb{N}$, $m, n \in \mathbb{Z}$, $-l \leq m, n \leq l$, and $-1 \leq x \leq 1$. Generalized spherical function is satisfied as:

$$(-1)^{m+n} \int_{-1}^{1} P_{m,n}^l(x) P_{m,n}^k(x) \mathrm{d}x = \frac{2}{2l+1} \delta_{lk}. \tag{2.19}$$

Therefore, Eq. (2.14a) can be expressed as follows:

$$\begin{aligned} \mathbf{P}(\boldsymbol{\Omega}, \boldsymbol{\Omega}') = \frac{1}{4\pi} \sum_{m=0}^{\infty} (2 - \delta_{0m}) \big[& \boldsymbol{\Phi}_1^{(m)}(\phi - \phi') \mathbf{A}^{(m)}(\mu, \mu') \mathbf{D}_1 \\ & + \boldsymbol{\Phi}_2^{(m)}(\phi - \phi') \mathbf{A}^{(m)}(\mu, \mu') \mathbf{D}_2 \big], \end{aligned} \tag{2.20}$$

$$\mathbf{D}_1 \equiv \begin{pmatrix} 1 & 0 & 0 & 0 \\ 0 & 1 & 0 & 0 \\ 0 & 0 & 0 & 0 \\ 0 & 0 & 0 & 0 \end{pmatrix}, \tag{2.21a}$$

$$\mathbf{D}_2 \equiv \begin{pmatrix} 0 & 0 & 0 & 0 \\ 0 & 0 & 0 & 0 \\ 0 & 0 & 1 & 0 \\ 0 & 0 & 0 & 1 \end{pmatrix}, \tag{2.21b}$$

$$\boldsymbol{\Phi}_1^{(m)} \equiv \begin{pmatrix} \cos m(\phi-\phi') & 0 & 0 & 0 \\ 0 & \cos m(\phi-\phi') & 0 & 0 \\ 0 & 0 & \sin m(\phi-\phi') & 0 \\ 0 & 0 & 0 & \sin m(\phi-\phi') \end{pmatrix}, \quad (2.22a)$$

$$\boldsymbol{\Phi}_2^{(m)} \equiv \begin{pmatrix} -\sin m(\phi-\phi') & 0 & 0 & 0 \\ 0 & -\sin m(\phi-\phi') & 0 & 0 \\ 0 & 0 & \cos m(\phi-\phi') & 0 \\ 0 & 0 & 0 & \cos m(\phi-\phi') \end{pmatrix}, \quad (2.22b)$$

On the other hand, by an expansion of $\boldsymbol{u}$ with the Fourier series, the *m*-th order of radiative transfer equation in the Fourier space is obtained as

$$\mu \frac{\mathrm{d}\boldsymbol{u}_k^{(m)}(t;\mu)}{\mathrm{d}t} = -\boldsymbol{u}_k^{(m)}(t;\mu) + \omega \mathbf{A}^{(m)}(\mu,\mu_0)\mathbf{D}_k \boldsymbol{F}_0 \exp\left(-\frac{t}{\mu_0}\right) + \omega \int \mathrm{d}\mu' \, \mathbf{A}^{(m)}(\mu,\mu')\boldsymbol{u}_k^{(m)}(t;\mu') \quad (k=1,2), \quad (2.23)$$

because:

$$\boldsymbol{u}(t;\boldsymbol{\Omega}) = \frac{1}{4\pi}\sum_{m=0}^{\infty}(2-\delta_{0m})\left[\boldsymbol{\Phi}_1^{(m)}(\phi-\phi_0)\boldsymbol{u}_1^{(m)}(t;\mu) + \boldsymbol{\Phi}_2^{(m)}(\phi-\phi')\boldsymbol{u}_2^{(m)}(t;\mu)\right]. \quad (2.24)$$

The above formulation makes it possible to use the discrete ordinate method. When an N-th order Gaussian quadrature $\left(\pm\mu_j, w_j\right)$ is adopted in the hemisphere, the radiance in the direction $\pm\mu_j$ is obtained as

$$\pm\mu_l \frac{\mathrm{d}\boldsymbol{u}_k^{(m)}(t;\pm\mu_l)}{\mathrm{d}t}$$
$$= -\boldsymbol{u}_k^{(m)}(t;\pm\mu_l) + \omega\mathbf{A}^{(m)}(\pm\mu_l,\mu_0)\mathbf{D}_k\boldsymbol{F}_0 \exp\left(-\frac{t}{\mu_0}\right)$$
$$+ \omega\sum_{j=1}^{N} w_j\left[\mathbf{A}^{(m)}(\pm\mu_l,\mu_j)\boldsymbol{u}_k^{(m)}(t;\mu_j) + \mathbf{A}^{(m)}(\pm\mu_l,-\mu_j)\boldsymbol{u}_k^{(m)}(t;-\mu_j)\right]$$
$$(k = 1,2), \tag{2.25}$$

Therefore, we can express the following equation by using matrix operator,

$$\pm\mathbf{M}\frac{\mathrm{d}\mathbf{U}_{k,\pm}^{(m)}}{\mathrm{d}t} = -\mathbf{U}_{k,\pm}^{(m)} + \mathbf{S}_{k,\pm}^{(m)} \exp\left(-\frac{t}{\mu_0}\right) + \mathbf{A}_{\pm}^{(m)}\mathbf{W}\mathbf{U}_{k,+}^{(m)} + \widehat{\mathbf{D}}\mathbf{A}_{\mp}^{(m)}\widehat{\mathbf{D}}\mathbf{W}\mathbf{U}_{k,-}^{(m)} \quad (k = 1,2), \tag{2.26}$$

where:

$$\mathbf{M} \equiv \{\boldsymbol{\mu}_k\delta_{kl}|k,l = 1,\cdots,N\} \in \mathbb{R}^{4N\times 4N} \quad \text{with} \quad \boldsymbol{\mu}_k = \mu_k\mathbf{E}_4, \tag{2.27a}$$

$$\mathbf{W} \equiv \{\mathbf{w}_k\delta_{kl}|k,l = 1,\cdots,N\} \in \mathbb{R}^{4N\times 4N} \quad \text{with} \quad \mathbf{w}_k = w_k\mathbf{E}_4, \tag{2.27b}$$

$$\widehat{\mathbf{D}} \equiv \{\mathbf{D}\delta_{kl}|k,l = 1,\cdots,N\} \in \mathbb{R}^{4N\times 4N}, \tag{2.27c}$$

$$\mathbf{S}_{k,\pm}^{(m)} \equiv \left\{\omega\mathbf{A}^{(m)}(\pm\mu_l,\mu_0)\mathbf{D}_k\boldsymbol{F}_{\mathrm{sol}}|l = 1,\cdots,N\right\} \in \mathbb{R}^{4N}, \tag{2.27d}$$

$$\mathbf{U}_{k,\pm}^{(m)} \equiv \left\{\boldsymbol{u}_k^{(m)}(t;\pm\mu_l)|l = 1,\cdots,N\right\} \in \mathbb{R}^{4N}, \tag{2.27e}$$

$$\mathbf{A}_{\pm}^{(m)} \equiv \left\{\omega\mathbf{A}^{(m)}(\pm\mu_k,\mu_l)|k,l = 1,\cdots,N\right\} \in \mathbb{R}^{4N\times 4N}, \tag{2.27f}$$

because:

$$\mathbf{A}^{(m)}(\pm\mu_l,-\mu_j) = \mathbf{D}\mathbf{A}^{(m)}(\mp\mu_l,\mu_j)\mathbf{D}. \tag{2.28}$$

Hence,

$$\mathbf{M}\frac{\mathrm{d}\boldsymbol{\Psi}_{k,\pm}^{(m)}}{\mathrm{d}t}=\left(\mathbf{S}_{k,+}^{(m)}\mp\widehat{\mathbf{D}}\mathbf{S}_{k,-}^{(m)}\right)\exp\left(-\frac{t}{\mu_0}\right)-\left[\mathbf{W}^{-1}-\left(\mathbf{A}_{+}^{(m)}\mp\widehat{\mathbf{D}}\mathbf{A}_{-}^{(m)}\right)\right]\mathbf{W}\boldsymbol{\Psi}_{k,\mp}^{(m)}\quad(k=1,2), \tag{2.29a}$$

$$\boldsymbol{\Psi}_{k,\pm}^{(m)}\equiv\mathbf{U}_{k,+}^{(m)}\pm\widehat{\mathbf{D}}\mathbf{U}_{k,-}^{(m)}\quad(k=1,2). \tag{2.29b}$$

The further formulation is obtained through eigenvalue decomposition. However, we require the direct eigenvalue decomposition including the complex variables, because $\mathbf{A}_{+}^{(m)}\mp\widehat{\mathbf{D}}\mathbf{A}_{-}^{(m)}$ is an anti-symmetric matrix. This is complicated compared to the case of the scalar approximation as follows:

$$\mathbf{M}_{\mathrm{I}}\frac{\mathrm{d}\boldsymbol{\Psi}_{\mathrm{I},\pm}^{(m)}}{\mathrm{d}t}=\left(\mathbf{S}_{\mathrm{I},+}^{(m)}\mp\mathbf{S}_{\mathrm{I},-}^{(m)}\right)\exp\left(-\frac{t}{\mu_0}\right)-\left[\mathbf{W}_{\mathrm{I}}^{-1}-\left(\mathbf{A}_{\mathrm{I},+}^{(m)}\mp\mathbf{A}_{\mathrm{I},-}^{(m)}\right)\right]\mathbf{W}_{\mathrm{I}}\boldsymbol{\Psi}_{\mathrm{I},\mp}^{(m)}. \tag{2.30}$$

where:

$$\mathbf{M}_{\mathrm{I}}\equiv\{\mu_k\delta_{kl}|k,l=1,\cdots,N\}\in\mathbb{R}^{N\times N}, \tag{2.31a}$$

$$\mathbf{W}_{\mathrm{I}}\equiv\{w_k\delta_{kl}|k,l=1,\cdots,N\}\in\mathbb{R}^{N\times N}, \tag{2.31b}$$

$$\mathbf{S}_{\mathrm{I},\pm}^{(m)}\equiv\left\{\omega\left[\mathbf{A}^{(m)}(\pm\mu_l,\mu_0)\right]_{11}F_{\mathrm{sol}}|l=1,\cdots,N\right\}\in\mathbb{R}^{N}, \tag{2.31c}$$

$$\mathbf{A}_{\mathrm{I},\pm}^{(m)}\equiv\left\{\omega\left[\mathbf{A}^{(m)}(\pm\mu_k,\mu_l)\right]_{11}|k,l=1,\cdots,N\right\}\in\mathbb{R}^{N\times N}, \tag{2.31d}$$

and Eq. (2.30) can be solved with the square root decomposition because $\mathbf{A}_{\mathrm{I},+}^{(m)}\mp\mathbf{A}_{\mathrm{I},-}^{(m)}$ is a symmetric matrix. Therefore, the more computational time is required in the vector RTM. In addition, the scalar RTM largely saves computational time, which increases by a power law of the matrix rank M as $2M^{1\sim2}$ compared with the full-vector RTM, and it is about 8 to 32 times.

We only obtain the solution of *m*-th order of the radiative transfer equation through the above procedure and then obtain the sky radiance by their sum. However, it requires computing with the significant large stream numbers, especially in the dust aerosol cases, because of the highly anisotropic phase function. Hence, it is unreasonable to use the analysis of the actual observation and needed an accelerating technology as discussed in Chapter 1.

2.4. Azimuth integral radiative transfer equation

From Eq. (2.24),

$$\int_0^{2\pi} \boldsymbol{u}(t;\boldsymbol{\Omega})\mathrm{d}\phi = \frac{1}{2}\left[\mathbf{D}_1\boldsymbol{u}_1^{(0)}(t;\mu) + \mathbf{D}_2\boldsymbol{u}_2^{(0)}(t;\mu)\right], \tag{2.32}$$

because:

$$\int_0^{2\pi} \cos m\phi \,\mathrm{d}\phi = \begin{cases} 2\pi & m = 0 \\ 0 & otherwise \end{cases}, \tag{2.33a}$$

$$\int_0^{2\pi} \sin m\phi \,\mathrm{d}\phi = 0. \tag{2.33b}$$

Therefore, we can obtain downward diffuse horizontal radiative flux $F_{\mathrm{df}}^{\downarrow}$ from zeroth order of Fourier decomposed radiative transfer equation (Eq. (2.32)) as the following equation:

$$F_{\mathrm{df}}^{\downarrow} = \int_0^1 \mu\mathrm{d}\mu \int_0^{2\pi} u_1(t;\boldsymbol{\Omega})\mathrm{d}\phi = \frac{1}{2}\int_0^1 \mu \boldsymbol{D}_1^{\mathrm{T}}\boldsymbol{u}_1^{(0)}(t;\mu)\mathrm{d}\mu\,, \tag{2.34a}$$

$$\boldsymbol{D}_1 \equiv [1,0,0,0]^{\mathrm{T}}. \tag{2.34b}$$

2.5. Computation with a highly anisotropic phase function

As mentioned in Section 2.3, a high order Fourier component is required to reconstruct the sky radiance distribution when the phase function is highly anisotropic. In the case of the azimuth integral radiative transfer equation (zeroth order approximation; Section 2.4), a large number of Legendre expansion is required (see Section 2.3). We consider cutting (truncating) the forward peak in scalar radiative transfer theory as follows:

$$P_{11}(x) = \frac{f}{2\pi}\delta(x) + P_{11}^{\mathrm{t}}(x), \tag{2.35}$$

where $\delta(x)$ denotes the delta function; P_{11} is the phase function for total radiance; P_{11}^{t} is truncated phase function for total radiance; f is truncation factor defined as:

$$f = 2\pi \int_{-1}^{1} [P_{11}(x) - P_{11}^{\mathrm{t}}(x)]\mathrm{d}x\,, \tag{2.36a}$$

because:

$$2\pi \int_{-1}^{1} P_{11}(x)\mathrm{d}x = 1. \tag{2.36b}$$

By renormalization, Eq. (2.35) is expressed as:

$$P_{11}(x) = \frac{f}{2\pi}\delta(x) + (1-f)P_{11}^{*}(x), \tag{2.37a}$$

where:

$$P_{11}^{*}(x) \equiv \frac{1}{1-f}P_{11}^{\mathrm{t}}(x). \tag{2.37b}$$

Here, the first term of the right-hand side of Eq. (2.37a) can be ignored from the scattering medium because of the significant forward strong peak. In this treatment, the scattering part of the optical thickness is scaled as $(1-f)\omega t$ where t is optical thickness. Therefore, optical thickness t^{*} with truncated phase function is obtained as:

$$t^{*} \equiv (1-f)\omega t + (1-\omega)t = (1-f\omega)t. \tag{2.38a}$$

The second term of the right-hand side in Eq. (2.38a) is the absorption part of the optical thickness. Therefore, single scattering albedo ω^{*} with truncated phase function is also obtained as:

$$\omega^{*} \equiv \frac{(1-f)\omega t}{(1-f\omega)t} = \frac{(1-f)\omega}{1-f\omega}. \tag{2.38b}$$

In conclusion, we obtain the radiative flux by calculation of the radiative transfer equation expressed by truncated phase function as follow:

$$-\mu\frac{\mathrm{d}u_{\mathrm{I}}^{*}(t^{*};\boldsymbol{\Omega})}{\mathrm{d}t^{*}}=u_{\mathrm{I}}^{*}(t^{*};\boldsymbol{\Omega})-e^{-\frac{t^{*}}{\mu_{0}}}\omega^{*}P_{11}^{*}(\boldsymbol{\Omega},\boldsymbol{\Omega}_{0})F_{\mathrm{sol}}-\int\mathrm{d}\boldsymbol{\Omega}'\,\omega^{*}P_{11}^{*}(\boldsymbol{\Omega},\boldsymbol{\Omega}')u_{\mathrm{I}}^{*}(t^{*};\boldsymbol{\Omega}'). \quad (2.39)$$

This formulation can be solved by finite Fourier order and spherical harmonics (*i.e.*, Eq. (2.14)). Note that the sky radiance computed by this consideration still contains the residual errors, especially in the aureole region.

Until now, several truncation methods were proposed (see Chapter 1). In this section, we describe following three methods: (1) delta-function (Section 2.5.1), (2), delta-fit (Section 2.5.2), and (3) delta-M (Section 2.5.3) methods. Rozanov and Laypustin (2010) reported the delta-M method is the best way in these methods (see Chapter 1).

2.5.1. delta-function method

Potter [1970] proposed the delta-function method, the first time proposing the truncation. In Potter [1970], the phase function is approximated as:

$$P_{11}^{\mathrm{t}}(\cos\Theta)=\begin{cases}P_{11}(\cos\Theta) & \alpha<\cos\Theta\leq 1\\ \exp\left[\dfrac{\cos\Theta}{\alpha}\ln P_{11}(\alpha)\right] & -1\leq\cos\Theta\leq\alpha\end{cases}. \quad (2.40)$$

where α is user defined truncation angle.

2.5.2. delta-fit method

In Hu et al. [2000], the phase function is approximated as:

$$P_{11}^{\mathrm{t}}(\cos\Theta)=\frac{1}{4\pi}\sum_{l=0}^{M^{*}}(2l+1)\alpha_{1}^{l}P_{l}(x)\,, \quad (2.41a)$$

where α_1^l is obtained by:

$$\int_{-1}^{\alpha}\left[1-\frac{1}{4\pi P_{11}(x)}\sum_{l=0}^{M^{*}}(2l+1)\alpha_{1}^{l}P_{l}(x)\right]^{2}\mathrm{d}x\rightarrow\min. \quad (2.41b)$$

Here, α is user defined truncation angle.

2.5.3. delta-M method

In Wiscombe [1977], the phase function is approximated as:

$$P_{11}^{\mathrm{t}}(\cos\Theta) = \frac{1}{4\pi}\sum_{l=0}^{M^*}(2l+1)(\alpha_1^l - f)P_l(x)\,, \tag{2.42a}$$

where α_1^l and f are defined by:

$$\alpha_1^l = 2\pi\int_{-1}^{1} P_{11}(x)P_l(x)\mathrm{d}x\,, \tag{2.42b}$$

$$f \equiv 2\pi\int_{-1}^{1} P_{11}(x)P_{M^*+1}(x)\mathrm{d}x\,. \tag{2.42c}$$

2.6. Efficient calculation methods (TMS and IMS) in the scalar approximation

The IMS method proposed by Nakajima and Tanaka [1988] can be used to correct the truncated sky radiances computed by the discrete ordinate and matrix operator method (Stamnes and Swanson [1981]; Nakajima and Tanaka [1986]; Stamnes et al. [1988]) with the delta-M method (Wiscombe [1977]) in the scalar approximation. The delta-M method is a truncation algorithm suitable for radiative flux calculations with a strong forward scattering phase function. It maintains low stream numbers, but the sky radiance calculation in the aureole region includes significant errors.

In the delta-M method, the phase function for total radiance P_{11}, is expressed by a Legendre polynomial and truncated by the M^*-th moment as follows (Wiscombe [1977]):

$$P_{11}(x) \approx \frac{1}{4\pi}\sum_{l=0}^{M_{\max}}(2l+1)\alpha_1^l P_l(x) = f\hat{P}_{11}(x) + (1-f)P_{11}^*(x), \tag{2.43a}$$

$$\hat{P}_{11} \equiv \frac{1}{4\pi}\sum_{l=0}^{M_{\max}}(2l+1)\hat{\alpha}_1^l P_l(x)\,, P_{11}^* = \frac{1}{4\pi}\sum_{l=0}^{M^*}(2l+1)\alpha^{*l}_1 P_l(x)\,, \tag{2.43b}$$

$$f \equiv \alpha_1^{M^*+1}, \tag{2.43c}$$

$$\alpha^{*l}_1 \equiv \frac{1}{1-f}(\alpha^l_1 - f\hat{\alpha}^l_1), \tag{2.43d}$$

$$\hat{\alpha}^l_1 \equiv \begin{cases} 1 & l < M^* + 1 \\ \dfrac{1}{f}\alpha^l_1 & otherwise \end{cases}, \tag{2.43e}$$

where M^* is the truncation order; $M_{\max}$ is the maximum order ($M_{\max} \gg M^*$); P_l and α^l_1 are the l-th Legendre function and coefficient, respectively; f is the truncation fraction that is uniquely given by the (M^*+1)-th Legendre coefficient $\alpha_1^{M^*+1}$ in the delta-M method; and $\hat{P}_{11}$ and P^*_{11} are the forward peak and truncated phase function, respectively. Note that this Legendre expansion of P_{11} is the same as the previous section with scalar approximation. The M value is approximately given by $2N$ when an N-th order Gaussian quadrature is adopted in the hemisphere for angular integration of the source term of the radiative transfer equation, including the phase function. In this truncation procedure of the Legendre series, a Gibbs type oscillation appears in the angular distribution of the phase function and simulated radiances. Then, the optical thickness t and single scattering albedo ω are also scaled as follows:

$$\mathrm{d}t^* = (1 - f\omega)\mathrm{d}t, \omega^* = \frac{1-f}{1-f\omega}\omega, \tag{2.44}$$

where t^* and ω^* are the scaled optical thickness and single scattering albedo, respectively. The radiative transfer equation in the truncation space is given as follows:

$$-\mu\frac{\mathrm{d}u^*_{\mathrm{I}}(t^*;\mathbf{\Omega})}{\mathrm{d}t^*} = u^*_{\mathrm{I}}(t^*;\mathbf{\Omega}) - e^{-\frac{t^*}{\mu_0}}\omega^* P^*_{11}(\mathbf{\Omega},\mathbf{\Omega}_0)F_{\mathrm{sol}} - \int \mathrm{d}\mathbf{\Omega}'\,\omega^* P^*_{11}(\mathbf{\Omega},\mathbf{\Omega}')u^*_{\mathrm{I}}(t^*;\mathbf{\Omega}'), \tag{2.45}$$

where u^*_{I} is the sky radiance at t^* along the unit vector $\mathbf{\Omega}$ in the direction (μ,ϕ) in truncation space.

Nakajima and Tanaka [1988] proposed two steps to reduce the computational errors in u^*_{I} calculated with a finite stream number N as summarized as,

$$u_{\mathrm{I}} \approx u^*_{\mathrm{I}} - u^*_{\mathrm{I,s}} + u'_{\mathrm{I,s}} + \hat{u}_{\mathrm{I}}. \tag{2.46}$$

The first three terms in the right-hand side of Eq. (2.46) are a single scattering correction named TMS for a process of subtracting the truncated single scattering solution $u^*_{\mathrm{I,s}}$ of Eq. (2.45) and adding a single scattering solution $u'_{\mathrm{I,s}}$ with the scaled original phase function $P_{11}/(1-f)$. Hence, in the homogeneous single layer,

$$\hat{u}_{\mathrm{I},1} \equiv -u^*_{\mathrm{I,s}} + u'_{\mathrm{I,s}} = \hat{\omega}\hat{P}_{11}(\mathbf{\Omega}, \mathbf{\Omega}_0)F_{\mathrm{sol}}g(t, \mu^*, \mu^*_0), \tag{2.47}$$

where:

$$\mu^* \equiv \frac{\mu}{1-f\omega}, \tag{2.48a}$$

$$\hat{\omega} \equiv \frac{f}{1-f\omega}\omega, \tag{2.48b}$$

$$g(\tau, \mu, \mu_0) \equiv \frac{1}{\mu}e^{-\frac{t}{\mu}}\int_0^t \mathrm{d}t \exp\left[\left(\frac{1}{\mu}-\frac{1}{\mu_0}\right)t\right], \tag{2.48c}$$

because:

$$u'_{\mathrm{I,s}}(t; \mathbf{\Omega}) = \frac{\omega^*}{1-f}P_{11}(\mathbf{\Omega}, \mathbf{\Omega}_0)F_{\mathrm{sol}}g(t, \mu^*, \mu^*_0), \tag{2.49a}$$

$$u^*_{\mathrm{I,s}}(t; \mathbf{\Omega}) = \omega^* P^*_{11}(\mathbf{\Omega}, \mathbf{\Omega}_0)F_{\mathrm{sol}}g(t, \mu^*, \mu^*_0). \tag{2.49b}$$

This TMS procedure suppresses the angular fluctuation in u^*_{I} caused by the delta-M truncation because both the truncated multiple scattering $u^*_{\mathrm{I,m}}(= u^*_{\mathrm{I}} - u^*_{\mathrm{I,s}})$ and the scaled original phase function do not include significant fluctuation. The last term of the right-hand side of Eq. (2.46) is a correction in the aureole region called IMS to add the residual scattering $\hat{u}_{\mathrm{I}}(= u_{\mathrm{I}} - u'_{\mathrm{I}})$ calculated from the following residual radiative transfer equation for the difference $u_{\mathrm{I}} - u'_{\mathrm{I}}$,

$$-\mu\frac{\mathrm{d}\hat{u}_{\mathrm{I}}}{\mathrm{d}t} = -\mu\left(\frac{\mathrm{d}u_{\mathrm{I}}}{\mathrm{d}t} - \frac{\mathrm{d}u'_{\mathrm{I}}}{\mathrm{d}t}\right) = \hat{u}_{\mathrm{I}} - \omega\int \mathrm{d}\mathbf{\Omega}'\, P_{11}(\mathbf{\Omega}, \mathbf{\Omega}')\hat{u}_{\mathrm{I}}(t; \mathbf{\Omega}') + J_1 + J_2 + J_3 + J_4, \tag{2.50a}$$

$$J_1(t;\mathbf{\Omega}) \equiv f\omega\left[u^*_{\mathrm{I,m}}(t;\mathbf{\Omega}) - \int \mathrm{d}\mathbf{\Omega}'\,\hat{P}_{11}(\mathbf{\Omega},\mathbf{\Omega}')u^*_{\mathrm{I,m}}(t;\mathbf{\Omega}')\right], \tag{2.50b}$$

$$J_2(t;\mathbf{\Omega}) \equiv \hat{\omega}\omega\Big[P_{11}(\mathbf{\Omega},\mathbf{\Omega}_0)F_{\mathrm{sol}}g(\tau,\mu^*,\mu_0^*) - (1-f)\int \mathrm{d}\mathbf{\Omega}'\,\hat{P}_{11}(\mathbf{\Omega},\mathbf{\Omega}')P^*_{11}(\mathbf{\Omega}',\mathbf{\Omega}_0)F_{\mathrm{sol}}g(t,\mu'^*,\mu_0^*)\Big], \tag{2.50c}$$

$$J_3(t;\mathbf{\Omega}) \equiv -\hat{\omega}\omega\int \mathrm{d}\mathbf{\Omega}'\,P_{11}(\mathbf{\Omega},\mathbf{\Omega}')\hat{P}_{11}(\mathbf{\Omega}',\mathbf{\Omega}_0)F_{\mathrm{sol}}g(t,\mu'^*,\mu_0^*), \tag{2.50d}$$

$$J_4(t;\mathbf{\Omega}) \equiv \omega e^{-\frac{t}{\mu_0^*}}P_{11}(\mathbf{\Omega},\mathbf{\Omega}_0)F_{\mathrm{sol}}\left[1-\exp\left(-\frac{f\omega t}{\mu_0}\right)\right], \tag{2.50e}$$

where J_1, J_2, J_3, and J_4 are source functions, and $u^*_{\mathrm{I,m}}$ is the multiple scattering radiance in the truncation space. The essential terms for the secondary order scattering are J_2, J_3, and J_4 because J_1 becomes very small (Nakajima and Tanaka [1988]). Using Eq. (2.43b), the relationship between $\hat{P}_{11}$ and P^*_{11} is given as follows:

$$\int \mathrm{d}\mathbf{\Omega}'\,\hat{P}_{11}(\mathbf{\Omega},\mathbf{\Omega}')P^*_{11}(\mathbf{\Omega}',\mathbf{\Omega}_0) = P^*_{11}(\mathbf{\Omega},\mathbf{\Omega}_0). \tag{2.51}$$

Hence, the total source function is given by Eqs. (2.50b–e) as follows:

$$J_2 + J_3 + J_4 \approx (1-f\omega)\hat{\omega}^2\left[2\hat{P}_{11}(\mathbf{\Omega},\mathbf{\Omega}_0) - \int \mathrm{d}\mathbf{\Omega}'\,\hat{P}_{11}(\mathbf{\Omega},\mathbf{\Omega}')\hat{P}_{11}(\mathbf{\Omega}',\mathbf{\Omega}_0)\right]F_{\mathrm{sol}}g(t,\mu_0^*,\mu_0^*), \tag{2.52}$$

where J_4 is expanded by the Taylor series around $f\omega t/\mu_0 \sim 0$ and truncated at a first order as

$$J_4(t;\mathbf{\Omega}) \approx \omega\hat{\omega}P_{11}(\mathbf{\Omega},\mathbf{\Omega}_0)F_{\mathrm{sol}}g(t,\mu_0^*,\mu_0^*). \tag{2.53}$$

In the case of the Legendre expansion of the phase function, the integral term in Eq. (2.51) is given as follows:

$$Z_{11} \equiv \int \mathrm{d}\boldsymbol{\Omega}'\, P_{11}(\boldsymbol{\Omega}, \boldsymbol{\Omega}') P_{11}(\boldsymbol{\Omega}', \boldsymbol{\Omega}_0) = \frac{1}{4\pi} \sum_{l=0}^{\infty} (2l+1)(\alpha_1^l)^2 P_l(x)\,. \tag{2.54}$$

Therefore, the secondary order scattering radiance $\hat{u}_{\mathrm{I},2}$ is given as follows:

$$\hat{u}_{\mathrm{I},2}(\tau, \boldsymbol{\Omega}) \approx (1 - f\omega)\hat{\omega}^2 \left[\hat{Z}_{11}(\boldsymbol{\Omega}, \boldsymbol{\Omega}_0) - 2\hat{P}_{11}(\boldsymbol{\Omega}, \boldsymbol{\Omega}_0)\right] F_{\mathrm{sol}} h(\tau, \mu, \mu_0^*, \mu_0^*), \tag{2.55}$$

$$h(\tau, \mu_2, \mu_1, \mu_0) = \frac{1}{\mu_2} \int_0^{\tau} \mathrm{d}t \exp\left[\frac{t-\tau}{\mu_2}\right] g(t, \mu_1, \mu_0). \tag{2.56}$$

According to Nakajima and Tanaka (1988), the IMS method has a good performance (< 1%) in an optical thickness < 1.

2.7. Sky radiances for the ground-based angular-scanning radiometer observations

When assuming a narrow spectral band filter response function, the direct solar and downward diffuse irradiances at the ground are directly expressed by the solution of the radiative transfer equation of Eqs. (2.6) and (2.13) as follows:

$$F_{\mathrm{ds}}(\lambda) = \frac{F_0}{d^2} \exp\left(-\frac{\tau(\lambda)}{\mu_0}\right), \tag{2.57a}$$

$$F_{\mathrm{df}}(\boldsymbol{\Omega}, \lambda) = \frac{1}{\mu} F_{\mathrm{ds}}(\lambda) \Delta_{\Omega} \left\{ \int_0^{\tau(\lambda)} \exp\left[(\tau - t)\left(\frac{1}{\mu_0} - \frac{1}{\mu}\right)\right] \omega(t;\lambda) P_{11}(\mathrm{t};\boldsymbol{\Omega};\lambda)\mathrm{d}t + Q(\boldsymbol{\Omega}, \lambda) \right\}, \tag{2.57b}$$

where F_{ds} is the sensor output current of the direct solar irradiances; F_{df} is the sensor output current of the diffuse irradiances, detected by the finite field of view (or solid view angle; SVA) Δ_{Ω}; F_0 is the calibration constant, which is the sensor output current of extra-terrestrial solar irradiance at the mean distance between the Earth and the sun as $F_0 \propto F_{\mathrm{sol}}$; d is the distance between Earth and the sun (AU) in the range of 0.983 to 1.017 AU; λ is the wavelength; and Q is the multiple scattering contribution. F_{ds} and F_{df} are treated in the SKYNET analysis as follows:

$$T(\lambda) = \frac{F_{\mathrm{ds}}(\lambda)d^2}{F_0(\lambda)} = \exp\left(-\frac{\tau(\lambda)}{\mu_0}\right), \tag{2.58a}$$

$$R(\mathbf{\Omega},\lambda) = \frac{\mu F_{\mathrm{df}}(\mathbf{\Omega},\lambda)}{F_{\mathrm{ds}}(\lambda)\Delta_\Omega} = \int_0^{\tau(\lambda)} \exp\left[(\tau - t)\left(\frac{1}{\mu_0} - \frac{1}{\mu}\right)\right] \omega(t;\lambda) P_{11}(\mathrm{t};\mathbf{\Omega};\lambda)\mathrm{d}t + Q(\mathbf{\Omega},\lambda)\,, \tag{2.58b}$$

where T is the transmittance same as Eq. (2.6); R is "normalized radiance" (Nakajima et al. [1996]; Nakajima et al. [2020]). Note that the unit of R is not radiance. Determination of T requires F_0, but R does not require F_0 because of the normalization (or canceled). Assuming a single homogeneous layer, diffuse intensity $L(\equiv T \times R) \propto F_{\mathrm{df}} \propto u_{\mathrm{I}}$ can be written as follows:

$$L(\mathbf{\Omega},\lambda) = \omega\tau P_{11}(\mathbf{\Omega},\lambda)E(\mu,\lambda) + Q(\mathbf{\Omega},\lambda)T(\lambda), \tag{2.59a}$$

$$E(\mu,\lambda) \equiv \begin{cases} T(\lambda) & \mu = \mu_0 \\ \left[\left(\frac{1}{\mu_0} - \frac{1}{\mu}\right)\tau(\lambda)\right]^{-1}\left[\exp\left(-\frac{\tau(\lambda)}{\mu}\right) - \exp\left(-\frac{\tau(\lambda)}{\mu_0}\right)\right] & \mu \neq \mu_0 \end{cases}. \tag{2.59b}$$

Hereafter, T and L are referred to as sky intensities.

Furthermore, assuming a wideband filter response function ψ, the convolved direct solar and diffuse irradiances ($\tilde{F}_{\mathrm{ds}}$ and $\tilde{F}_{\mathrm{df}}$) can be obtained through convolution of Eq. (2.57) as follows:

$$\tilde{F}_{\mathrm{ds}}(\lambda) = \int \psi(\lambda)F_{\mathrm{ds}}(\lambda)\mathrm{d}\lambda = \frac{1}{d^2}\int \psi(\lambda)F_0(\lambda)T(\lambda)\mathrm{d}\lambda\,, \tag{2.60a}$$

$$\tilde{F}_{\mathrm{df}}(\mathbf{\Omega};\lambda) = \int \psi(\lambda)F_{\mathrm{df}}(\mathbf{\Omega};\lambda)\mathrm{d}\lambda = \frac{\Delta\Omega}{\mu d^2}\int \psi(\lambda)F_0(\lambda)L(\mathbf{\Omega},\lambda)\mathrm{d}\lambda\,, \tag{2.60b}$$

$$\tilde{F}_0(\lambda) = \int \psi(\lambda)F_0(\lambda)\mathrm{d}\lambda \propto \int \psi(\lambda)F_{\mathrm{sol}}(\lambda)\mathrm{d}\lambda\,. \tag{2.60c}$$

Hence, the convolved variables ($\tilde{T}$, $\tilde{L}$, and $\tilde{R}$) of T, L, and R are defined as follows:

$$\tilde{T}(\lambda) = \frac{\tilde{F}_{\mathrm{ds}}(\lambda)d^2}{\tilde{F}_0(\lambda)} = \frac{\int \psi(\lambda)F_{\mathrm{sol}}(\lambda)T(\lambda)\mathrm{d}\lambda}{\int \psi(\lambda)F_{\mathrm{sol}}(\lambda)\mathrm{d}\lambda}, \tag{2.61a}$$

$$\tilde{R}(\boldsymbol{\Omega},\lambda)=\frac{\mu\tilde{F}_{\mathrm{df}}(\boldsymbol{\Omega},\lambda)}{\tilde{F}_{\mathrm{ds}}(\lambda)\Delta\Omega}=\frac{\tilde{L}(\boldsymbol{\Omega},\lambda)}{\tilde{T}(\lambda)}=\frac{\int\psi(\lambda)F_{\mathrm{sol}}(\lambda)L(\boldsymbol{\Omega},\lambda)\mathrm{d}\lambda}{\int\psi(\lambda)F_{\mathrm{sol}}(\lambda)T(\lambda)\mathrm{d}\lambda}, \tag{2.61b}$$

$$\tilde{L}(\boldsymbol{\Omega},\lambda)\equiv\tilde{T}(\lambda)\tilde{R}(\boldsymbol{\Omega},\lambda)=\frac{\int\psi(\lambda)F_{\mathrm{sol}}(\lambda)L(\boldsymbol{\Omega},\lambda)\mathrm{d}\lambda}{\int\psi(\lambda)F_{\mathrm{sol}}(\lambda)\mathrm{d}\lambda}. \tag{2.61c}$$

Although the sky radiances at weak gas absorption regions, such as the 340, 380, 400, 500, 675, 870, and 1020 nm bands in sky-radiometer observations, can be regarded to be narrow spectral bands (Eq. (2.57)), the sky radiances at gas absorption regions, such as the 940 nm band in sky-radiometer observations, require the convolution (Eq. (2.60)).

2.8. Convolved sky radiances by the correlated *k*-distribution technique

When using the numerical computation, the convolved sky radiance is obtained by quadrature of a finite interval. Traditionally, several look-up tables with different resolutions (*e.g.*, LOWTRAN, MODTRAN, and HITRAN) called "band models" have been developed for different purposes. However, it is still challenging to effectively (rapidly yet accurately) obtain the narrow-band sky radiance in gas absorption bands because of complicated line absorption (Fig. 2.9). One of the sophisticated techniques is the correlated *k*-distribution method (Lacis and Oinas [1991]; Fu and Liou [1992]). The radiance computation with the correlated *k*-distribution assumption is a quadrature numerical integration in the specific spectral regions extended from the *k*-distribution computation method for inhomogeneous atmosphere (Lacis and Oinas [1991]; Fu and Liou [1992]). This section only treats one species case, such as around 940 nm, because multiple species case is complicated by overlapping.

The gas absorption coefficient is a function of wavenumber κ, pressure p, and temperature K. Band model causes the residual errors in the sky radiance computation because the gas absorption coefficient has a chaotical value in the wavenumber space (Fig. 2.9). However, when we sort the gas absorption coefficient in the specific band according to the absorption, the probability density of the absorption can be obtained. If the sort order does not change to K and p, the information of the complex line shape is conserved in cumulative probability density space. Therefore, we can obtain the band-average of T and L by quadrature integration in cumulative probability density space as follows:

$$\bar{T}^{\mathrm{CKD}}(\bar{\lambda})=\sum_{j=1}^{N_{\mathrm{ch}}}\xi_j T_{\mathrm{ckd}}^{(j)}(\bar{\lambda}), \tag{2.62a}$$

$$\bar{L}^{\mathrm{CKD}}(\boldsymbol{\Omega},\bar{\lambda}) = \sum_{j=1}^{N_{\mathrm{ch}}} \xi_i T_{\mathrm{ckd}}^{(j)}(\bar{\lambda}) R_{\mathrm{ckd}}^{(j)}(\boldsymbol{\Omega},\bar{\lambda}), \tag{2.62b}$$

where $\bar{T}^{\mathrm{CKD}}$ and $\bar{L}^{\mathrm{CKD}}$ are, respectively, the band-average of T and L with the CKD method; $\bar{\lambda}$ is the central wavelength and $\int_{\Delta_\kappa} \frac{\mathrm{d}\kappa}{\kappa^2} = \Delta_\kappa \bar{\lambda}^2$; N_{ch} is the number of quadrature points; $T_{\mathrm{ckd}}^{(j)}$ and $R^{(j)}$ are the transmittance and normalized radiance at *j*-th quadrature point of the *k*-distribution, respectively; ξ_j is the *j*-th quadrature weight of the *k*-distribution and is normalized to

$$\sum_{j=1}^{N_{\mathrm{ch}}} \xi_j = 1. \tag{2.63}$$

Note that Eq. (2.62) assumes that extra-terrestrial solar irradiance is nearly constant among sub-bands. Thus, convolved radiances ($\hat{T}^{\mathrm{CKD}}$ and $\hat{L}^{\mathrm{CKD}}$) for the filter response function $\psi(\lambda)$ are determined as follows:

$$\hat{T}^{\mathrm{CKD}}(\lambda) = \frac{\sum^{N_{\mathrm{band}}} \bar{\psi}(\bar{\lambda}) \cdot \bar{F}_{\mathrm{sol}}(\bar{\lambda}) \cdot \bar{T}^{\mathrm{CKD}}(\bar{\lambda}) \cdot \Delta_\kappa \bar{\lambda}^2}{\sum^{N_{\mathrm{band}}} \bar{\psi}(\bar{\lambda}) \cdot \bar{F}_{\mathrm{sol}}(\bar{\lambda}) \cdot \Delta_\kappa \bar{\lambda}^2}, \tag{2.64a}$$

$$\hat{L}^{\mathrm{CKD}}(\boldsymbol{\Omega},\lambda) = \frac{\sum^{N_{\mathrm{band}}} \bar{\psi}(\bar{\lambda}) \cdot \bar{F}_{\mathrm{sol}}(\bar{\lambda}) \cdot \bar{L}^{\mathrm{CKD}}(\boldsymbol{\Omega};\bar{\lambda}) \cdot \Delta_\kappa \bar{\lambda}^2}{\sum^{N_{\mathrm{band}}} \bar{\psi}(\bar{\lambda}) \cdot \bar{F}_{\mathrm{sol}}(\bar{\lambda}) \cdot \Delta_\kappa \bar{\lambda}^2}, \tag{2.64b}$$

$$\bar{F}_{\mathrm{sol}}(\bar{\lambda}) \equiv \frac{\int_{\Delta_\kappa} F_{\mathrm{sol}}(\lambda) \frac{\mathrm{d}\kappa}{\kappa^2}}{\Delta_\kappa \bar{\lambda}^2}, \tag{2.64c}$$

$$\bar{\psi}(\bar{\lambda}) \equiv \frac{\int_{\Delta_\kappa} \psi(\lambda) \frac{\mathrm{d}\kappa}{\kappa^2}}{\Delta_\kappa \bar{\lambda}^2}, \tag{2.64d}$$

where $\bar{F}_{\mathrm{sol}}$ and $\bar{\psi}$ are the band averaged extra-terrestrial solar irradiance and the stepwise filter response function, respectively; Δ_κ is the sub-band interval in wavenumber space; N_{band} is the number of sub-bands. Here, $\hat{T}$ and $\tilde{T}$ in Eq. (2.61a) ($\hat{L}$ and $\tilde{L}$ in Eq. (2.61c))

are not entirely synonymous, but they are generally equivalent based on assumptions that the extra-terrestrial solar irradiance and filter response function are nearly constant across sub-bands.

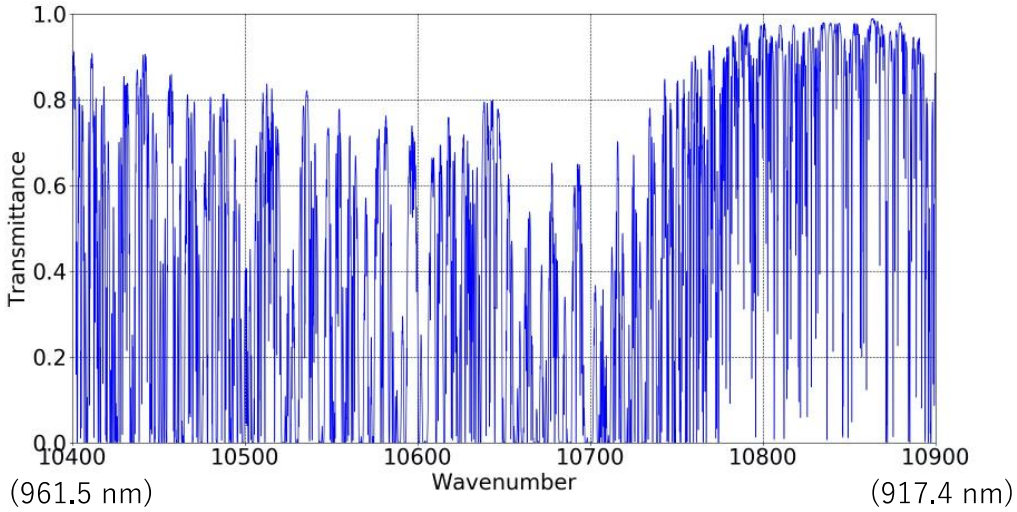

Figure 2.9: Transmittance of water vapor line absorption around 940 nm under the US standard atmosphere with line-by-line approach described in Chapter 5.

References

[1] Chandrasekhar, S., 1960: Radiative transfer. Dover publications, Inc., New York., ISBN 0-486-60590-6.

[2] Dubovik, O., Smirnov, A., Holben, B. N., King, M. D., Kaufman, Y. J., Eck, T. F., and Slutsker, I.: Accuracy assessments of aerosol optical properties retrieved from Aerosol Robotic Network (AERONET) Sun and sky radiance measurements, J. Geophys. Res., 105, 9791–9806, 2000

[3] Dubovik, O., Sinyuk, A., Lapyonok, T., Holben, B. N., Mishchenko, M., Yang, P., Eck, T. F., Volte, H., Muñoz, O., Veihelmann, B., van der Zande, W. J., Leon, J.-F., Sorokin, M., and Slutsker, I.: Application of spheroid models to account for aerosol particle nonsphericity in remote sensing of desert dust, J. Geophys. Res., 111, D11208, doi:10.1029/2005JD006619, 2006

[4] Evans K.F., 1998: The spherical harmonics discrete ordinate method for three-dimensional atmospheric radiative transfer. J. Atmos. Sci., 55, 429–446

[5] Fu, Q., and K. N. Liou, 1992: On the correlated k-distribution method for radiative transfer in nonhomogeneous atmospheres, *J. Atmos. Sci.*, **49**, 2139–2156.

[6] Hovenier JW, Van der Mee C, Domke H., 2004: Transfer of polarized light in planetary atmospheres: basic concepts and practical methods. Dordrecht: Kluwer Academic Publishers.

[7] Hu Y. X., B. Wielicki, B. Lin, G. Gibson, S. C. Tsay, K. Stamnes, and T. Wong, 2000: δ-fit: a fast and accurate treatment of particle scattering phase functions with weighted singular-value decomposition least-squares fitting, J. Quant. Spectrosc. Radiat. Transfer, 65, 681–690

[8] Lacis, A. A., and V. A. Oinas, 1991: Description if the correlated k-distribution method for modeling nongray gaseous absorption, thermal emission, and multiple scattering in vertically inhomogeneous atmospheres, *J. Geophys. Res.*, **96**, 9027–9063.

[9] Li, L., K. Li, L. Blarel, and M. Wendisch, 2014: A method to calculate Stokes parameters and angle of polarization of skylight from polarized CIMEL sun/sky radiometers, J. Quant. Spectrosc. Radiat. Transfer, 149, 334–346.

[10] Min, Q., and M. Duan, 2004: A successive order of scattering model for solving vector radiative transfer in the atmosphere, J. Quant. Spectrosc. Radiat. Transfer, 87, 243–259

[11] Momoi, M., H. Irie, M. Sekiguchi, T. Nakajima, H. Takenaka, K. Miura, and K. Aoki, Rapid, accurate computation of narrow-band sky radiance in the 940 nm gas absorption region using the correlated *k*-distribution method for sun-photometer observations, Prog. Earth Planet. Sci., 9, 10, https://doi.org/10.1186/s40645-022-00467-6, 2022.

[12] Nakajima, T., and M. Tanaka, 1986: Matrix formulations for the transfer of solar

radiation in a plane-parallel scattering atmosphere. J. Quant. Spectrosc. Radiat. Transfer, 35, 13–21

[13] Nakajima, T., and M. Tanaka, 1988: Algorithms for radiative intensity calculations in moderately thick atmospheres using a truncation approximation. J. Quant. Spectrosc. Radiat. Transfer, 40, 51–69

[14] Nakajima, T., M. Tanaka, M. Yamano, M. Shiobara, K. Arao, and Y. Nakanishi, 1989: Aerosol Optical Characteristics in the Yellow Sand Events Observed in May, 1982 at Nagasaki-Part II Models, J. Meteorol. Soc. Japan, 67, 279-291, https://doi.org/10.2151/jmsj1965.67.2_279

[15] Nakajima, T., Tonna, G., Rao, R., Boi, P., Kaufman, Y., and Holben, B.: Use of Sky brightness measurements from ground for remote sensing of particulate polydispersions, Appl. Opt., 35, 2672-2686, 1996

[16] Nakajima, T., M. Campanelli, H. Che, V. Estellés, H. Irie, S. Kim, J. Kim, D. Liu, T. Nishizawa, G. Pandithurai, V. K. Soni, B. Thana, N. Tugjsurn, K. Aoki, S. Go, M. Hashimoto, A. Higurashi, S. Kazadzis, P. Khatri, N. Kouremeti, R. Kudo, F. Marenco, M. Momoi, S.S. Ningombam, C. L. Royder, A. Uchiyama, and A. Yamazaki, 2020b: An overview of and issues with sky radiometer technology and SKYNET, *Atmos. Meas. Tech.*, **13**, 4195-4218, https://doi.org/10.5194/amt-13-4195-2020.

[17] Ota, Y., A. Higurashi, T. Nakajima, and T. Yokota, 2010: Matrix formulations of radiative transfer including the polarization effect in a coupled atmosphere–ocean system. *J. Quant. Spectrosc. Radiat. Transfer*, **111**, 878–894

[18] Potter, J. F., 1970: The delta function approximation in radiative transfer theory, *J. Atmos. Sci.*, **27**, 943–949.

[19] Rozanov, V. V., and A. I. Lyapustin, 2010: Similarity of radiative transfer equation: error anal- ysis of phase function truncation techniques. *J. Quant. Spectrosc. Radiat. Transfer*, **111**, 1964–1979

[20] Siewert CE, 1981: On the equation of transfer relevant to the scattering of polarized light. *Astrophys J*, 245, 1080–6

[21] Siewert CE, 1982: On the phase matrix basic to the scattering of polarized light, *Astron Astrophys*, 109, 195–200

[22] Stamnes, K., and R. Swanson, 1981: A new look at the discrete ordinate method. for radiative transfer calculations in anisotropically scattering atmospheres. J. Atmos. Sci., 38, 387-398.

[23] Stamnes, K., S.-C. Tsay, W. Wiscombe, and K. Jayaweera, 1988: Numerically stable algorithm for discrete-ordinate-method radiative transfer in multiple scattering and emitting layered media. Appl. Opt., 27, 2502-2509.

[24] Stokes, G. G., 1852: On the composition and resolution of streams of polarized light from different sources. Transactions of the Cambridge Philosophical Society, 9, 399.

[25] Wiscombe W., 1977: The delta-M method: rapid yet accurate radiative flux calculations for strongly asymmetric phase functions, *J Atmos Sci*, 34, 1408–22.

[26] Young F., 2012: University Physics with Modern Physics Thirteenth Edition, PEARSON, 1521p

Chapter 3: Inversion problem

This section provides a brief outline of the inversion problem, especially multi-term least square fitting, based on the textbook by Rogers [2000] and the paper of Dubovik and King [2000]. In this section, superscripts M and R indicate measurement and estimation variables, respectively.

3.1. Forward model

We define a function $\mathcal{F}_1$ which convert $\boldsymbol{X} \in \mathbb{R}^{N_\mathrm{x}}$ to $\boldsymbol{Y}_1 \in \mathbb{R}^{N_\mathrm{y}}$ as:

$$\boldsymbol{Y}_1 = \mathcal{F}_1(\boldsymbol{X}). \tag{3.1}$$

In Eq. (3.1), $\boldsymbol{X}$ and $\boldsymbol{Y}_1$ are independent (or explanatory) and dependent variable vectors, respectively. Here, when observed $\boldsymbol{X}$ with noise $\boldsymbol{\varepsilon}_\mathbf{x}$, $\boldsymbol{Y}_1$ are directly obtained from Eq. (3.1) as:

$$\boldsymbol{Y}_1 = \mathcal{F}_1(\boldsymbol{X}^\mathrm{M}) = \mathcal{F}_1(\boldsymbol{X} + \boldsymbol{\varepsilon}_\mathbf{x}). \tag{3.2}$$

In contrast, it is challenging to obtain $\boldsymbol{X}$ from $\boldsymbol{Y}_1$ with noise $\boldsymbol{\varepsilon}$ unless inverse function ${\mathcal{F}_1}^{-1}$ can be formulated and requires the inverse problem described in the next section.

3.2. Least square fitting

This section describes the least square fitting (or least square method, maximum likelihood method), which obtains $\boldsymbol{X}$ from $\boldsymbol{Y}_1^\mathrm{M}$. First, the residuals $G(\boldsymbol{X})$ between $\mathcal{F}_1(\boldsymbol{X})$ and $\boldsymbol{Y}_1^\mathrm{M}$ is defined as:

$$G(\boldsymbol{X}) = [\boldsymbol{Y}_1^\mathrm{M} - \mathcal{F}_1(\boldsymbol{X})]^\mathrm{T}\mathbf{S}_1^{-1}[\boldsymbol{Y}_1^\mathrm{M} - \mathcal{F}_1(\boldsymbol{X})] \rightarrow \boldsymbol{\varepsilon}_\mathrm{y}^\mathrm{T}\mathbf{S}_1^{-1}\boldsymbol{\varepsilon}_\mathrm{y}, \tag{3.3}$$

where $\mathbf{S}_1$ is the weight matrix ($\in \mathbb{R}^{N_\mathrm{y} \times N_\mathrm{y}}$); G is the cost function. The second term of the right-hand side is obtained when $\boldsymbol{X}$ is true values because $\boldsymbol{Y}_1^\mathrm{R} \approx \boldsymbol{Y}_1^\mathrm{M} + \boldsymbol{\varepsilon}_\mathrm{y}$. Then, by using the covariance matrix of $\boldsymbol{Y}_1^\mathrm{M}$ as $\mathbf{S}_1$, the second term of Eq. (3.3) is 1. Therefore, $\boldsymbol{X}$ can be estimated by minimizing $G(\boldsymbol{X})$ to 1. In other words, $\boldsymbol{X}$ is the maximum likelihood value when the differential of $G(\boldsymbol{X})$ equals 0. Using Eq. (3.3), the differential of $G(\boldsymbol{X})$ is expressed as:

$$\nabla G = -\mathbf{K}_1{}^{\mathrm{T}}\mathbf{S}_1^{-1}[\boldsymbol{Y}_1^{\mathrm{M}} - \mathcal{F}_1(\boldsymbol{X})] \in \mathbb{R}^{N_{\mathrm{x}}}, \tag{3.4}$$

$$\mathbf{K}_1{}^{\mathrm{T}} \equiv \left[\nabla\mathcal{F}_1^{(1)}(\boldsymbol{X}),\cdots,\nabla\mathcal{F}_1^{(N_{\mathrm{y}})}(\boldsymbol{X})\right]^{\mathrm{T}} \in \mathbb{R}^{N_{\mathrm{y}}\times N_{\mathrm{x}}}, \tag{3.5a}$$

$$\boldsymbol{Y}_1^{\mathrm{R}} = \mathcal{F}_1(\boldsymbol{X}) \equiv \left[\mathcal{F}_1^{(1)}(\boldsymbol{X}),\cdots,\mathcal{F}_1^{(N_{\mathrm{y}})}(\boldsymbol{X})\right]^{\mathrm{T}} \in \mathbb{R}^{N_{\mathrm{y}}}, \tag{3.5b}$$

where $\mathbf{K}_1$ is the Jacobian matrix. Now, we consider $\mathcal{F}_1$ as a linear operator. From Eq. (3.4), the maximum likelihood values are obtained as:

$$\boldsymbol{X} = \left(\mathbf{K}_1{}^{\mathrm{T}}\mathbf{S}_1^{-1}\mathbf{K}_1\right)^{-1}\mathbf{K}_1{}^{\mathrm{T}}\mathbf{S}_1^{-1}\boldsymbol{Y}_1^{\mathrm{M}}, \tag{3.6a}$$

because:

$$\nabla G = -\mathbf{K}_1{}^{\mathrm{T}}\mathbf{S}_1^{-1}\left[\boldsymbol{Y}_1^{\mathrm{M}} - \mathbf{K}_1{}^{\mathrm{T}}\boldsymbol{X}\right] = 0. \tag{3.6b}$$

Next, when $\mathcal{F}$ is a non-linear operator, $\boldsymbol{X}$ can be estimated near $\boldsymbol{X}_0$ by first order Taylor expansion as:

$$\boldsymbol{X} = \boldsymbol{X}_{(0)} + \left(\mathbf{K}_1{}^{\mathrm{T}}\mathbf{S}_1^{-1}\mathbf{K}_1\right)^{-1}\mathbf{K}_1{}^{\mathrm{T}}\mathbf{S}_1^{-1}\left[\boldsymbol{Y}_1^{\mathrm{M}} - \mathcal{F}_1\left(\boldsymbol{X}_{(0)}\right)\right], \tag{3.7a}$$

because:

$$\nabla G = -\left(\mathbf{K}_1{}^{\mathrm{T}}\mathbf{S}_1^{-1}\mathbf{K}_1\right)^{-1}\mathbf{K}_1{}^{\mathrm{T}}\mathbf{S}_1^{-1}\left[\boldsymbol{Y}_1^{\mathrm{M}} - \mathcal{F}_1(\boldsymbol{X}_1) + \mathbf{K}_1{}^{\mathrm{T}}\boldsymbol{X}_{(0)} - \mathbf{K}_1{}^{\mathrm{T}}\boldsymbol{X}\right] = 0. \tag{3.7b}$$

Hence, we can obtain the maximum likelihood values with iteration.

3.3. Multi-term least square fitting

The advanced case is to be constrained by several functions ($\mathcal{F}_1, \mathcal{F}_2, \cdots$). When $\boldsymbol{Y}_1, \boldsymbol{Y}_2, \cdots$ corresponding to $\mathcal{F}_1, \mathcal{F}_2, \cdots$ is independent of each other, G is obtained as:

$$G(\boldsymbol{X}) = \sum_j \left[\boldsymbol{Y}_j^{\mathrm{M}} - \mathcal{F}_j(\boldsymbol{X})\right]^{\mathrm{T}} \mathbf{S}_j^{-1} \left[\boldsymbol{Y}_j^{\mathrm{M}} - \mathcal{F}_j(\boldsymbol{X})\right], \tag{3.8a}$$

because:

$$G(\boldsymbol{X}) = \begin{pmatrix} \boldsymbol{Y}_1^{\mathrm{M}} - \mathcal{F}_1(\boldsymbol{X}) \\ \boldsymbol{Y}_2^{\mathrm{M}} - \mathcal{F}_2(\boldsymbol{X}) \\ \vdots \end{pmatrix}^{\mathrm{T}} \begin{pmatrix} \mathbf{S}_1 & 0 & 0 \\ 0 & \mathbf{S}_2 & 0 \\ 0 & 0 & \ddots \end{pmatrix}^{-1} \begin{pmatrix} \boldsymbol{Y}_1^{\mathrm{M}} - \mathcal{F}_1(\boldsymbol{X}) \\ \boldsymbol{Y}_2^{\mathrm{M}} - \mathcal{F}_2(\boldsymbol{X}) \\ \vdots \end{pmatrix}. \tag{3.8b}$$

Hence, the maximum likelihood values in non-linear functions ($\mathcal{F}_1, \mathcal{F}_2, \cdots$) are estimated as follows:

$$\boldsymbol{X} = \boldsymbol{X}_{(0)} + \left(\sum_j \mathbf{K}_j{}^{\mathrm{T}} \mathbf{S}_j^{-1} \mathbf{K}_j \right)^{-1} \left\{ \sum_j \mathbf{K}_j{}^{\mathrm{T}} \mathbf{S}_j^{-1} \left[\boldsymbol{Y}_j^{\mathrm{M}} - \mathcal{F}_j\left(\boldsymbol{X}_{(0)}\right)\right] \right\}. \tag{3.9}$$

This formulation is often used for regularization as below:

(1) L2 regularization (or *a priori* constraint)

This constraint can be used when the solution space ($\boldsymbol{X}_{\mathrm{a}} \pm \sqrt{\mathbf{S}_{\mathrm{a}}}$) is known. Eq. (3.9) is expressed as below:

$$\boldsymbol{X} = \boldsymbol{X}_{(0)} + \left(\mathbf{K}_1{}^{\mathrm{T}} \mathbf{S}_1^{-1} \mathbf{K}_1 + \mathbf{S}_{\mathrm{a}}^{-1}\right)^{-1} \left\{ \mathbf{K}_1{}^{\mathrm{T}} \mathbf{S}_1^{-1} \left[\boldsymbol{Y}_1^{\mathrm{M}} - \mathcal{F}_1\left(\boldsymbol{X}_{(0)}\right)\right] - \mathbf{S}_{\mathrm{a}}^{-1} \left(\boldsymbol{X}_{(0)} - \boldsymbol{X}_{\mathrm{a}}\right) \right\}. \tag{3.10a}$$

(2) Tikhonov regularization (*e.g.*, Phillip [1962] and Twomey [1963])

This constraint helps smooth adjacent values of $\boldsymbol{X}$. Eq. (3.9) is expressed as below:

$$\boldsymbol{X} = \boldsymbol{X}_{(0)} + \left(\mathbf{K}_1{}^{\mathrm{T}} \mathbf{S}_1^{-1} \mathbf{K}_1 - \mathbf{S}_{\mathrm{a}}^{-1}\right)^{-1} \left\{ \mathbf{K}_1{}^{\mathrm{T}} \mathbf{S}_1^{-1} \left[\boldsymbol{Y}_1^{\mathrm{M}} - \mathcal{F}_1\left(\boldsymbol{X}_{(0)}\right)\right] - \mathbf{S}_{\mathrm{a}}^{-1} \boldsymbol{X}_{(0)} \right\}. \tag{3.10b}$$

References

[1] Dubovik, O. and M. D. King, 2000: A flexible inversion algorithm for retrieval of aerosol optical properties from sun and sky radiance measurements, *J. Geophys. Res.*, **105**, 20673–20696

[2] Phillips, D. L., 1962: A technique for the numerical solution of certain integral equations of the first kind, J. ACM, 9, 84-97

[3] Rodgers, C. D., 2000: Inverse Method for Atmospheric Sounding, World Sci., Singapore, 256 pp.

[4] Twomey, S., 1963: On the numerical solution of Fredholm integral equations of the first kind by the inversion of the linear system produced by quadrature, J. Assoc. Comput. Mach. 10, 97

Chapter 4: Efficient calculation methods "P^n-IMS" of radiative intensity including the polarization effect in moderately thick atmospheres

In this section, we developed a system of correction methods named P^n-IMS (Improved Multiple and Single scattering approximation by n-th order multiple scattering correction of the forward Peak) by extending the TMS and IMS methods using the full-vector treatment of PSTAR (Ota et al. [2010]). Section 4.1 describes the theoretical considerations in vector radiative transfer theory with the delta-M method (Wiscombe [1977]; Ota et al. [2010]). Section 4.2 then discusses the performance of the P^n-IMS methods as determined from numerical tests. This chapter is primarily based on Momoi et al. [2022].

4.1. Theoretical considerations

This section provides a theoretical consideration of the P^n-IMS methods, including the polarization effects based on the vector radiative theory. The P^n-IMS methods were developed as extended versions of the TMS and IMS methods, first and second order scattering corrections in scalar approximation developed by Nakajima and Tanaka [1988] described in Section 2.4. As discussed below, the P^n-IMS methods can be formulated similarly to the scalar approximation in the TMS and IMS methods.

According to Ogawa et al. [1989] and Ota et al. [2010], the delta-M method is also valid in the vector radiative transfer equation with truncating the phase matrix $\mathbf{P}$ as follows:

$$\mathbf{P}(\Theta) = f\widehat{\mathbf{P}}(\Theta) + (1-f)\mathbf{P}^*(\Theta), \tag{4.1a}$$

$$\widehat{\mathbf{P}}(\Theta) \sim \frac{1}{2\pi}\delta(\Theta)\mathbf{E}_4, \tag{4.1b}$$

where $\delta(\Theta)$ denotes the delta function, and $\mathbf{E}_4$ is the 4×4 unit matrix. In the truncation space, the l-th coefficient matrix $\mathbf{B}_l^*$ and $\widehat{\mathbf{B}}_l$ of spherical function for $\mathbf{P}^*$ and $\widehat{\mathbf{P}}$ are expressed as:

$$\mathbf{B}_l^* \equiv \frac{1}{1-f}\left(\mathbf{B}_l - f\widehat{\mathbf{B}}_l\right), \tag{4.2a}$$

$$\widehat{\mathbf{B}}_l \equiv \begin{cases} \begin{pmatrix} 1 & 0 & 0 & 0 \\ 0 & 0 & 0 & 0 \\ 0 & 0 & 0 & 0 \\ 0 & 0 & 0 & 1 \end{pmatrix} & l = 0, 1 \\ \mathbf{E}_4 & 1 < l < M^* + 1 \\ \dfrac{1}{f}\mathbf{B}_l & otherwise \end{cases}. \tag{4.2b}$$

Using Eq. (4.2), the forward peak phase matrix is a delta-like function shown in Fig. 4.1.

The TMS method described in Section 2.6 is then applied to the vector radiative transfer equation by extension Eqs. (2.46-47) (Ota et al. [2010]) as follows:

$$\boldsymbol{u}' = \boldsymbol{u}^* + \widehat{\boldsymbol{u}}_1, \tag{4.3a}$$

$$\widehat{\boldsymbol{u}}_1 \equiv \widehat{\omega}\widehat{\mathbf{P}}(\boldsymbol{\Omega}, \boldsymbol{\Omega}_0)\boldsymbol{F}_{\mathrm{sol}} g(t, \mu^*, \mu_0^*), \tag{4.3b}$$

where $\boldsymbol{u}'$ and $\boldsymbol{u}^*$ are the Stokes radiance vectors corresponding to the scalar radiances u_{I}' and u_{I}^*, respectively. Therefore, we can express the additional scattering $\widehat{\boldsymbol{u}}(= \boldsymbol{u} - \boldsymbol{u}')$ similarly to that in Eq. (2.50) as follows:

$$-\mu\frac{\mathrm{d}\widehat{\boldsymbol{u}}}{\mathrm{d}t} = \widehat{\boldsymbol{u}} - \omega\int \mathrm{d}\boldsymbol{\Omega}'\,\mathbf{P}(\boldsymbol{\Omega}, \boldsymbol{\Omega}')\widehat{\boldsymbol{u}}(t; \boldsymbol{\Omega}') + \boldsymbol{J}_1 + \boldsymbol{J}_2 + \boldsymbol{J}_3 + \boldsymbol{J}_4, \tag{4.4a}$$

$$\boldsymbol{J}_1(t; \boldsymbol{\Omega}) \equiv f\omega\left[\boldsymbol{u}_{\mathrm{m}}^*(t; \boldsymbol{\Omega}) - \int \mathrm{d}\boldsymbol{\Omega}'\,\widehat{\mathbf{P}}(\boldsymbol{\Omega}, \boldsymbol{\Omega}')\boldsymbol{u}_{\mathrm{m}}^*(t; \boldsymbol{\Omega}')\right], \tag{4.4b}$$

$$\begin{aligned}\boldsymbol{J}_2(t; \boldsymbol{\Omega}) \equiv \widehat{\omega}\omega\Big[&\mathbf{P}(\boldsymbol{\Omega}, \boldsymbol{\Omega}_0)\boldsymbol{F}_{\mathrm{sol}} g(\tau, \mu^*, \mu_0^*) \\ &- (1-f)\int \mathrm{d}\boldsymbol{\Omega}'\,\widehat{\mathbf{P}}(\boldsymbol{\Omega}, \boldsymbol{\Omega}')\mathbf{P}^*(\boldsymbol{\Omega}', \boldsymbol{\Omega}_0)\boldsymbol{F}_{\mathrm{sol}} g(t, \mu'^*, \mu_0^*)\Big],\end{aligned} \tag{4.4c}$$

$$\boldsymbol{J}_3(t; \boldsymbol{\Omega}) \equiv -\widehat{\omega}\omega\int \mathrm{d}\boldsymbol{\Omega}'\,\mathbf{P}(\boldsymbol{\Omega}, \boldsymbol{\Omega}')\widehat{\mathbf{P}}(\boldsymbol{\Omega}', \boldsymbol{\Omega}_0)\boldsymbol{F}_{\mathrm{sol}} g(t, \mu'^*, \mu_0^*), \tag{4.4d}$$

$$\boldsymbol{J}_4(t;\boldsymbol{\Omega}) \equiv \omega e^{-\frac{t}{\mu_0^*}} \mathbf{P}(\boldsymbol{\Omega},\boldsymbol{\Omega}_0)\boldsymbol{F}_{\mathrm{sol}} \left[1 - \exp\left(-\frac{f\omega t}{\mu_0}\right)\right], \tag{4.4e}$$

where $\boldsymbol{u}_{\mathrm{m}}^*$ is the multiple scattering of $\boldsymbol{u}^*$. The relationship between $\widehat{\mathbf{P}}$ and $\mathbf{P}^*$ can be expressed in the same manner as in Eq. (2.51), as follows:

$$\int \mathrm{d}\boldsymbol{\Omega}'\, \widehat{\mathbf{P}}(\boldsymbol{\Omega},\boldsymbol{\Omega}')\mathbf{P}^*(\boldsymbol{\Omega}',\boldsymbol{\Omega}_0) = \mathbf{P}^*(\boldsymbol{\Omega},\boldsymbol{\Omega}_0). \tag{4.5a}$$

because:

$$\widehat{\mathbf{B}}_l \mathbf{B}_l^* = \mathbf{B}_l^*. \tag{4.5b}$$

Therefore, we can obtain the total source function of the second order scattering radiance $\widehat{\boldsymbol{u}}_2$ as follows:

$$\boldsymbol{J}_2 + \boldsymbol{J}_3 + \boldsymbol{J}_4 \approx (1 - f\omega)\widehat{\omega}^2 \left[2\widehat{\mathbf{P}}(\boldsymbol{\Omega},\boldsymbol{\Omega}_0) - \int \mathrm{d}\boldsymbol{\Omega}'\, \widehat{\mathbf{P}}(\boldsymbol{\Omega},\boldsymbol{\Omega}')\widehat{\mathbf{P}}(\boldsymbol{\Omega}',\boldsymbol{\Omega}_0)\right] \boldsymbol{F}_{\mathrm{sol}} g(t,\mu_0^*,\mu_0^*). \tag{4.6}$$

Equation (4.6) is similar to Eq. (2.52), but the second term on the right-hand side needs complex numbers because of the matrix product $\mathbf{P}(\boldsymbol{\Omega},\boldsymbol{\Omega}')\mathbf{P}(\boldsymbol{\Omega}',\boldsymbol{\Omega}_0)$. Using Eq. (2.14), the second term in Eq. (4.6) is given as follows:

$$\int \mathrm{d}\boldsymbol{\Omega}'\, \mathbf{P}(\boldsymbol{\Omega},\boldsymbol{\Omega}')\mathbf{P}(\boldsymbol{\Omega}',\boldsymbol{\Omega}_0) = \mathbf{Z}_2(\boldsymbol{\Omega},\boldsymbol{\Omega}_0) + \frac{1}{2}\int \mathrm{d}\mu'\, \mathbf{P}_{\mathrm{s}}^{(0)}(\mu,\mu')\mathbf{P}_{\mathrm{s}}^{(0)}(\mu',\mu_0), \tag{4.7}$$

$$\mathbf{Z}_n(\boldsymbol{\Omega},\boldsymbol{\Omega}_0) = \frac{1}{4\pi}\sum_{m=0}^{\infty}(2-\delta_{0m})\left[\mathbf{Z}_{\mathrm{c},n}^{(m)}(\mu,\mu_0)\cos m(\phi-\phi_0) + \mathbf{Z}_{\mathrm{s},n}^{(m)}(\mu,\mu_0)\sin m(\phi-\phi_0)\right], \tag{4.8a}$$

$$\mathbf{Z}_{\mathrm{c},n}^{(m)}(\mu,\mu_0) \equiv \frac{1}{2}\left[\mathbf{C}_n^{(m)}(\mu,\mu_0) + \mathbf{D}\mathbf{C}_n^{(m)}(\mu,\mu_0)\mathbf{D}\right], \tag{4.8b}$$

$$\mathbf{Z}_{\mathrm{s},n}^{(m)}(\mu,\mu_0) \equiv \frac{1}{2}\left[\mathbf{C}_n^{(m)}(\mu,\mu_0)\mathbf{D} - \mathbf{D}\mathbf{C}_n^{(m)}(\mu,\mu_0)\right], \tag{4.8c}$$

$$\mathbf{C}_n^{(m)}(\mu,\mu_0) \equiv \sum_{l=m}^{\infty}(2l+1)\frac{(l-m)!}{(l+m)!}\mathbf{P}_l^m(\mu)[\mathbf{B}_l]^n\mathbf{P}_l^m(\mu_0)\,. \tag{4.8d}$$

Note that $\mathbf{Z}_1(\boldsymbol{\Omega},\boldsymbol{\Omega}_0)=\mathbf{P}(\boldsymbol{\Omega},\boldsymbol{\Omega}_0)$. The second term in Eq. (4.7) is small because it is a constant value in the emerging angle μ and $\boldsymbol{u}'$ is already corrected by the TMS method, except in the aureole region. Therefore Eq. (4.7) is approximated as follows:

$$\int \mathrm{d}\boldsymbol{\Omega}'\,\mathbf{P}(\boldsymbol{\Omega},\boldsymbol{\Omega}')\mathbf{P}(\boldsymbol{\Omega}',\boldsymbol{\Omega}_0) \sim \mathbf{Z}_2(\boldsymbol{\Omega},\boldsymbol{\Omega}_0). \tag{4.9}$$

Hence, the second order scattering radiance $\widehat{\boldsymbol{u}}_2(=\boldsymbol{u}-\boldsymbol{u}')$ is obtained from Eqs. (4.5) and (4.9) as follows:

$$\widehat{\boldsymbol{u}}_2(\tau,\boldsymbol{\Omega}) \approx (1-f\omega)\widehat{\omega}^2\left[\hat{\mathbf{Z}}_2(\boldsymbol{\Omega},\boldsymbol{\Omega}_0)-2\hat{\mathbf{Z}}_1(\boldsymbol{\Omega},\boldsymbol{\Omega}_0)\right]\boldsymbol{F}_{\mathrm{sol}}h(\tau,\mu,\mu_0^*,\mu_0^*). \tag{4.10}$$

The sky radiances in the aureole regions are significantly improved by correcting the second order scattering correction. However, the residual errors in the aureole regions remain in the case of a turbid aerosol-laden atmosphere discussed in the following section. Therefore, we consider further scattering $\widehat{\boldsymbol{u}}_3$ from the following residual radiative transfer equation similar formulation in Eq. (4.4) as:

$$-\mu\frac{\mathrm{d}\widehat{\boldsymbol{u}}}{\mathrm{d}t} = \widehat{\boldsymbol{u}} - \omega\int \mathrm{d}\boldsymbol{\Omega}'\,\mathbf{P}(\boldsymbol{\Omega},\boldsymbol{\Omega}')\widehat{\boldsymbol{u}}(t;\boldsymbol{\Omega}') + \boldsymbol{J}_5 + \boldsymbol{J}_6, \tag{4.11a}$$

$$\boldsymbol{J}_5(t;\boldsymbol{\Omega}) \equiv \omega\int \mathrm{d}\boldsymbol{\Omega}'\,\mathbf{P}(\boldsymbol{\Omega},\boldsymbol{\Omega}')\widehat{\boldsymbol{u}}_2(t;\boldsymbol{\Omega}'), \tag{4.11b}$$

$$\boldsymbol{J}_6(t;\boldsymbol{\Omega}) \equiv \omega\mathbf{P}(\boldsymbol{\Omega},\boldsymbol{\Omega}_0)\boldsymbol{F}_{\mathrm{sol}}\left[\exp\left(-\frac{t}{\mu_0^*}\right)-\exp\left(-\frac{t}{\mu_0}\right)-\widehat{\omega}g(t,\mu_0^*,\mu_0^*)\right]. \tag{4.11c}$$

Eq. (4.11b) is expressed by Eqs. (4.5) and (4.7-9) as follows:

$$\boldsymbol{J}_5(t;\boldsymbol{\Omega}) = \omega(1-f\omega)\widehat{\omega}^2\left[\mathbf{P}-f\hat{\mathbf{Z}}_3+2f\hat{\mathbf{Z}}_2-f\hat{\mathbf{Z}}_1\right]\boldsymbol{F}_{\mathrm{sol}}h(\tau,\mu,\mu_0^*,\mu_0^*). \tag{4.12}$$

Therefore, we can obtain the total source function of the third scattering radiance $\widehat{\boldsymbol{u}}_3$ as

follows:

$$\boldsymbol{J}_5 + \boldsymbol{J}_6 = -(1 - f\omega)^2 \widehat{\omega}^3 \left[\hat{\mathbf{Z}}_3(\boldsymbol{\Omega}, \boldsymbol{\Omega}_0) - 2\hat{\mathbf{Z}}_2(\boldsymbol{\Omega}, \boldsymbol{\Omega}_0) + \hat{\mathbf{Z}}_1(\boldsymbol{\Omega}, \boldsymbol{\Omega}_0)\right] \boldsymbol{F}_{\mathrm{sol}} h(\tau, \mu, \mu_0^*, \mu_0^*), \quad (4.13a)$$

because:

$$-(1 - f\omega)\widehat{\omega}^2 h(\tau, \mu, \mu_0^*, \mu_0^*) = \exp\left(-\frac{t}{\mu_0^*}\right) - \exp\left(-\frac{t}{\mu_0}\right) - \widehat{\omega} g(t, \mu_0^*, \mu_0^*). \quad (4.13b)$$

Hence, $\widehat{\boldsymbol{u}}_3$ is given as:

$$\widehat{\boldsymbol{u}}_3 = (1 - f\omega)^2 \widehat{\omega}^3 \left[\hat{\mathbf{Z}}_3(\boldsymbol{\Omega}, \boldsymbol{\Omega}_0) - 2\hat{\mathbf{Z}}_2(\boldsymbol{\Omega}, \boldsymbol{\Omega}_0) + \hat{\mathbf{Z}}_1(\boldsymbol{\Omega}, \boldsymbol{\Omega}_0)\right] \boldsymbol{F}_{\mathrm{sol}} h_2(\tau, \mu, \mu_0, \mu_0^*), \quad (4.14)$$

where h_2 is defined as:

$$h_2(\tau, \mu_2, \mu_1, \mu_0) \equiv \frac{1}{\mu_2} \int_0^\tau dt \exp\left[\frac{t - \tau}{\mu_2}\right] h(\tau, \mu_1, \mu_0, \mu_0). \quad (4.15)$$

Additionally, the procedure can be generalized for any *n*-th order scattering ($n \geq 2$) as follows:

$$\widehat{\boldsymbol{u}}_n = (1 - f\omega)^{n-1} \widehat{\omega}^n \left[\hat{\mathbf{Z}}_{n-2}(\boldsymbol{\Omega}, \boldsymbol{\Omega}_0) - 2\hat{\mathbf{Z}}_{n-1}(\boldsymbol{\Omega}, \boldsymbol{\Omega}_0) + \hat{\mathbf{Z}}_n(\boldsymbol{\Omega}, \boldsymbol{\Omega}_0)\right] \boldsymbol{F}_{\mathrm{sol}} h_{n-1}(\tau, \mu, \mu_0, \mu_0^*), \quad (4.16)$$

where:

$$\hat{\mathbf{Z}}_0(\boldsymbol{\Omega}, \boldsymbol{\Omega}_0) \equiv \mathbf{0}, \quad (4.17a)$$

$$h_j(\tau, \mu, \mu_0, \mu_0^*) \equiv \begin{cases} h(\tau, \mu, \mu_0^*, \mu_0^*), & j = 1 \\ \dfrac{1}{\mu} \displaystyle\int_0^\tau \mathrm{d}t \exp\left[\frac{t - \tau}{\mu}\right] h_{j-1}(\tau, \mu_0, \mu_0, \mu_0^*), & otherwise \end{cases}, \quad (4.17b)$$

because:

$$-\mu \frac{\mathrm{d}\widehat{\boldsymbol{u}}_j}{\mathrm{d}t} = \widehat{\boldsymbol{u}}_j + \omega \int \mathrm{d}\boldsymbol{\Omega}' \, \mathbf{P}(\boldsymbol{\Omega}, \boldsymbol{\Omega}') \widehat{\boldsymbol{u}}_{j-1}(t; \boldsymbol{\Omega}') \quad (j \geq 4), \quad (4.18a)$$

$$\int \mathrm{d}\boldsymbol{\Omega}'\, \mathbf{P}^*(\boldsymbol{\Omega}, \boldsymbol{\Omega}')\widehat{\boldsymbol{u}}_j(t; \boldsymbol{\Omega}') = \mathbf{0} \quad (j \geq 3), \tag{4.18b}$$

$$\int \mathrm{d}\boldsymbol{\Omega}'\, \widehat{\mathbf{P}}(\boldsymbol{\Omega}, \boldsymbol{\Omega}')\widehat{\mathbf{Z}}_{j-1}(\boldsymbol{\Omega}', \boldsymbol{\Omega}_0) \sim \widehat{\mathbf{Z}}_j(\boldsymbol{\Omega}, \boldsymbol{\Omega}_0) \quad (j \geq 2), \tag{4.18c}$$

and this formulation is satisfied with a scalar approximation.

In conclusion, the reconstructed sky radiance $\boldsymbol{u}$ is given as:

$$\boldsymbol{u}(t; \boldsymbol{\Omega}) \approx \widetilde{\boldsymbol{u}}(t; \boldsymbol{\Omega}; n) \equiv \boldsymbol{u}^*(t; \boldsymbol{\Omega}) + \sum_{j=1}^{n} \widehat{\boldsymbol{u}}_j\,. \tag{4.19}$$

In the present study, $\widetilde{\boldsymbol{u}}(t; \boldsymbol{\Omega}; 1)$, $\widetilde{\boldsymbol{u}}(t; \boldsymbol{\Omega}; 2)$ and $\widetilde{\boldsymbol{u}}(t; \boldsymbol{\Omega}; 3)$ are referred as P^1-IMS, P^2-IMS, and P^3-IMS, respectively. Note that, the P^1- and P^2-IMS methods are extended versions of the TMS and IMS methods.

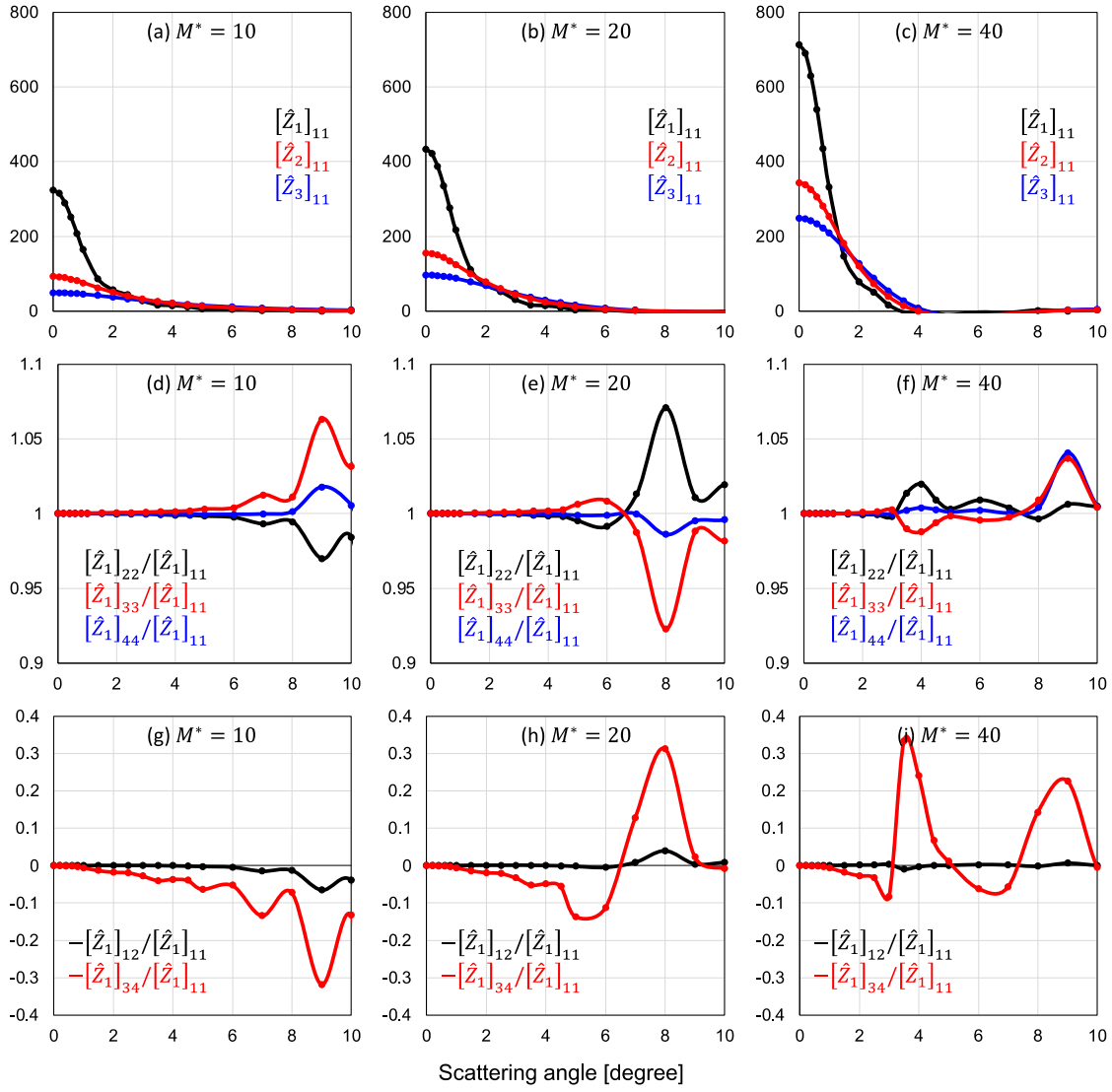

Figure 4.1: Forward peak matrix for dust1 aerosol (Table 4.1) at 340 nm in scattering angle of 10 degree.

4.2. Numerical tests

The previous section theoretically proposed the P^n-IMS methods (P^1-, P^2-, and P^3-IMS methods), including polarization effects by extending the TMS and IMS methods in the scalar approximation. Nakajima and Tanaka [1988] studied the numerical performance of the IMS method in the scalar approximation with various aerosols. The reference sky radiances were calculated by the discrete ordinate method with significantly large angular quadrature stream numbers in the hemisphere (N) and corrected using the ordinary single scattering correction method named MS. They set the maximum stream number as $\max\{N\} \sim 90$ for computational convenience as determined by $f < 0.01$ for each test phase function. They identified an adequate number applicable in a moderately thick atmosphere to maintain a low computational burden. In the present study, we investigated the performance of the P^n-IMS methods under several aerosol/cloud conditions with several N values in a similar way to Nakajima and Tanaka [1988]. However, we used the PSTAR version 4 (PSTAR4; Ota et al. [2010]) and decomposed $\mathbf{P}$ up to a maximum order of $M_{\max} = 200$ for the computation of $\widehat{\mathbf{Z}}_n$ in Eq. (4.8). Then, reference values of $\boldsymbol{u}$ at ground level for validation were computed with $N = 100$ ($M_{\max} = 200$) using the MS method (labeled as "DOM" in tables and figures). The significant N value is sufficient to compute the multiple scattering in the test aerosol conditions, even in the aureole region. Then the reference values were compared with the results of the P^1-IMS ($\tilde{\boldsymbol{u}}(t; \boldsymbol{\Omega}; 1)$), P^2-IMS ($\tilde{\boldsymbol{u}}(t; \boldsymbol{\Omega}; 2)$), and P^3-IMS ($\tilde{\boldsymbol{u}}(t; \boldsymbol{\Omega}; 3)$) methods. An Intel FORTRAN compiler compiled PSTAR4 with the Intel Math Kernel Library on a DELL Precision 3640 machine (OS: Ubuntu 20.04LTS; CPU: Intel Xeon W-1290P 3.7 GHz; RAM: ECC 32 GB). We used the scalar mode and full-vector mode of PSTAR, referred to as IPOL1 and IPOL4, respectively. Note that the PSTAR also has a semi-vector mode without V component, for which computational burden is lower than in the full-vector mode. The P^n-IMS methods can work in such reduced-rank matrix computation to be implemented to semi-vector RTMs.

The dataset consists of the four aerosol models of Dubovik et al. [2000] ("water-soluble", "dust1", "dust2", and "biomass-burning") and the water-cloud model of PSTAR4 under the US standard atmosphere at $\theta_0 = 30, 50, 70^{\circ}$, emerging angle $\theta = 0\ (1)\ 85^{\circ}$, and relative azimuth angle $\phi - \phi_0 = 0\ (1)\ 5, 7, 10\ (5)\ 180^{\circ}$ of the hemisphere at wavelengths of 340, 500, and 1020 nm. Particles of water-soluble and biomass-burning aerosols and water-cloud are assumed to be spherical, and the particles of the dust1 and dust2 aerosols are assumed to be both spherical and spheroidal. The spheroidal particles were assumed to have an axis ratio of 0.6, consistent with the values for Asian yellow sand dust particles reported by Nakajima et al. [1989]. The scattering kernel of spheroidal particles was developed by Dubovik et al. [2006]. Further details are provided in Table 4.1 where f is given by the

aerosol/cloud truncation fraction f_{p} defined as:

$$f = \frac{\omega_{\mathrm{p}}\tau_{\mathrm{p}}}{\tau_{\mathrm{R}} + \omega_{\mathrm{p}}\tau_{\mathrm{p}}} f_{\mathrm{p}}, \tag{4.20}$$

where τ_{p} and ω_{p} are the aerosol/cloud optical thickness and single scattering albedo, respectively; τ_{R} is Rayleigh scattering, which is 0.712 (340 nm), 0.143 (500 nm), and 0.008 (1020 nm) at ground level in the US standard atmosphere. In the computation, atmospheres were assumed to be inhomogeneous, consisting of six homogeneous layers divided at seven boundary altitudes (0, 2, 4, 6, 8, 10, and 120 km). According to Nakajima and Tanaka [1988], the narrow-angle scattering in the aureole region does not depend on the vertical inhomogeneity. This is because the zenith angles of ray paths are not different too much from each other, of which the particular case is the single scattering radiance in the almucantar plane ($\theta = \theta_0$). On the other hand, scattering out of the aureole region depends on the vertical stratification. A simple example is the single scattering radiance in the principal plane. Sky radiances depend on the atmospheric vertical structure described in Chapter 2. In the case of high order scattering corrections, Nakajima and Tanaka [1988] concluded that the vertical inhomogeneity does not affect the accuracy of their proposed methods (TMS and IMS methods) through extensive computer simulations. Therefore, in this study, the MS and P^1-IMS methods were calculated from the inhomogeneous layering, and the P^2- and P^3-IMS methods were applied to the optically averaged homogeneous atmosphere in the same way as in Nakajima and Tanaka [1988].

In the actual observation, $(u_{\mathrm{I}} \pm u_{\mathrm{Q}})/2$, $(u_{\mathrm{I}} \pm u_{\mathrm{U}})/2$, and $(u_{\mathrm{I}} \pm u_{\mathrm{V}})/2$ are measured instead of u_{Q}, u_{U}, and u_{V}; therefore, it is important to evaluate the relative error or signal to noise ratio, which is defined as:

$$\varepsilon_j = \frac{u_j - u_j^{\mathrm{DOM}}}{u_{\mathrm{I}}^{\mathrm{DOM}}}, \tag{4.21}$$

where u_j denotes a component of $\boldsymbol{u}$ ($j = \mathrm{I, Q, U, V}$). Note that ε_{I} is the relative error of the total radiance u_{I}. The present study evaluated $\boldsymbol{u}$ but not u_{V} because u_{V} is not affected by the correction of the MS and P^n-IMS methods and is often much smaller than the other parameters.

We investigated the performance of the P^n-IMS methods following three aspects: (1) correcting performance in the downward sky radiances (Section 4.2.1), (2) energy conservation (Section 4.2.2), and (3) accelerating performance (Section 4.2.3).

Table 4.1: Aerosol and cloud models used in the numerical test.

	Dust1	Dust2	Water-soluble	Biomass-burning	Water-cloud
Mode 1: Radius [μm]/width of mode	0.1/0.6	0.1/0.6	0.118/0.6	0.132/0.4	8.0/0.41
Mode 2: Radius [μm]/width of mode	3.4/0.8	1.17/0.6	1.17/0.6	4.5/0.6	-
Volume ratio of mode 1 to mode 2	0.066	0.066	2	4	-
Refractive index	1.53-0.008*i*	1.53-0.008*i*	1.45-0.0035*i*	1.52-0.01*i*	1.33-0*i*
Particle shape	Sphere or Spheroid	Sphere or Spheroid	Sphere	Sphere	Sphere
Scale height [km]	2	2	2	2	Set in PSTAR4
Properties (Sphere particles)					
Single scattering albedo: 340/500/1020 nm	0.811/0.803/0.845	0.844/0.866/0.922	0.970/0.965/0.956	0.948/0.937/0.858	1.00/1.00/1.00
Aerosol optical thickness: 340/500/1020 nm	1.25/1.00/0.866	1.09/1.00/1.01	1.79/1.00/0.348	1.91/1.00/0.178	0.989/1.00/1.03
Aerosols/clouds truncation fraction					
M = 10: 340/500/1020 nm	0.271/0.303/0.227	0.239/0.191/0.070	0.031/0.037/0.041	0.008/0.011/0.052	0.484/0.471/0.430
M = 20: 340/500/1020 nm	0.199/0.196/0.104	0.118/0.068/0.011	0.013/0.013/0.006	0.005/0.008/0.030	0.450/0.435/0.346
M = 40: 340/500/1020 nm	0.113/0.091/0.030	0.030/0.011/0.000	0.003/0.002/0.000	0.003/0.005/0.010	0.396/0.347/0.207
M = 200: 340/500/1020 nm	0.005/0.002/0.000	0.000/0.000/0.000	0.000/0.000/0.000	0.000/0.000/0.000	0.083/0.026/0.000

4.2.1. Performance of the P^n-IMS methods for the downward sky radiances

Figure 4.2 shows ε_{I} computed by IPOL4 for MS, P^1-IMS, and P^2-IMS methods with $N = 5$ and an aerosol/cloud optical thickness at 500 nm (AOT500) of 0.1 for the dust1 spherical model at $\theta_0 = 30^{\mathrm{O}}$. The u_{I} in the MS method shows a fluctuation of $\varepsilon_{\mathrm{I}} \sim 1.6\%$ caused by the truncation order of a spherical harmonics decomposition ($\cos m\Theta$) of the phase matrix at M^*, as shown in Fig. 4.3. As Nakajima and Tanaka [1988], the P^1-IMS method remove this fluctuation more effectively than the MS method, but overestimates in the aureole region (~2.4% in Fig. 4.2). The P^2-IMS method, additional correction for the second order of forward scattering, provides a good computation even in the aureole region ($\max\{\varepsilon_{\mathrm{I}}\} \sim 0.4\%$ in the hemisphere). The radiances for the Q and U components, u_{Q} (Fig. 4.4) and u_{U} (Fig. 4.5) have residual errors near the horizon because multiple scattering contributes to the backward scattering region and near the horizon. There is no significant fluctuation in the results obtained using both the MS and P^1-IMS methods, but the results obtained using the delta-M method contain fluctuations. In the case of $N = 5$, the maximum values of ε_{Q} and ε_{U} are within 0.2% and 0.24%, respectively. These values are similar to the sky-radiometer's measurement uncertainty ($\sim 0.5\%$), as discussed in Section 6.2.1. Using the P2-IMS method, the values of $\boldsymbol{u}$ can be obtained accurately even with a low N (~ 5) in a thin atmosphere because the high order scattering of $\widehat{\mathbf{P}}$ makes a minor contribution. However, it is challenging to obtain accurate results in a thick turbid atmosphere with a low N and within the second order scattering correction. Figure 4.6 shows ε_{I} computed by IPOL4 for MS, P^1-IMS, and P^2-IMS methods with $N = 5$ and AOT500 = 2.0 for the dust1 spherical model at $\theta_0 = 30^{\mathrm{O}}$. The amplitude of the fluctuation by the delta-M truncation is more significant than that obtained at AOT500 = 0.1 (Fig. 4.2). These fluctuations are caused by the truncation

order of the spherical harmonics decomposition ($\cos m\Theta$) of the phase matrix at M^*, as shown in Fig. 4.3. Those also present within the results obtained by the MS method. Almost all of the fluctuations are removed by the P[1]-IMS correction. In the aureole region, the P[2]-IMS method can remove most of the residual errors that occur when using the P[1]-IMS method, but a 4% fluctuating error remains in the aureole region due to the high order scattering of $\widehat{\mathbf{P}}$. There are fluctuating errors in the other parameters u_{Q} (Fig. 4.7) and u_{U} (Fig. 4.8) in a relatively thick atmosphere at AOT500 = 2.0 in the results obtained from both the MS and P[1]-IMS methods, which differs from the results obtained in thin atmospheres in Figs. 4.4 and 4.5. These fluctuations are suppressed by the high order scattering correction in both u_{Q} and u_{U} from ~0.13% (P[1]-IMS) to ~0.05% (P[2]-IMS) at $N = 5$. However, those values are small in magnitude, even in the MS method, because the values of u_{Q} and u_{U} become small with increasing AOT due to multiple scattering, which results in the radiation field becoming unpolarized. This suggests that it is sufficient to compute u_{Q} and u_{U} with single scattering corrections (*i.e.*, MS and P[1]-IMS methods) at low N values to analyze remote sensing observational data.

The P[2]-IMS method reconstructs the sky radiance distribution well in a thin atmosphere containing a highly anisotropic aerosol phase function (or large f). However, the residual errors in the aureole region remain significant in the relatively thick atmospheres at AOT500 = 2.0 because the high order multiple scattering of $\widehat{\mathbf{P}}$ is not negligible. Using the P[3]-IMS method, these errors in the aureole region can be fully removed. Figure 4.9 shows the relationship between the stream numbers N and residual errors in u_{I} obtained with the P[1]-, P[2]-, and P[3]-IMS methods for the dust1 spherical model at $\theta_0 = 50, \text{and } 70^{\mathrm{O}}$ and AOT500 = 1.0 in the almucantar plane ($\theta = \theta_0$). In the case of the P[1]- and P[2]-IMS methods, low stream numbers ($N = 5$ and 7) produce fluctuating errors in the forward scattering region ($|\phi - \phi_0| < 30^{\mathrm{o}}$), especially for high θ_0 values because of the strong multiple scattering by the long slant optical path, obtained by $1/\cos\theta_0$ in the plane-parallel atmosphere. Increasing N suppresses the fluctuations. The results obtained using the P[3]-IMS method are improved compared to those obtained using the lower order scattering corrections (P[1]- and P[2]-IMS methods). The P[3]-IMS method removes the residual errors even at $N = 7$.

Table 4.2 summarizes the performances of the MS and P[*n*]-IMS methods for various aerosol and water-cloud models with $N = 5$ and 10. IPOL4 with the P[3]-IMS method at $N = 5$ is accurate enough to compute the Stokes vector within 1% errors in AOT500 < 1.0 in most of the emerging angles for all the aerosol models in the present test. However, when using the P[2]-IMS method, the maximum error reaches 2.5% for the dust1 spheroid model at AOT500 = 1.0 with $N = 5$. Therefore, N must be 10 or more to suppress the error to within 1% for AOT500 = 1.0. In conclusion, for safety reasons, we recommend using the P[3]-IMS

method with $N = 10$ in aerosol atmospheres, where $M^* = 20$ because $M^* = 2 \times N$. This value is also valid for the calculations at other wavelengths (340 and 1020 nm) in AOT500 < 1.0 (Tables 4.3). The performance at 340 nm and with an AOT500 of 1.0 is worse than that at 500 nm, except for the P^3-IMS method. This is because the multiple scattering becomes dominant with decreasing wavelength and increasing optical thickness (Table 4.1, Figs. 4.10 and 4.11). Therefore, the residual errors in the u_I of the P^2-IMS method at 340 nm reach 5.2% in the dust1 spheroid model at AOT500 = 1.0. However, the residual errors in the u_I of the P^3-IMS method are less than 0.6% at 340 nm under the same conditions. Meanwhile, in the water-cloud atmosphere with AOT500 = 2.0, none of the correction methods in this section (MS and P^n-IMS methods) are accurate, although the maximum relative error of the P^3-IMS method in the hemisphere is the smallest among the correction methods. This increased error might be caused by a strong forward peak function of cloud particles and the lack of decomposition of $\mathbf{P}$ even at $M_{\max} = 200$.

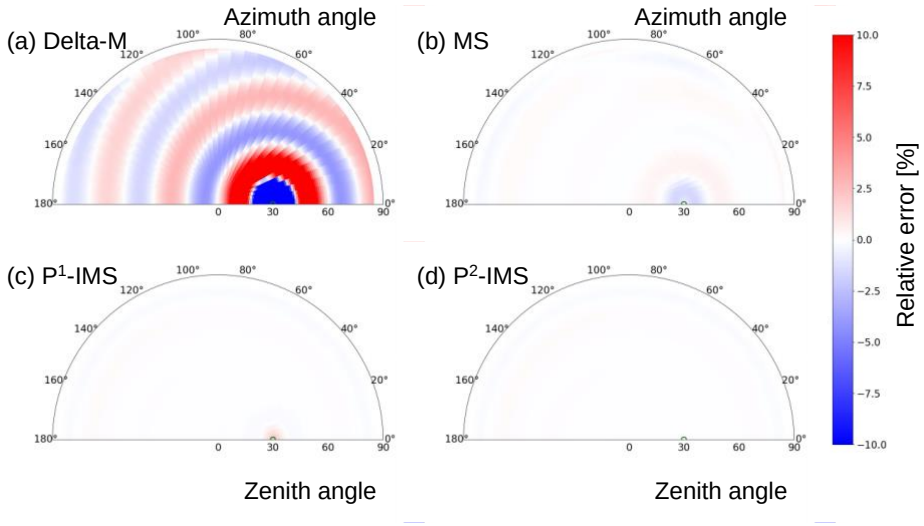

Figure 4.2: Angular distributions of the relative error (color map) in the downward total radiance u_I at 500 nm computed by IPOL4 for the results obtained by the MS, P^1-IMS, and P^2-IMS methods with $N = 5$ and AOT500 = 0.1 for the dust1 spherical model at $\theta_0 = 30^O$ (green circles). (a) delta-M method, (b) MS method, (c) P^1-IMS method, and (d) P^2-IMS method.

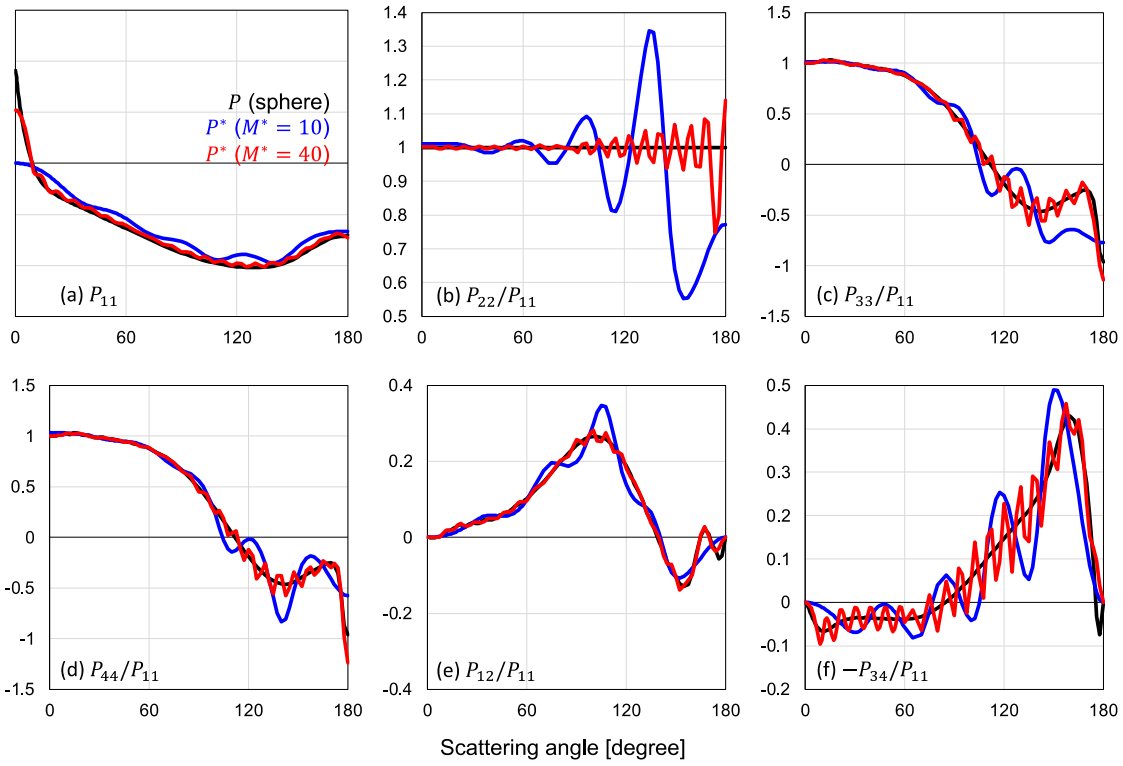

Figure 4.3: Phase matrix of dust1 spherical model at 500 nm. Blue, blue, and red lines show the phase matrix of true, truncated up to $M^* = 10$, and $M^* = 40$.

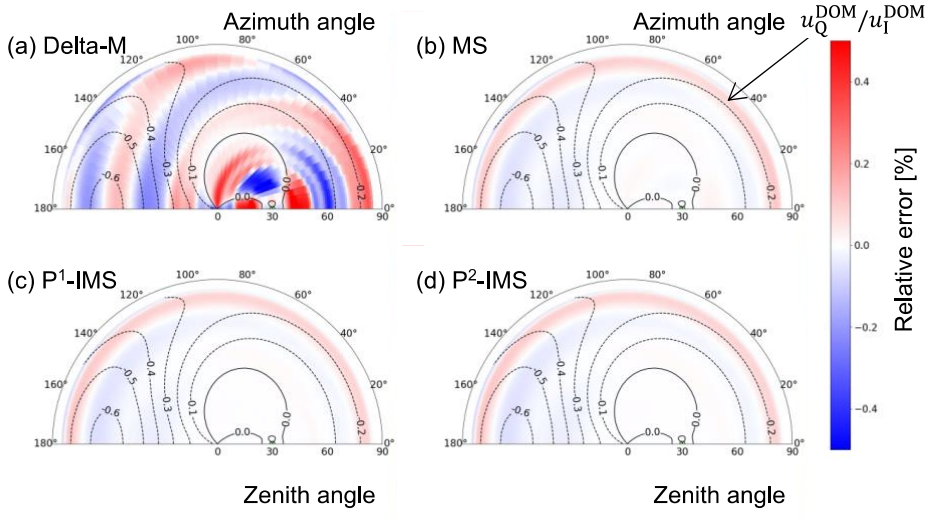

Figure 4.4: Angular distributions of the relative error (color map) in the downward Q component radiance u_Q at 500 nm computed by IPOL4 for the results obtained by the MS, P¹-IMS, and P²-IMS method with $N = 5$ and AOT500 = 0.1 for the dust1 spherical model at $\theta_0 = 30^O$ (green circles). Contour lines show the ratio of u_I to u_Q at an interval of 0.1. (a) delta-M method, (b) MS method, (c) P¹-IMS method, and (d) P²-IMS method.

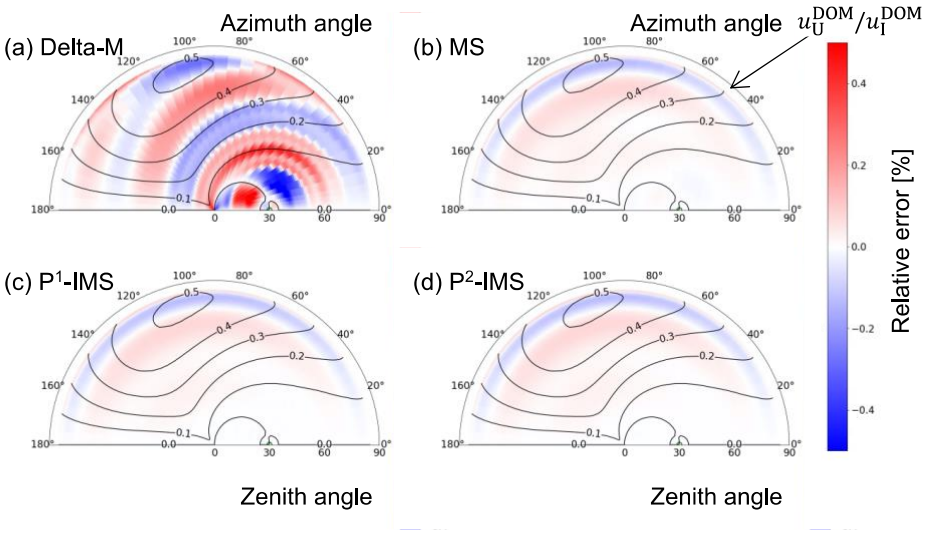

Figure 4.5: Same as Fig. 4.2, but for the U component radiance u_U.

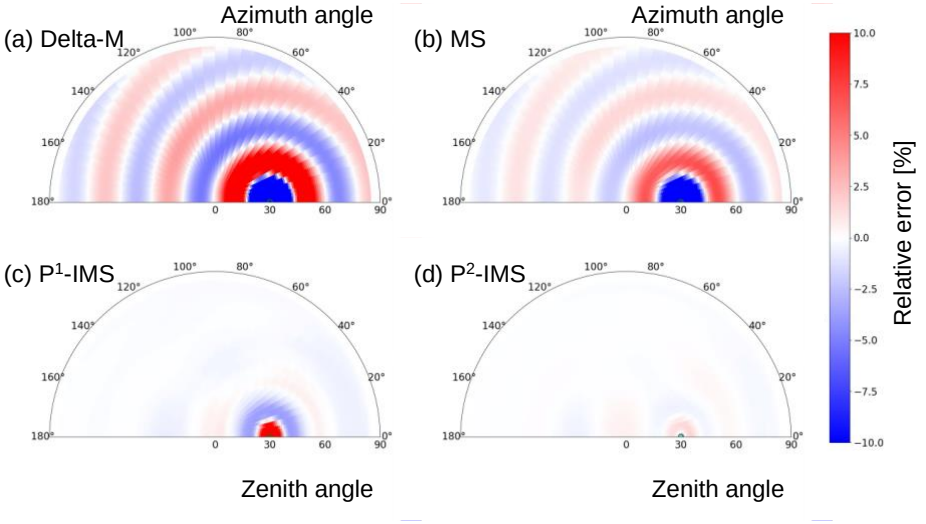

Figure 4.6: Same as Fig. 4.1, but for AOT500 = 2.0.

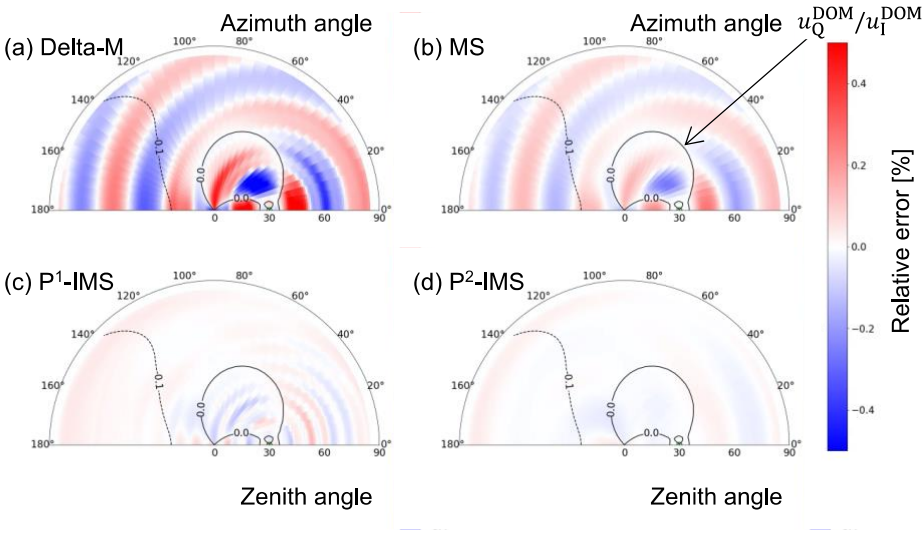

Figure 4.7: Same as Fig. 4.2, but for AOT500 = 2.0.

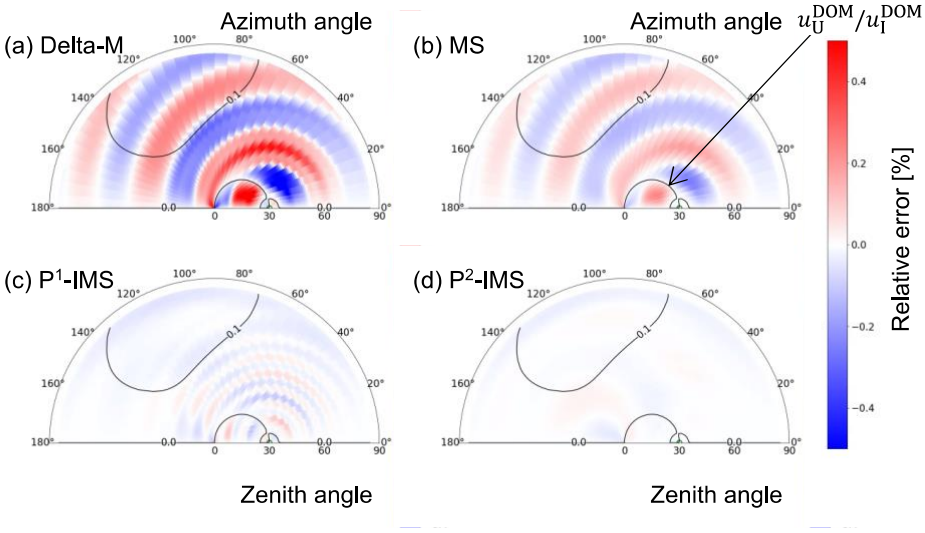

Figure 4.8: Same as Fig. 4.3, but for AOT500 = 2.0.

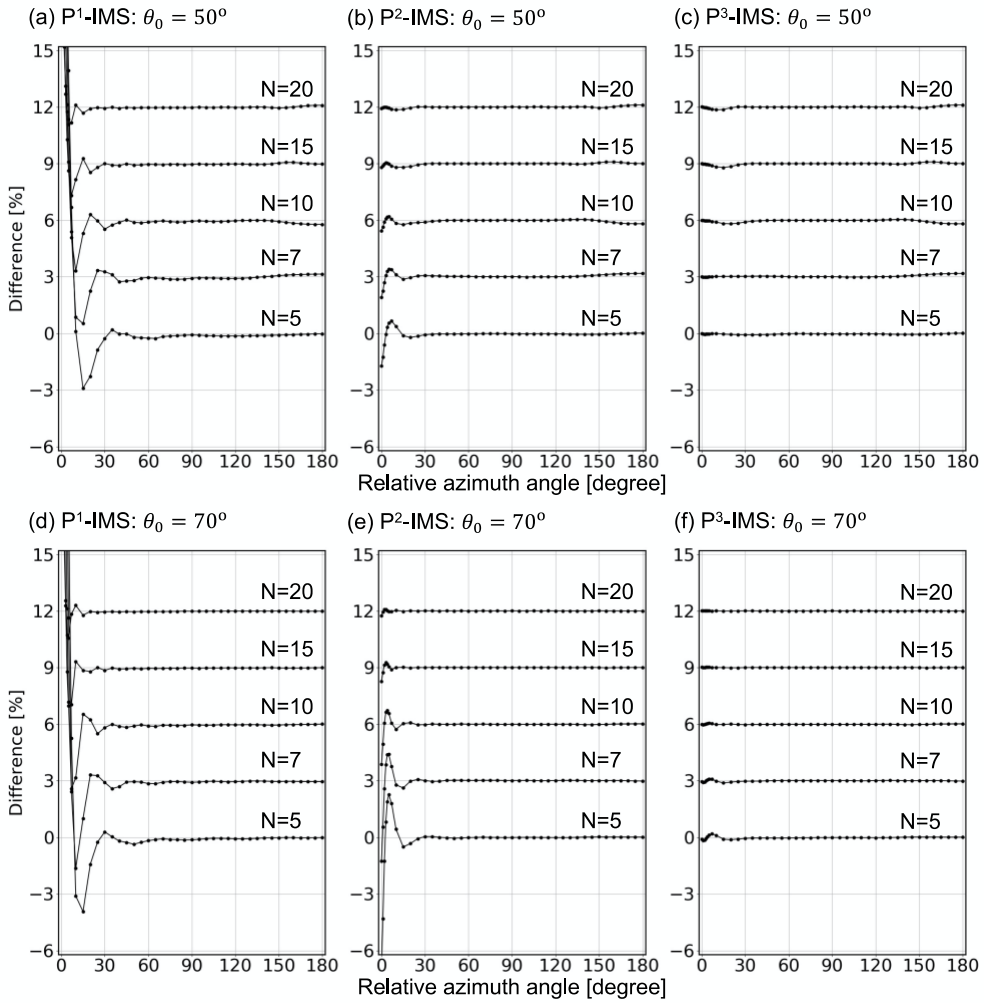

Figure 4.9: Angular distributions of the relative error in downward total radiances u_I at 500 nm computed by IPOL4 for the results obtained by the P[1]-, P[2]-, and P[3]-IMS methods with $N = 5, 7, 10, 15, 20$ and AOT500 = 1.0 for the dust1 spherical model at $\theta_0 = 50, \text{and } 70^O$ in the almucantar plane ($\theta = \theta_0$). The profiles for the various streams were successively shifted by 3% for display purposes.

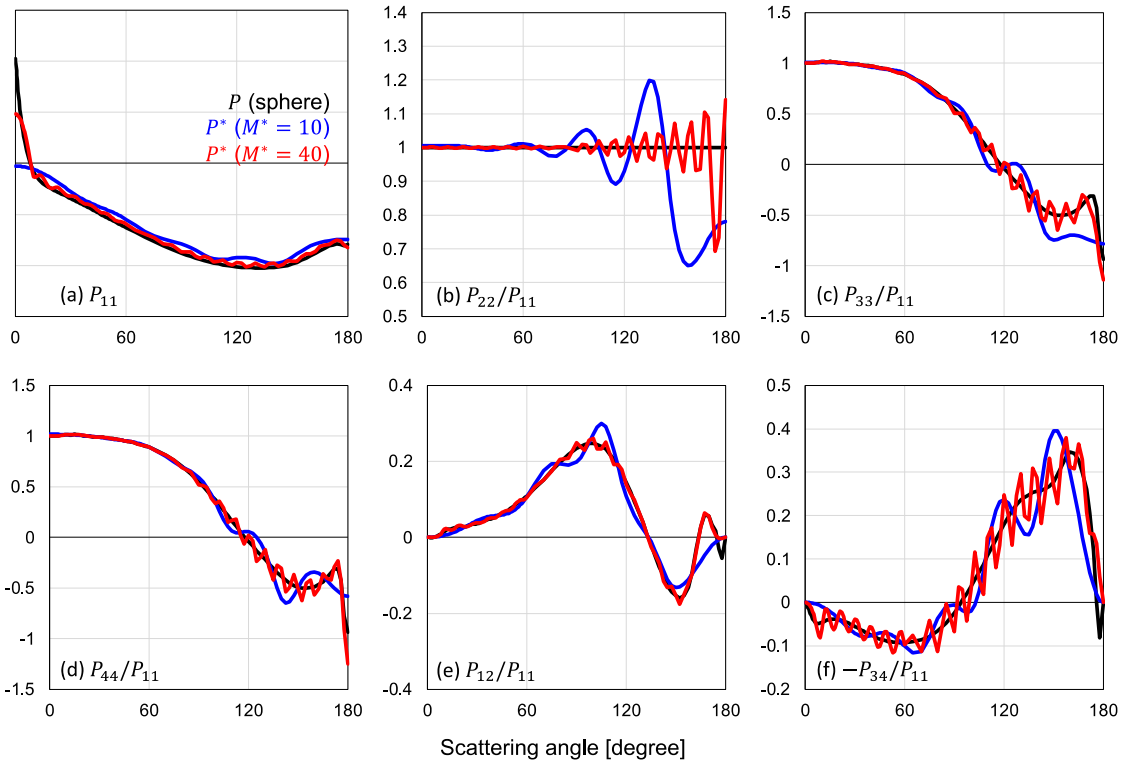

Figure 4.10: Same as Fig. 4.3, but for 340 nm.

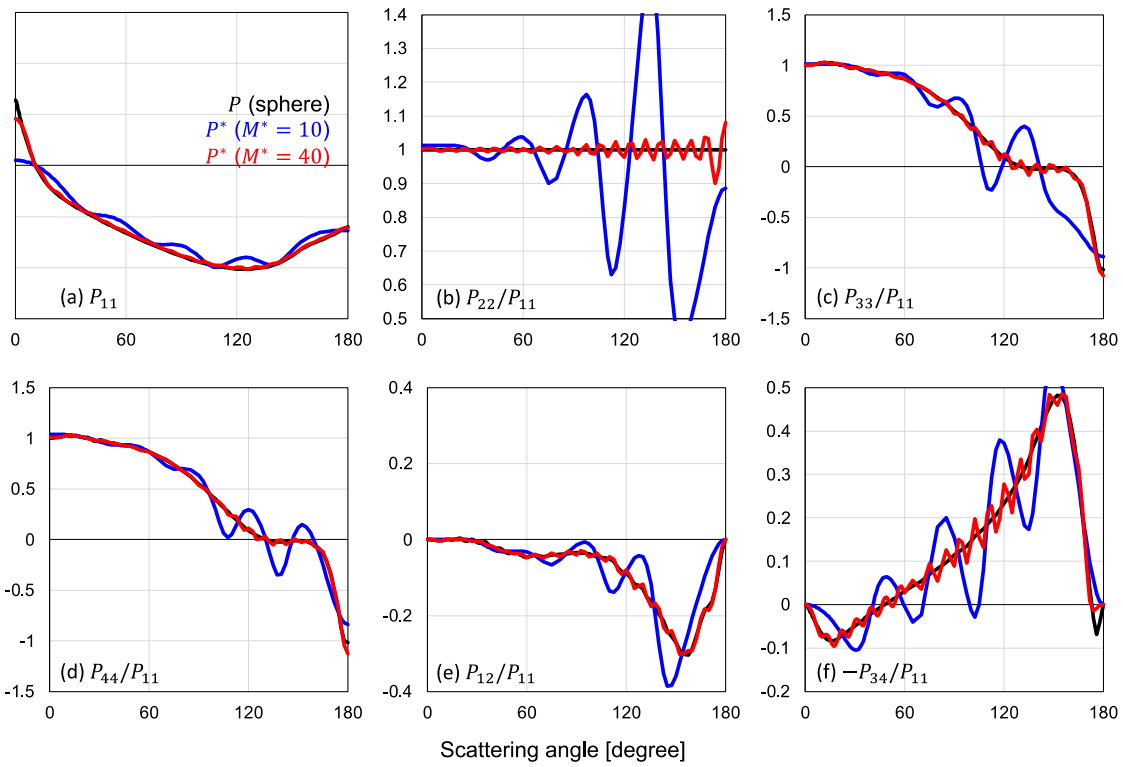

Figure 4.11: Same as Fig. 4.3, but for 1020 nm.

Table 4.2: Maximum values of $\varepsilon_j = \left(u_j - u_j^{\mathrm{DOM}}\right)/u_{\mathrm{I}}^{\mathrm{DOM}}$ $(j = \mathrm{I}, \mathrm{Q}, \mathrm{U})$ in downward radiances at 500 nm for $N = 5, 10$; the unit is 1/1000. (a) Performance for $N = 5$. (b) Performance for $N = 10$.

(a) N = 5		AOT500 = 0.1				AOT500 = 1.0				AOT500 = 2.0			
		MS	P^1-IMS	P^2-IMS	P^3-IMS	MS	P^1-IMS	P^2-IMS	P^3-IMS	MS	P^1-IMS	P^2-IMS	P^3-IMS
	θ_0	I / Q / U	I / Q / U	I / Q / U	I / Q / U	I / Q / U	I / Q / U	I / Q / U	I / Q / U	I / Q / U	I / Q / U	I / Q / U	I / Q / U
Dust1 (sphere)	30	16/ 2/ 2	24/ 2/ 2	4/ 2/ 2	4/ 2/ 2	148/ 2/ 2	271/ 1/ 1	9/ 0/ 0	4/ 0/ 0	253/ 3/ 3	609/ 1/ 1	41/ 0/ 0	5/ 0/ 0
	50	22/ 1/ 3	33/ 1/ 3	4/ 1/ 3	4/ 1/ 3	193/ 2/ 2	380/ 1/ 1	17/ 0/ 0	5/ 0/ 0	309/ 3/ 3	888/ 1/ 1	79/ 0/ 0	5/ 0/ 0
	70	45/ 4/ 3	63/ 4/ 2	7/ 4/ 2	7/ 4/ 2	314/ 3/ 3	819/ 1/ 1	69/ 0/ 0	12/ 0/ 0	401/ 3/ 3	2161/ 1/ 1	353/ 1/ 0	61/ 0/ 0
Dust1 (spheoid)	30	16/ 2/ 2	26/ 2/ 2	4/ 2/ 2	4/ 2/ 2	147/ 1/ 1	285/ 0/ 0	10/ 0/ 0	5/ 0/ 0	250/ 2/ 2	645/ 1/ 0	47/ 1/ 0	7/ 1/ 0
	50	22/ 1/ 3	35/ 1/ 3	4/ 1/ 3	4/ 1/ 3	191/ 1/ 2	401/ 0/ 0	20/ 0/ 0	5/ 0/ 0	305/ 2/ 2	945/ 0/ 1	92/ 0/ 1	5/ 0/ 0
	70	44/ 4/ 3	66/ 4/ 2	7/ 4/ 2	7/ 4/ 2	309/ 2/ 2	871/ 1/ 0	80/ 0/ 0	12/ 0/ 0	395/ 2/ 2	2348/ 1/ 1	417/ 0/ 0	62/ 0/ 0
Dust2 (sphere)	30	8/ 2/ 3	13/ 3/ 3	5/ 3/ 3	5/ 3/ 3	65/ 2/ 1	131/ 1/ 1	8/ 1/ 0	8/ 1/ 0	110/ 1/ 1	265/ 1/ 1	10/ 0/ 0	10/ 0/ 0
	50	10/ 1/ 4	17/ 1/ 4	5/ 1/ 4	5/ 1/ 4	85/ 3/ 2	177/ 1/ 1	5/ 0/ 0	5/ 0/ 0	133/ 1/ 1	356/ 1/ 1	16/ 0/ 0	7/ 0/ 0
	70	21/ 6/ 3	32/ 5/ 3	9/ 5/ 3	9/ 5/ 3	137/ 4/ 3	338/ 1/ 1	14/ 1/ 1	7/ 1/ 1	153/ 2/ 1	609/ 1/ 1	57/ 1/ 0	37/ 1/ 1
Dust2 (spheroid)	30	9/ 2/ 3	13/ 2/ 3	5/ 2/ 3	5/ 2/ 3	62/ 1/ 0	132/ 0/ 0	9/ 0/ 0	9/ 0/ 0	105/ 1/ 0	268/ 0/ 0	12/ 0/ 0	12/ 0/ 0
	50	9/ 1/ 4	17/ 1/ 4	5/ 1/ 4	5/ 1/ 4	82/ 1/ 1	179/ 0/ 0	6/ 0/ 0	6/ 0/ 0	127/ 0/ 0	360/ 1/ 1	17/ 0/ 0	9/ 0/ 0
	70	20/ 5/ 3	32/ 5/ 3	9/ 5/ 3	9/ 5/ 3	131/ 1/ 1	342/ 1/ 1	15/ 0/ 0	7/ 0/ 0	146/ 0/ 0	611/ 1/ 1	58/ 0/ 0	35/ 0/ 0
Water-soluble	30	2/ 0/ 1	2/ 0/ 1	2/ 0/ 1	2/ 0/ 1	7/ 0/ 0	19/ 0/ 0	1/ 0/ 0	1/ 0/ 0	11/ 0/ 0	32/ 0/ 0	1/ 0/ 0	1/ 0/ 0
	50	2/ 0/ 1	3/ 0/ 1	2/ 0/ 1	2/ 0/ 1	9/ 0/ 0	24/ 0/ 0	0/ 0/ 0	0/ 0/ 0	13/ 0/ 0	39/ 0/ 0	0/ 0/ 0	0/ 0/ 0
	70	3/ 2/ 1	5/ 2/ 1	3/ 2/ 1	3/ 2/ 1	14/ 0/ 0	41/ 0/ 0	1/ 0/ 0	1/ 0/ 0	12/ 0/ 0	40/ 0/ 0	2/ 0/ 0	2/ 0/ 0
Biomass burning	30	1/ 0/ 0	1/ 0/ 0	1/ 0/ 0	1/ 0/ 0	1/ 1/ 0	2/ 1/ 0	1/ 1/ 0	1/ 1/ 0	2/ 0/ 0	8/ 0/ 0	0/ 0/ 0	0/ 0/ 0
	50	2/ 1/ 0	2/ 1/ 0	2/ 1/ 0	2/ 1/ 0	1/ 0/ 1	2/ 0/ 1	1/ 0/ 1	1/ 0/ 1	3/ 0/ 0	10/ 0/ 0	0/ 0/ 0	0/ 0/ 0
	70	2/ 1/ 0	2/ 1/ 0	2/ 1/ 0	2/ 1/ 0	1/ 1/ 0	4/ 1/ 0	1/ 1/ 0	1/ 1/ 0	5/ 0/ 0	18/ 0/ 0	1/ 0/ 0	1/ 0/ 0
Water-cloud	30	54/ 1/ 2	46/ 1/ 1	4/ 1/ 1	4/ 1/ 1	396/ 6/ 6	553/ 3/ 3	39/ 1/ 2	25/ 1/ 2	589/ 8/ 8	1378/ 4/ 3	135/ 1/ 2	36/ 1/ 2
	50	69/ 1/ 2	62/ 1/ 2	4/ 0/ 2	4/ 0/ 2	474/ 7/ 7	804/ 3/ 3	52/ 2/ 3	26/ 1/ 3	660/ 8/ 8	2167/ 5/ 3	285/ 1/ 2	35/ 1/ 2
	70	130/ 5/ 7	119/ 2/ 2	5/ 2/ 1	5/ 2/ 1	648/ 35/ 23	1965/ 11/ 8	243/ 4/ 4	32/ 2/ 2	753/ 13/ 8	6823/ 8/ 7	1578/ 4/ 2	159/ 2/ 2

(b) N = 10		AOT500 = 0.1				AOT500 = 1.0				AOT500 = 2.0			
		MS	P^1-IMS	P^2-IMS	P^3-IMS	MS	P^1-IMS	P^2-IMS	P^3-IMS	MS	P^1-IMS	P^2-IMS	P^3-IMS
	θ_0	I / Q / U	I / Q / U	I / Q / U	I / Q / U	I / Q / U	I / Q / U	I / Q / U	I / Q / U	I / Q / U	I / Q / U	I / Q / U	I / Q / U
Dust1 (sphere)	30	8/ 1/ 1	15/ 1/ 1	2/ 1/ 1	2/ 1/ 1	78/ 0/ 0	154/ 0/ 0	9/ 0/ 0	9/ 0/ 0	139/ 0/ 0	326/ 1/ 1	15/ 0/ 0	14/ 0/ 0
	50	12/ 0/ 1	20/ 0/ 1	2/ 0/ 1	2/ 0/ 1	103/ 0/ 1	212/ 0/ 0	6/ 0/ 0	6/ 0/ 0	175/ 0/ 0	456/ 0/ 0	24/ 0/ 0	9/ 0/ 0
	70	23/ 1/ 1	37/ 1/ 1	3/ 1/ 1	3/ 1/ 1	173/ 0/ 0	425/ 0/ 0	21/ 0/ 0	4/ 0/ 0	242/ 0/ 0	952/ 1/ 1	94/ 0/ 0	20/ 0/ 0
Dust1 (spheoid)	30	8/ 1/ 1	15/ 1/ 1	1/ 1/ 1	1/ 1/ 1	78/ 0/ 0	164/ 0/ 0	9/ 0/ 0	9/ 0/ 0	138/ 0/ 0	349/ 0/ 0	15/ 0/ 0	14/ 0/ 0
	50	12/ 0/ 1	21/ 0/ 1	2/ 0/ 1	2/ 0/ 1	103/ 0/ 0	226/ 0/ 0	7/ 0/ 0	6/ 0/ 0	174/ 0/ 0	490/ 0/ 0	29/ 0/ 0	9/ 0/ 0
	70	23/ 1/ 1	39/ 1/ 1	3/ 1/ 1	3/ 1/ 1	172/ 0/ 0	457/ 0/ 0	25/ 0/ 0	4/ 0/ 0	239/ 0/ 0	1039/ 0/ 0	114/ 0/ 0	20/ 0/ 0
Dust2 (sphere)	30	2/ 0/ 0	3/ 0/ 0	1/ 0/ 0	1/ 0/ 0	14/ 0/ 0	29/ 0/ 0	7/ 0/ 0	7/ 0/ 0	26/ 0/ 0	55/ 0/ 0	9/ 0/ 0	9/ 0/ 0
	50	2/ 0/ 0	4/ 0/ 0	1/ 0/ 0	1/ 0/ 0	19/ 0/ 0	38/ 0/ 0	4/ 0/ 0	4/ 0/ 0	32/ 0/ 0	69/ 0/ 0	6/ 0/ 0	6/ 0/ 0
	70	4/ 1/ 0	7/ 0/ 0	2/ 0/ 0	2/ 0/ 0	31/ 0/ 0	67/ 0/ 0	3/ 0/ 0	3/ 0/ 0	40/ 0/ 0	100/ 0/ 0	4/ 0/ 0	4/ 0/ 0
Dust2 (spheroid)	30	2/ 0/ 0	3/ 0/ 0	1/ 0/ 0	1/ 0/ 0	14/ 0/ 0	31/ 0/ 0	6/ 0/ 0	6/ 0/ 0	26/ 0/ 0	58/ 0/ 0	8/ 0/ 0	8/ 0/ 0
	50	2/ 0/ 0	4/ 0/ 0	1/ 0/ 0	1/ 0/ 0	19/ 0/ 0	41/ 0/ 0	4/ 0/ 0	4/ 0/ 0	32/ 0/ 0	74/ 0/ 0	5/ 0/ 0	5/ 0/ 0
	70	4/ 0/ 0	8/ 0/ 0	2/ 0/ 0	2/ 0/ 0	31/ 0/ 0	71/ 0/ 0	2/ 0/ 0	2/ 0/ 0	39/ 0/ 0	105/ 0/ 0	5/ 0/ 0	4/ 0/ 0
Water-soluble	30	0/ 0/ 0	0/ 0/ 0	0/ 0/ 0	0/ 0/ 0	2/ 0/ 0	4/ 0/ 0	0/ 0/ 0	0/ 0/ 0	3/ 0/ 0	7/ 0/ 0	0/ 0/ 0	0/ 0/ 0
	50	0/ 0/ 0	1/ 0/ 0	0/ 0/ 0	0/ 0/ 0	3/ 0/ 0	5/ 0/ 0	0/ 0/ 0	0/ 0/ 0	4/ 0/ 0	9/ 0/ 0	0/ 0/ 0	0/ 0/ 0
	70	1/ 0/ 0	1/ 0/ 0	0/ 0/ 0	0/ 0/ 0	4/ 0/ 0	9/ 0/ 0	0/ 0/ 0	0/ 0/ 0	4/ 0/ 0	8/ 0/ 0	0/ 0/ 0	0/ 0/ 0
Biomass burning	30	0/ 0/ 0	1/ 0/ 0	0/ 0/ 0	0/ 0/ 0	2/ 0/ 0	6/ 0/ 0	0/ 0/ 0	0/ 0/ 0	3/ 0/ 0	11/ 0/ 0	0/ 0/ 0	0/ 0/ 0
	50	0/ 0/ 0	1/ 0/ 0	0/ 0/ 0	0/ 0/ 0	3/ 0/ 0	8/ 0/ 0	0/ 0/ 0	0/ 0/ 0	4/ 0/ 0	13/ 0/ 0	0/ 0/ 0	0/ 0/ 0
	70	1/ 0/ 0	1/ 0/ 0	0/ 0/ 0	0/ 0/ 0	4/ 0/ 0	13/ 0/ 0	0/ 0/ 0	0/ 0/ 0	4/ 0/ 0	17/ 0/ 0	0/ 0/ 0	0/ 0/ 0
Water-cloud	30	48/ 1/ 2	40/ 0/ 2	4/ 0/ 2	4/ 0/ 2	358/ 4/ 5	472/ 2/ 3	31/ 1/ 3	25/ 1/ 3	536/ 5/ 5	1136/ 3/ 3	95/ 1/ 3	30/ 1/ 3
	50	63/ 1/ 2	54/ 0/ 2	4/ 0/ 2	4/ 0/ 2	431/ 5/ 5	678/ 2/ 3	37/ 1/ 3	26/ 1/ 3	606/ 5/ 5	1742/ 4/ 3	196/ 1/ 3	26/ 1/ 3
	70	114/ 3/ 4	104/ 1/ 2	5/ 1/ 2	5/ 1/ 2	598/ 17/ 12	1589/ 4/ 3	168/ 2/ 2	23/ 1/ 2	700/ 6/ 4	4968/ 5/ 5	999/ 2/ 2	96/ 1/ 2

Table 4.3: Maximum values of $\varepsilon_j = \left(u_j - u_j^{\mathrm{DOM}}\right)/u_{\mathrm{I}}^{\mathrm{DOM}}$ $(j = \mathrm{I}, \mathrm{Q}, \mathrm{U})$ in downward radiances at 340 and 1020 nm for $N = 10$; the unit is 1/1000. (a) Performance at 340 nm. (b) Performance at 1020 nm.

(a) 340 nm		AOT500 = 0.1				AOT500 = 1.0				AOT500 = 2.0			
		MS	P^1-IMS	P^2-IMS	P^3-IMS	MS	P^1-IMS	P^2-IMS	P^3-IMS	MS	P^1-IMS	P^2-IMS	P^3-IMS
	θ_0	I / Q / U	I / Q / U	I / Q / U	I / Q / U	I / Q / U	I / Q / U	I / Q / U	I / Q / U	I / Q / U	I / Q / U	I / Q / U	I / Q / U
Dust1 (sphere)	30	10/ 0/ 0	19/ 0/ 0	0/ 0/ 0	0/ 0/ 0	110/ 0/ 0	214/ 0/ 0	5/ 0/ 0	3/ 0/ 0	190/ 0/ 0	466/ 0/ 0	24/ 0/ 0	5/ 0/ 0
	50	14/ 0/ 0	26/ 0/ 0	0/ 0/ 0	0/ 0/ 0	142/ 0/ 0	297/ 0/ 0	10/ 0/ 0	2/ 0/ 0	230/ 0/ 0	664/ 0/ 0	47/ 0/ 0	3/ 0/ 0
	70	27/ 0/ 0	50/ 0/ 0	2/ 0/ 0	2/ 0/ 0	213/ 0/ 0	612/ 0/ 0	40/ 0/ 0	5/ 0/ 0	235/ 0/ 0	1355/ 0/ 0	179/ 0/ 0	29/ 0/ 0
Dust1 (spheoid)	30	11/ 0/ 0	21/ 0/ 0	0/ 0/ 0	0/ 0/ 0	111/ 0/ 0	231/ 0/ 0	7/ 0/ 0	3/ 0/ 0	192/ 0/ 0	509/ 0/ 0	31/ 0/ 0	5/ 0/ 0
	50	15/ 0/ 0	28/ 0/ 0	0/ 0/ 0	0/ 0/ 0	143/ 0/ 0	322/ 0/ 0	13/ 0/ 0	2/ 0/ 0	232/ 0/ 0	731/ 0/ 0	60/ 0/ 0	3/ 0/ 0
	70	28/ 0/ 0	54/ 0/ 0	2/ 0/ 0	2/ 0/ 0	216/ 0/ 0	674/ 0/ 0	52/ 0/ 0	6/ 0/ 0	242/ 0/ 0	1582/ 0/ 0	241/ 0/ 0	30/ 0/ 0
Dust2 (sphere)	30	3/ 0/ 0	7/ 0/ 0	0/ 0/ 0	0/ 0/ 0	35/ 0/ 0	73/ 0/ 0	6/ 0/ 0	6/ 0/ 0	61/ 0/ 0	144/ 0/ 0	10/ 0/ 0	10/ 0/ 0
	50	4/ 0/ 0	9/ 0/ 0	0/ 0/ 0	0/ 0/ 0	46/ 0/ 0	97/ 0/ 0	3/ 0/ 0	3/ 0/ 0	75/ 0/ 0	186/ 0/ 0	5/ 0/ 0	5/ 0/ 0
	70	8/ 0/ 0	17/ 0/ 0	1/ 0/ 0	1/ 0/ 0	70/ 0/ 0	172/ 0/ 0	5/ 0/ 0	3/ 0/ 0	74/ 0/ 0	239/ 0/ 0	13/ 0/ 0	6/ 0/ 0
Dust2 (spheroid)	30	3/ 0/ 0	7/ 0/ 0	0/ 0/ 0	0/ 0/ 0	34/ 0/ 0	75/ 0/ 0	6/ 0/ 0	5/ 0/ 0	61/ 0/ 0	147/ 0/ 0	9/ 0/ 0	9/ 0/ 0
	50	4/ 0/ 0	9/ 0/ 0	0/ 0/ 0	0/ 0/ 0	45/ 0/ 0	100/ 0/ 0	3/ 0/ 0	3/ 0/ 0	74/ 0/ 0	192/ 0/ 0	6/ 0/ 0	5/ 0/ 0
	70	8/ 0/ 0	17/ 0/ 0	1/ 0/ 0	1/ 0/ 0	69/ 0/ 0	177/ 0/ 0	5/ 0/ 0	3/ 0/ 0	75/ 0/ 0	252/ 0/ 0	14/ 0/ 0	6/ 0/ 0
Water-soluble	30	0/ 0/ 0	1/ 0/ 0	0/ 0/ 0	0/ 0/ 0	3/ 0/ 0	8/ 0/ 0	0/ 0/ 0	0/ 0/ 0	3/ 0/ 0	8/ 0/ 0	0/ 0/ 0	0/ 0/ 0
	50	0/ 0/ 0	1/ 0/ 0	0/ 0/ 0	0/ 0/ 0	3/ 0/ 0	9/ 0/ 0	0/ 0/ 0	0/ 0/ 0	2/ 0/ 0	6/ 0/ 0	0/ 0/ 0	0/ 0/ 0
	70	1/ 0/ 0	2/ 0/ 0	0/ 0/ 0	0/ 0/ 0	2/ 0/ 0	6/ 0/ 0	0/ 0/ 0	0/ 0/ 0	0/ 0/ 0	0/ 0/ 0	0/ 0/ 0	0/ 0/ 0
Biomass burning	30	0/ 0/ 0	1/ 0/ 0	0/ 0/ 0	0/ 0/ 0	1/ 0/ 0	5/ 0/ 0	0/ 0/ 0	0/ 0/ 0	1/ 0/ 0	7/ 0/ 0	0/ 0/ 0	0/ 0/ 0
	50	0/ 0/ 0	1/ 0/ 0	0/ 0/ 0	0/ 0/ 0	1/ 0/ 0	6/ 0/ 0	0/ 0/ 0	0/ 0/ 0	1/ 0/ 0	5/ 0/ 0	0/ 0/ 0	0/ 0/ 0
	70	0/ 0/ 0	1/ 0/ 0	0/ 0/ 0	0/ 0/ 0	1/ 0/ 0	5/ 0/ 0	0/ 0/ 0	0/ 0/ 0	0/ 0/ 0	0/ 0/ 0	0/ 0/ 0	0/ 0/ 0
Water-cloud	30	48/ 0/ 0	44/ 0/ 0	16/ 0/ 0	16/ 0/ 0	395/ 4/ 4	534/ 3/ 3	169/ 1/ 1	141/ 1/ 1	591/ 5/ 5	1316/ 4/ 4	249/ 2/ 1	173/ 1/ 1
	50	63/ 0/ 0	60/ 0/ 0	17/ 0/ 0	17/ 0/ 0	459/ 4/ 4	773/ 3/ 3	200/ 1/ 1	149/ 1/ 1	662/ 5/ 5	2052/ 5/ 4	262/ 1/ 1	137/ 1/ 1
	70	107/ 1/ 1	116/ 1/ 1	23/ 0/ 0	21/ 0/ 0	628/ 4/ 4	1863/ 5/ 4	221/ 1/ 1	79/ 1/ 1	759/ 3/ 3	6203/ 6/ 5	1378/ 2/ 2	130/ 1/ 1

(b) 1020 nm		AOT500 = 0.1				AOT500 = 1.0				AOT500 = 2.0			
		MS	P^1-IMS	P^2-IMS	P^3-IMS	MS	P^1-IMS	P^2-IMS	P^3-IMS	MS	P^1-IMS	P^2-IMS	P^3-IMS
	θ_0	I / Q / U	I / Q / U	I / Q / U	I / Q / U	I / Q / U	I / Q / U	I / Q / U	I / Q / U	I / Q / U	I / Q / U	I / Q / U	I / Q / U
Dust1 (sphere)	30	6/ 1/ 1	6/ 1/ 1	4/ 1/ 1	4/ 1/ 1	25/ 0/ 0	56/ 0/ 0	7/ 0/ 0	7/ 0/ 0	45/ 0/ 0	112/ 0/ 0	11/ 0/ 0	11/ 0/ 0
	50	8/ 0/ 1	8/ 0/ 1	5/ 0/ 1	5/ 0/ 1	34/ 0/ 0	76/ 0/ 0	6/ 0/ 0	6/ 0/ 0	59/ 0/ 0	149/ 0/ 0	7/ 0/ 0	7/ 0/ 0
	70	11/ 2/ 1	14/ 1/ 1	6/ 1/ 1	6/ 1/ 1	56/ 1/ 0	141/ 0/ 0	3/ 0/ 0	3/ 0/ 0	83/ 0/ 0	262/ 0/ 0	11/ 0/ 0	5/ 0/ 0
Dust1 (spheoid)	30	6/ 1/ 1	6/ 1/ 1	3/ 1/ 1	3/ 1/ 1	25/ 0/ 0	59/ 0/ 0	7/ 0/ 0	7/ 0/ 0	45/ 0/ 0	117/ 0/ 0	10/ 0/ 0	10/ 0/ 0
	50	7/ 0/ 1	8/ 0/ 1	5/ 0/ 1	5/ 0/ 1	34/ 0/ 0	79/ 0/ 0	5/ 0/ 0	5/ 0/ 0	58/ 0/ 0	156/ 0/ 0	7/ 0/ 0	7/ 0/ 0
	70	11/ 1/ 1	15/ 1/ 1	5/ 1/ 1	5/ 1/ 1	57/ 0/ 0	148/ 0/ 0	4/ 0/ 0	4/ 0/ 0	81/ 0/ 0	273/ 0/ 0	12/ 0/ 0	6/ 0/ 0
Dust2 (sphere)	30	1/ 0/ 0	1/ 0/ 0	1/ 0/ 0	1/ 0/ 0	1/ 0/ 0	2/ 0/ 0	1/ 0/ 0	1/ 0/ 0	2/ 0/ 0	3/ 0/ 0	1/ 0/ 0	1/ 0/ 0
	50	1/ 0/ 0	1/ 0/ 0	1/ 0/ 0	1/ 0/ 0	1/ 0/ 0	2/ 0/ 0	0/ 0/ 0	0/ 0/ 0	2/ 0/ 0	3/ 0/ 0	1/ 0/ 0	1/ 0/ 0
	70	1/ 0/ 0	1/ 0/ 0	1/ 0/ 0	1/ 0/ 0	2/ 0/ 0	3/ 0/ 0	0/ 0/ 0	0/ 0/ 0	2/ 0/ 0	3/ 0/ 0	0/ 0/ 0	0/ 0/ 0
Dust2 (spheroid)	30	1/ 0/ 0	1/ 0/ 0	1/ 0/ 0	1/ 0/ 0	1/ 0/ 0	2/ 0/ 0	1/ 0/ 0	1/ 0/ 0	2/ 0/ 0	3/ 0/ 0	1/ 0/ 0	1/ 0/ 0
	50	1/ 0/ 0	1/ 0/ 0	1/ 0/ 0	1/ 0/ 0	1/ 0/ 0	2/ 0/ 0	0/ 0/ 0	0/ 0/ 0	2/ 0/ 0	4/ 0/ 0	1/ 0/ 0	1/ 0/ 0
	70	1/ 0/ 0	1/ 0/ 0	1/ 0/ 0	1/ 0/ 0	2/ 0/ 0	4/ 0/ 0	0/ 0/ 0	0/ 0/ 0	2/ 0/ 0	4/ 0/ 0	0/ 0/ 0	0/ 0/ 0
Water-soluble	30	1/ 0/ 0	1/ 0/ 0	1/ 0/ 0	1/ 0/ 0	0/ 0/ 0	0/ 0/ 0	0/ 0/ 0	0/ 0/ 0	0/ 0/ 0	1/ 0/ 0	0/ 0/ 0	0/ 0/ 0
	50	1/ 0/ 0	1/ 0/ 0	1/ 0/ 0	1/ 0/ 0	0/ 0/ 0	0/ 0/ 0	0/ 0/ 0	0/ 0/ 0	0/ 0/ 0	1/ 0/ 0	0/ 0/ 0	0/ 0/ 0
	70	1/ 0/ 0	1/ 0/ 0	1/ 0/ 0	1/ 0/ 0	0/ 0/ 0	1/ 0/ 0	0/ 0/ 0	0/ 0/ 0	1/ 0/ 0	1/ 0/ 0	0/ 0/ 0	0/ 0/ 0
Biomass burning	30	1/ 0/ 1	1/ 0/ 1	1/ 0/ 1	1/ 0/ 1	2/ 0/ 0	4/ 0/ 0	1/ 0/ 0	1/ 0/ 0	4/ 0/ 0	7/ 0/ 0	0/ 0/ 0	0/ 0/ 0
	50	1/ 0/ 1	1/ 0/ 1	1/ 0/ 1	1/ 0/ 1	3/ 0/ 1	5/ 0/ 1	1/ 0/ 1	1/ 0/ 1	5/ 0/ 0	9/ 0/ 0	0/ 0/ 0	0/ 0/ 0
	70	1/ 1/ 0	1/ 1/ 0	1/ 1/ 0	1/ 1/ 0	5/ 1/ 0	9/ 1/ 0	1/ 1/ 0	1/ 1/ 0	10/ 0/ 0	18/ 0/ 0	0/ 0/ 0	0/ 0/ 0
Water-cloud	30	30/ 4/ 4	31/ 2/ 2	8/ 2/ 2	8/ 2/ 2	228/ 4/ 3	349/ 1/ 1	12/ 1/ 0	9/ 1/ 0	353/ 2/ 2	790/ 2/ 2	52/ 1/ 0	10/ 1/ 0
	50	41/ 3/ 5	42/ 4/ 3	11/ 4/ 3	11/ 4/ 3	282/ 4/ 4	491/ 2/ 2	22/ 1/ 1	7/ 1/ 0	407/ 2/ 2	1153/ 2/ 2	101/ 1/ 0	8/ 1/ 0
	70	78/ 5/ 7	80/ 3/ 6	13/ 3/ 5	13/ 3/ 5	407/ 5/ 5	1065/ 3/ 3	88/ 1/ 1	13/ 1/ 1	463/ 2/ 2	2663/ 2/ 2	413/ 1/ 1	73/ 1/ 0

4.2.2. Evaluation of energy conservation computed from the sky radiances corrected by the P^n-IMS methods

Although correction methods (MS and P^n-IMS) can improve the calculation of Stokes vector $\boldsymbol{u}$, these methods do not always meet the energy conservation requirements due to the large modification of the forward peak function by the single scattering correction. Because the delta-M method truncates the phase function and assumes the conservation of angular moments of the phase function up to truncation order M^*, the radiative flux in the hemisphere can be accurately calculated (Wiscombe [1977]). Meanwhile, in the MS and P^1-IMS methods, the diffuse horizontal radiative flux $F_{\mathrm{df}}^{\downarrow}$, an essential variable for studying the energy budget, is not conserved by the corrections, as shown in Fig. 4.12. This is because these methods focus on better representation of the angular dependence of the radiance without posing the conservation constraint of horizontal radiative fluxes or angular integration variables. As shown in Fig. 4.12, the MS and P^1-IMS methods under- and over-estimate the diffuse horizontal radiative flux, respectively, due to the significant residual errors in the aureole regions in these methods. From Eq. (4.3), the diffuse horizontal radiative flux of the P^1-IMS methods in the homogeneous single layer is expressed as:

$$F_{\mathrm{df}}^{\downarrow} - F_{\mathrm{df}}^{*\downarrow} = \widehat{\omega} \int_0^1 \mu g(t, \mu^*, \mu_0^*) \mathrm{d}\mu \int_0^{2\pi} \boldsymbol{D}_1^{\mathrm{T}} \widehat{\mathbf{P}}(\boldsymbol{\Omega}, \boldsymbol{\Omega}_0) \boldsymbol{F}_{\mathrm{sol}} \mathrm{d}\phi \,. \tag{4.21}$$

where $F_{\mathrm{df}}^{*\downarrow}$ is the diffuse horizontal radiative flux with the delta-M truncation. Using Eqs. (2.2-3), Eq. (4.21) is written as:

$$F_{\mathrm{df}}^{\downarrow} - F_{\mathrm{df}}^{*\downarrow} = \widehat{\omega} F_{\mathrm{sol}} \int_0^1 \mu g(t, \mu^*, \mu_0^*) \mathrm{d}\mu \int_0^{2\pi} \hat{P}_{11}(\boldsymbol{\Omega}, \boldsymbol{\Omega}_0) \mathrm{d}\phi \,. \tag{4.22}$$

In Eq. (4.22), the right-hand side is positive because $\hat{P}_{11}$ is the strong forward peak with a finite broadening. Thus, the diffuse horizontal radiative flux of the P^1-IMS method is overestimated. This error reaches 4% at $\theta_0 = 70^{\mathrm{O}}$ with AOT500 = 1.0 and gets improved with increasing N. In the case of both the P^2-IMS and P^3-IMS methods, their diffuse horizontal radiative fluxes are in good agreement (within 0.16%) with those of DOM for $N = 5$. This suggests that the P^2-IMS and P^3-IMS methods are suitable correction methods and can reduce the error caused by the MS and P^1-IMS methods in the horizontal radiative flux. We tried higher order scattering by Eq. (4.16) and found the series convergence rapidly (Fig. 4.1), so that the P^3-IMS method seems to be enough for total radiance calculation.

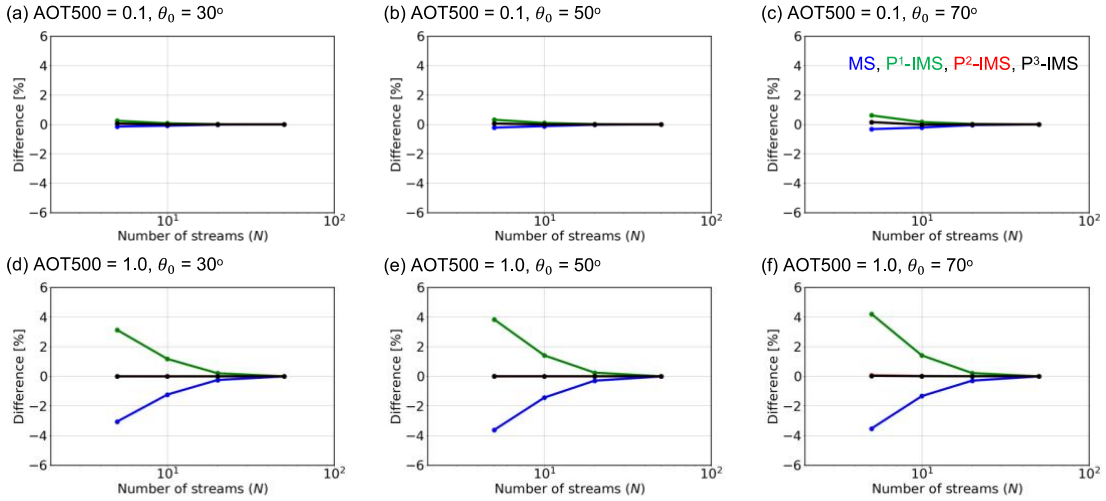

Figure 4.12: Relative errors in the downward diffuse horizontal radiative flux $F_{\mathrm{df}}^{\downarrow}$ computed from the total radiances u_{I} of the MS, P¹-IMS, P²-IMS, and P³-IMS methods at 500 nm for the dust1 spherical model. Blue, green, red, and black lines show the results obtained from the MS, P¹-IMS, P²-IMS, and P³-IMS methods, respectively. The contours for P²-IMS (red) and P³-IMS (black) are almost overlapped.

4.2.3. Performance of the computation speed by using the P^n-IMS methods

Finally, we investigate the computation efficiency of the correction methods. Basically, the P²-IMS and P³-IMS methods require more computational time than the single scattering corrections (MS and P¹-IMS) because of the decomposition of $\mathbf{P}$ up to $M_{\max}$ that is required to compute $\widehat{\mathbf{Z}}_n$ in Eq. (4.8). Figure 4.13 shows the relationship between the stream number N and mean CPU time T_{c} of PSTAR4 in the case of the dust1 spherical model at AOT500 = 0.2 and $\theta_0 = 70^{\mathrm{o}}$. Increasing N causes a rapid increase in the computational load as compensation for improving the accuracy, and T_{c} reaches 1.5×10^2 seconds (= 2.5 minutes) at $N = 50$ with IPOL4. It is not feasible to consume significant computational time in the large dataset generated by sky remote sensing observations. Therefore, it is recommended that a suitably low N should be selected to save computational time and meet the required accuracy for applications. In the case of scalar approximation, the IMS method produced a low maximum relative error of 0.3% at $N = 10$ with a low computational time of 0.5 seconds. The IMS method needs additional time for computing $\hat{u}_{\mathrm{I}}$ in each $\boldsymbol{\Omega}$ after correction by the TMS method. Figure 4.13 indicates that this additional time t_{Ω} for the $\hat{u}_{\mathrm{I}}$ in each $\boldsymbol{\Omega}$ is given as follows:

$$T_{\mathrm{c}}^{\mathrm{IMS}} = T_{\mathrm{c}}^{\mathrm{TMS}} + N_{\Omega} t_{\Omega}, \tag{4.23}$$

where N_{Ω} is the number of directions; and $T_{\mathrm{c}}^{\mathrm{TMS}}$ and $T_{\mathrm{c}}^{\mathrm{IMS}}$ are the CPU time of the TMS and IMS methods, respectively. Figure 4.13 indicates that t_{Ω} is 1.3×10^{-4} seconds. When keeping the accuracy within 0.3% and assuming the sky measurement data of $N_{\Omega} = 24$, IPOL1 with the IMS method needs 7.4×10^{-2} seconds at $N = 10$, but IPOL1 with the TMS method needs 4.6 seconds at $N = 50$. Therefore, IPOL1 with the IMS method is about 50-fold faster than the TMS method. This relationship is also found in the case of IPOL4 with the P^2- and P^1-IMS methods. Because the vector RTM consumes more time in the discrete ordinate and matrix operator method than the scalar RTM as discussed in Section 2.3 (8 to 32 times required), there is a large advantage in using the P^2- and P^3-IMS methods. To analyze the sky measurement data with IPOL4, both the P^2- and P^3-IMS methods needs 0.80 seconds at $N = 10$, but the P^1-IMS method needs 1.5×10^2 seconds at $N = 50$ because $t_{\Omega} = 1.5 \times 10^{-4}$ seconds (P^2-IMS) and 2.4×10^{-4} seconds (P^3-IMS). Therefore, using high order scattering correction methods (P^2-IMS and P^3-IMS) significantly improves the computational efficiency and is 187-fold faster than single scattering correction (P^1-IMS).

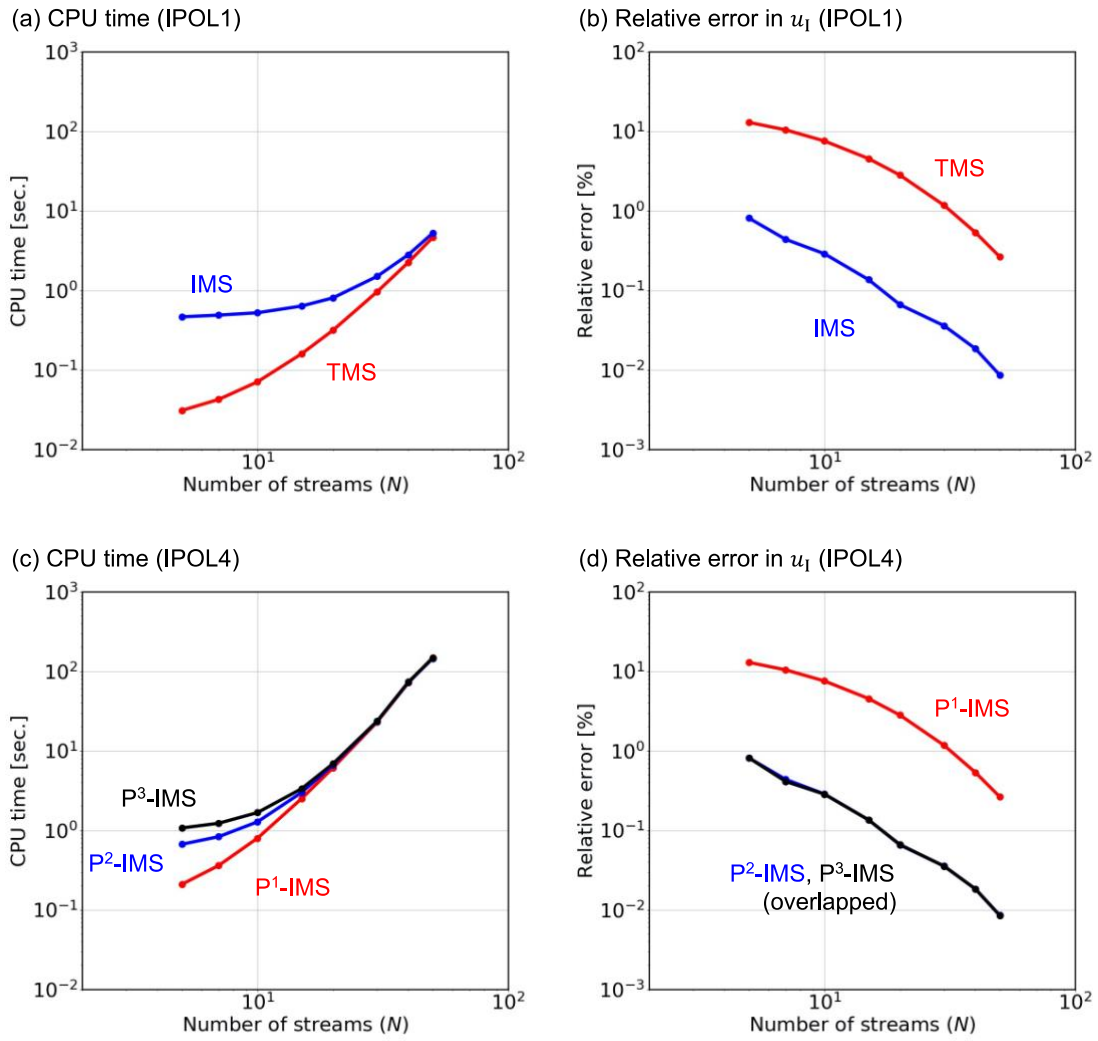

Figure 4.13: Relationships between the number of streams and mean CPU times with the TMS/IMS methods for IPOL1 and the P^n-IMS methods for IPOL4 at the dust1 spherical model with AOT500 = 0.2 at $\theta_0 = 70^o$. The top and bottom panels show the results of IPOL1 and IPOL4, respectively.

4.3. Conclusions

This section formulated a system of radiance correction methods named P^n-IMS methods for efficient calculations of radiative intensity, including polarization effects under aerosol-laden atmospheres. These methods maintain energy conservation and angular moments of the phase matrix and Stokes vector radiance field in the capacity of the delta-M truncation. The P^1- and P^2-IMS methods are extended versions of the TMS and IMS methods, which are first and second scattering corrections of the forward peak function in the scalar approximation of the radiation field. We then developed a novel correction method named P^3-IMS, which treats third order scattering in addition to the P^2-IMS method. A series of numerical tests were performed to confirm that the P^1-IMS method is accurate enough to reconstruct the Stokes parameters (Q and U components) within 0.2%, except for the total radiance. However, the total radiance in the solar aureole region needs a higher order scattering correction by the P^2- and P^3-IMS methods. Numerical tests indicated that the P^2- and P^3-IMS methods can attain accuracy within 5 and 1%, respectively, with a low hemispheric quadrature stream numbers ($N \sim 10$) in the spectral region of 340-1020 nm in AOT500 < 1. We recommend using $N = 5$ to 10 depending on the magnitude of the truncation fraction depending on the problem. We plan to compare P^n-IMS methods with others (*e.g.*, Hioki et al. [2016] and Waquet and Herman [2019]). Moreover, we apply our present methods to forward scattering phenomena other than aerosol cases that produce a strong polarization, such as polarization field simulation of 22° halo of ice crystals and forward scattering of reflected direct solar radiation from the ocean surface.

References

[1] Dubovik, O., Smirnov, A., Holben, B. N., King, M. D., Kaufman, Y. J., Eck, T. F., and Slutsker, I.: Accuracy assessments of aerosol optical properties retrieved from Aerosol Robotic Network (AERONET) Sun and sky radiance measurements, J. Geophys. Res., 105, 9791–9806, 2000

[2] Dubovik, O., Sinyuk, A., Lapyonok, T., Holben, B. N., Mishchenko, M., Yang, P., Eck, T. F., Volte, H., Muñoz, O., Veihelmann, B., van der Zande, W. J., Leon, J.-F., Sorokin, M., and Slutsker, I.: Application of spheroid models to account for aerosol particle nonsphericity in remote sensing of desert dust, J. Geophys. Res., 111, D11208, doi:10.1029/2005JD006619, 2006

[3] Hioki, S., P. Yang, G. W. Kattawar, and Y. Hu, 2016: Truncation of the scattering phase matrix for vector radiative transfer simulation, *J. Quant. Spectrosc. Radiat. Transfer*, **183**, 70–77

[4] Momoi, M., H. Irie, T. Nakajima, and M. Sekiguchi, Efficient calculation of radiative intensity including the polarization effect in moderately thick atmospheres using a truncation approximation, J. Quant. Spectrosc. Radiat. Transfer, 277, 107976, https://doi.org/10.1016/j.jqsrt.2021.107976, 2022.

[5] Nakajima, T., and M. Tanaka, 1988: Algorithms for radiative intensity calculations in moderately thick atmospheres using a truncation approximation. J. Quant. Spectrosc. Radiat. Transfer, 40, 51–69

[6] Nakajima, T., M. Tanaka, M. Yamano, M. Shiobara, K. Arao, and Y. Nakanishi, 1989: Aerosol Optical Characteristics in the Yellow Sand Events Observed in May, 1982 at Nagasaki-Part II Models, J. Meteorol. Soc. Japan, 67, 279-291, https://doi.org/10.2151/jmsj1965.67.2_279

[7] Ogawa, H., M. Tanaka, and T. Nakajima, 1989: A Simple Expression for the Additional Sky Radiance Produced by Polarization Effects, *J. Meteorol. Soc. Jpn.*, **67** (5), 877–888.

[8] Ota, Y., A. Higurashi, T. Nakajima, and T. Yokota, 2010: Matrix formulations of radiative transfer including the polarization effect in a coupled atmosphere–ocean system. *J. Quant. Spectrosc. Radiat. Transfer*, **111**, 878–894

[9] Waquet, F., and M. Herman, 2019: The truncation problem, *J. Quant. Spectrosc. Radiat. Transfer*, **229**, 80-91

[10] Wiscombe W., 1977: The delta-M method: rapid yet accurate radiative flux calculations for strongly asymmetric phase functions, *J Atmos Sci*, 34, 1408–22.

Chapter 5: Information on the angular distribution of the diffuse radiance in the water vapor absorption regions of 940 nm

The angular distribution of the diffuse radiances at 940 nm is rarely used, although data have accumulated since the launch of the sky-radiometer. Section 5.1 describes new look-up tables developed for the correlated *k*-distribution method around 940 nm for a survey of information on the angular distribution of diffuse radiance at the water vapor absorption regions. Section 5.2 describes the information of aerosols and water vapor amount on the angular distribution at 940 nm by numerical tests. The contents of this chapter are based on the papers of Momoi et al. [2020; 2022], as mentioned in each section.

5.1. Look-up tables of the *k* distribution in the gas absorption region of 940 nm for efficient computation of the narrow-band sky radiance of angular-scanning radiometer data

This section is mainly based on Momoi et al. [2022]. We developed a series of new look-up tables (LUTs) for the *k*-distribution at the water vapor absorption band named WV-CKD and installed it in the RSTAR7 to enable fast yet accurate computation of the sky radiances at the 940 nm band for estimating PWV. Using the WV-CKD, we performed a series of simulations to study information contents of PWV and aerosol properties in sky radiances at the water vapor absorption band. Section 5.1.1 shows the accuracy of the sky radiances computed with the standard CKD (hereafter SN-CKD) of the RSTAR7; Section 5.1.2 describes the methods and experimental setup of creating the WV-CKD and its specification; Section 5.1.3 provides their performance with error analysis.

5.1.1. Challenges regarding the standard *k*-distribution look-up table in RSTAR7

In RSTAR7, gas absorption is considered for H_2O, CO_2, O_3, N_2O, CO, CH_4, and O_2 using HITRAN 2004 database (Rothman et al. [2005]) and MT_CKD version 1 (Mlawer et al. [2012]) for continuum absorptions. Gas absorption is calculated by the CKD method (Lacis and Oinas [1991]; Fu and Liou [1992]) from the LUT of the *k* distribution (ckd.g.ch_2_2e3), which generates 2 Gaussian quadrature points without optimization of quadrature number in

each band. The resolution of the SN-CKD at wavenumber (k) is $\mathrm{d}\log_{10} k = 5 \times 10^{-4}$ ($\mathrm{d}k \approx 12.2\ \mathrm{cm}^{-1}$ at 940 nm). In the weak gas absorption regions (*e.g.*, 340, 380, 400, 500, 675, 870, and 1020 nm in the sky-radiometer measurements), the uncertainty of the gas absorption can be negligible because gas absorption is small relative to the extinction of other substances (Rayleigh scattering and/or aerosols). However, in the case of around 940 nm, careful consideration of the quadrature number is essential because of the complex water vapor line absorptions. Therefore, we validated the radiance calculation with the SN-CKD around 940 nm (10000–10900 cm^{-1} (1000–917 nm)) by the line-by-line approach (hereafter LBL method) with the simulated band-averaged sky intensities for sub-bands ($\bar{T} = \frac{\bar{F}_{\mathrm{ds}}}{\bar{F}_0}$ and $\bar{L} = \frac{\mu \bar{F}_{\mathrm{df}}(\boldsymbol{\Omega},\lambda)}{\bar{F}_0(\lambda)\Delta_\Omega}$). The LBL method is based on the line absorption from HITRAN 2012 (Rothman et al. [2013]) and the continuum absorption from MT_CKD version 3.2 (Mlawer et al. [2012]). Note that HITRAN2020 (Gordon et al. [2022]) was recently published, but no significant difference can be seen around 940 nm from HITRAN2012. The band-averaged sky intensities for sub-bands were computed by RSTAR7 with the IMS method (Nakajima and Tanaka [1988]). The validation dataset (CA-DB) consists of the radiances at ground level for continental averaged aerosol conditions (Hess et al. [1999]); with AOTs of 0.05, 0.20, and 1.00 at 940 nm; solar zenith angles of 30, 50, and 70 degrees in two sky-radiometer observation planes – almucantar ($\theta = \theta_0$) and principal ($\phi = \phi_0$) –; and PWV from 0.5 to 6 cm at an interval of 0.5 cm. The vertical atmospheric profile is the US standard atmosphere employed in the RSTAR7. Extra-terrestrial solar irradiance was averaged at the sub-band ($\mathrm{d}\log_{10} k$) level. Therefore, $\bar{T}^{\mathrm{LBL}}$ and $\bar{L}^{\mathrm{LBL}}$ derived with the LBL method are obtained as follows:

$$\bar{T}^{\mathrm{LBL}}(\bar{\lambda}) = \frac{1}{\int_{\Delta_\kappa} \frac{\mathrm{d}\kappa}{\kappa^2}} \int_{\Delta_\kappa} T_{\mathrm{p}}(\lambda) T_{\mathrm{R}}(\lambda) T_{\mathrm{H2O}}(\lambda) T_{\mathrm{cont}}(\lambda) \frac{\mathrm{d}\kappa}{\kappa^2}, \tag{5.1a}$$

$$\bar{L}^{\mathrm{LBL}}(\boldsymbol{\Omega}, \bar{\lambda}) = \frac{1}{\int_{\Delta_\kappa} \frac{\mathrm{d}\kappa}{\kappa^2}} \int_{\Delta_\kappa} T_{\mathrm{p}}(\lambda) T_{\mathrm{R}}(\lambda) T_{\mathrm{H2O}}(\lambda) T_{\mathrm{cont}}(\lambda) R(\boldsymbol{\Omega}, \lambda) \frac{\mathrm{d}\kappa}{\kappa^2}, \tag{5.1b}$$

where T_{p} and T_{R} are the monochromatic transmittances of aerosol extinction and Rayleigh scattering, respectively; T_{H2O} is the monochromatic transmittance of water vapor absorption (line and self-continuum); and T_{cont} is the monochromatic transmittance of the O_2 and O_3 continuum absorption. Because the differential interval of the numerical integration is too

small ($\mathrm{d}\kappa = 0.01\ \mathrm{cm}^{-1}$) for the LBL method, T_{H2O} is obtained using Eq. (2.6) as follows:

$$\ln[T_{\mathrm{H2O}}(\lambda)] = -m_0 \int_0^z \left[\sigma_{\mathrm{H2O,line}}(K, p, \lambda) + \sigma_{\mathrm{H2O,cont}}(K, \lambda)\right] dz\,, \tag{5.2}$$

where $\sigma_{\mathrm{H2O,line}}$ and $\sigma_{\mathrm{H2O,cont}}$ are the absorption coefficients [/m] of the water vapor line and self-continuum absorption, respectively; K is the temperature; p is the pressure; and z is the thickness of the atmosphere. Figure 5.1 shows the maximum errors ($\varepsilon_{\bar{I}\max}$) of $\bar{T}$ and $\bar{L}$ with the SN-CKD compared with the LBL method, as described:

$$\varepsilon^2_{\bar{T},\mathrm{RT}}(\bar{\lambda}; \theta_0, w, \tau_{\mathrm{p}}) = \left(\ln \frac{\bar{T}^{\mathrm{LBL}}}{\bar{T}^{\mathrm{CKD}}}\right)^2\,, \tag{5.3a}$$

$$\varepsilon^2_{\bar{L},\mathrm{RT}}(\bar{\lambda}; \boldsymbol{\Omega}, \theta_0, w, \tau_{\mathrm{p}}) = \left(\ln \frac{\bar{L}^{\mathrm{LBL}}}{\bar{L}^{\mathrm{CKD}}}\right)^2\,, \tag{5.3b}$$

$$\begin{aligned}\varepsilon^2_{\bar{I}\max}(\bar{\lambda}) = \max\{&\varepsilon^2_{\bar{T},\mathrm{RT}}(\bar{\lambda}), \varepsilon^2_{\bar{L},\mathrm{RT}}(\bar{\lambda}) | \theta_0 = 30\ (20)\ 70^{\mathrm{o}}; w = 0.5\ \ (0.5\ )\ 6\ \mathrm{cm}; \tau_{\mathrm{p}} \\ &= 0.05, 0.2, 1.0\}.\end{aligned} \tag{5.4}$$

The root mean square errors of $\varepsilon_{\bar{I}\max}$ for CA-DB were 8.24×10^{-1} at 10000–10902 cm^{-1}, and 1.16 at 10411–10864 cm^{-1} (961–920 nm). This error propagates to convolved sky intensities. As a result, the error of convolved sky intensities for sky-radiometer observation reaches 2.21×10^{-1} larger than $\sigma_{F_{\mathrm{ds}}}$ as discussed in Section 6.2. One reason for this significant error is updates of the absorption database. From HITRAN 2004 to HITRAN 2012, the number of water vapor absorption lines in this band increased more than fourfold. Another reason is the lack of quadrature numbers producing significant error under the US atmosphere.

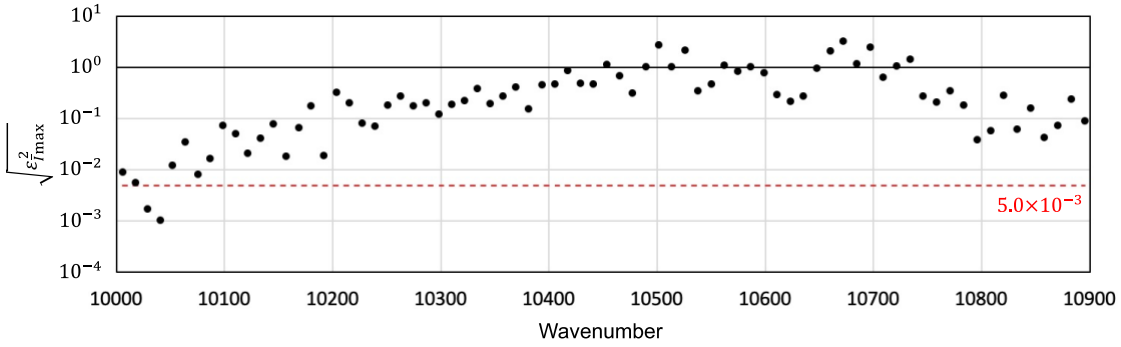

Figure 5.1: The maximum residual error of using the SN-CKD compared with the LBL method using CA-DB.

5.1.2. Method to create the new *k*-distribution look-up table and its specification

This study constructed a new LUT of the *k* distribution at 10 cm^{-1} intervals Δ_κ from 10000 cm^{-1} to 10900 cm^{-1} (hereafter WV-CKD-10) by optimizing the quadrature number with the LBL method. Radiation around 940 nm is attenuated mainly through aerosol extinction, Rayleigh scattering, and gas absorption, including O_2 continuum, O_3 continuum, and water vapor absorption (self-continuum and line). Therefore, WV-CKD-10 consists of 3 LUTs (Table 5.1): quadrature weights, water vapor *k* distribution, and O_2 and O_3 continuums. Those LUTs were created from HITRAN 2012 and MT_CKD version 3.2. The quadrature number was optimized for $\bar{E}(\mu,\lambda)$ in each sub-band under six AFGL standard atmospheres (US standard, Tropical, Mid-latitude summer, Mid-latitude winter, High-latitude summer, and High-latitude winter) in RSTAR7 by a linear search from 2 to 64. The WV-CKD optimally consists of the minimum quadrature number corresponding to the number of executions of RTM. In this study, the maximum error $\sqrt{\varepsilon_E^2}$ of $E(\mu,\lambda)$ for $\Delta_\kappa = 10\ \mathrm{cm}^{-1}$ is satisfied at values less than 5.0×10^{-3}. Then, the quadrature pairs (point and weight) were also optimized with the Gauss–Newton method. Thus, these tables are intended to compute the gas absorption in Earth atmosphere. After creating of the WV-CKD-10, we validated it with CA-DB, as described in the previous sub-section for the validation dataset of the SN-CKD.

Figure 5.2a shows the sub-band quadrature number, and Fig. 5.2b shows the maximum error $\sqrt{\varepsilon_{I\max}^2}$, which was satisfied at values less than 5.0×10^{-3} for 10000–10900 cm^{-1}. The quadrature number consists in the range of 3–15 at 10000–10900 cm^{-1} and 4–15 at 10410–10870 cm^{-1} (961–920 nm) (Fig. 5.3). The median of the quadrature numbers is seven at 10000–10900 cm^{-1} and eight at 10410–10870 cm^{-1} (961–920 nm)

because the complex water vapor line absorptions around 940 nm require many quadrature points to maintain accuracy. Thus, using the WV-CKD-10 is ≥ 100-fold more rapid than the LBL method, because the band-averaged radiance at 10 cm^{-1} must be computed 1000 times with the LBL method (= 10 $cm^{-1}/0.01\ cm^{-1}$) in RSTAR7 (Table 5.2).

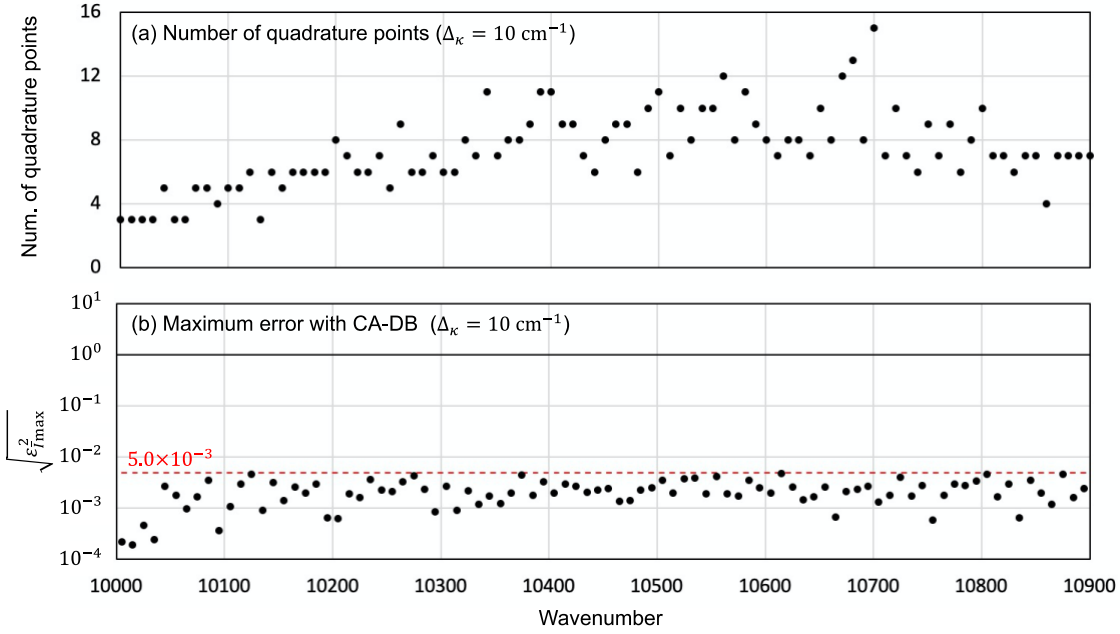

Figure 5.2: The architecture of WV-CKD-10. The top panel shows the quadrature numbers in the sub-band. The bottom panel shows the maximum residual error compared with the LBL method using CA-DB.

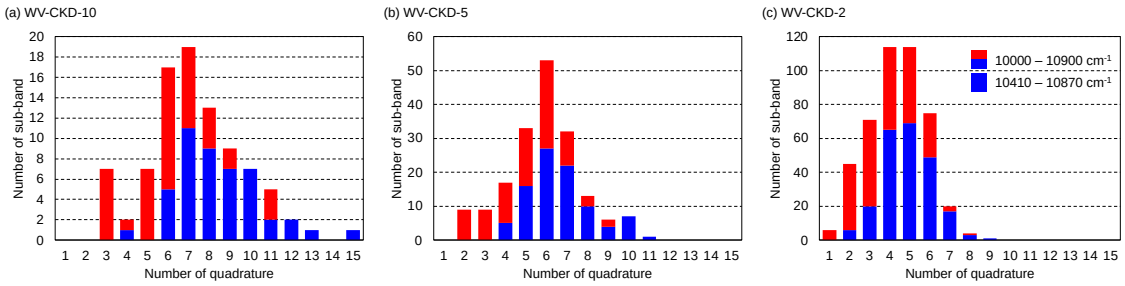

Figure 5.3: The histogram of the quadrature numbers of WV-CKDs

Table 5.1: Look-up tables of the WV-CKD-10.

File name	Data type	Data	Data size
con10k-11k.10.dat	Real*8	O_2 continuum O_3 continuum	432KB [KW=100, KCON=2, KP=27, KT=10]
h2o10k-11k.10.dat	Real*8	H_2O line absorption H_2O self continuum	6912KB [KW=100, KCH=32, KP=27, KT=10]
wgt10k-11k.10.dat	Real*8	Quadrature weights	25.6KB [KW=100, KCH=32]

Table 5.2: WV-CKD specifications

	WV-CKD-2	WV-CKD-5	WV-CKD-10	LBL
Resolution	2 cm^{-1}	5 cm^{-1}	10 cm^{-1}	0.01 cm^{-1}
Maximum error of $E(\mu,\lambda)$: $(\varepsilon_E^2)^{1/2}$	11.2×10^{-3}	7.1×10^{-3}	5.0×10^{-3}	–
Median quadrature numbers (10000 – 10900 cm^{-1})	4	6	7	–
Median quadrature numbers (10410 – 10870 cm^{-1})	5	6	8	–
Mean computation times (10000 – 10900 cm^{-1})	2.18 /cm^{-1}	1.18 /cm^{-1}	0.734 /cm^{-1}	100 /cm^{-1}
Mean computation times (10410 – 10870 cm^{-1})	2.44 /cm^{-1}	1.33 /cm^{-1}	0.848 /cm^{-1}	100 /cm^{-1}
$D\Phi$ of Eq. 5.9 (FWHM = 5 nm)	0.176	0.280	0.394	–
$D\Phi$ of Eq. 5.9 (FWHM = 10 nm)	0.124	0.198	0.278	–
$D\Phi$ of Eq. 5.9 (FWHM = 15 nm)	0.102	0.162	0.228	–

5.1.3. Error sources of the WV-CKD

CKD method assumes two things as discussed in Chapter 2: (1) line shape in wavenumber space is consistent through all temperature and pressure levels, and (2) extra solar irradiance is nearly constant through sub-band. The former assumption appears in $\varepsilon_{I\max}^2$ and propagates the uncertainty of the convolved values, which are observational elements of the radiometer. This section investigated those assumptions.

5.1.3.1.Error estimation

From Eq. (2.62), the band-averaged T and L with the WV-CKD-10 are expressed as

$$\bar{T}^{\mathrm{CKD}}(\bar{\lambda}) = \bar{T}_{\mathrm{p}}(\bar{\lambda})\bar{T}_{\mathrm{R}}(\bar{\lambda})\bar{T}_{\mathrm{cont}}(\bar{\lambda})\sum_{j=1}^{N_{\mathrm{ch}}}\xi_j T_{\mathrm{H2O,ckd}}^{(j)}(\bar{\lambda}), \tag{5.5a}$$

$$\bar{L}^{\mathrm{CKD}}(\boldsymbol{\Omega},\bar{\lambda}) = \bar{T}_{\mathrm{p}}(\bar{\lambda})\bar{T}_{\mathrm{R}}(\bar{\lambda})\bar{T}_{\mathrm{cont}}(\bar{\lambda})\sum_{j=1}^{N_{\mathrm{ch}}}\xi_j T_{\mathrm{H2O,ckd}}^{(j)}(\bar{\lambda})R^{(j)}(\boldsymbol{\Omega},\lambda)\,, \tag{5.5b}$$

where $\bar{T}_{\mathrm{p}}$ and $\bar{T}_{\mathrm{R}}$ are the band-averaged values of T_{p} and T_{R}, respectively; $T_{\mathrm{H2O,ckd}}^{(j)}$ is the transmittance at *j*-th quadrature point of the water vapor *k* distribution. The residual errors ($\varepsilon_{\hat{T},\mathrm{RT}}$ and $\varepsilon_{\hat{L},\mathrm{RT}}$) of $\hat{T}$ and $\hat{L}$ with the WV-CKD-10 are smaller than that of $\bar{T}$ ($\varepsilon_{\bar{T},\mathrm{RT}}^2$) and $\bar{L}$ ($\varepsilon_{\bar{L},\mathrm{RT}}^2$) by convolution of the filter response function and expressed as follows:

$$\begin{aligned}
\varepsilon_{\hat{T},\mathrm{RT}}^2 &= \left(\ln\frac{\sum^{N_{\mathrm{band}}}\bar{\psi}\cdot\bar{F}_{\mathrm{sol}}\cdot\bar{T}^{\mathrm{CKD}}\cdot\Delta_\kappa\bar{\lambda}^2}{\sum^{N_{\mathrm{band}}}\bar{\psi}\cdot\bar{F}_{\mathrm{sol}}\cdot\bar{T}^{\mathrm{LBL}}\cdot\Delta_\kappa\bar{\lambda}^2}\right)^2 \\
&\sim \left(\frac{\sum^{N_{\mathrm{band}}}\bar{\psi}\cdot\bar{F}_{\mathrm{sol}}\cdot\bar{T}^{\mathrm{CKD}}(\boldsymbol{\Omega})\cdot\Delta_\kappa\bar{\lambda}^2 - \sum^{N_{\mathrm{band}}}\bar{\psi}\cdot\bar{F}_{\mathrm{sol}}\cdot\bar{T}^{\mathrm{LBL}}(\boldsymbol{\Omega})\cdot\Delta_\kappa\bar{\lambda}^2}{\sum^{N_{\mathrm{band}}}\bar{\psi}\cdot\bar{F}_{\mathrm{sol}}\cdot\bar{T}^{\mathrm{LBL}}(\boldsymbol{\Omega})\cdot\Delta_\kappa\bar{\lambda}^2}\right)^2 \\
&= \frac{\sum^{N_{\mathrm{band}}}\left[\bar{\psi}\cdot\bar{F}_{\mathrm{sol}}\cdot\bar{T}^{\mathrm{LBL}}\cdot\varepsilon_{\bar{T},\mathrm{RT}}\cdot\Delta_\kappa\bar{\lambda}^2\right]^2}{\left[\sum^{N_{\mathrm{band}}}\bar{\psi}\cdot\bar{F}_{\mathrm{sol}}\cdot\bar{T}^{\mathrm{LBL}}\cdot\Delta_\kappa\bar{\lambda}^2\right]^2}
\end{aligned}, \tag{5.6a}$$

$$\begin{aligned}
\varepsilon_{\hat{L},\mathrm{RT}}^2(\boldsymbol{\Omega}) &= \left(\ln\frac{\sum^{N_{\mathrm{band}}}\bar{\psi}\cdot\bar{F}_{\mathrm{sol}}\cdot\bar{L}^{\mathrm{CKD}}(\boldsymbol{\Omega})\cdot\Delta_\kappa\bar{\lambda}^2}{\sum^{N_{\mathrm{band}}}\bar{\psi}\cdot\bar{F}_{\mathrm{sol}}\cdot\bar{L}^{\mathrm{LBL}}(\boldsymbol{\Omega})\cdot\Delta_\kappa\bar{\lambda}^2}\right)^2 \\
&\sim \left(\frac{\sum^{N_{\mathrm{band}}}\bar{\psi}\cdot\bar{F}_{\mathrm{sol}}\cdot\bar{L}^{\mathrm{CKD}}(\boldsymbol{\Omega})\cdot\Delta_\kappa\bar{\lambda}^2 - \sum^{N_{\mathrm{band}}}\bar{\psi}\cdot\bar{F}_{\mathrm{sol}}\cdot\bar{L}^{\mathrm{LBL}}(\boldsymbol{\Omega})\cdot\Delta_\kappa\bar{\lambda}^2}{\sum^{N_{\mathrm{band}}}\bar{\psi}\cdot\bar{F}_{\mathrm{sol}}\cdot\bar{L}^{\mathrm{LBL}}(\boldsymbol{\Omega})\cdot\Delta_\kappa\bar{\lambda}^2}\right)^2 \\
&= \frac{\sum^{N_{\mathrm{band}}}\left[\bar{\psi}\cdot\bar{F}_{\mathrm{sol}}\cdot\bar{L}^{\mathrm{LBL}}(\boldsymbol{\Omega})\cdot\varepsilon_{\bar{L},\mathrm{RT}}\cdot\Delta_\kappa\bar{\lambda}^2\right]^2}{\left[\sum^{N_{\mathrm{band}}}\bar{\psi}\cdot\bar{F}_{\mathrm{sol}}\cdot\bar{L}^{\mathrm{LBL}}(\boldsymbol{\Omega})\cdot\Delta_\kappa\bar{\lambda}^2\right]^2},
\end{aligned} \tag{5.6b}$$

$$\varepsilon_{\hat{I}\max}^2 = \max\left\{\varepsilon_{\hat{T},\mathrm{RT}}^2, \varepsilon_{\hat{L},\mathrm{RT}}^2(\boldsymbol{\Omega})\right\}. \tag{5.7}$$

If we roughly assume $\bar{T}_{\mathrm{H2O}}$ randomly distributes in the range of $\bar{T}_{\mathrm{H2O,min}} = 0$ to $\bar{T}_{\mathrm{H2O,max}} = 1$, $\varepsilon_{\hat{T},\mathrm{RT}}^2$ and $\varepsilon_{\hat{L},\mathrm{RT}}^2$ are obtained as follows:

$$\varepsilon^2_{\hat{T},\mathrm{RT}} \sim \varepsilon^2_{\hat{L},\mathrm{RT}} \sim D^2\Phi^2 < \varepsilon^2_{\bar{I}\max} >, \tag{5.8}$$

where $<>$ indicates an averaging operation;

$$D^2 \equiv \frac{<(\overline{T}^{\mathrm{LBL}})^2>}{(<\overline{T}^{\mathrm{LBL}}>)^2} \sim \frac{\int_{\overline{T}_{\mathrm{H2O,min}}}^{\overline{T}_{\mathrm{H2O,max}}} x^2 \mathrm{d}x}{\overline{T}_{\mathrm{H2O,max}} - \overline{T}_{\mathrm{H2O,min}}} \Big/ \left(\frac{\int_{\overline{T}_{\mathrm{H2O,min}}}^{\overline{T}_{\mathrm{H2O,max}}} x \mathrm{d}x}{\overline{T}_{\mathrm{H2O,max}} - \overline{T}_{\mathrm{H2O,min}}} \right)^2 = \frac{4}{3} \approx 1.33, \tag{5.9a}$$

$$\Phi^2 \equiv \frac{\sum^{N_{\mathrm{band}}} \left[\bar{\psi} \cdot \bar{F}_{\mathrm{sol}} \cdot \Delta_\kappa \bar{\lambda}^2 \right]^2}{\left[\sum^{N_{\mathrm{band}}} \bar{\psi} \cdot \bar{F}_{\mathrm{sol}} \cdot \Delta_\kappa \bar{\lambda}^2 \right]^2} \sim (0.242)^2. \tag{5.9b}$$

In Eq. (5.8), $\varepsilon_{\bar{T},\mathrm{RT}} \sim \varepsilon_{\bar{L},\mathrm{RT}} \sim < \varepsilon^2_{\bar{I}\max} >$. The second expression on the right-hand side of Eq. (5.9b) is an estimate for the situation in which full width at half maximum (FWHM) is 10 nm at the central wavelength of 940 nm with the Extra-terrestrial solar spectrum reported by Coddington et al. [2021]. Moreover, the residual ($\varepsilon_{\hat{R},\mathrm{RT}}$) of the convolved normalized radiance ($\hat{R}$) is obtained as follows:

$$\hat{R}^{\mathrm{CKD}}(\mathbf{\Omega}) \equiv \frac{\hat{L}^{\mathrm{CKD}}(\mathbf{\Omega})}{\hat{T}^{\mathrm{CKD}}} = \hat{R}^{\mathrm{LBL}}(\mathbf{\Omega}) e^{\varepsilon_{\hat{R},\mathrm{RT}}(\Theta)} = \hat{R}^{\mathrm{LBL}}(\mathbf{\Omega}) e^{\varepsilon_{\hat{L},\mathrm{RT}}(\Theta) - \varepsilon_{\hat{T},\mathrm{RT}}}, \tag{5.10a}$$

$$\varepsilon^2_{\hat{R}\max} = \max\left\{ \varepsilon^2_{\hat{R},\mathrm{RT}}(\mathbf{\Omega}) \right\}. \tag{5.10b}$$

Using Eqs. (5.4) and (5.8), $\varepsilon^2_{\bar{I}\max}$ is roughly estimated as $\varepsilon^2_{\bar{I}\max} \sim D^2\Phi^2 < \varepsilon^2_{\bar{I}\max} > \sim (D\Phi\varepsilon_E)^2$ and the expected residual errors of radiances simulated with the WV-CKD-10 are estimated as follows:

$$\varepsilon^2_{\hat{T},\mathrm{RT}} \sim \varepsilon^2_{\hat{L},\mathrm{RT}} \leq \varepsilon^2_{\bar{I}\max} \sim (D\Phi\varepsilon_E)^2 \sim (0.278)^2 \times (5.0 \times 10^{-3})^2 \ll \sigma^2_{F_{\mathrm{ds}}} \leq \sigma^2_{F_{\mathrm{df}}}. \tag{5.11}$$

5.1.3.2. Fluctuation of extra-terrestrial solar irradiance in the sub-band

Theoretically, the band-averaged sky intensities determined through the LBL method are obtained with Eq. (2.61) as follows:

$$\acute{T}(\lambda) = \frac{\int_{\Delta_\kappa} F_{\mathrm{sol}}(\lambda) T(\lambda) \frac{\mathrm{d}\kappa}{\kappa^2}}{\int_{\Delta_\kappa} F_{\mathrm{sol}}(\lambda) \frac{\mathrm{d}\kappa}{\kappa^2}} = \frac{\int_{\Delta_\kappa} F_{\mathrm{sol}}(\lambda) T(\lambda) \frac{\mathrm{d}\kappa}{\kappa^2}}{\Delta_\kappa \bar{\lambda}^2 \bar{F}_{\mathrm{sol}}^2}, \tag{5.12a}$$

$$\acute{L}(\boldsymbol{\Omega}, \lambda) = \frac{\int_{\Delta_\kappa} F_{\mathrm{sol}}(\lambda) L(\boldsymbol{\Omega}, \lambda) \frac{\mathrm{d}\kappa}{\kappa^2}}{\int_{\Delta_\kappa} F_{\mathrm{sol}}(\lambda) \frac{\mathrm{d}\kappa}{\kappa^2}} = \frac{\int_{\Delta_\kappa} F_{\mathrm{sol}}(\lambda) L(\boldsymbol{\Omega}, \lambda) \frac{\mathrm{d}\kappa}{\kappa^2}}{\Delta_\kappa \bar{\lambda}^2 \bar{F}_{\mathrm{sol}}^2}. \tag{5.12b}$$

In this instance, F_{sol} is nearly constant within Δ_κ, then $\acute{T} \sim \bar{T}$ and $\acute{L} \sim \bar{L}$. Therefore, the influence of $\bar{T}$ and $\bar{L}$ based on the wavelength dependency of F_{sol}.

5.1.4. Evaluation of the WV-CKD

To evaluate sky radiance at ground level in detail, we constructed a fine-scale LUT of the k distribution ($\Delta_\kappa = 2, 5\ \mathrm{cm}^{-1}$; hereinafter, WV-CKD-2 and WV-CKD-5, respectively) in the same manner as described in Sec. 5.1.2; however, $\sqrt{\varepsilon_E^2}$ was satisfied at values below 11.2×10^{-3} and 7.1×10^{-3} to keep the accuracy of the $10\ \mathrm{cm}^{-1}$ band-averaged sky intensities below 5.0×10^{-3} (the same as WV-CKD-10). The details of WV-CKD-2 and WV-CKD-5 are summarized in Table 5.2. Figure 5.4 shows the sub-band quadrature number of WV-CKD-2 (Fig. 5.4b) and WV-CKD-5 (Fig. 5.4a). The quadrature numbers of WV-CKD-2 and WV-CKD-5 consist in the range of 1 to 9 and 2 to 11, respectively (Fig. 5.3). The medians of the quadrature numbers of WV-CKD-2 and WV-CKD-5 are 4 and 6, respectively. Therefore, using all of the WV-CKD developed here is ≥ 46-fold more rapid than the LBL method. The simulation (dataset consisting of the radiances at ground level under several aerosol conditions from Dubovik et al. [2000]; hereinafter, DU-DB) was conducted for two aerosol types reported by Dubovik et al. [2000] and two atmospheric profiles, described in Table 5.3. The atmospheric profiles were used for the SKYNET Chiba site (35.63N, 140.10E) and were obtained from NCEP reanalysis 1 data for 2018 (Fig. 5.5). The sky radiances were convoluted using filter response functions for three Gaussian shapes (FWHM: 5, 10, 15 nm) at two central wavelengths of 936 and 940 nm (Fig. 5.6). The extra-terrestrial solar irradiance was obtained from Coddington et al. [2021].

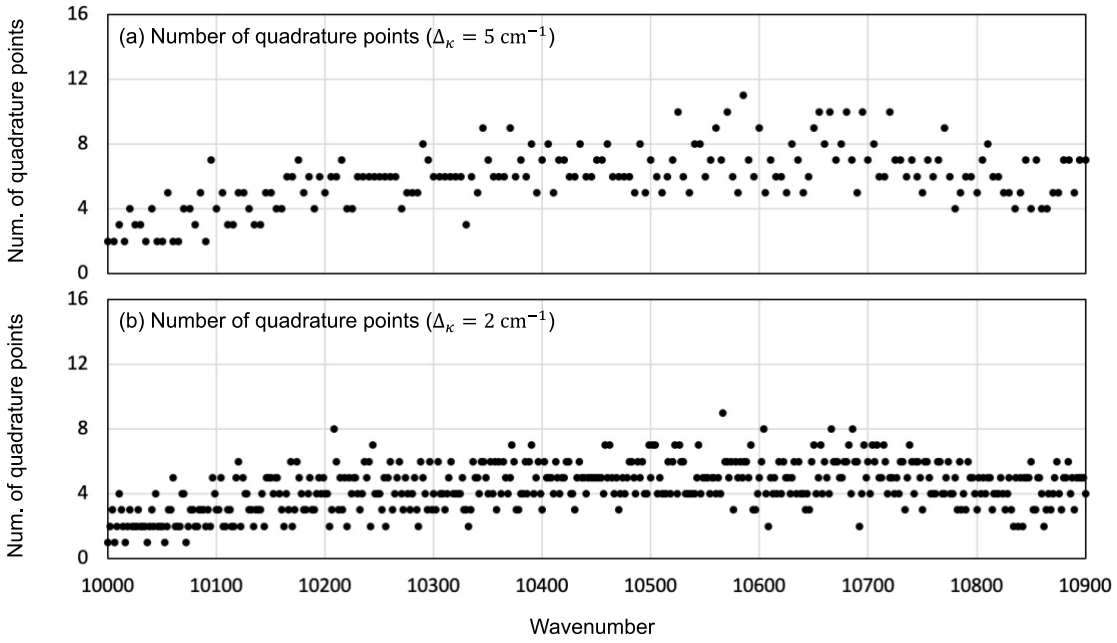

Figure 5.4: The quadrature numbers of WV-CKD-5 (top) and WV-CKD-2 (bottom).

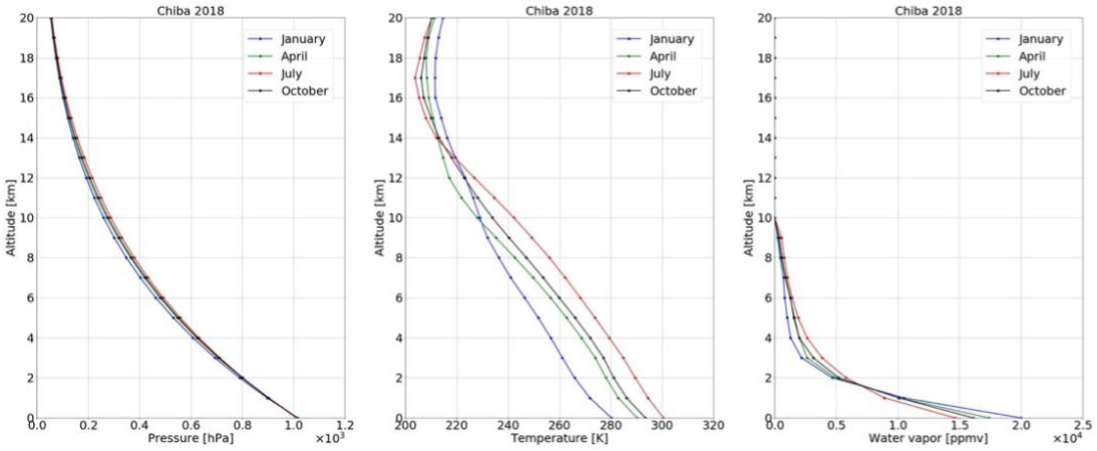

Figure 5.5: Monthly mean atmospheric vertical profiles at the SKYNET Chiba site in 2018 obtained from NCEP reanalysis 1 data. Left and center panels are vertical profiles of pressure, and temperature, respectively. Right panel is the vertical profile of water vapor normalized to PWV of 2 cm.

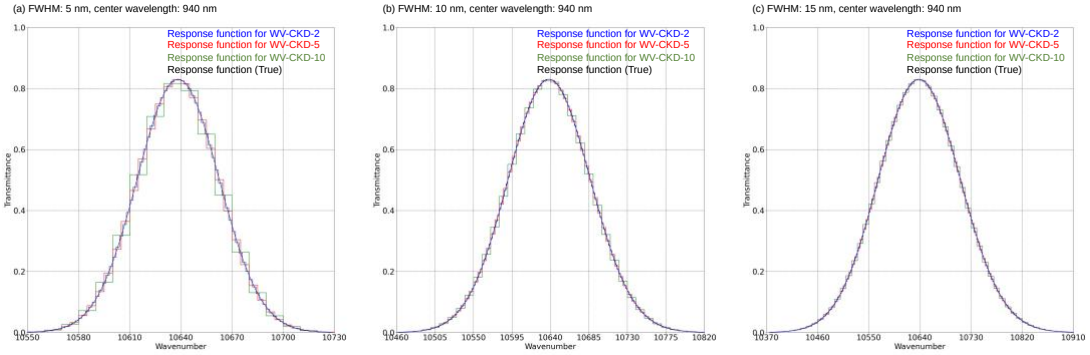

Figure 5.6: Filter response functions (FWHM: 5, 10, and 15 nm). Black lines are true filter response functions at central wavelengths of 940 nm. Blue, red, and green lines show stepwise functions integrated at the sub-band level for WV-CKD-2, WV-CKD-5, and WV-CKD-10, respectively.

Table 5.3: Description of the simulation data used in Sec 5.1.4 (DU-DB).

Element	Variable	Type 1	Type 2	Type 3	Type 4
Aerosol	Component (Dubovik et al. [2000])	Water-soluble		Biomass burning	
	Vertical profile	$\exp(-z/H)$, $H = 2$ km		$\exp(-z/H)$, $H = 4$ km	
	Optical depth at 500 nm	0.2		0.4	
Atmosphere	Vertical profile	Chiba Jan	Chiba-Apr	Chiba-Jul	Chiba-Oct
	PWV	0.78 cm	1.79 cm	4.64 cm	2.58 cm
Geometry	Solar zenith angle	60 degree		40 degree	

5.1.4.1. Comparison with convolved sky intensities with the stepwise filter response function

$\hat{T}^{\mathrm{LBL}}$, $\hat{L}^{\mathrm{LBL}}$, and $\hat{R}^{\mathrm{LBL}}$ assume that the extra-terrestrial solar irradiance and filter response function are nearly constant in each sub-band. Therefore, this section aims to evaluate whether the WV-CKD can be used for aerosol and atmospheric vertical profiles other than the six AFGL standard atmospheres with continental averaged aerosols used for creating the WV-CKDs.

Tables 5.4 and 5.5 summarize the maximum residuals between the LBL and CKD methods. The expected values ($D\Phi\sqrt{\varepsilon_E^2}$) estimated by Eq. (5.8) in each simulation are also

shown in Tables 5.4 and 5.5. The $\sqrt{\varepsilon_{\hat{I}\max}^2}$ values of using all WV-CKD are smaller than 1.64×10^{-3}, as similar to the expected residual errors ($D\Phi\sqrt{\varepsilon_E^2} = 2.0 \times 10^{-3}, 1.4 \times 10^{-3}$ and 1.1×10^{-3} at FWHMs of 5, 10, and 15 nm, respectively). This finding suggests that the WV-CKD can be used under conditions other than the six AFGL standard atmospheres with continental averaged aerosols even with several rough assumptions. Therefore, the expected residual error ($D\Phi\sqrt{\varepsilon_E^2}$) is a useful benchmark of $\hat{T}^{\mathrm{CKD}}$ and $\hat{L}^{\mathrm{CKD}}$. Additionally, $\sqrt{\varepsilon_{\hat{R}\max}^2}$ values were smaller than 3.97×10^{-4} and much smaller than $\sqrt{\varepsilon_{\hat{I}\max}^2}$. This difference is because the normalized radiance cancels the residual error of $\hat{T}^{\mathrm{CKD}}$ and the residual error of $\hat{L}^{\mathrm{CKD}}$, as shown in Eq. (7.10). Then it suggests the residual error of $\hat{L}^{\mathrm{CKD}}$ is correlated to $\hat{T}^{\mathrm{CKD}}$. In contrast, the $\sqrt{\varepsilon_{\hat{I}\max}^2}$ values of using the SN-CKD were more significant, from 7.53×10^{-3} to 2.21×10^{-1}, which are not negligible relative to the uncertainty of sky-radiometer observations $\sigma_{F_{\mathrm{ds}}}$ in Chapter 6. Then, $\sqrt{\varepsilon_{\hat{R}\max}^2}$ obtained using the SN-CKD is better than $\sqrt{\varepsilon_{\hat{I}\max}^2}$, but reaches 6.71×10^{-2} at the FWHM of 5 nm and 3.89×10^{-2} at the FWHM of 10 nm.

Table 5.4: Maximum residual errors of the convoluted radiances assuming sub-band averaged extra-terrestrial solar irradiance and a filter response function at a central wavelength of 936 nm. ALM and PPL are, respectively, almucantar and principal of sky-radiometer observational planes.

FWHM [nm]	5				10				15			
Database	SNCKD	WVCKD2	WVCKD5	WVCKD10	SNCKD	WVCKD2	WVCKD5	WVCKD10	SN-CKD	WVCKD2	WVCKD5	WVCKD10
Type 1 (ALM)												
$\lvert\varepsilon_{\check{I}\max}\rvert$ ($\times 10^{-3}$)	221	0.451	0.205	0.063	145	0.165	0.022	0.140	110	0.173	0.117	0.193
$\lvert\varepsilon_{\check{R}\max}\rvert$ ($\times 10^{-3}$)	12.7	0.016	0.053	0.024	8.13	0.005	0.019	0.062	7.00	0.002	0.014	0.071
(PPL)												
$\lvert\varepsilon_{\check{I}\max}\rvert$ ($\times 10^{-3}$)	221	0.451	0.331	0.063	145	0.375	0.071	0.140	110	0.421	0.169	0.193
$\lvert\varepsilon_{\check{R}\max}\rvert$ ($\times 10^{-3}$)	23.2	0.057	0.126	0.024	21.2	0.216	0.074	0.183	18.2	0.249	0.055	0.265
Type 2 (ALM)												
$\lvert\varepsilon_{\check{I}\max}\rvert$ ($\times 10^{-3}$)	127	1.038	0.437	0.123	107	0.624	0.441	0.239	86.8	0.573	0.436	0.296
$\lvert\varepsilon_{\check{R}\max}\rvert$ ($\times 10^{-3}$)	23.3	0.019	0.013	0.032	17.4	0.002	0.038	0.054	14.0	0.026	0.045	0.042
(PPL)												
$\lvert\varepsilon_{\check{I}\max}\rvert$ ($\times 10^{-3}$)	194	1.038	0.619	0.123	136	0.624	0.550	0.239	105	0.573	0.525	0.296
$\lvert\varepsilon_{\check{R}\max}\rvert$ ($\times 10^{-3}$)	67.1	0.397	0.183	0.046	28.8	0.265	0.109	0.065	18.0	0.169	0.089	0.105
Type 3 (ALM)												
$\lvert\varepsilon_{\check{I}\max}\rvert$ ($\times 10^{-3}$)	93.2	1.470	0.512	0.214	7.58	1.213	0.311	0.218	17.9	1.000	0.249	0.178
$\lvert\varepsilon_{\check{R}\max}\rvert$ ($\times 10^{-3}$)	14.4	0.005	0.035	0.002	11.9	0.043	0.048	0.037	8.19	0.067	0.065	0.052
(PPL)												
$\lvert\varepsilon_{\check{I}\max}\rvert$ ($\times 10^{-3}$)	93.2	1.470	0.541	0.214	43.2	1.213	0.405	0.218	41.8	1.006	0.329	0.178
$\lvert\varepsilon_{\check{R}\max}\rvert$ ($\times 10^{-3}$)	86.7	0.177	0.035	0.084	38.9	0.075	0.094	0.085	24.0	0.067	0.080	0.052
Type 4 (ALM)												
$\lvert\varepsilon_{\check{I}\max}\rvert$ ($\times 10^{-3}$)	144	0.996	0.520	0.205	114	0.611	0.501	0.254	91.3	0.573	0.465	0.293
$\lvert\varepsilon_{\check{R}\max}\rvert$ ($\times 10^{-3}$)	14.4	0.020	0.011	0.023	11.7	0.006	0.028	0.037	10.1	0.015	0.033	0.033
(PPL)												
$\lvert\varepsilon_{\check{I}\max}\rvert$ ($\times 10^{-3}$)	176	0.996	0.578	0.205	128	0.611	0.557	0.254	98.7	0.573	0.517	0.293
$\lvert\varepsilon_{\check{R}\max}\rvert$ ($\times 10^{-3}$)	32.5	0.180	0.058	0.026	13.4	0.139	0.056	0.037	10.1	0.094	0.052	0.043
Expected residual error												
$D\Phi(\varepsilon_E^2)^{1/2}$ ($\times 10^{-3}$)			2.0				1.4				1.1	

Table 5.5: As described for Table 5.4, but for 940 nm

FWHM [nm]	5				10				15			
Database	SNCKD	WVCKD2	WVCKD5	WVCKD10	SNCKD	WVCKD2	WVCKD5	WVCKD10	SN-CKD	WVCKD2	WVCKD5	WVCKD10
Type 1 (ALM)												
$\lvert\varepsilon_{\check{I}\max}\rvert$ ($\times 10^{-3}$)	72.8	0.018	0.261	0.646	136	0.166	0.099	0.199	128	0.169	0.028	0.097
$\lvert\varepsilon_{\check{R}\max}\rvert$ ($\times 10^{-3}$)	1.66	0.007	0.046	0.060	3.71	0.005	0.029	0.051	4.77	0.006	0.018	0.051
(PPL)												
$\lvert\varepsilon_{\check{I}\max}\rvert$ ($\times 10^{-3}$)	72.8	0.329	0.260	0.719	136	0.391	0.099	0.407	128	0.416	0.037	0.217
$\lvert\varepsilon_{\check{R}\max}\rvert$ ($\times 10^{-3}$)	24.0	0.347	0.112	0.073	28.2	0.230	0.052	0.208	25.6	0.253	0.047	0.263
Type 2 (ALM)												
$\lvert\varepsilon_{\check{I}\max}\rvert$ ($\times 10^{-3}$)	80.0	0.472	0.228	0.185	127	0.631	0.275	0.157	116	0.573	0.324	0.236
$\lvert\varepsilon_{\check{R}\max}\rvert$ ($\times 10^{-3}$)	11.5	0.033	0.044	0.039	14.8	0.019	0.024	0.029	15.3	0.002	0.028	0.033
(PPL)												
$\lvert\varepsilon_{\check{I}\max}\rvert$ ($\times 10^{-3}$)	85.3	0.472	0.506	0.185	140	0.631	0.378	0.216	130	0.573	0.356	0.235
$\lvert\varepsilon_{\check{R}\max}\rvert$ ($\times 10^{-3}$)	11.5	0.295	0.278	0.283	14.8	0.203	0.103	0.088	15.3	0.159	0.033	0.033
Type 3 (ALM)												
$\lvert\varepsilon_{\check{I}\max}\rvert$ ($\times 10^{-3}$)	26.7	1.639	0.335	0.087	44.2	1.486	0.407	0.169	35.7	1.136	0.342	0.101
$\lvert\varepsilon_{\check{R}\max}\rvert$ ($\times 10^{-3}$)	11.0	0.011	0.053	0.018	12.5	0.007	0.040	0.022	11.6	0.026	0.045	0.040
(PPL)												
$\lvert\varepsilon_{\check{I}\max}\rvert$ ($\times 10^{-3}$)	47.0	1.639	0.455	0.087	75.6	1.486	0.445	0.169	65.5	1.136	0.389	0.101
$\lvert\varepsilon_{\check{R}\max}\rvert$ ($\times 10^{-3}$)	20.3	0.170	0.119	0.018	31.4	0.104	0.040	0.022	29.8	0.039	0.048	0.040
Type 4 (ALM)												
$\lvert\varepsilon_{\check{I}\max}\rvert$ ($\times 10^{-3}$)	80.3	0.465	0.374	0.013	130	0.638	0.331	0.277	119	0.573	0.346	0.296
$\lvert\varepsilon_{\check{R}\max}\rvert$ ($\times 10^{-3}$)	7.72	0.033	0.030	0.021	9.73	0.020	0.016	0.016	10.3	0.006	0.018	0.022
(PPL)												
$\lvert\varepsilon_{\check{I}\max}\rvert$ ($\times 10^{-3}$)	81.9	0.465	0.497	0.121	136	0.638	0.382	0.300	126	0.573	0.369	0.296
$\lvert\varepsilon_{\check{R}\max}\rvert$ ($\times 10^{-3}$)	7.72	0.150	0.123	0.129	9.73	0.102	0.051	0.039	10.3	0.083	0.024	0.022
Expected residual error												
$D\Phi(\varepsilon_E^2)^{1/2}$ ($\times 10^{-3}$)			2.0				1.4				1.1	

5.1.4.2. Comparison with convolved sky intensities with the smooth filter response function

$\tilde{T}^{\mathrm{LBL}}$, $\tilde{T}^{\mathrm{LBL}}$, and $\tilde{T}^{\mathrm{LBL}}$ are calculated by the LBL method and convolved with the smooth filter response function and high- resolution ($0.01\ \mathrm{cm}^{-1}$) extra-terrestrial solar irradiance data of Coddington et al. [2021]. This section provides a comprehensive assessment of $\hat{T}^{\mathrm{CKD}}$, $\hat{L}^{\mathrm{CKD}}$, and $\hat{R}^{\mathrm{CKD}}$. The residual errors of the convolved sky intensities are defined as follows:

$$\varepsilon_{\tilde{T}}^2 = \left(\ln\frac{\hat{T}^{\mathrm{CKD}}}{\tilde{T}^{\mathrm{LBL}}}\right)^2 = \left[\ln\left(\frac{\sum^{N_s}\bar{\psi}\cdot\bar{F}_{\mathrm{sol}}\cdot\bar{T}^{\mathrm{CKD}}\cdot\Delta_\kappa\bar{\lambda}^2}{\sum^{N_s}\bar{\psi}\cdot\bar{F}_{\mathrm{sol}}\cdot\Delta_\kappa\bar{\lambda}^2}\Big/\frac{\int\psi(\lambda)F_{\mathrm{sol}}(\lambda)T^{\mathrm{LBL}}(\lambda)\mathrm{d}\lambda}{\int\psi(\lambda)F_{\mathrm{sol}}(\lambda)\mathrm{d}\lambda}\right)\right]^2 \sim \varepsilon_{\hat{T},\mathrm{RT}}^2 + \varepsilon_{\tilde{T},\mathrm{FRF}}^2, \tag{5.13a}$$

$$\varepsilon_{\tilde{L}}^2(\mathbf{\Omega}) = \left(\ln\frac{\hat{L}^{\mathrm{CKD}}}{\tilde{L}^{\mathrm{LBL}}}\right)^2 = \left[\ln\left(\frac{\sum^{N_s}\bar{\psi}\cdot\bar{F}_{\mathrm{sol}}\cdot\bar{L}^{\mathrm{CKD}}(\mathbf{\Omega})\cdot\Delta_\kappa\bar{\lambda}^2}{\sum^{N_s}\bar{\psi}\cdot\bar{F}_{\mathrm{sol}}\cdot\Delta_\kappa\bar{\lambda}^2}\Big/\frac{\int\psi(\lambda)F_{\mathrm{sol}}(\lambda)L^{\mathrm{LBL}}(\mathbf{\Omega},\lambda)\mathrm{d}\lambda}{\int\psi(\lambda)F_{\mathrm{sol}}(\lambda)\mathrm{d}\lambda}\right)\right]^2 \sim \varepsilon_{\hat{L},\mathrm{RT}}^2 + \varepsilon_{\tilde{L},\mathrm{FRF}}^2, \tag{5.13b}$$

$$\varepsilon_{\tilde{R}}^2(\mathbf{\Omega}) = \left[\ln\left(\frac{\hat{L}^{\mathrm{CKD}}}{\hat{T}^{\mathrm{CKD}}}\Big/\frac{\tilde{L}^{\mathrm{LBL}}}{\tilde{T}^{\mathrm{LBL}}}\right)\right]^2 = \left[\ln\left(\frac{\sum^{N_s}\bar{\psi}\cdot\bar{F}_{\mathrm{sol}}\cdot\bar{L}^{\mathrm{CKD}}(\mathbf{\Omega})\cdot\Delta_\kappa\bar{\lambda}^2}{\sum^{N_s}\bar{\psi}\cdot\bar{F}_{\mathrm{sol}}\cdot\bar{T}^{\mathrm{CKD}}\cdot\Delta_\kappa\bar{\lambda}^2}\Big/\frac{\int\psi(\lambda)F_{\mathrm{sol}}(\lambda)L^{\mathrm{LBL}}(\mathbf{\Omega},\lambda)\mathrm{d}\lambda}{\int\psi(\lambda)F_{\mathrm{sol}}(\lambda)T^{\mathrm{LBL}}(\lambda)\mathrm{d}\lambda}\right)\right]^2, \tag{5.13c}$$

where $\varepsilon_{\tilde{T},\mathrm{FRF}}^2$ and $\varepsilon_{\tilde{L},\mathrm{FRF}}^2$ are the residual errors arising from the assumptions of the solar irradiance and filter response function. The maximum residuals can be obtained as follows:

$$\varepsilon_{\tilde{I}\max}^2 = \max\left\{\varepsilon_{\tilde{T}}^2, \varepsilon_{\tilde{L}}^2(\mathbf{\Omega})\right\}, \tag{5.14a}$$

$$\varepsilon_{\tilde{R}\max}^2 = \max\left\{\varepsilon_{\tilde{R}}^2(\mathbf{\Omega})\right\}. \tag{5.14b}$$

The angular distribution of the normalized radiances simulated for type 2 of DU-DB is shown in Figure 5.7. Although the convolved $\tilde{R}$ with the SN-CKD arises significant errors in backward scattering and the zenith region (approximately 1.5%), that with the WV-CKDs showed better performance (< 0.1%). Tables 5.6 and 5.7 summarize $\varepsilon_{\tilde{I}\max}^2$ and $\varepsilon_{\tilde{R}\max}^2$ for the simulation with DU-DB. Although the finer Δ_κ is a good choice to treat the shape of the

filter response function, Tables do not follow this trend. This is because a significant wavelength dependency of extra-terrestrial solar irradiance (Coddington et al. [2021]) might affect the performance more than the shape of the response function. Then, the residual errors of using the WV-CKD-2 and WV-CKD-5 are within 3×10^{-3}. In the case of an FWHM of 5 nm, the residual errors of using the WV-CKD-10 are significantly large (> 1%) by the assumption of the stepwise function. In contrast, $\hat{R}^{\mathrm{CKD}}$ was less affected than $\hat{T}^{\mathrm{CKD}}$ and $\hat{L}^{\mathrm{CKD}}$ ($\sqrt{\varepsilon^2_{\hat{R}\max}} \leq 1.1 \times 10^{-3}$), following the relationship between $\varepsilon^2_{\hat{R}\max}$ and $\varepsilon^2_{\hat{I}\max}$ described in Section 5.1.4.1.

With an FWHM of 10 nm, corresponding to a sky-radiometer specification, $\sqrt{\varepsilon^2_{\hat{I}\max}}$ for the WV-CKD-2, WV-CKD-5, and WV-CKD-10 is less than 3.2×10^{-3}, 1.3×10^{-3}, and 4.0×10^{-3}, respectively. Then, $\sqrt{\varepsilon^2_{\hat{R}\max}}$ for using the WV-CKD-2, WV-CKD-5, and WV-CKD-10 is less than 0.5×10^{-3}, 0.4×10^{-3}, and 1.1×10^{-3}, respectively. These values are significantly smaller than $\sqrt{\varepsilon^2_{\hat{I}\max}}$ and $\sqrt{\varepsilon^2_{\hat{R}\max}}$ of using the SN-CKD ($\leq 1.5 \times 10^{-1}$ and $\leq 3.9 \times 10^{-2}$, respectively). Based on the comparison with $\sqrt{\varepsilon^2_{\hat{I}\max}}$ in the previous section, $\hat{T}^{\mathrm{CKD}}$and $\hat{L}^{\mathrm{CKD}}$ with the WV-CKD-10 are affected by the fluctuation of the extra-terrestrial solar irradiance and filter response function.

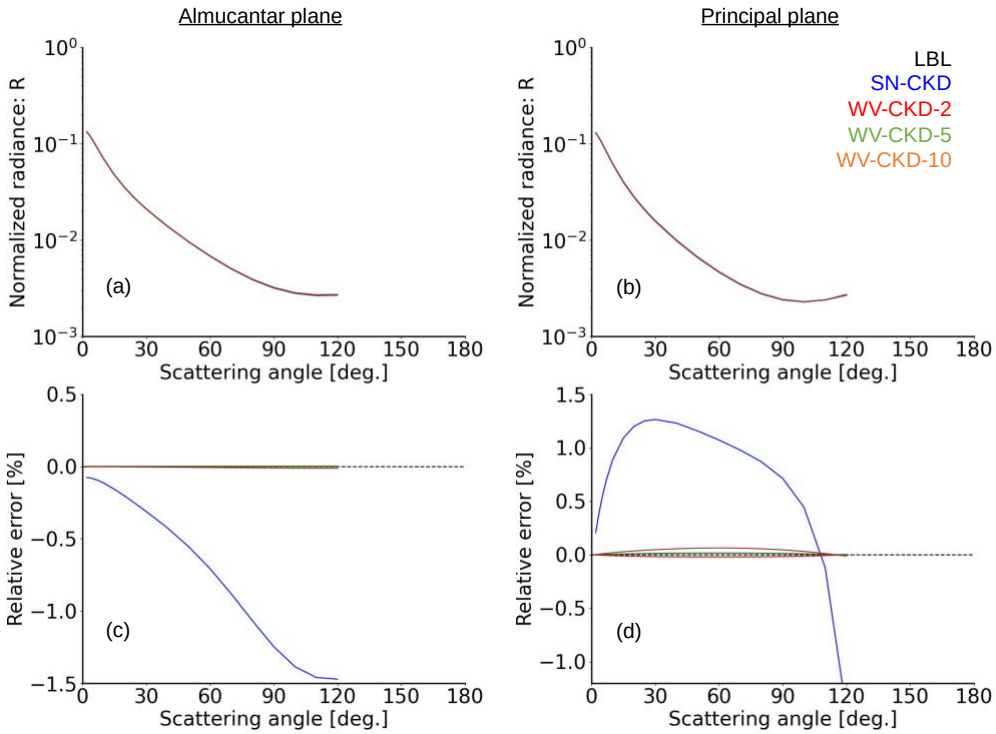

Figure 5.7: Angular distributions of normalized radiances simulated for type 2 (Table 5.3) in the almucantar and principal planes with an FWHM of 10 nm and a central wavelength of 940 nm. (a, b) Convoluted normalized radiance, *R*. (c, d) Relative errors of using the SN-CKD and WV-CKD. Note that lines in top panels overlap.

Table 5.6: As described for Table 5.4, but the reference radiances were computed without assumptions.

FWHM [nm]	5				10				15			
Database	SNCKD	WVCKD2	WVCKD5	WVCKD10	SNCKD	WVCKD2	WVCKD5	WVCKD10	SN-CKD	WVCKD2	WVCKD5	WVCKD10
Type 1 (ALM)												
$\lvert\varepsilon_{\bar{I}\max}\rvert$ ($\times 10^{-3}$)	211	0.247	0.961	5.043	147	1.740	0.398	0.919	112	1.521	0.246	0.772
$\lvert\varepsilon_{\bar{R}\max}\rvert$ ($\times 10^{-3}$)	12.8	0.108	0.090	0.053	7.94	0.471	0.355	0.506	6.99	0.309	0.189	0.308
(PPL)												
$\lvert\varepsilon_{\bar{I}\max}\rvert$ ($\times 10^{-3}$)	211	0.247	0.961	5.038	147	1.740	0.398	0.919	112	1.521	0.295	0.772
$\lvert\varepsilon_{\bar{R}\max}\rvert$ ($\times 10^{-3}$)	21.4	0.169	0.221	0.422	21.6	0.531	0.355	0.602	18.4	0.492	0.189	0.417
Type 2 (ALM)												
$\lvert\varepsilon_{\bar{I}\max}\rvert$ ($\times 10^{-3}$)	113	1.569	1.905	4.271	111	2.706	0.631	2.850	88.5	1.871	0.523	1.286
$\lvert\varepsilon_{\bar{R}\max}\rvert$ ($\times 10^{-3}$)	23.0	0.162	0.162	0.061	17.1	0.523	0.371	0.390	14.0	0.251	0.114	0.119
(PPL)												
$\lvert\varepsilon_{\bar{I}\max}\rvert$ ($\times 10^{-3}$)	182	1.569	1.905	4.588	139	2.706	0.631	2.850	106	1.871	0.610	1.286
$\lvert\varepsilon_{\bar{R}\max}\rvert$ ($\times 10^{-3}$)	68.8	0.808	0.178	0.379	28.1	0.523	0.395	1.058	17.8	0.251	0.114	0.359
Type 3 (ALM)												
$\lvert\varepsilon_{\bar{I}\max}\rvert$ ($\times 10^{-3}$)	108	2.897	2.402	2.901	8.69	3.153	1.197	3.982	19.6	1.728	0.555	1.158
$\lvert\varepsilon_{\bar{R}\max}\rvert$ ($\times 10^{-3}$)	13.9	0.093	0.119	0.168	11.6	0.468	0.325	0.160	8.20	0.161	0.110	0.077
(PPL)												
$\lvert\varepsilon_{\bar{I}\max}\rvert$ ($\times 10^{-3}$)	108	2.897	2.402	3.330	47.2	3.153	1.197	3.982	43.5	1.728	0.555	1.104
$\lvert\varepsilon_{\bar{R}\max}\rvert$ ($\times 10^{-3}$)	87.0	0.570	0.185	0.597	38.5	0.468	0.325	0.514	23.9	0.161	0.073	0.024
Type 4 (ALM)												
$\lvert\varepsilon_{\bar{I}\max}\rvert$ ($\times 10^{-3}$)	130	1.378	1.807	4.176	118	2.339	0.353	2.521	92.9	1.647	0.655	1.189
$\lvert\varepsilon_{\bar{R}\max}\rvert$ ($\times 10^{-3}$)	14.2	0.108	0.113	0.128	11.5	0.435	0.342	0.319	10.1	0.215	0.171	0.154
(PPL)												
$\lvert\varepsilon_{\bar{I}\max}\rvert$ ($\times 10^{-3}$)	163	1.378	1.807	4.375	131	2.339	0.353	2.521	100	1.643	0.655	1.159
$\lvert\varepsilon_{\bar{R}\max}\rvert$ ($\times 10^{-3}$)	33.4	0.363	0.113	0.327	13.1	0.435	0.342	0.345	10.1	0.211	0.130	0.124
Expected residual error												
$D\Phi(\varepsilon_E^2)^{1/2}$ ($\times 10^{-3}$)			2.0				1.4				1.1	

Table 5.7: As described for Table 5.5, but the reference radiances were computed without assumptions.

FWHM [nm]	5				10				15			
Database	SNCKD	WVCKD2	WVCKD5	WVCKD10	SNCKD	WVCKD2	WVCKD5	WVCKD10	SN-CKD	WVCKD2	WVCKD5	WVCKD10
Type 1 (ALM)												
$\lvert\varepsilon_{\bar{I}\max}\rvert$ ($\times 10^{-3}$)	83.6	0.369	0.190	11.72	139	0.767	1.078	1.333	130	1.494	0.549	0.357
$\lvert\varepsilon_{\bar{R}\max}\rvert$ ($\times 10^{-3}$)	1.40	0.075	0.210	0.761	3.62	0.160	0.142	0.305	4.71	0.242	0.184	0.262
(PPL)												
$\lvert\varepsilon_{\bar{I}\max}\rvert$ ($\times 10^{-3}$)	83.6	0.878	0.695	11.72	139	0.767	1.133	1.333	130	1.494	0.597	0.357
$\lvert\varepsilon_{\bar{R}\max}\rvert$ ($\times 10^{-3}$)	25.6	0.509	0.504	2.463	28.7	0.394	0.142	0.685	25.8	0.468	0.184	0.403
Type 2 (ALM)												
$\lvert\varepsilon_{\bar{I}\max}\rvert$ ($\times 10^{-3}$)	93.5	0.317	0.724	16.77	131	0.942	1.152	2.875	117	1.855	0.686	1.019
$\lvert\varepsilon_{\bar{R}\max}\rvert$ ($\times 10^{-3}$)	11.6	0.048	0.148	0.378	14.7	0.182	0.164	0.242	15.2	0.277	0.205	0.227
(PPL)												
$\lvert\varepsilon_{\bar{I}\max}\rvert$ ($\times 10^{-3}$)	98.0	0.333	0.724	16.77	144	0.942	1.369	2.875	132	1.855	0.808	1.019
$\lvert\varepsilon_{\bar{R}\max}\rvert$ ($\times 10^{-3}$)	11.6	0.047	0.857	2.323	14.7	0.182	0.217	0.505	15.2	0.277	0.205	0.233
Type 3 (ALM)												
$\lvert\varepsilon_{\bar{I}\max}\rvert$ ($\times 10^{-3}$)	40.6	1.034	1.417	19.19	48.8	0.648	0.936	3.572	37.4	1.848	0.536	1.113
$\lvert\varepsilon_{\bar{R}\max}\rvert$ ($\times 10^{-3}$)	11.3	0.049	0.114	0.134	12.5	0.171	0.173	0.213	11.5	0.256	0.190	0.202
(PPL)												
$\lvert\varepsilon_{\bar{I}\max}\rvert$ ($\times 10^{-3}$)	60.6	1.077	1.417	19.19	80.0	0.648	1.022	3.572	67.1	1.848	0.566	1.113
$\lvert\varepsilon_{\bar{R}\max}\rvert$ ($\times 10^{-3}$)	20.1	0.049	0.339	0.807	31.2	0.171	0.173	0.213	29.7	0.256	0.190	0.202
Type 4 (ALM)												
$\lvert\varepsilon_{\bar{I}\max}\rvert$ ($\times 10^{-3}$)	93.5	0.391	0.466	16.35	134	0.767	1.265	2.839	120	1.647	0.809	0.966
$\lvert\varepsilon_{\bar{R}\max}\rvert$ ($\times 10^{-3}$)	7.82	0.017	0.116	0.279	9.72	0.130	0.140	0.206	10.2	0.218	0.187	0.211
(PPL)												
$\lvert\varepsilon_{\bar{I}\max}\rvert$ ($\times 10^{-3}$)	94.6	0.389	0.466	16.35	140	0.754	1.305	2.827	127	1.634	0.809	0.945
$\lvert\varepsilon_{\bar{R}\max}\rvert$ ($\times 10^{-3}$)	7.82	0.017	0.357	0.938	9.72	0.117	0.124	0.194	10.2	0.205	0.167	0.190
Expected residual error												
$D\Phi(\varepsilon_E^2)^{1/2}$ ($\times 10^{-3}$)			2.0				1.4				1.1	

5.2. Information about the aerosols and PWV on the angular distribution of the convolved normalized radiances at 940 nm

A pioneering study about the aerosols and PWV on the angular distribution of $\tilde{R}$ at 940 nm was conducted by Momoi et al. [2020] using the SN-CKD. However, as discussed in the previous section, the SN-CKD is unsuitable for narrow-band computation and causes a significant residual error in the simulated radiances. Therefore, we reconducted the sensitivity tests with the WV-CKD-2. Through all results from the simulation (Figs. 5.8-11), the only magnitude of $\tilde{R}$ differed between SN-CKD (dotted lines in figures) and WV-CKD-2 (solid lines in figures). The relationships between $\tilde{R}$ around 940 nm, PWV, and aerosols are consistent with the pioneering study by Momoi et al. [2020]. Therefore, the following discussions are based on Momoi et al. [2020].

We examined the sensitivity of $\tilde{R}$ at 940 nm in the two observation planes to PWV, aerosol optical properties, and aerosol vertical profiles by simulation using the RSTAR7 with both SN-CKD and WV-CKD-2. The simulation was conducted with two aerosol types based on Kudo et al. [2016]. One is the continental average condition contained water-soluble, soot, and insoluble particles. The other is the transported dust condition contained the mineral-dust particles in the upper atmosphere in the continental average condition described in Table 5.8. The complex refractive index and the size distribution of those aerosol components are referred to Hess et al. [1999]. All aerosols except mineral-dust particles are spherical particles and the mineral-dust particles are spheroidal particles with an axis ratio of 0.6, representing the yellow sand particles reported by Nakajima et al. [1989]. The radiances are convolved with a filter response function that has an FWHM of 10 nm and a central wavelength of 940 nm.

Figure 5.8 shows the dependencies of $\tilde{R}$ in the almucantar plane on PWV for continental average aerosol with AOTs of 0.02 and 0.20 at 940 nm. The simulations were conducted for the SZA of 70°. $\tilde{R}$ decreases with increasing PWV regardless of the AOT. This suggests that the angular distribution of $\tilde{R}$ independent to $\tilde{F}_0$, has the information of PWV. When scattering properties ($= \omega\tau P_{11}$) of the aerosol and Rayleigh scattering is not changed in the finite range of $\psi(\lambda)$, the dependencies of $\tilde{R}$ on PWV cannot be observed in the single scattering of the radiative transfer equation in the almucantar plane as:

$$\tilde{R}(\boldsymbol{\Omega},\lambda) \approx \omega(\tilde{\lambda})\tau(\tilde{\lambda})P_{11}(\boldsymbol{\Omega},\tilde{\lambda}) + \frac{\int \psi(\lambda)F_{\mathrm{sol}}(\lambda)T_{\mathrm{H2O}}(\lambda)T_{\mathrm{cont}}(\lambda)Q(\boldsymbol{\Omega},\lambda)\mathrm{d}\lambda}{\int \psi(\lambda)F_{\mathrm{sol}}(\lambda)T_{\mathrm{H2O}}(\lambda)T_{\mathrm{cont}}(\lambda)\mathrm{d}\lambda}. \qquad (5.15)$$

where $\tilde{\lambda}$ is effective wavelength as $\tilde{\lambda} = \int \psi(\lambda)\lambda\mathrm{d}\lambda \,/\, \int \psi(\lambda)\mathrm{d}\lambda$. Note that this is correct only for $\tilde{R}(\theta = \theta_0)$, and not for $\tilde{R}(\theta \neq \theta_0)$ and $\tilde{F}_{\mathrm{df}}$, because total optical thickness (or total

transmittance including gas absorptions) contributes to the single scattering approximation of both $\tilde{R}(\theta \neq \theta_0)$ and $\tilde{F}_{\mathrm{df}}$. However, the second term for the multiple scattering includes the influence of water vapor absorption and creates the dependencies of $\tilde{R}$ on PWV. Therefore, the sensitivity of PWV depends on the scattering angle shown in Figure 5.8. The dependency of $\tilde{R}$ on PWV at the forward scattering angles is not strong, but $\tilde{R}$ at the backward scattering angles between 90° and 120° changes with PWV. Thus, the range of the scattering angle for $\tilde{R}$ is an essential factor.

Figure 5.9 illustrates the dependency of $\tilde{R}$ on PWV for different observation planes. The simulation was conducted for transported dust aerosol (Table 5.8) with an AOT of 0.06 at 940 nm at an SZA of 70° in the almucantar and principal planes. The transported dust aerosol is composed of coarse particles, which have larger impacts on the angular distribution of $\tilde{R}$ at the near-infrared wavelength than fine particles. The dependency of R in the almucantar plane on PWV is the same as in Fig. 5.8. The dependency of $\tilde{R}$ on PWV is also found in the principal plane. $\tilde{R}$ increases with increasing PWV at $\theta \ll \theta_0$ and decreases with increasing PWV at $\theta \gg \theta_0$. Although the dependency of $\tilde{R}$ on PWV in the almucantar plane is strong at the backward scattering angles, that in the principal plane is strong around the zenith. Then, $\tilde{R}$ in the principal plane is more sensitive to PWV than $\tilde{R}$ in the almucantar plane because the single scattering of $\tilde{R}$ includes gas absorption in addition to Rayleigh and aerosol scattering.

In theory, the maximum scattering angle of the principal plane is $\theta_0 + 90°$ and that of the almucantar plane is $2\theta_0$. When the SZA is small, the principal plane is more advantageous for PWV estimation (Chapter 6) because the principal plane has a broader scattering angle than the almucantar plane. Figure 5.10 is the same as Fig. 5.9 but for an SZA of 30°. The maximum scattering angle of the principal plane ($\max\{\Theta\} = 120°$) is larger than that of the almucantar plane ($\max\{\Theta\} = 60°$). Hence, PWV retrieval using the principal plane is more effective compared to that using the almucantar plane. However, according to the previous study of the sky radiances at aerosol channels by Torres et al. [2014], the aerosol vertical profile also influences on $\tilde{R}$ in the principal plane, although this influence can be negligible for $\tilde{R}$ in the almucantar plane. Figure 5.11 shows the angular distribution of $\tilde{R}$ in the two observation planes for the different heights of the transported dust layer. $\tilde{R}$ in the principal plane at 940 nm also has the information of the aerosol vertical profile larger than that at aerosol channels. Consequently, the principal plane is suitable for estimating PWV when the aerosol vertical profile is known, but the almucantar plane is better when the aerosol vertical profile is not known.

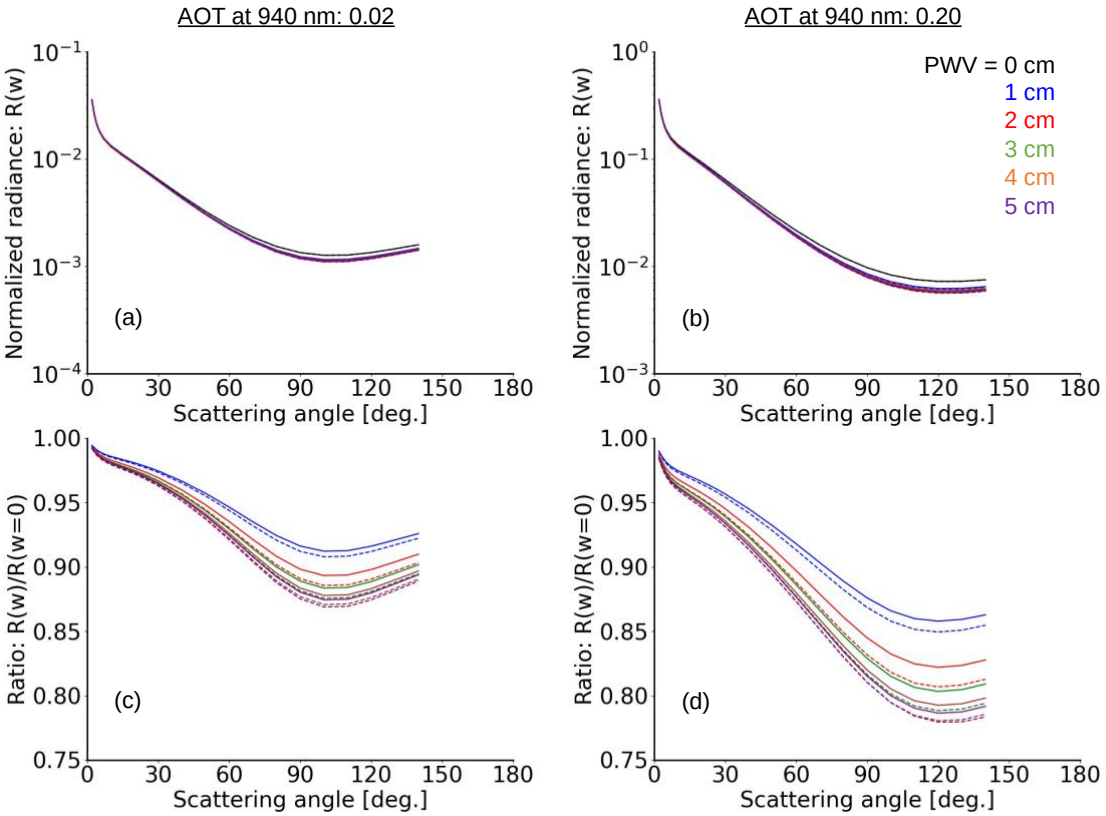

Figure 5.8: Angular distributions of simulated normalized radiances for continental average aerosol (Table 5.8) in the almucantar plane with AOTs of 0.02 and 0.20 at 940 nm. Simulations were conducted for a SZA of 70 degrees and PWV (w) = 0, 1, 2, 3, 4, and 5 cm. (a, b) Convolved R. (c, d) Ratio of $R(w)$ to $R(w = 0)$. Solid lines show radiances obtained with the SN-CKD and dashed lines show radiances obtained with the WV-CKD-2.

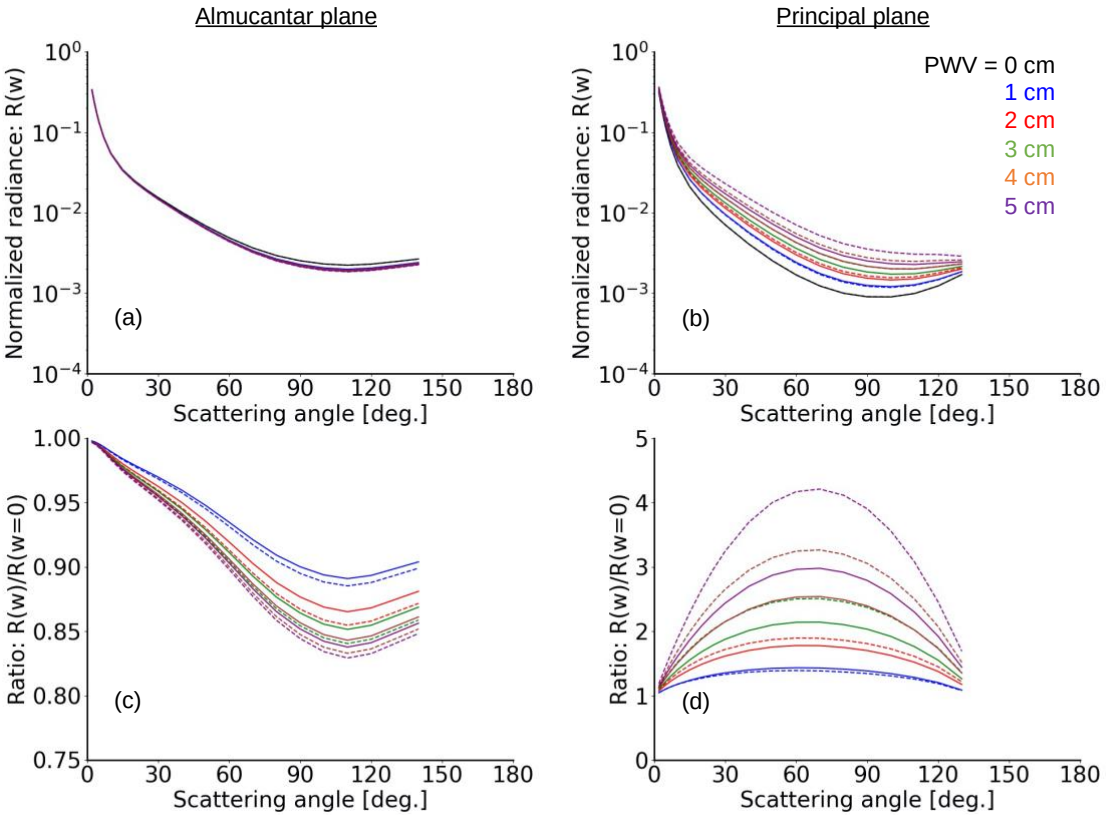

Figure 5.9: Angular distributions of simulated normalized radiances for transported dust aerosols (Table 5.8) in the almucantar and principal planes with an AOT of 0.06 at 940 nm. Simulations were conducted for a SZA of 70 degrees and PWV (w) = 0, 1, 2, 3, 4, and 5 cm. (a, b) Convolved R. (c, d) Ratio of $R(w)$ to $R(w = 0)$. Solid lines show radiances obtained with the SN-CKD and dashed lines show radiances obtained with the WV-CKD-2.

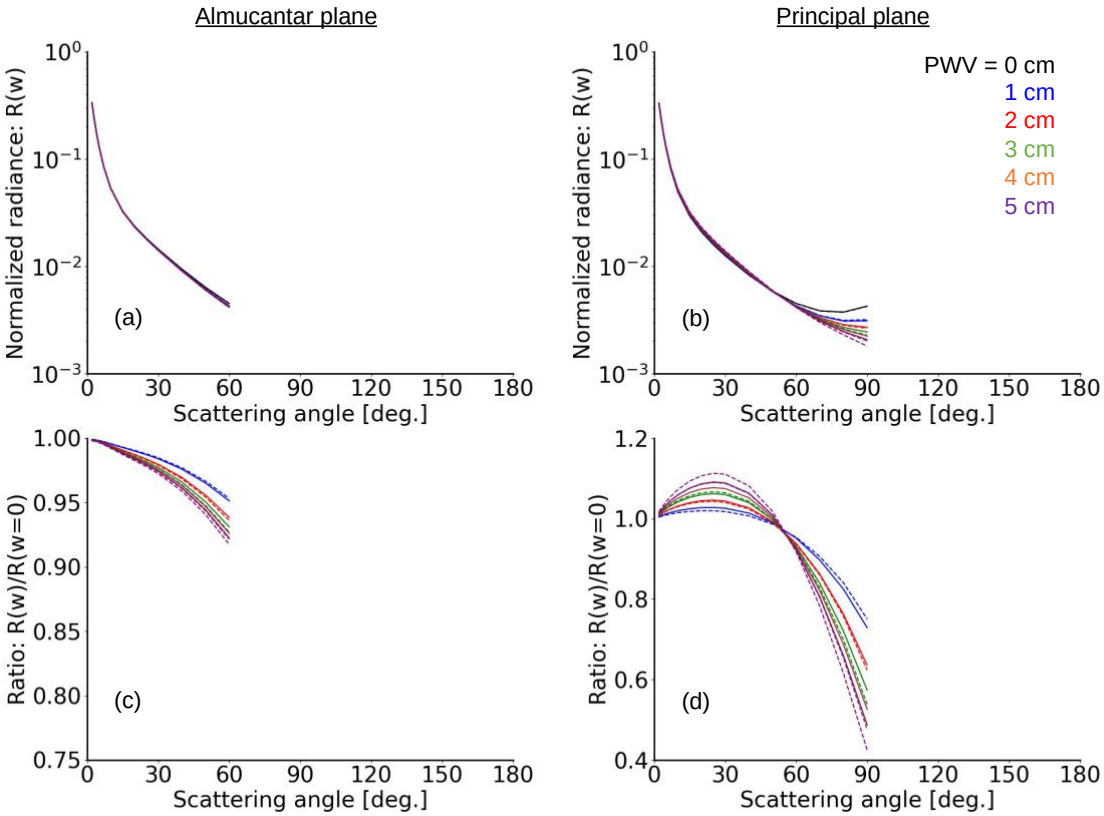

Figure 5.10: As described for Fig. 5.9, but at a SZA of 30 degrees.

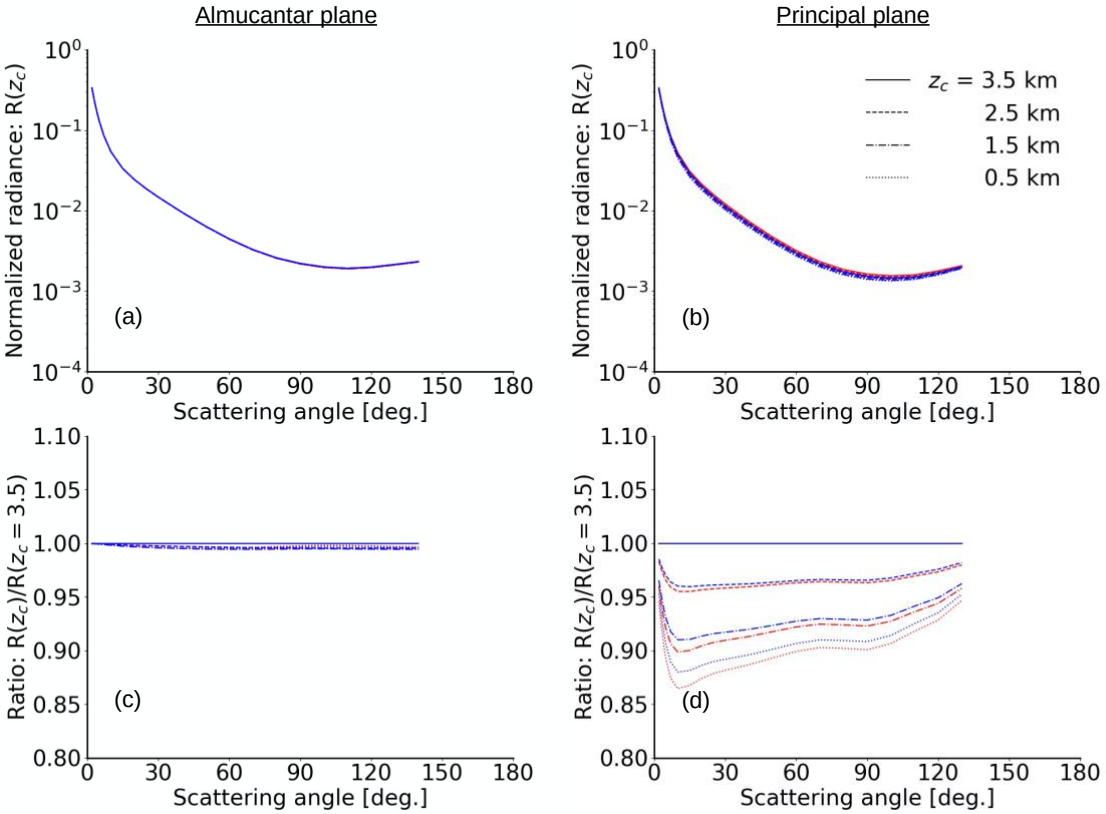

Figure 5.11: Angular distributions of simulated normalized radiances for transported dust aerosols (Table 5.8) in the almucantar and principal planes with an AOT of 0.06 at 940 nm. Simulations were conducted for a SZA of 70 degrees and PWV (w) = 2 cm. The height of the dust layer (z_c) was varied to 0.5, 1.5, 2.5, and 3.5 km. (a, b) Convolved R. (c, d) Ratio of $R(z_c)$ to $R(z_c = 3.5\ \text{km})$. Red lines show radiances obtained with the SN-CKD and blue lines show radiances obtained with the WV-CKD-2. Note that lines in top and left panels overlap.

Table 5.8: Microphysical and optical properties and vertical profiles of aerosols used in Section 5.2.

Aerosol	Components	Size distribution		Refractive index at 940 nm		Relative weight in total optical thickness at 500 nm	Vertical profile
		Mode radius (μm)	Mode width	Real	Imaginary		
Continental average	Water-soluble	0.18	0.81	1.43	0.0074	0.90	$\exp(-z/H)$, H = 8 km
	Soot	0.05	0.69	1.75	0.44	0.07	$\exp(-z/H)$, H = 4 km
	Insoluble	5.98	0.92	1.52	0.008	0.03	$\exp(-z/H)$, H = 2 km
Transported dust	Dust	3.23	0.79	1.53	0.004	0.25	$\frac{1}{\sqrt{2\pi\sigma}}\exp\left(-\frac{(z-z_c)}{2\sigma^2}\right)$, z_c = 3.5 km σ = 0.4 km
	Water-soluble	0.18	0.81	1.43	0.0074	0.67	$\exp(-z/H)$, H = 8 km
	Soot	0.05	0.69	1.75	0.44	0.05	$\exp(-z/H)$, H = 4 km
	Insoluble	5.98	0.92	1.52	0.008	0.03	$\exp(-z/H)$, H = 2 km

5.3. Conclusions

We developed new LUTs for the CKD method in the water vapor absorption region around 940 nm (WV-CKD) to study information contents on narrow-band sky radiances around 940 nm in Earth atmosphere. By comparing the sky radiance at ground level with the line-by-line approach (LBL method), this study found challenges facing the standard look-up table in RSTAR7 (SN-CKD) for reconstructing the narrow-band sky radiances around 940 nm. The root mean square error of the maximum error in sub-bands for the SN-CKD is 116% across the range of 10411–10864 cm^{-1} (961–920 nm). This large error might arise from the updated database and low quadrature number of 2. In this study, three *k*-distribution look-up tables (WV-CKD-2, WV-CKD-5, and WV-CKD-10) at different resolutions ($\Delta_\kappa = 2, 5, 10\ \mathrm{cm}^{-1}$) were created. The quadrature values (weight and point) and numbers of the WV-CKDs were optimized using sky radiances of the single-scattering approximation at ground level in Earth atmosphere with an accuracy of ≤ 0.5% for sub-bands of $10\ \mathrm{cm}^{-1}$. The quadrature number affected computational efficiency. The mean quadrature number of WV-CKD-2, WV-CKD-5, and WV-CKD-10 are 2.18, 1.18, and 0.73 $/\mathrm{cm}^{-1}$, respectively. Thus, using the WV-CKDs are ≥ 46-fold more rapid than the LBL method.

Further evaluation of the WV-CKD was conducted for two aerosol types and four

vertical profiles different from the conditions optimizing the tables. The residual errors of convoluted sky radiances ($\hat{T}^{\mathrm{CKD}}$ and $\hat{L}^{\mathrm{CKD}}$) were similar to the expected errors observed while optimizing quadrature numbers. This finding suggests that using the WV-CKD has versatility for actual atmospheric conditions. The convolved normalized radiance $\hat{R}^{\mathrm{CKD}}$ is less affected by residual errors of using the WV-CKD than $\hat{T}^{\mathrm{CKD}}$ and $\hat{L}^{\mathrm{CKD}}$ because $\hat{R}^{\mathrm{CKD}}$ cancels the residual errors of both $\hat{T}^{\mathrm{CKD}}$ and $\hat{L}^{\mathrm{CKD}}$. Additionally, while the error in $\hat{T}^{\mathrm{CKD}}$ and $\hat{L}^{\mathrm{CKD}}$ with the SN-CKD is within 15%, the WV-CKD achieves convolved sky intensities with an accuracy of $\leq 0.3\%$ at an FWHM of 10 nm, equaling the FWHM of the sky-radiometer. $\hat{R}^{\mathrm{CKD}}$ is more accurate within 0.1% lower than the measurement uncertainties (approximately 0.5%).

By thoroughly investigating the information of aerosols and PWV in the sky radiance at 940 nm, the information is different in two observational planes. The sky radiance in the almucantar plane depends on PWV. On the other hand, that in the principal plane depends on PWV and aerosol vertical profile. Consequently, the principal plane is suitable for retrieving PWV when the aerosol vertical profile is known, but the almucantar plane is better when the aerosol vertical profile is not known.

References

[1] Coddington, O. M., Richard, E. C., Harber, D., Pilewskie, P., Woods, T. N., Chance, K., et al., 2021: The TSIS-1 Hybrid Solar Reference Spectrum. Geophysical Research Letters, 48, e2020GL091709. https://doi.org/10.1029/2020GL091709

[2] Dubovik, O., Smirnov, A., Holben, B. N., King, M. D., Kaufman, Y. J., Eck, T. F., and Slutsker, I.: Accuracy assessments of aerosol optical properties retrieved from Aerosol Robotic Network (AERONET) Sun and sky radiance measurements, J. Geophys. Res., 105, 9791–9806, 2000

[3] Fu, Q., and K. N. Liou, 1992: On the correlated k-distribution method for radiative transfer in nonhomogeneous atmospheres, *J. Atmos. Sci.*, **49**, 2139–2156.

[4] Gordon, I.E., L.S. Rothman, R.J. Hargreaves, R. Hashemi, E.V. Karlovets, F.M. Skinner, E.K. Conway, C. Hill, R.V. Kochanov, Y. Tan, P. Wcisło, A.A. Finenko, K. Nelson, P.F. Bernath, M. Birk, V. Boudon, A. Campargue, K.V. Chance, A. Coustenis, B.J. Drouin, J.–M. Flaud, R.R. Gamache, J.T. Hodges, D. Jacquemart, E.J. Mlawer, A.V. Nikitin, V.I. Perevalov, M. Rotger, J. Tennyson, G.C. Toon, H. Tran, V.G. Tyuterev, E.M. Adkins, A. Baker, A. Barbe, E. Canè, A.G. Császár, A. Dudaryonok, O. Egorov, A.J. Fleisher, H. Fleurbaey, A. Foltynowicz, T. Furtenbacher, J.J. Harrison, J.–M. Hartmann, V.–M. Horneman, X. Huang, T. Karman, J. Karns, S. Kassi, I. Kleiner, V. Kofman, F. Kwabia–Tchana, N.N. Lavrentieva, T.J. Lee, D.A. Long, A.A. Lukashevskaya, O.M. Lyulin, V.Yu. Makhnev, W. Matt, S.T. Massie, M. Melosso, S.N. Mikhailenko, D. Mondelain, H.S.P. Müller, O.V. Naumenko, A. Perrin, O.L. Polyansky, E. Raddaoui, P.L. Raston, Z.D. Reed, M. Rey, C. Richard, R. Tóbiás, I. Sadiek, D.W. Schwenke, E. Starikova, K. Sung, F. Tamassia, S.A. Tashkun, J. Vander Auwera, I.A. Vasilenko, A.A. Vigasin, G.L. Villanueva, B. Vispoel, G. Wagner, A. Yachmenev, and S.N. Yurchenko, The HITRAN2020 molecular spectroscopic database, J. Quant. Spectrosc. Radiat. Transfer, 277, 107949, https://doi.org/10.1016/j.jqsrt.2021.107949, 2022.

[5] Hess, M., P. Koepke, and I. Schult, 1999: Optical properties of aerosols and clouds: the software package OPAC, *B. Am. Meteorol. Soc.*, **79**, 831–844

[6] Kudo, R., T. Nishizawa, and T. Aoyagi, 2016: Vertical profiles of aerosol optical properties and the solar heating rate estimated by combining sky radiometer and lidar measurements, *Atmos. Meas. Tech.*, **9**, 3223–3243, doi:10.5194/amt-9-3223-2016

[7] Lacis, A. A., and V. A. Oinas, 1991: Description if the correlated k-distribution method for modeling nongray gaseous absorption, thermal emission, and multiple scattering in vertically inhomogeneous atmospheres, *J. Geophys. Res.*, **96**, 9027–9063.

[8] Mlawer, E.J., V.H. Payne, J. Moncet, J. S. Delamere, M.J. Alvarado and D.C. Tobin, 2012: Development and recent evaluation of the MT_CKD model of continuum

absorption, *Phil. Trans. R. Soc. A*, **370**, 2520–2556, https://doi.org/10.1098/rsta.2011.0295

[9] Momoi, M., R. Kudo, K. Aoki, T. Mori, K. Miura, H. Okamoto, H. Irie, Y. Shoji, A. Uchiyama, O. Ijima, M. Takano, and T. Nakajima, Development of on-site self-calibration and retrieval methods for sky-radiometer observations of precipitable water vapor, Atmos. Meas. Tech., 13, 2635–2658, https://doi.org/10.5194/amt-13-2635-2020, 2020.

[10] Momoi, M., H. Irie, M. Sekiguchi, T. Nakajima, H. Takenaka, K. Miura, and K. Aoki, Rapid, accurate computation of narrow-band sky radiance in the 940 nm gas absorption region using the correlated *k*-distribution method for sun-photometer observations, Prog. Earth Planet. Sci., 9, 10, https://doi.org/10.1186/s40645-022-00467-6, 2022.

[11] Torres, B., O. Duvobik, C. Toledano, A. Berjon, V. E. Cachorro, T. Lapyonok, P. Litvinov, and P. Goloub, 2014: Sensitivity of aerosol retrieval to geometrical configuration of ground-based sun/sky radiometer observation, *Atmos. Chem. Phys.*, **14**, 847-875

Chapter 6: Application to the ground-based angular-scanning radiometer observation

Chapters 4 and 5 developed an efficient calculation method (P^n-IMS) and an optimized gas absorption table (WV-CKD). These studies aim to apply the method to the analysis of the ground-based angular-scanning radiometer observation network, especially in the SKYNET (Nakajima et al. [2020]). This section installs these methods on the analysis programs (SKYMAP and DSRAD) developed by Momoi et al. [2020] and investigates their effects. The contents of this chapter are based on the papers of Momoi et al. [2020; 2022a; 2022b], as mentioned in each section.

6.1. Sky-radiometer and SKYNET

6.1.1. Sky-radiometer

This chapter mainly uses a sky-radiometer manufactured by Prede Co., Ltd. (Japan). Several types are launched for user requests, *e.g.*, POM-01MKII & MKIII (ship), POM-01 (land), and POM-02 (land) (Fig. 6.1). As discussed in Chapter 1, the SKYNET has deployed a sky-radiometer at 100 sites or more globally for the aerosol-cloud-radiation interaction research. The sky-radiometer measures $\tilde{F}_{\mathrm{ds}}$ every 1 min, and $\tilde{F}_{\mathrm{df}}$ (Eqs. 2.60a-b) at scattering angles Θ = 2 (1) 5, 7, 10 (5) 30 (10) 160° in the almucantar and principal planes (Fig. 6.2) every 10 min.

(a) POM-01MKII

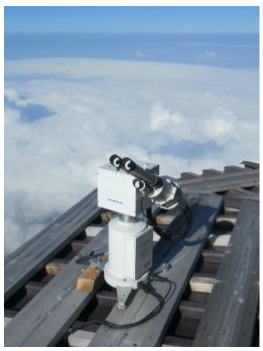

(b) POM-02

Figure 6.1: Sky-radiometer

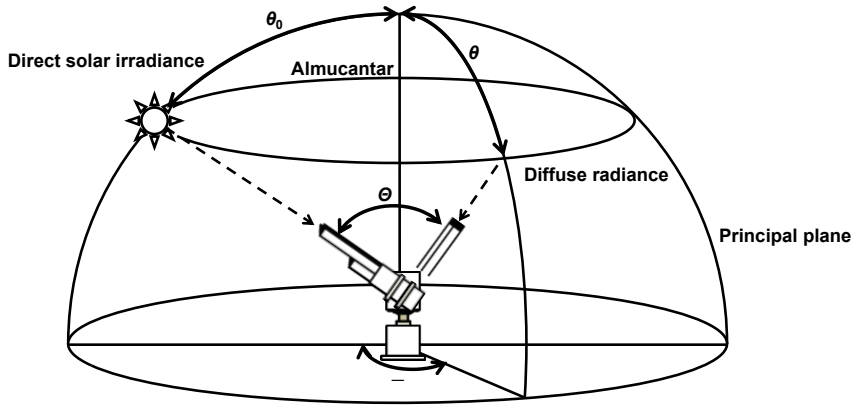

Figure 6.2: Observation planes (almucantar and principal planes) of the sky-radiometer.

6.1.2. Analysis program used in the SKYNET framework

Several programs have been developed for the sky-radiometer observation data (Nakajima et al. [1996]; Kobayashi et al. [2006; 2010]; Hashimoto et al. [2012]; Kudo et al. [2016]). Those programs estimate aerosol optical and microphysical properties from the transmittance of the direct incident beam and angular distribution of the normalized radiance at aerosol channels. Recently, Momoi et al. [2020] proposed a new algorithm named SKYMAP to estimate PWV from the angular distribution of the diffuse radiances at the water vapor channel in addition to aerosol optical and microphysical properties. Moreover, Kudo et al. [2021] tried to estimate columnar ozone amount from sky radiances at 315 nm.

The international SKYNET, the international observational network of the sky-radiometer, is organized in 7 regional sub-networks, including China, Europe, India, Japan, Korea, Mongolia, and Southeast Asia. These sub-networks have managed their observation sites and data processing flow (Nakajima et al. [2020]). The international SKYNET has International SKYNET Data Center (ISDC; https://www.skynet-isdc.org) managed by National Institute for Environmental Studies (NIES), which plays the standard sky-radiometer data analysis and data accumulation from sub-networks. The ISDC recently implemented 2 data flows developed by the European SKYNET radiometers network (ESR) and Center for Environmental Remote Sensing (CEReS). These flows are based on the SKYRAD.pack: the ESR flow uses version 4.2 (V42; Nakajima et al. [1996]); the CEReS flow (SR-CEReS; Irie et al. [2019]) mainly uses version 5.0 (V50; Hashimoto et al. [2012]). Moreover, the ESR uses SKYRAD.pack MRI version 2.0 (Kudo et al. [2021]) for aerosol estimations from sky radiances at aerosol channels.

Table 6.1 summarizes the feature of the V42 and V50. Both programs use the same

scalar RTM (RSTAR6; Nakajima and Tanaka [1986]) with the IMS method (Nakajima and Tanaka [1988]) under homogeneous single layer assumption. However, the inversion constraint has the difference between smoothness constraint (or Tikhonov regularization) and a priori constraint (or L2 regularization).

Table 6.1: Analysis programs. SDF, CR, NS-ratio, PWV are size distribution, complex refractive index, non-spherical ratio, and precipitable water vapor

	SKYRAD.pack Version 4.2	SKYRAD.pack Version 5.0	SKYMAP version 2.0
Reference	Nakajima et al. [1996]	Hashimoto et al. [2012]	**MK20, MI22a, and MI22b**
Distributor	OpenCLASTR		First author upon request
Estimation parameter	SDF and CR		SDF, CR, NS-ratio, and PWV
LSM solver	Gauss-Newton		Gauss-Newton
Regularization	Smoothness constraint (Tikhonov reg.)	A priori constraint (L2 reg.)	Smoothness constraint (Tikhonov reg. + **MK20**)
RTM	RSTAR6 (NT86)		RpSTAR7 (NT86, OH10)
RTM type	Scalar (unpolarized radiance)		Scalar/Vector
Aureole correction	IMS (NT88)		**P^{3}IMS (MI22a)**
Solar irradiance	*Not used*		Thuillier+03, Coddington+21
Convoluted function	Monochromatic		Multiple stepwise functions
Aerosol shape	Sphere		Sphere + Spheroid (DS06)
Gas absorption	O_3 continuum		**H_2O**, CO_2, O_3, N_2O, CO, CH_4, and O_2 (RSTAR; **MI22b**)
Vertical profile	Single layer		Multi layers up to 50

DS06: Dubovik et al. [2006]
NT86: Nakajima and Tanaka [1986]
NT88: Nakajima and Tanaka [1988]
OH10: Ota et al. [2010]
MK20: Momoi et al. [2020]
MI22a: Momoi et al. [2022a]
MI22b: Momoi et al. [2022b]

6.2. Algorithm of aerosols and PWV estimations from angular distributions: SKYMAP version 2.0

SKYMAP program was developed for PWV estimation from the angular distribution of the normalized radiances of the sky-radiometer observation by Momoi et al. [2020]. This section provides detailed information about the SKYMAP and its procedure, which is based on the papers of Momoi et al. [2020; 2022a; 2022b].

6.2.1. Covariance matrix of the measurement

This section is based on the paper of Momoi et al. [2022b]. The sky-radiometer measures $\tilde{T}$ and $\tilde{R}$. The variances of $\ln\tilde{T}$ and $\ln\tilde{R}_i$ $(i \in \mathbb{N})$ are expressed under the assumption that $\tilde{F}_{\mathrm{ds}}$, $\tilde{F}_{\mathrm{df}}$, and $\tilde{F}_0$ are independent of each other as follows:

$$\mathrm{Var}\left(\ln\tilde{T}\right) = \mathrm{Var}\left(\ln\tilde{F}_{\mathrm{ds}} - \ln\tilde{F}_0\right) = \sigma_{F_{\mathrm{ds}}}^2 + \sigma_{F_0}^2, \tag{6.1a}$$

$$\mathrm{Var}\left(\ln\tilde{R}_i\right) = \mathrm{Var}\left(\ln\tilde{F}_{\mathrm{df}} - \ln\tilde{F}_{\mathrm{ds}}\right) = \sigma_{F_{\mathrm{df}}}^2 + \sigma_{F_{\mathrm{ds}}}^2, \tag{6.1b}$$

where $\mathrm{Var}(a)$ is the variance of a; σ_{F_0} is the standard deviation of the sky-radiometer calibration constant; $\sigma_{F_{\mathrm{ds}}}$ and $\sigma_{F_{\mathrm{df}}}$ are the standard deviations of sky-radiometer measurements ($\ln F_{\mathrm{ds}}$ and $\ln F_{\mathrm{df}}$, respectively). Note that $\tilde{F}_{\mathrm{ds}}$ and $\tilde{F}_{\mathrm{df}}$ assume independence in each other. The covariance of $\ln\tilde{T}$ with $\ln\tilde{R}_i$ and normalized radiances of each scattering angle, $\ln\tilde{R}_i$ and $\ln\tilde{R}_j$ $(i \neq j \in \mathbb{N})$, are not zeros because $\tilde{R}$ are the ratio of $\tilde{F}_{\mathrm{df}}$ to $\tilde{F}_{\mathrm{ds}}$ and obtained as follows:

$$\mathrm{Cov}\left(\ln\tilde{T}, \ln\tilde{R}_i\right) = -\sigma_{F_{\mathrm{ds}}}^2, \tag{6.2a}$$

$$\mathrm{Cov}\left(\ln\tilde{R}_i, \ln\tilde{R}_j\right) = \sigma_{F_{\mathrm{ds}}}^2, \tag{6.2b}$$

where $\mathrm{Cov}(a, b)$ is the covariance between a and b.

In this study, we estimate $\sigma_{F_{\mathrm{ds}}}$ from the circumsolar domain of $\pm1^{\mathrm{o}}$ by $\pm1^{\mathrm{o}}$ around the sun at every 0.1^{o} interval for the calibration of the solid view angle by the solar disk scan method (Nakajima et al. [1996; 2020]; Boi et al. [1999]; Uchiyama et al. [2018b]). The solar disk scan method provides a solar aureole angular distribution for the radiometer (Fig 6.3), which reduces observational noise with a Gaussian filter. Therefore, the uncertainty of the direct solar irradiances $\sigma_{F_{\mathrm{ds}}}$ is calculated from the difference (Δ_f) of aureole irradiances based on observational and Gaussian-filtered data, as follows:

$$\Delta_f = \ln f^{\mathrm{obs}} - \ln f^{\mathrm{gf}}, \tag{6.3}$$

where f^{obs} and f^{gf} are the observational and Gaussian-filtered aureole irradiances, respectively. Because the magnitude of the solar aureole angular distribution differs at large scattering angles ($\Theta \geq 0.3^{\mathrm{o}}$), we used a range of 0.3°. Figure 6.4 shows an example histogram of the differences at 340, 500, and 940 nm using sky-radiometer POM-02 (S/N PS2501401) measurements on February 27th and 28th, 2020 in Akiruno, Tokyo (35.751N, 139.323E). Table

6.2 lists the uncertainties of $\tilde{F}_{\mathrm{ds}}$ and indicates that the standard deviation of sky-radiometer measurements ($\sigma_{F_{\mathrm{ds}}}$) at all wavelengths is less than 5.0×10^{-3}. Then, $\sigma_{F_{\mathrm{ds}}}$ has a larger value than $\sigma_{F_{\mathrm{ds}}}$ because $\tilde{F}_{\mathrm{ds}}$ and $\tilde{F}_{\mathrm{df}}$ are measured with the same detector, but $\tilde{F}_{\mathrm{ds}} \gg \tilde{F}_{\mathrm{df}}$ by aerosol anisotropic phase function. Therefore, we treat the uncertainty of sky-radiometer measurements in the diffuse radiances as $\sigma_{F_{\mathrm{df}}}^2 = \sigma_{F_{\mathrm{ds}}}^2 + \sigma_{\mathrm{M}}^2$ where σ_{M}^2 are called the extra uncertainty and estimated from the result of the multi-term least square fitting described in the below section.

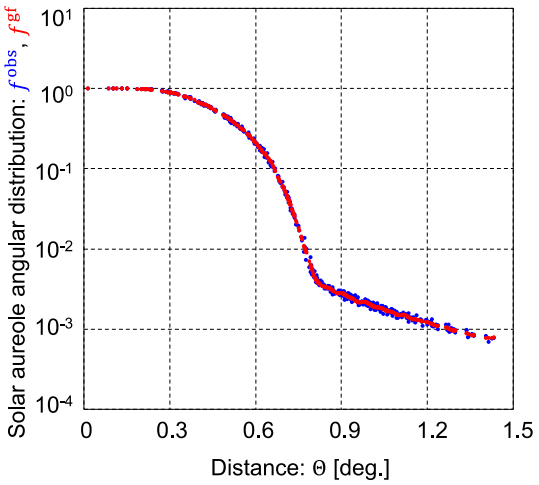

Figure 6.3: Example solar aureole angular distributions of the sky-radiometer at 500 nm obtained with the solar disk scan method on February 27, 2020 at Akiruno, Japan. Blue dots are measured values and red dots show the response function with noise reduction using a Gaussian filter.

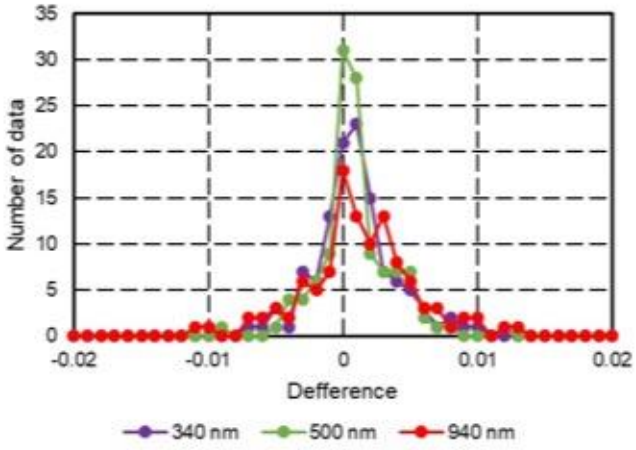

Figure 6.4: Example histogram of the differences at 340, 500, and 940 nm of the sky-radiometer measurements on February 27 and 28, 2020 in Akiruno, Japan.

Table 6.2: Uncertainty of $\widetilde{F}_{ds}$ based on a comparison between f^{obs} and f^{gf}

Wavelength	Num. of data	Standard deviation
315 nm	127	5.0×10^{-3}
340 nm	117	3.0×10^{-3}
380 nm	104	1.9×10^{-3}
400 nm	122	2.7×10^{-3}
500 nm	119	2.9×10^{-3}
675 nm	114	4.1×10^{-3}
870 nm	135	6.5×10^{-3}
1020 nm	105	4.3×10^{-3}
940 nm	110	4.3×10^{-3}
1627 nm	56	4.8×10^{-3}
2200 nm	57	4.4×10^{-3}

6.2.2. Forward model

The forward model of the SKYMAP consists of 3 models, including the aerosol scattering model (Section 6.2.2.1), gas absorption model (Section 6.2.2.2), and radiative transfer model (Section 6.2.2.3).

6.2.2.1. Aerosol optical and microphysical properties

This section is based on the paper of Momoi et al. [2020]. Aerosol volume size distribution assumes the homogeneous aerosol species and consists of 20-modal lognormal size distributions in the range from 0.02 to 20.0 μm (Nakajima et al. [1996]; Hashimoto et al. [2012]) illustrated in Fig. 6.5a as follows:

$$\frac{\mathrm{d}V(r)}{\mathrm{d}\ln r} = \sum_{k=1}^{20} C_k \exp\left[-\frac{1}{2}\left(\frac{\ln r - \ln r_k}{s}\right)^2\right], \tag{6.4a}$$

$$\ln r_k = \ln(0.02\mu\mathrm{m}) + \frac{2k-1}{2}\ln \Delta_r\,, \tag{6.4b}$$

$$\mathrm{s} \equiv \frac{\ln \Delta_r}{\eta}, \tag{6.4c}$$

$$\ln \Delta_r \equiv \frac{1}{20}(\ln(20\mu\text{m}) - \ln(0.02\mu\text{m})) = \frac{3}{20}\ln 10\,, \tag{6.4d}$$

where C_k, r_k, and s are volume, radius, and width of each lognormal distribution function; η is a parameter and fixed at 1.65. The η values affect the shape of the aerosol volume size distribution and the width of $\frac{\mathrm{d}V(r)}{\mathrm{d}\ln r}$ is larger than that of each lognormal size distribution s. The width of the lognormal size distribution should be small to deal with the complicated and step variations in $\frac{\mathrm{d}V(r)}{\mathrm{d}\ln r}$. However, $\frac{\mathrm{d}V(r)}{\mathrm{d}\ln r}$ cannot represent a natural curve if η is large and s is small (Fig. 6.5). Hence, we have to find the maximum value of η for making $\frac{\mathrm{d}V(r)}{\mathrm{d}\ln r}$ a natural curve. When C_k is constant, such value of η minimizes the roughness of $\frac{\mathrm{d}V(r)}{\mathrm{d}\ln r}$, and $\frac{\mathrm{d}V(r)}{\mathrm{d}\ln r}$ approaches to a flat shape. For a simple formulation, we consider the function $A(x)$ which consists of the multimodal normal distribution function B_i with a constant height. $A(x)$ and B_i are expressed as

$$A(x) = \sum_{k=-\infty}^{\infty} B_k(x) = \sum_{k=-\infty}^{\infty} \exp\left[-\frac{\eta^2}{2}\left(\frac{x-k\xi}{\xi}\right)^2\right], \tag{6.5}$$

where $k\xi$ and $\frac{\xi}{\eta}$ are the mean and standard deviation, respectively. Its differential is written as

$$\frac{dA}{dx} = \sum_{k=-\infty}^{\infty} \frac{dB_k}{dx} = \sum_{k=-\infty}^{\infty} -\eta^2\left(\frac{x-k\xi}{\xi}\right)\exp\left[-\frac{\eta^2}{2}\left(\frac{x-k\xi}{\xi}\right)^2\right]. \tag{6.6}$$

When the shape of $A(x)$ approaches to be flat, the difference between local maximum and minimum values of $A(x)$ is approximately 0. Because $\frac{dB_j}{dx}$ equals 0 at $x = j\xi$ $(j \in \mathbb{Z})$, $A(x)$ has the local maximum and minimum at $x = j\xi$ and $\left(j+\frac{1}{2}\right)\xi$ in $j \le \frac{x}{\xi} < j+1$. The difference Δ between the local maximum and minimum values is obtained as

$$\Delta = 1 - \frac{A\left(\frac{2j+1}{2}\xi\right)}{A(j\xi)}. \tag{6.7}$$

Figure 6.6 shows the relation between η and Δ. The value of Δ increases drastically at around $\eta = 1.5$. In addition, the shape of $\frac{\mathrm{d}V(r)}{\mathrm{dln}r}$ is unnatural when $\eta = 2.0$ (Fig. 6.5). Therefore, the value of η should be selected from the values around $\eta = 1.5$. In this study, we fixed η at 1.65. This value represents the natural curve of $\frac{\mathrm{d}V(r)}{\mathrm{dln}r}$ and satisfies that the value of Δ is small enough, $\Delta = 3.0 \times 10^{-3}$. Note that both V42 and V50 use $\eta \approx 0.863$ (or $s = 0.4$).

In this study, the aerosol consists of spherical and spheroid particles. The spheroid particles used here were the kernels developed by Dubovik et al. [2006], with an aspect ratio set at 0.6, representing the yellow sand particles reported by Nakajima et al. [1989]. The phase matrix is expressed as follows:

$$\tau_{\mathrm{ext}}(\lambda) = \sum_k C_k[(1-\beta)K_{\mathrm{ext}}^{\mathrm{S}}(\lambda, m_{\mathrm{Re}}, m_{\mathrm{Im}}, r_k) + \beta K_{\mathrm{ext}}^{\mathrm{NS}}(\lambda, m_{\mathrm{Re}}, m_{\mathrm{Im}}, r_k)], \tag{6.8a}$$

$$\tau_{\mathrm{sca}}(\lambda)\mathbf{P}(\Theta, \lambda) = \sum_k C_k[(1-\beta)\mathbf{K}^{\mathrm{S}}(\Theta, \lambda, m_{\mathrm{Re}}, m_{\mathrm{Im}}, r_k) + \beta \mathbf{K}^{\mathrm{NS}}(\Theta, \lambda, m_{\mathrm{Re}}, m_{\mathrm{Im}}, r_k)], \tag{6.8b}$$

where $\tau_{\mathrm{ext/sca}}$ is the optical thickness of extinction and scattering; β is the fraction of the non-spherical particles; $\mathbf{K}^{\mathrm{S}}$ and $\mathbf{K}^{\mathrm{NS}}$ are the scattering kernels for spherical and non-spherical particles, respectively; $K_{\mathrm{ext}}^{\mathrm{S}}$ and $K_{\mathrm{ext}}^{\mathrm{NS}}$ are the kernels of extinction properties for spherical and non-spherical particles, respectively; m_{Re} and m_{Im} are the real and imaginary parts of the refractive index, respectively.

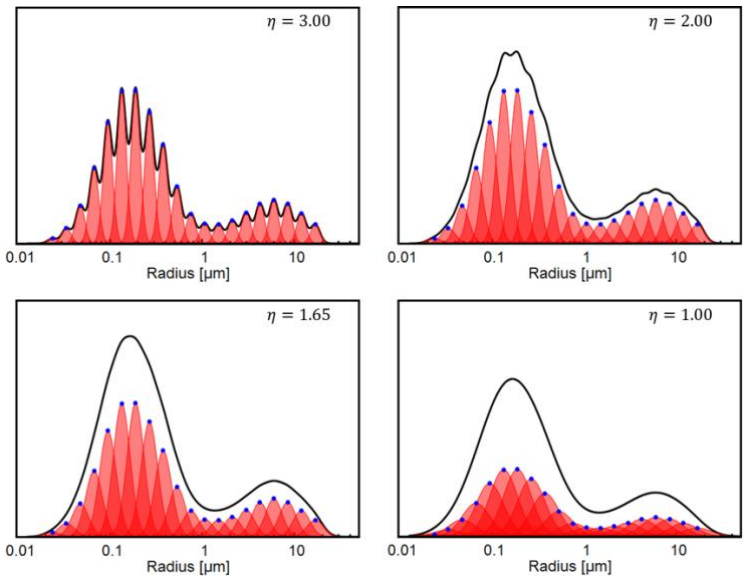

Figure 6.5: Relationship between the volume size distribution and η. The black line is the volume size distribution, which is computed by integrating 20-modal lognormal distribution functions (red lines). Blue circles are the peak volume of lognormal size distribution.

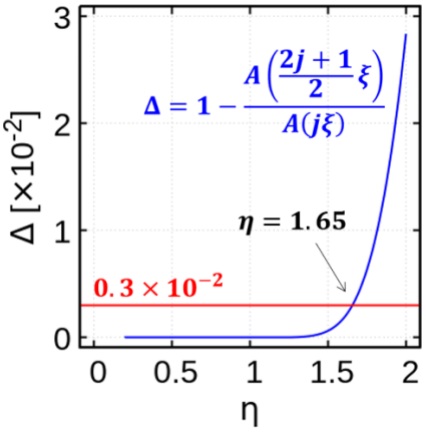

Figure 6.6: Relationship between the parameter η and the difference Δ.

6.2.2.2. Gas absorption

This section is based on the paper of Momoi et al. [2022b]. Gas absorptions are calculated with the CKD method (Lacis and Oinas [1991]; Fu and Liou [1992]) using the SN-CKD at the aerosol channels and the WV-CKD (Chapter 5) at the water vapor channel. Those specifications are described in Chapter 5.

6.2.2.3. Radiative transfer model

This section is based on the paper of Momoi et al. [2022a]. $\tilde{T}$ and $\tilde{R}$ are computed from the aerosol optical and microphysical properties and gas absorptions using the RTM. The SKYMAP version 2.0 uses a new code RpSTAR7 (Nakajima and Tanaka [1986; 1988]; Sekiguchi and Nakajima [2008]; Ota et al. [2010]; Momoi et al. [2022a]) which has scalar and full-vector modes with the P^n-IMS methods (see Chapter 4).

6.2.3. Inversion scheme with the multi-term least square fitting

This section is based on the papers of Momoi et al. [2020; 2022b]. It is an inverse problem to solve the aerosol properties and PWV from sky irradiances. The estimate parameters consisting of the volume size distribution and complex refractive index are estimated by minimizing the cost function $G(\boldsymbol{X})$ with the iteration by the Gauss-Newton method as follows:

$$G(\boldsymbol{X}) = (\boldsymbol{Y}_{\mathrm{o}}^{\mathrm{M}} - \boldsymbol{Y}_{\mathrm{o}}^{\mathrm{R}})^{\mathrm{T}} \mathbf{S}_{\mathrm{o}}^{-1} (\boldsymbol{Y}_{\mathrm{o}}^{\mathrm{M}} - \boldsymbol{Y}_{\mathrm{o}}^{\mathrm{R}}) + \boldsymbol{Y}_{\mathrm{a}}{}^{\mathrm{T}} \mathbf{S}_{\mathrm{a}}^{-1} \boldsymbol{Y}_{\mathrm{a}}, \tag{6.9a}$$

$$\boldsymbol{X}_{j+1} = \boldsymbol{X}_j + \left(\mathbf{K}_{\mathrm{o}}{}^{\mathrm{T}} \mathbf{S}_{\mathrm{o}}^{-1} \mathbf{K}_{\mathrm{o}} + \mathbf{K}_{\mathrm{a}}{}^{\mathrm{T}} \mathbf{S}_{\mathrm{a}}^{-1} \mathbf{K}_{\mathrm{a}}\right)^{-1} \left[\mathbf{K}_{\mathrm{o}}{}^{\mathrm{T}} \mathbf{S}_{\mathrm{o}}^{-1} (\boldsymbol{Y}_{\mathrm{o}}^{\mathrm{M}} - \boldsymbol{Y}_{\mathrm{o}}^{\mathrm{R}}) - \mathbf{K}_{\mathrm{a}}{}^{\mathrm{T}} \mathbf{S}_{\mathrm{a}}^{-1} \boldsymbol{Y}_{\mathrm{a}}\right], \tag{6.9b}$$

where $\boldsymbol{Y}_{\mathrm{o}}^{\mathrm{M}}$ and $\boldsymbol{Y}_{\mathrm{a}}$, respectively, measurement and constraint vectors; $\boldsymbol{Y}_{\mathrm{o}}^{\mathrm{R}}$ are vector corresponding to $\boldsymbol{Y}_{\mathrm{o}}^{\mathrm{M}}$ calculated by the forward model (Section 6.2.2); $\mathbf{K}_{\mathrm{o}}$ and $\mathbf{K}_{\mathrm{a}}$ are Jacobian matrixes; $\mathbf{S}_{\mathrm{o}}$ and $\mathbf{S}_{\mathrm{a}}$ are covariance matrixes; $\boldsymbol{X}_j$ is the state vector at j-th iteration which consists estimate parameters. The state vector is defined as:

$$\boldsymbol{X}_j = \left(\ln C_1, \cdots, \ln C_{20}, \ln \beta, \ln m_{\mathrm{Re},1}, \cdots, \ln m_{\mathrm{Re},N_{\mathrm{w}}}, \ln m_{\mathrm{Im},1}, \cdots, \ln m_{\mathrm{Im},N_{\mathrm{w}}}, w\right)^{\mathrm{T}}, \tag{6.10}$$

where N_{w} is the number of wavelengths.

The vector $\boldsymbol{Y}_{\mathrm{o}}$ and covariance matrix $\mathbf{S}_{\mathrm{o}}$ is defined as

$$\boldsymbol{Y}_{\mathrm{o}} = \begin{pmatrix} \boldsymbol{Y}_{\mathrm{o}}^{(1)} \\ \vdots \\ \boldsymbol{Y}_{\mathrm{o}}^{(N_{\mathrm{w}})} \end{pmatrix}, \tag{6.11a}$$

$$\mathbf{S}_{\mathrm{o}} = \begin{pmatrix} \mathbf{S}_{\mathrm{o}}^{(1)} & 0 & 0 \\ 0 & \ddots & 0 \\ 0 & 0 & \mathbf{S}_{\mathrm{o}}^{(N_{\mathrm{w}})} \end{pmatrix}, \tag{6.11b}$$

where $\boldsymbol{Y}_{\mathrm{o}}^{(j)}$ and $\mathbf{S}_{\mathrm{o}}^{(j)}$ are, respectively, the j-th wavelength measurement vector and covariance matrix. The vector $\boldsymbol{Y}_{\mathrm{o}}^{(j)}$ and matrix $\mathbf{S}_{\mathrm{o}}^{(j)}$ are expressed as:

$$\boldsymbol{Y}_{\mathrm{o}}^{(i)} = \left(\ln \tilde{T}, \ln \tilde{R}_1, \cdots, \ln \tilde{R}_{N_{\mathrm{s}}}\right)^{\mathrm{T}} \quad (i = 1, \cdots, N_{\mathrm{w}}), \tag{6.12a}$$

$$\mathbf{S}_{\mathrm{o}}^{(j)} = \begin{pmatrix} \sigma_{F_0}^2 + \sigma_{F_{\mathrm{ds}}}^2 & -\sigma_{F_{\mathrm{ds}}}^2 & \cdots & -\sigma_{F_{\mathrm{ds}}}^2 & -\sigma_{F_{\mathrm{ds}}}^2 \\ -\sigma_{F_{\mathrm{ds}}}^2 & 2\sigma_{F_{\mathrm{ds}}}^2 + \sigma_{\mathrm{M}}^2 & & \sigma_{F_{\mathrm{ds}}}^2 & \sigma_{F_{\mathrm{ds}}}^2 \\ \vdots & & \ddots & & \vdots \\ -\sigma_{F_{\mathrm{ds}}}^2 & \sigma_{F_{\mathrm{ds}}}^2 & & 2\sigma_{F_{\mathrm{ds}}}^2 + \sigma_{\mathrm{M}}^2 & \sigma_{F_{\mathrm{ds}}}^2 \\ -\sigma_{F_{\mathrm{ds}}}^2 & \sigma_{F_{\mathrm{ds}}}^2 & \cdots & \sigma_{F_{\mathrm{ds}}}^2 & 2\sigma_{F_{\mathrm{ds}}}^2 + \sigma_{\mathrm{M}}^2 \end{pmatrix} \quad (j = 1, \cdots, N_{\mathrm{w}}). \tag{6.12b}$$

To conduct stable analysis, $\boldsymbol{Y}_{\mathrm{a}}$ is introduced to constraint (or regularization), which consists of the smoothness constraint of the second derivatives for the complex refractive index and for the adjacent volume size spectrum similar as previous studies (Nakajima et al. [1996]; Dubovik and King [2000]) as follows:

$$y_{\mathrm{a}}^{\mathrm{Re},j} = \left(\frac{\ln m_{\mathrm{Re},j} - \ln m_{\mathrm{Re},j+1}}{\ln \lambda_j - \ln \lambda_{j+1}} - \frac{\ln m_{\mathrm{Re},j+1} - \ln m_{\mathrm{Re},j+2}}{\ln \lambda_{j+1} - \ln \lambda_{j+2}} \right) \quad (j = 1, \cdots, N_w - 2), \tag{6.13a}$$

$$y_{\mathrm{a}}^{\mathrm{Im},j} = \left(\frac{\ln m_{\mathrm{Im},j} - \ln m_{\mathrm{Im},j+1}}{\ln \lambda_j - \ln \lambda_{j+1}} - \frac{\ln m_{\mathrm{Im},j+1} - \ln m_{\mathrm{Im},j+2}}{\ln \lambda_{j+1} - \ln \lambda_{j+2}} \right) \quad (j = 1, \cdots, N_w - 2), \tag{6.13b}$$

$$y_{\mathrm{a}}^{\mathrm{Vol},k} = (\ln C_{k-1} - \ln C_k) - (\ln C_k - \ln C_{k+1}) \quad (k = 1, \cdots, 20), \tag{6.14a}$$

$$C_0 \equiv 0.01 \times \min\{C_k | k = 1, \cdots, 20\}, \tag{6.14b}$$

$$C_{21} \equiv 0.01 \times \min\{C_k | r_k > r_b, k = 1, \cdots, 20\}, \tag{6.14c}$$

where $y_{\mathrm{a}}^{\mathrm{Re},j}$, $y_{\mathrm{a}}^{\mathrm{Im},j}$, and $y_{\mathrm{a}}^{\mathrm{Vol},k}$ are, respectively, constraints of wavelength dependence of refractive index (real and imaginary parts), and smoothness of volume size spectrum. Therefore, total constraint vector $\boldsymbol{Y}_{\mathrm{a}}$ is described using $\boldsymbol{Y}_{\mathrm{Re}}(\equiv \{y_{\mathrm{a}}^{\mathrm{Re},j}\})$, $\boldsymbol{Y}_{\mathrm{Im}}(\equiv \{y_{\mathrm{a}}^{\mathrm{Im},j}\})$,

and $\boldsymbol{Y}_{\mathrm{Vol}}(\equiv \{y_{\mathrm{a}}^{\mathrm{Vol},k}\})$ as:

$$\boldsymbol{Y}_{\mathrm{a}} = \begin{pmatrix} \boldsymbol{Y}_{\mathrm{Re}} \\ \boldsymbol{Y}_{\mathrm{Im}} \\ \boldsymbol{Y}_{\mathrm{Vol}} \end{pmatrix}, \tag{6.15a}$$

and corresponded covariance matrix $\mathbf{S}_{\mathrm{a}}$ is expressed as:

$$\mathbf{S}_{\mathrm{a}} = \begin{pmatrix} \mathbf{S}_{\mathrm{Re}} & 0 & 0 \\ 0 & \mathbf{S}_{\mathrm{Im}} & 0 \\ 0 & 0 & \mathbf{S}_{\mathrm{Vol}} \end{pmatrix}, \tag{6.15b}$$

where $\mathbf{S}_{\mathrm{Re}}$, $\mathbf{S}_{\mathrm{Im}}$, and $\mathbf{S}_{\mathrm{Vol}}$ correspond to $\boldsymbol{Y}_{\mathrm{Re}}$, $\boldsymbol{Y}_{\mathrm{Im}}$, and $\boldsymbol{Y}_{\mathrm{Vol}}$ and the diagonal elements of $\mathbf{S}_{\mathrm{Re}}$, $\mathbf{S}_{\mathrm{Im}}$, and $\mathbf{S}_{\mathrm{Vol}}$ are, respectively, 0.2, 1.25, and 1.6.

By the error propagation from measurement vector to state vector, the covariance matrix of the state vector $\mathbf{S}_{\mathrm{x}}$ is given as

$$\mathbf{S}_{\mathrm{x}}^{-1} = \mathbf{K}_{\mathrm{o}}{}^{\mathrm{T}}\mathbf{S}_{\mathrm{o}}^{-1}\mathbf{K}_{\mathrm{o}} + \mathbf{K}_{\mathrm{a}}{}^{\mathrm{T}}\mathbf{S}_{\mathrm{a}}^{-1}\mathbf{K}_{\mathrm{a}}, \tag{6.16}$$

Eq. (6.16) suggests the uncertainty of the state vector can be estimated if the extra uncertainty σ_{M}^2 is known.

6.2.4. Procedure of the sky-radiometer data analysis with SKYMAP package

The SKYNET developed the procedure of the sky-radiometer analysis consisting of 5 steps (Fig. 6.7; Momoi et al. [2020]; Nakajima et al. [2020]): (1) Level-1 analysis, (2) aerosol channel calibration, (3) Level-2 analysis, (4) WV analysis, and (5) water vapor channel calibration. Step 1 to 3 is the standard procedure in the SKYNET (Nakajima et al. [2020]) and step 3 to 5 is the on-site self-calibration procedure at the water vapor channel (Momoi et al. [2020]). The Level-1 analysis estimates the scattering part of the aerosol optical thickness from estimating volume spectrums assumed the complex refractive index using normalized radiances around the aureole region at aerosol channels, which does not require the calibration constant. After estimating the scattering aerosol optical thickness during the observational period, the calibration constant at aerosol channels is calculated with the on-site self-calibration method, *e.g.*, the Improved Langley method (IL method; Nakajima et al. [1996]; Campanelli et al. [2004; 2007]; Uchiyama et al. [2018a]) and the cross Improved Langley

method (XIL method; Nakajima et al. [2020]). Then, aerosol properties at aerosol channels are retrieved from the transmittance of the direct solar irradiance and the angular distribution of the normalized radiance at aerosol channels (Level-2 analysis). By interpolating the aerosol properties at the water vapor channel, the precipitable water vapor is retrieved from the angular distribution of the normalized radiance at the water vapor channel (WV analysis) proposed in Momoi et al. [2020]. Finally, the calibration constant at the water vapor channel is estimated by the procedure of Momoi et al. [2020]. This section shows the detail of each process and the error propagation.

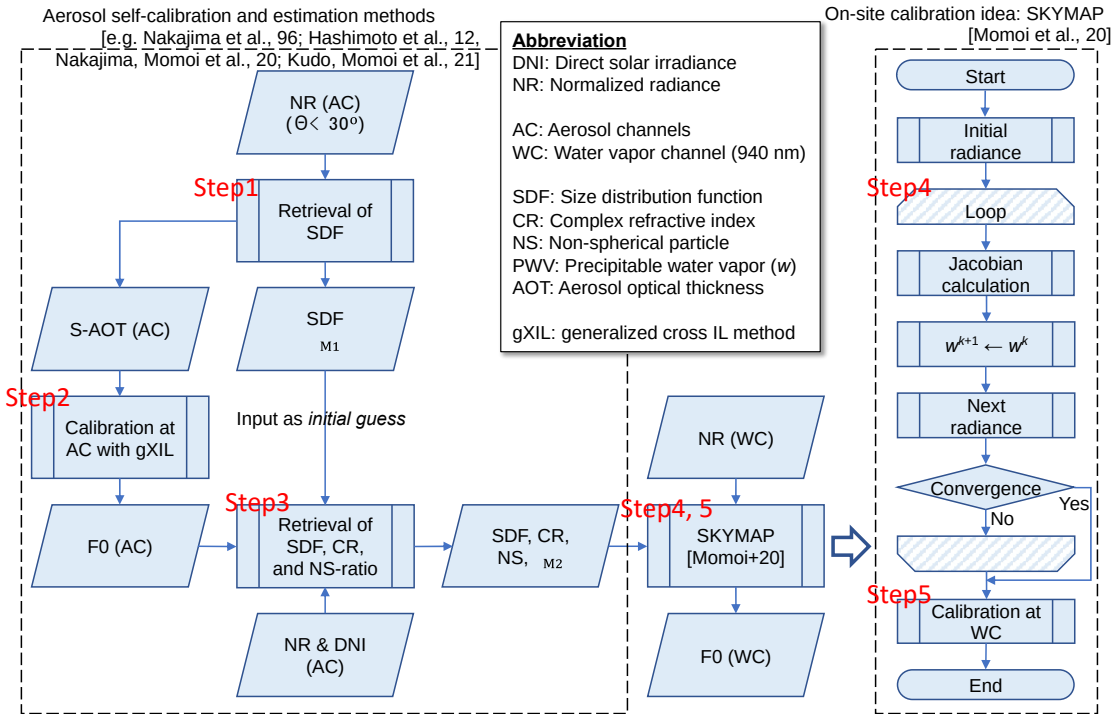

Figure 6.7: Diagram of the SKYMAP package.

6.2.4.1.Level-1 analysis

The covariance matrix of the estimate parameters in each process is propagated from the previous step and observational errors, but the extra uncertainty is unknown. Therefore, we estimate it from the residual errors of the multi-term least square fitting in the Level-1 analysis.

In the Level-1 analysis, the state vector of Eq. (6.12a) is only size distribution functions ($\boldsymbol{X}_j = [\ln C_1, \cdots, \ln C_{20}]^{\mathrm{T}}$). The observational vector consists of $\tilde{R}$ in the aerosol region ($\Theta \leq 30^{\mathrm{o}}$) at aerosol channels. The covariance matrix is, therefore, given as

$$\mathbf{S}_{\mathrm{o}}^{(j)} = \begin{pmatrix} 2\sigma_{F_{\mathrm{ds}}}^2 + \sigma_{\mathrm{M1}}^2 & \cdots & \sigma_{F_{\mathrm{ds}}}^2 & \sigma_{F_{\mathrm{ds}}}^2 \\ \sigma_{F_{\mathrm{ds}}}^2 & & \sigma_{F_{\mathrm{ds}}}^2 & \sigma_{F_{\mathrm{ds}}}^2 \\ \vdots & & & \vdots \\ \sigma_{F_{\mathrm{ds}}}^2 & \cdots & \sigma_{F_{\mathrm{ds}}}^2 & 2\sigma_{F_{\mathrm{ds}}}^2 + \sigma_{\mathrm{M1}}^2 \end{pmatrix} \quad (j = 1,\cdots, N_{\mathrm{w}}). \tag{6.17}$$

and the inverse matrix as follows:

$$\left[\mathbf{S}_{\mathrm{o}}^{(j)}\right]^{-1} = \left(\sigma_{F_{\mathrm{ds}}}^2 + \sigma_{\mathrm{M1}}^2\right)^{-1}\left[\mathbf{E}_{N_{\mathrm{s}}} - \frac{\sigma_{F_{\mathrm{ds}}}^2}{(N_{\mathrm{s}}+1)\sigma_{F_{\mathrm{ds}}}^2 + \sigma_{\mathrm{M1}}^2}\boldsymbol{v}_{\mathrm{L1}}\boldsymbol{v}_{\mathrm{L1}}^{\mathrm{T}}\right] \quad (j = 1,\cdots, N_{\mathrm{w}}), \tag{6.18a}$$

where N_{s} is the number of scattering angle; $\mathbf{E}_{N_{\mathrm{s}}}$ is the unit matrix ($\in \mathbb{R}^{N_{\mathrm{s}}\times N_{\mathrm{s}}}$);

$$\boldsymbol{v}_{\mathrm{L1}} \equiv (1,1,\cdots,1)^{\mathrm{T}} \in \mathbb{R}^{N_{\mathrm{s}}}. \tag{6.18b}$$

Now, the cost function $G_{\mathrm{o}}^{(j)}(\boldsymbol{X})$ of the measurement vector is defined as:

$$G_{\mathrm{o}}^{(j)}(\boldsymbol{X}) = \left[\boldsymbol{Y}_{\mathrm{o}}^{\mathrm{M}(j)} - \boldsymbol{Y}_{\mathrm{o}}^{\mathrm{R}(j)}\right]^{\mathrm{T}}\left[\mathbf{S}_{\mathrm{o}}^{(j)}\right]^{-1}\left[\boldsymbol{Y}_{\mathrm{o}}^{\mathrm{M}(j)} - \boldsymbol{Y}_{\mathrm{o}}^{\mathrm{R}(j)}\right] \quad (j = 1,\cdots, N_{\mathrm{w}}). \tag{6.19a}$$

Hence,

$$G(\boldsymbol{X}) = \sum_{j=1}^{N_{\mathrm{w}}} G_{\mathrm{o}}^{(j)}(\boldsymbol{X}) + \boldsymbol{Y}_{\mathrm{a}}{}^{\mathrm{T}}\mathbf{S}_{\mathrm{a}}^{-1}\boldsymbol{Y}_{\mathrm{a}}, \tag{6.19b}$$

Using Eq. (6.18), $G_{\mathrm{o}}^{(j)}(\boldsymbol{X})$ is expressed as:

$$G_{\mathrm{o}}^{(j)}(\boldsymbol{X}) = \frac{1}{\sigma_{F_{\mathrm{ds}}}^2 + \sigma_{\mathrm{M1}}^2}\left[\sum_{k}\epsilon_{k,j}^2 - \sum_{k,l}\frac{\sigma_{F_{\mathrm{ds}}}^2}{(N_{\mathrm{s}}+1)\sigma_{F_{\mathrm{ds}}}^2 + \sigma_{\mathrm{M1}}^2}\epsilon_{k,j}\epsilon_{l,j}\right] \quad (j = 1,\cdots, N_{\mathrm{w}}), \tag{6.20b}$$

where:

$$\boldsymbol{Y}_{\mathrm{o}}^{\mathrm{M}(j)} - \boldsymbol{Y}_{\mathrm{o}}^{\mathrm{R}(j)} = \left(\epsilon_{1,j}, \epsilon_{2,j},\cdots, \epsilon_{N_{\mathrm{s}},j}\right)^{\mathrm{T}} \in \mathbb{R}^{N_{\mathrm{s}}} \quad (j = 1,\cdots, N_{\mathrm{w}}), \tag{6.20c}$$

When $\sigma_{F_{\mathrm{ds}}}^2$ and σ_{M1}^2 are exact, $G_{\mathrm{o}}^{(j)}(\boldsymbol{X}) = N_{\mathrm{s}}$ (Kudo et al. [2021]). In other words, we can obtain σ_{M1}^2 from residuals $G_{\mathrm{o}}^{(j)}(\boldsymbol{X}) - N_{\mathrm{s}}$ as follows:

$$\left[\sigma_{\mathrm{M1}}^{(j)}\right]^2 = \frac{N_{\mathrm{s}}+1}{N_{\mathrm{s}}}\left[\frac{1}{N_{\mathrm{s}}}\left(G_{\mathrm{o}}^{(j)}\Big|_{\sigma_{\mathrm{M}}^2=0}\right) - 1\right]\sigma_{F_{\mathrm{ds}}}^2 \quad (j = 1,\cdots,N_{\mathrm{w}}). \tag{6.21}$$

However, in the above procedure, $\boldsymbol{Y}_{\mathrm{o}}^{\mathrm{R}(j)}$ is calculated from the state vector estimated with σ_{M1}^2 from Eq. (6.9). We converge σ_{M1}^2 (and $\boldsymbol{X}_\infty$) by iteration.

6.2.4.2. Calibration at aerosol channels with cross Improved Langley method using generalized least square method

Nakajima et al. [2020] proposed the XIL method. Traditionally, calibration is carried out under stable conditions by the standard Langley-plot (SL) method determining $\tilde{F}_0$ from the intercept of $m_0 - \ln\tilde{F}_{\mathrm{ds}}$ plot. It is a challenge to use the SL method at the observation site because the SL method regards $\tau = const.$ throughout the day. Nakajima et al. [1996] solved this issue by estimating τ_{sca} from $\tilde{R}(\Theta \le 30^{\mathrm{o}})$ and using $m_0\tau_{\mathrm{sca}} - \ln\tilde{F}_{\mathrm{ds}}$ plot. Recently, Nakajima et al. [2020] proposed the further improved version named XIL method treating $\ln\tilde{F}_{\mathrm{ds}} - m_0\tau_{\mathrm{sca}}$ plot because the uncertainty of estimation parameter is expected to be larger than that of $\ln\tilde{F}_{\mathrm{ds}}$. In this study, by Section 6.2.4.1 and Eq. (6.16), the covariance matrix of the state vector can be obtained. Thus, we determined $\tilde{F}_0$ with generalized least square fitting (gXIL method) as following formulations. First, regression of $\ln\tilde{F}_{\mathrm{ds}} - m_0\tau_{\mathrm{sca}}$ is defined as:

$$y = a_0 + a_1 x, \tag{6.22}$$

where $y \equiv m_0\tau_{\mathrm{sca}}$, $x \equiv \ln\left(\tilde{F}_{\mathrm{ds}}d^2\right)$, $a_0 = \omega\ln\tilde{F}_0$, and $a_1 = -\omega$. Using generalized least square fitting, we can obtain the coefficients a_0 and a_1 as follows:

$$a_0 = \frac{\sum_j \sigma_{y_j}^{-2}\cdot x_j^2 \sum_j \sigma_{y_j}^{-2}\cdot y_j - \sum_j \sigma_{y_j}^{-2}\cdot x_j \sum_j \sigma_{y_j}^{-2}\cdot x_j\cdot y_j}{\sum_j \sigma_{y_j}^{-2}\cdot\sum_j \sigma_{y_j}^{-2}\cdot x_j^2 - \left(\sum_j \sigma_{y_j}^{-2}\cdot x_j\right)^2}, \tag{6.23a}$$

$$a_1 = \frac{-\sum_j \sigma_{y_j}^{-2}\cdot x_j \sum_j \sigma_{y_j}^{-2}\cdot y_j + \sum_j \sigma_{y_j}^{-2} \sum_j \sigma_j^{-2}\cdot x_j\cdot y_j}{\sum_j \sigma_{y_j}^{-2}\cdot\sum_j \sigma_{y_j}^{-2}\cdot x_j^2 - \left(\sum_j \sigma_{y_j}^{-2}\cdot x_j\right)^2}, \tag{6.23b}$$

where σ_{y_j} is the uncertainty of the j-th $m_0\tau_{\mathrm{sca}}$ data calculated from Eq. (6.16). The variance of a_0 and a_1 is given as:

$$\mathrm{Var}(a_0) = \frac{\sum_i \sigma_{y_j}^{-2} \cdot x_j^2}{\sum_j \sigma_{y_j}^{-2} \cdot \sum_j \sigma_{y_j}^{-2} \cdot x_j^2 - \left(\sum_j \sigma_{y_j}^{-2} \cdot x_j\right)^2}, \tag{6.24a}$$

$$\mathrm{Var}(a_1) = \frac{\sum_j \sigma_{y_j}^{-2}}{\sum_j \sigma_{y_j}^{-2} \cdot \sum_j \sigma_{y_j}^{-2} \cdot x_j^2 - \left(\sum_j \sigma_{y_j}^{-2} \cdot x_j\right)^2}, \tag{6.24b}$$

$$\mathrm{Cov}(a_0, a_1) = -\frac{\sum_j \sigma_{y_j}^{-2} \cdot x_j}{\sum_j \sigma_{y_j}^{-2} \cdot \sum_j \sigma_{y_j}^{-2} \cdot x_j^2 - \left(\sum_j \sigma_{y_j}^{-2} \cdot x_j\right)^2}. \tag{6.24c}$$

Therefore, the maximum likelihood calibration constant and variance are given as:

$$\ln \tilde{F}_0 = \frac{\sum_j \sigma_{y_j}^{-2} \cdot x_j^2 \sum_j \sigma_{y_j}^{-2} \cdot y_j - \sum_j \sigma_{y_j}^{-2} \cdot x_j \sum_j \sigma_{y_j}^{-2} \cdot x_j \cdot y_j}{\sum_j \sigma_{y_j}^{-2} \cdot x_j \sum_j \sigma_{y_j}^{-2} \cdot y_j - \sum_j \sigma_{y_j}^{-2} \sum_j \sigma_j^{-2} \cdot x_j \cdot y_j}, \tag{6.25a}$$

$$\mathrm{Var}\left(\ln \tilde{F}_0\right) = \sigma_{\tilde{F}_0}^2 = \left(\frac{1}{a_1}\right)^2 \left[\mathrm{Var}(a_0) + \left(\frac{a_0}{a_1}\right)^2 \mathrm{Var}(a_1) - 2\frac{a_0}{a_1}\mathrm{Cov}(a_0, a_1)\right]. \tag{6.25b}$$

6.2.4.3. Level-2 analysis

In Level-2 analysis, the state vector of Eq. (6.12a) consists of the full element of the aerosol microphysical and optical properties excepted w ($\boldsymbol{X}_i = \left[\ln C_1, \cdots, \ln C_{20}, \ln \beta, \ln m_{\mathrm{Re},1}, \cdots, \ln m_{\mathrm{Re},N_{\mathrm{w}}}, \ln m_{\mathrm{Im},1}, \cdots, \ln m_{\mathrm{Im},N_{\mathrm{w}}}\right]^{\mathrm{T}}$) and the observational vector consists of $\tilde{T}$ and $\tilde{R}$ in full scattering angle at aerosol channels. The covariance of the observational vector in Eq. (6.12b) consists of $\sigma_{F_{\mathrm{ds}}}^2$, $\sigma_{F_0}^2$, and σ_{M1}^2 and the extra uncertainty (σ_{M2}^2) is estimated by the similar formulation of Level-1 analysis (Section 6.2.4.2) as follows:

$$\left(\sigma_{\mathrm{M2}}^{(j)}\right)^2 = \frac{(N_{\mathrm{s}}+1)\left(\sigma_{F_{\mathrm{ds}}}^2 + N_{\mathrm{s}}\sigma_{F_0}^2\right)}{N_{\mathrm{s}}\left[\sigma_{F_{\mathrm{ds}}}^2 + (N_{\mathrm{s}}-1)\sigma_{F_0}^2\right]}\left[\frac{1}{N_{\mathrm{s}}+1}\left(G_{\mathrm{o}}^{(j)}\Big|_{\sigma_{\mathrm{M}}^2=0}\right) - 1\right]\sigma_{F_{\mathrm{ds}}}^2 \quad (j = 1, \cdots, N_{\mathrm{w}}). \tag{6.26}$$

6.2.4.4. WV analysis

In WV analysis, the state vector of Eq. (6.12a) consists of w ($\boldsymbol{X}_i = [w]$) and the observational vector consists of $\tilde{R}$ in full scattering angle at the water vapor channel. Thus, the extra uncertainty (σ_{M3}^2) is estimated as follows:

$$\left(\sigma_{\mathrm{M3}}^{(j)}\right)^2 = \frac{\sigma_{F_{\mathrm{df}}}^2 + N_{\mathrm{s}}\sigma_{F_{\mathrm{ds}}}^2}{\sigma_{F_{\mathrm{df}}}^2 + (N_{\mathrm{s}}-1)\sigma_{F_{\mathrm{ds}}}^2}\left[\frac{1}{N_{\mathrm{s}}}\left(G_{\mathrm{o}}^{(j)}\Big|_{\sigma_{\mathrm{M}}^2=0}\right) - 1\right]\sigma_{F_{\mathrm{df}}}^2 \quad (j = 1,\cdots,N_{\mathrm{w}}). \tag{6.27}$$

6.3. Algorithm of aerosol and PWV estimations from direct solar irradiances: DSRAD version 2.0

This section is primarily based on the paper of Momoi et al. [2020]. The sky-radiometer measures the angular distribution of $\tilde{F}_{\mathrm{df}}$ every 10 min but measures $\tilde{F}_{\mathrm{ds}}$ every 1 min. We can estimate PWV from $\tilde{F}_{\mathrm{ds}}$ with the DSRAD by determining the calibration constant with the SKYMAP. Table 6.3 shows the references of the DSRAD algorithm. This algorithm consists of two steps. First, aerosol optical thicknesses at aerosol channels are calculated using $\tilde{F}_{\mathrm{ds}}$. The aerosol optical thickness at the water vapor channel is interpolated from the values at 870 and 1020 nm by linear interpolation in the log-log plane. Second, the convolved transmittance of the water vapor, $\tilde{T}_{\mathrm{H2O}}^{\mathrm{M}}$, is calculated from the calibrated direct solar irradiance.

Table 6.3: References and methodologies of the DSRAD version 2.0.

	DSRAD version 2.0
Solar coordinates	Nagasawa [1999]
Refraction correction	Nagasawa [1999]
Sun-Earth distance	Nagasawa [1999]
Optical air mass	Gueymard [2001]
Rayleigh scattering	Fröhlich and Shaw [1980]; Young[1981]
Ozone absorption	RSTAR7
Water vapor absorption	RSTAR7, Momoi et al. [submitted manuscript, 2021]
Filter response function	Stepwise function
PWV estimation	Gauss-Newton method

6.3.1. Aerosol optical thickness

The aerosol optical thickness τ_{p} is obtained from Beer-Lambert's law Eq. (2.61a) as follows:

$$\tau_{\mathrm{p}} = \frac{1}{m_{0,\mathrm{p}}}\left[\ln\left(\frac{\tilde{F}_{\mathrm{ds}}d^2}{\tilde{F}_0}\right) - m_{0,\mathrm{R}}\tau_{\mathrm{R}} - m_{0,\mathrm{H2O}}\ln\tilde{T}_{\mathrm{H2O}} - m_{0,\mathrm{O3}}\ln\tilde{T}_{\mathrm{O3}}\right], \tag{6.28}$$

where $\tilde{T}_{\mathrm{O3}}$ is the convolved transmittance of atmospheric ozone; $m_{0,\mathrm{p}}$, $m_{0,\mathrm{R}}$, $m_{0,\mathrm{H2O}}$, and $m_{0,\mathrm{O3}}$ are, respectively, optical air mass of aerosol extinction, Rayleigh scattering, water vapor absorption, and ozone absorption, which is given by formulations of Gueymard [2001]; τ_{R} is Rayleigh scattering optical thickness given by Fröhlich and Shaw [1980] as:

$$\tau_{\mathrm{R}}(\lambda) = \frac{p}{p_0}\cdot 0.00864\lambda^{-\left(3.916+0.074\lambda+\frac{0.050}{\lambda}\right)}, \tag{6.29}$$

where p_0 is standard pressure (1 atm). In the case of aerosol channels, $\ln\tilde{T}_{\mathrm{H2O}}$ and/or other gas absorptions can be ignored. Thus, aerosol optical thickness is given by subtracting the Raleigh scattering optical thickness.

6.3.2. Physics-based PWV estimation method

PWV is estimated from the convolved transmittance at the water vapor channel using the following formula:

$$\tilde{T}^{\mathrm{M}}_{\mathrm{H2O}} - \frac{\sum^{N_{\mathrm{s}}}\bar{\psi}\cdot\bar{F}_{\mathrm{sol}}\cdot\bar{T}^{\mathrm{CKD}}(w)\cdot\Delta_\kappa\bar{\lambda}^2}{\sum^{N_{\mathrm{s}}}\bar{\psi}\cdot\bar{F}_{\mathrm{sol}}\cdot\Delta_\kappa\bar{\lambda}^2} = 0, \tag{6.30a}$$

$$\tilde{T}^{\mathrm{M}}_{\mathrm{H2O}} \equiv \frac{\tilde{F}_{\mathrm{ds}}d^2}{\tilde{F}_0} - m_{0,\mathrm{R}}\tau_{\mathrm{R}} - m_{0,\mathrm{p}}\tau_{\mathrm{p,int}}. \tag{6.30b}$$

where $\tau_{\mathrm{p,int}}$ is the aerosol optical thickness at 940 nm interpolated from that at 870 and 1020 nm by linear interpolation in the log-log plane. Eq. (6.30a) is solved using the Gauss–Newton method.

6.3.3. Cloud screening

To ensure the quality of the data and avoid cloud contamination, we adopt the method of Smirnov et al. [2000] with two main differences, similar to Estellés et al. [2012]. First, an aerosol optical thickness at 500 nm > 2 is considered cloud-affected data. Second, the triplet

of the aerosol optical thickness in Smirnov et al. [2000] is built from the pre/post 1 min data instead of 30 seconds.

6.3.4. Error analysis on PWV estimation

In this section, the influence of the uncertainty of aerosol optical thickness and calibration constant at water vapor channel on PWV is roughly discussed using the empirical equation of Bruegge et al. [1992]. PWV is described using the adjustment parameters as follows

$$w = \frac{1}{m_0}\left(-\frac{\ln \tilde{T}_{\mathrm{H20}}}{a}\right)^{\frac{1}{b}} \text{ [cm]}, \tag{6.31}$$

The uncertainty of PWV ϵ_{PWV} is given from the partial differentiation of Eq. (6.31) with respect to $\ln \tilde{T}_{\mathrm{H20}}$ as follows

$$\epsilon_{\mathrm{PWV}} = \frac{\partial w}{\partial \ln \tilde{T}_{\mathrm{H20}}}\epsilon_{\ln \tilde{T}_{\mathrm{H2O}}} = \frac{w}{b \ln \tilde{T}_{\mathrm{H20}}}\epsilon_{\ln \tilde{T}_{\mathrm{H2O}}}, \tag{6.32}$$

where $\epsilon_{\ln \tilde{T}_{\mathrm{H20}}}$ is the uncertainty of $\tilde{T}_{\mathrm{H20}}$. Using Eq. (6.32) with the adjusting parameters of the sky-radiometer, with a = 0.620 and b = 0.625 as the coefficient values for the trapezoidal spectral response function (Uchiyama et al. [2018a]), we write the uncertainty of PWV as

$$\epsilon_{\mathrm{PWV}} = -\frac{w}{ab}(m_0 w)^{-b}\epsilon_{\ln \tilde{T}_{\mathrm{H20}}} = -\frac{w}{0.388}(m_0 w)^{-0.625}\epsilon_{\ln \tilde{T}_{\mathrm{H20}}}, \tag{6.33}$$

Uncertainty of the calibration constant

If the uncertainty of the aerosol optical thickness is ignored, the uncertainty of $\tilde{T}_{\mathrm{H20}}$ is the uncertainty of the calibration constant. The uncertainty of PWV is -0.238 cm where $m_0 = 3.0$, $w = 5.0$ cm, and $\epsilon_{\ln \tilde{T}_{\mathrm{H20}}} = 0.1$.

Uncertainty of the aerosol optical thickness

If the uncertainty of the calibration constant at the water vapor channel is ignored, the uncertainty of $\tilde{T}_{\mathrm{H20}}$ is given from Eq. (6.30b) as follows

$$\epsilon_{\ln \tilde{T}_{\mathrm{H20}}} = m_0 \epsilon_{\mathrm{AOT}}, \tag{6.34}$$

where ϵ_{AOT} is the uncertainty of the aerosol optical thickness at 940 nm. The uncertainty of PWV is written by Eqs. (6.33) and (6.34) as

$$\epsilon_{\mathrm{PWV}} = -\frac{1}{0.388}(m_0 w)^{0.375}\epsilon_{\mathrm{AOT}} = -0.214\ [\mathrm{cm}], \tag{6.35}$$

where $m_0 = 3.0$, $w = 5.0$ cm, and $\epsilon_{\mathrm{AOT}} = 0.03$.

6.4. Polarization effect on aerosol estimations using numerical tests

This section investigated the polarization effect on the aerosol estimation with using the simulated data, including $\tilde{T}$ and $\tilde{R}$ at 340, 380, 400, 500, 675, 870, and 1020 nm. We simulated the sky radiances in the almucantar plane ($\theta = \theta_0$) with three different aerosol conditions - water-soluble, dust (dust 1 in Chapter 4), and biomass burning - described in Dubovik et al. [2000] and Table 4.1. $\tilde{R}$ was computed by RpSTAR7 with the P^3-IMS method (Momoi et al. [2022a]; Chapter 4) at a ground albedo of 0.1 through all wavelengths. Figure 6.8 shows the difference in $\tilde{R}$ at 340 nm with perturbed aerosol properties (volume ratio of mode 1 to mode 2 (C_r), complex refractive index, mode radii (r_1 and r_2), mode widths (s_1 and s_2)) at SZA of 30 and 70° and AOT500 = 0.1 for the water-soluble aerosols ($C_r = 2.0$, $m_{\mathrm{Re}} = 1.45$, $m_{\mathrm{Im}} = 0.0035$, $r_1 = 0.118$, $r_2 = 1.17$, and $s_1 = s_2 = 0.6$; Table 4.1). Black lines in Fig. 6.8 show the difference of $\tilde{R}$ between IPOL1 and IPOL4 as similarly shown in Fig. 1.1. In addition to aerosol properties, the polarization effect appears on $\tilde{R}$ and becomes weak relative to the parameter about SDF (r_1, r_2, s_1 and s_2) by increasing AOT500. Therefore, we conducted the sensitivity tests using three aerosol types for three turbid conditions (AOT500 = 0.05, 0.2, and 1.0) under a US standard atmosphere adopted in RpSTAR7 with IPOL1 and IPOL4 (DUDB-R and DUDB-P, respectively), as summarized in Table 6.4. To consider the actual condition, we adopt random errors into sky radiances: σ_{M} is randomly given in the range of 0.01 to 0.05; $\sigma_{\tilde{F}_0}$ is 0.02; $\sigma_{\tilde{F}_{\mathrm{ds}}}$ is 0.005, as reported by Section 6.2.1. A calibration uncertainty is caused by an error in processes to determine a calibration constant. The calibration uncertainty is given from some filed campaigns compared with other instruments, as summarized in Nakajima et al. [2020].

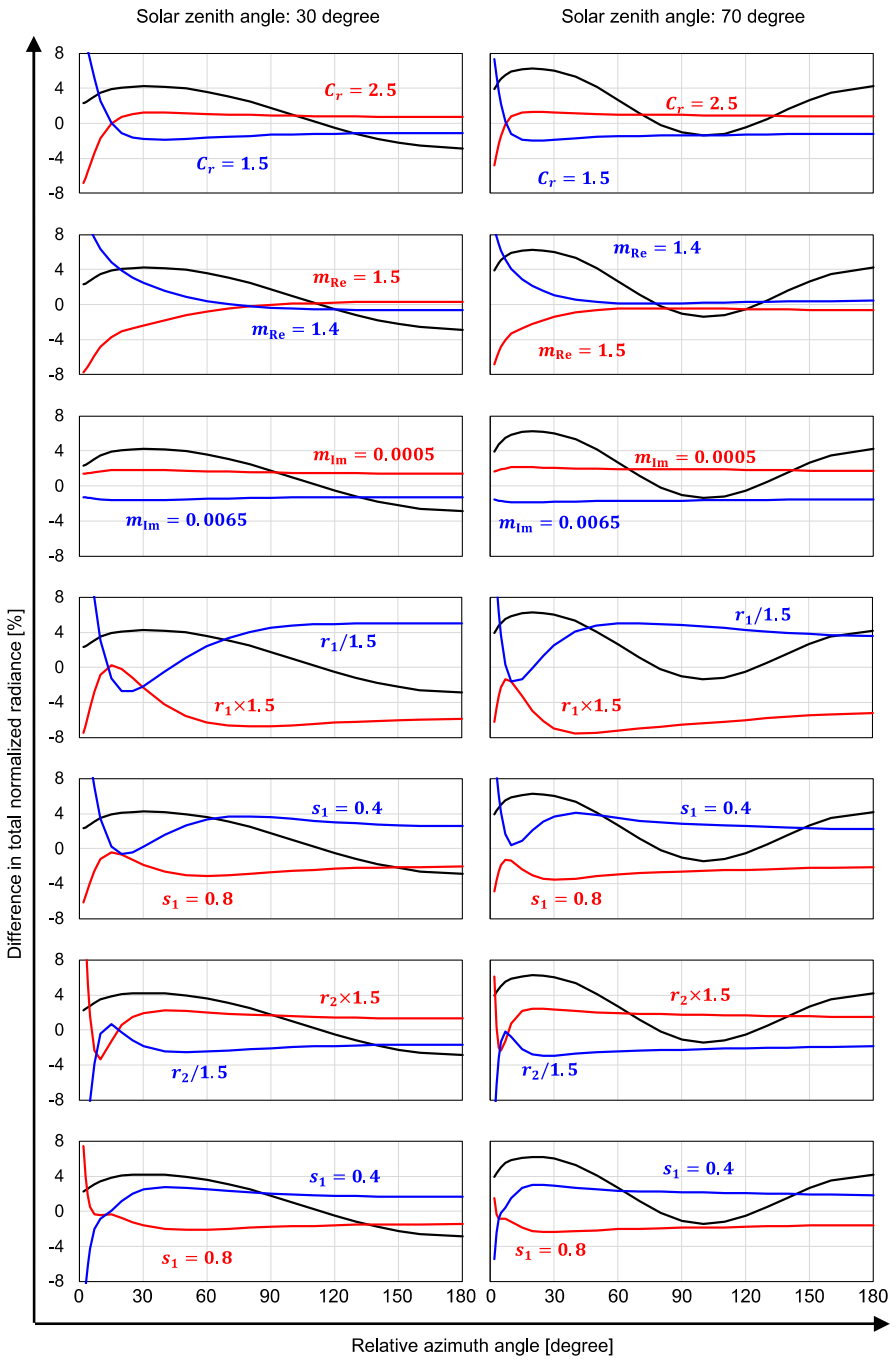

Figure 6.8: The difference in $\tilde{R}$ of water-soluble aerosols at 340 nm with perturbed aerosol properties (volume ratio of mode 1 to mode 2 C_r, complex refractive index, mode radii r_1 and r_2, mode widths s_1 and s_2) at SZA of 30 and 70° and AOT500 = 0.1. Black line shows the difference of $\tilde{R}$ between IPOL1 and IPOL4 as similarly shown in Fig. 1.1.

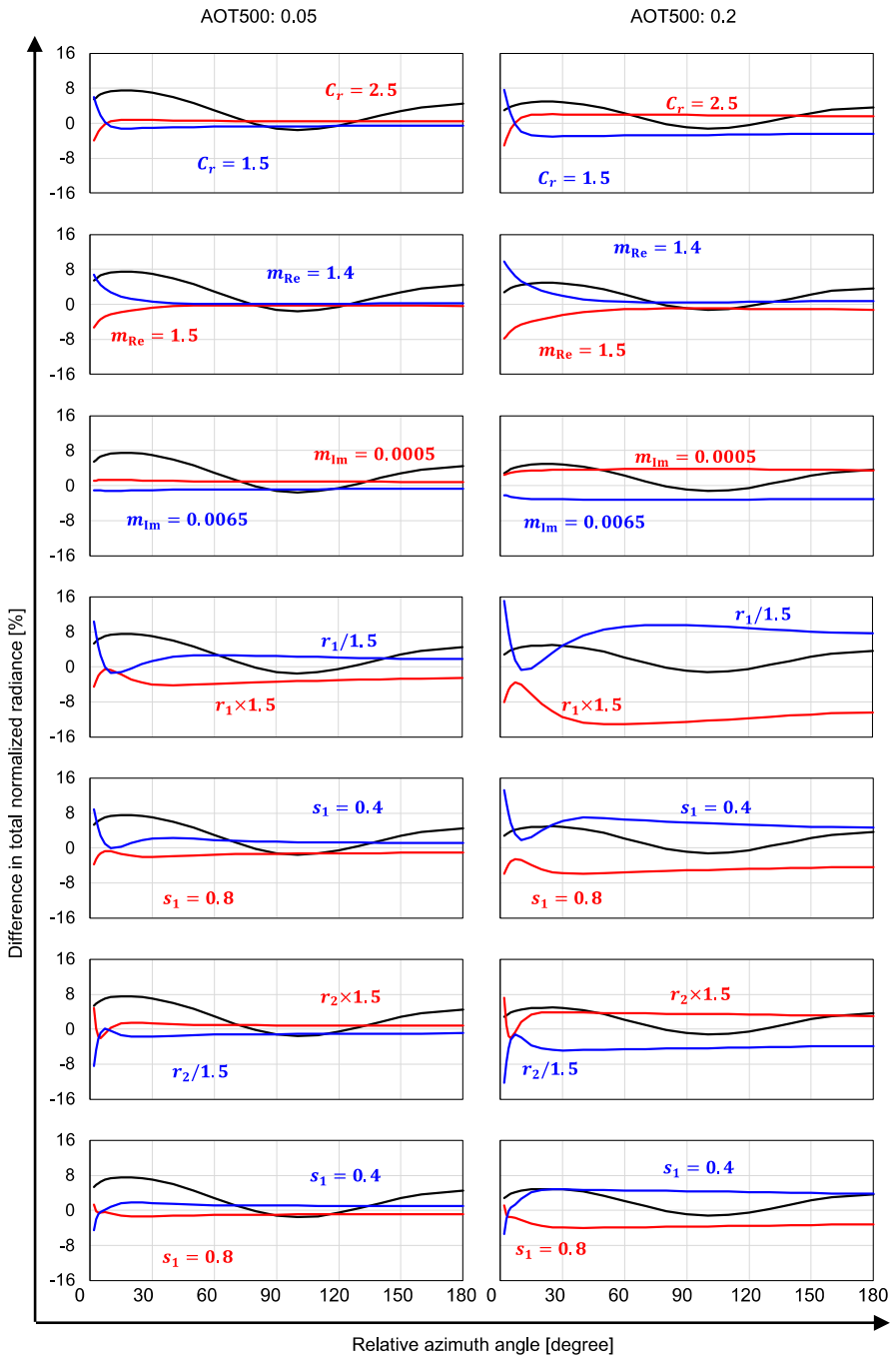

Figure 6.9: As described in Fig. 6.8, but at SZA of 70º and AOT500 of 0.05 and 0.2.

Table 6.4: Description of DUDB-R and DUDB-P.

		Water soluble	Dust	Biomass burning
Aerosol	Component	See Table 4.1		
	Vertical profile	$\exp(-z/H)$, H = 2 km		
	Optical depth at 500 nm	0.05, 0.2, and 1.0		
Atmosphere	Vertical profile	US standard atmosphere		
Geometry	Solar zenith angle	Random in the range of 15 to 75 degrees		
	Ground surface	Lambertian at a surface albedo of 0.1 in all wavelengths		
$\sigma_{F_{\mathrm{ds}}}$ in Eqs. (6.1-2)		0.5% in all wavelengths		
σ_{F_0} in Eqs. (6.1-2)		2.5% in all wavelengths		
σ_{M} in Eqs. (6.1-2)		Random in the range of 1% to 5% in all wavelengths		

6.4.1. Comparison of three algorithms for sky-radiometer data analysis

Before evaluating the polarization effect on the aerosol estimation, we evaluated the potential performance of the SKYMAP version 2.0 with IPOL1 (hereafter, SK2R), V42, and V50 using the DB-R dataset. To avoid including the abnormal data, we screened the estimated data by the root mean squared percentage errors ($\varepsilon_{\mathrm{Ret}}$) of the sky radiances of 0.1, where $\varepsilon_{\mathrm{Ret}}$ is defined as:

$$\varepsilon_{\mathrm{Ret}} = \sqrt{\frac{1}{N_{\mathrm{w}}(1+N_{\mathrm{s}})}\sum_{j}^{N_{\mathrm{w}}}\left[\left(\frac{\tilde{T}_j^{\mathrm{R}}-\tilde{T}_j^{\mathrm{M}}}{\tilde{T}_j^{\mathrm{M}}}\right)^2+\sum_{k}^{N_{\mathrm{s}}}\left(\frac{\tilde{R}_{k,j}^{\mathrm{R}}-\tilde{R}_{k,j}^{\mathrm{M}}}{\tilde{R}_{k,j}^{\mathrm{M}}}\right)^2\right]}. \qquad (6.36)$$

Those process reduced 33.1% (744 data; AOT500 = 0.05: 505 data, 0.2: 104 data, and 1.0: 135 data), 15.3% (344 data; AOT500 = 0.05: 305 data, 0.2: 19 data, and 1.0: 20 data), and 11.2% (1 data; AOT500 = 0.05: 92 data, 0.2: 87 data, and 1.0: 74 data) of the estimated data of DUDB-R using the V42, V50, and SK2R, respectively (Fig. 6.10).

Figures 6.11-13 show the size distribution function (SDF) of three aerosol dispersions at AOT500 of 0.05, 0.2, and 1.0. The SDF of 0.1 – 4 μm is retrieved stably through all dispersions and AOT500s, even with random noise in the measurement values. In other words, the estimation of the small (< 0.1 μm) or large (> 4 μm) of the SDF has the significant uncertainty because of lack of information about them on $\tilde{T}$ and $\tilde{R}$, as discussed in Nakajima et al. [1996] and Dubovik et al. [2000]. As shown in Table 6.1, the SK2R is almost the same as the V42. This is because both use the Tikhonov regularization for the constraint of the volume size distribution and the wavelength dependency of the refractive index. In

addition, by the edge constraint of Eq. (6.14b-c), the SK2R becomes more stable than the V42 through all AOT500 (Figs. 6.11-13). The results of the V42 at AOT500 of 0.05 are poor convergence because of the treatment of the variance. In the SK2R, the variance of $\tilde{T}$ is given for $\ln\tilde{T}$ as described in Section 6.2.1. Thus, $\mathrm{Var}(\ln\tilde{T}) = \mathrm{Var}(m_0\tau) = const.$ In contrast, the variance in the V42 is given for $\ln\tau$ as $\mathrm{Var}(\ln\tau) \propto (0.1/\tau_\mathrm{p})^2$. When the thin aerosol-laden atmosphere (*e.g.*, AOT500 = 0.05), the retrievals become unstable because the variance of the direct solar irradiance in the V42 is small.

Although the SDF with the V50 is more stable than that with others in 0.2 – 20 μm, systematic errors arise in the small (< 0.1 μm) or large (> 4 μm) of the SDF due to L2 regularization. However, the errors are also found around the local minimum of the bimodal distribution for biomass burning aerosols, especially at AOT500 = 0.05. One reason is the treatment of the variance of $\tilde{T}$ and $\tilde{R}$. The variance of $\tilde{T}$ in the V50 is the similar as the SK2R as $\mathrm{Var}(\tau)$, but that of $\tilde{R}$ is given as $\mathrm{Var}(\ln\tilde{R}) \propto (0.05 + 0.05/\tau_\mathrm{p} + 0.04)^2$ differed from the others given as $\mathrm{Var}(\ln\tilde{R}) = const.$ Thus, when small AOT500, *a priori* constraint works much stronger than the measurement elements and convergences around the *a priori* values. Those numerical tests indicate that our SKYMAP algorithm better estimates the SDF than others under the bimodal aerosol conditions and/or thin atmosphere.

Tables 6.5-7 show the means for the residual errors of the optical properties with the V42, V50, and SK2R, respectively. All algorithms have no significant difference, except in the real part of the refractive index (RR) and single scattering albedo (SSA). RR of the V42 has large uncertainty through all AOT500s compared to others, so that the uncertainty of SSA increases.

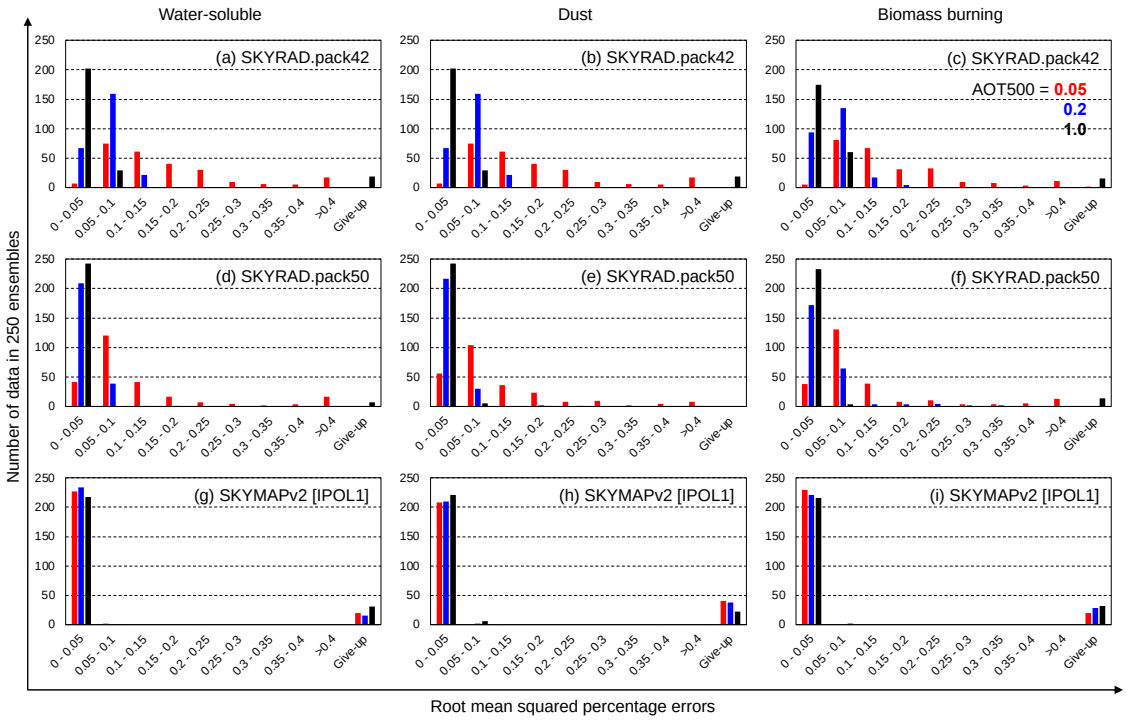

Figure 6.10: Histogram of the root mean squared percentage errors of the measurement vectors. The result of DUDB-R with (a-c) V42, (d-f) V50, and (g-i) SK2R. Red, blue, and black show the results at AOT500 of 0.05, 0.2, and 1.0, respectively.

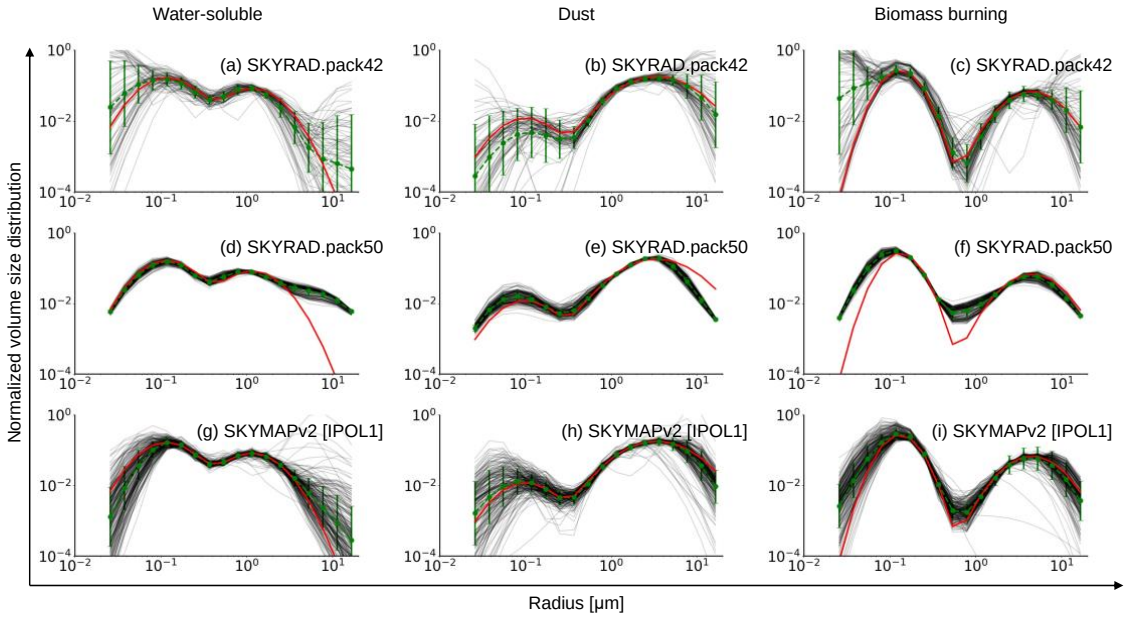

Figure 6.11: SDF of the DUDB-R at AOT500 of 0.05 with (a-c) V42, (d-f) V50, and (g-i) SK2R. Black lines are each retrieval result. Red lines are the "true" value. Green lines and error bars are, respectively, means and standard deviations of the ensembles.

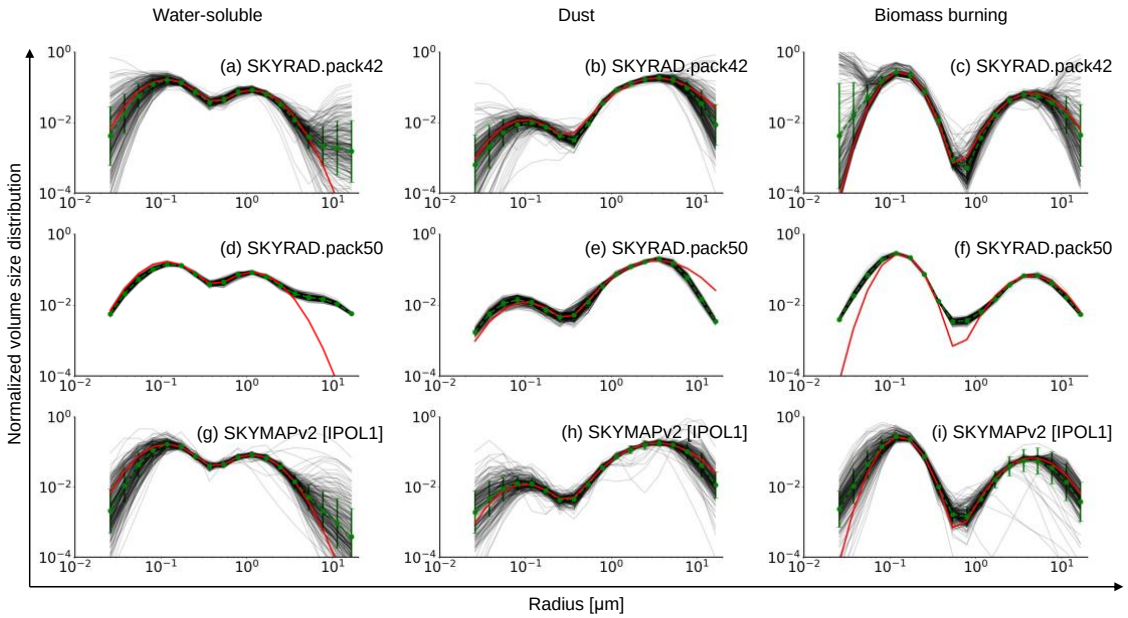

Figure 6.12: As described in Fig. 6.11, but at AOT500 of 0.2.

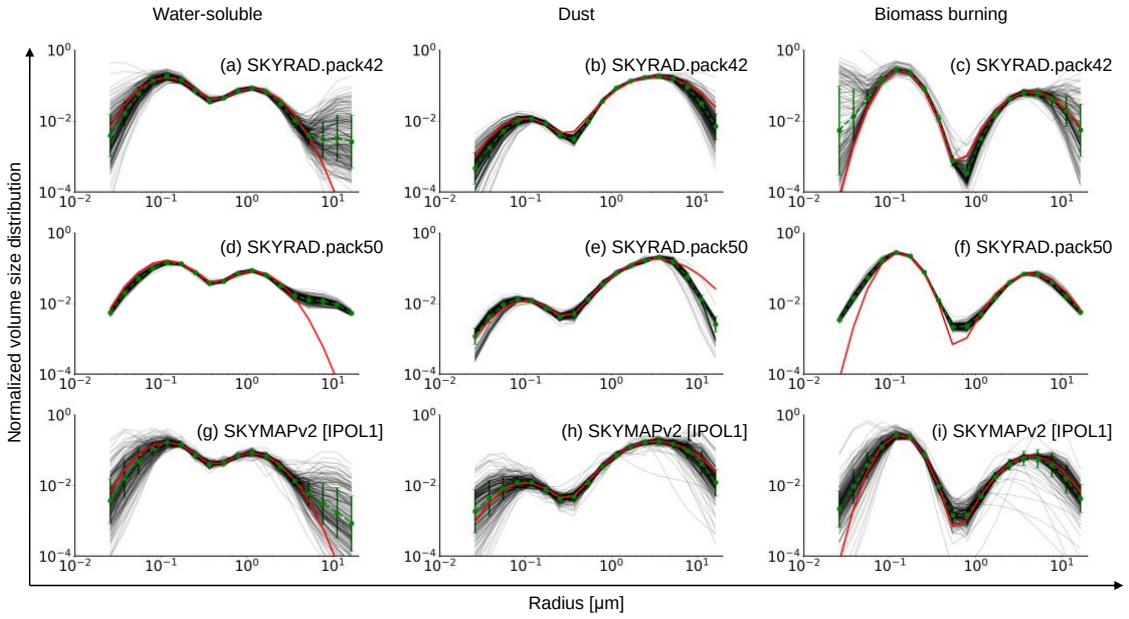

Figure 6.13: As described in Fig. 6.11, but at AOT500 of 1.0.

Table 6.5: Means and standard deviations of the residual errors of the optical properties estimated with V42 for the DUDB-R. AOT, SSA, AAOT, RR, and RI are aerosol optical thickness, single scattering albedo, absorption aerosol optical thickness, real part of the refractive index, and imaginary part of the refractive index, respectively.

		Water-soluble			Dust			Biomass burning		
	AOT500	0.05	0.2	1.0	0.05	0.2	1.0	0.05	0.2	1.0
AOT	340 nm	0.01±0.02	0.00±0.01	0.00±0.02	0.00±0.01	-0.01±0.01	-0.02±0.02	0.01±0.01	0.00±0.01	0.00±0.03
	500 nm	0.00±0.01	0.00±0.01	0.00±0.01	0.00±0.01	0.00±0.01	-0.02±0.01	0.00±0.01	0.00±0.01	0.00±0.02
	1020 nm	0.00±0.01	0.00±0.01	0.01±0.01	0.00±0.01	0.00±0.01	0.00±0.01	0.00±0.01	0.00±0.01	0.01±0.02
SSA	340 nm	-0.05±0.11	0.00±0.03	0.00±0.01	0.02±0.12	0.02±0.05	0.00±0.01	-0.02±0.11	0.01±0.04	0.00±0.01
	500 nm	-0.10±0.12	-0.04±0.08	0.00±0.02	-0.01±0.13	0.00±0.06	0.00±0.01	-0.09±0.14	-0.03±0.07	-0.01±0.03
	1020 nm	-0.16±0.19	-0.08±0.11	-0.01±0.05	-0.01±0.09	0.01±0.04	0.00±0.01	-0.16±0.25	-0.08±0.16	-0.01±0.09
AAOT	340 nm	0.01±0.02	0.00±0.01	0.00±0.02	0.00±0.01	-0.01±0.01	-0.01±0.01	0.00±0.01	0.00±0.01	0.00±0.02
	500 nm	0.01±0.01	0.01±0.02	0.00±0.02	0.00±0.01	0.00±0.01	-0.01±0.01	0.01±0.01	0.01±0.02	0.01±0.03
	1020 nm	0.01±0.01	0.01±0.01	0.01±0.02	0.00±0.01	0.00±0.01	0.00±0.01	0.00±0.01	0.01±0.01	0.00±0.02
RR	340 nm	0.01±0.08	0.02±0.06	-0.01±0.05	0.02±0.08	0.01±0.05	0.00±0.03	-0.05±0.10	-0.01±0.07	-0.03±0.05
	500 nm	0.00±0.06	0.01±0.04	0.00±0.03	0.00±0.07	-0.01±0.03	-0.02±0.02	-0.04±0.10	-0.01±0.06	-0.02±0.04
	1020 nm	0.00±0.03	0.01±0.02	0.01±0.02	-0.01±0.02	-0.02±0.02	-0.02±0.01	-0.03±0.10	-0.01±0.05	-0.02±0.04
RI [%]	340 nm	162±341	8±119	-1±30	33±151	-3±74	-3±12	-13±119	-28±70	-13±24
	500 nm	288±357	173±294	7±67	59±142	12±78	-4±10	47±125	41±114	0±45
	1020 nm	334±372	252±335	43±134	20±95	-6±32	0±13	65±126	69±126	8±85

Table 6.6: As described in Table 6.5, but for V50.

		Water-soluble			Dust			Biomass burning		
	AOT500	0.05	0.2	1.0	0.05	0.2	1.0	0.05	0.2	1.0
AOT	340 nm	0.00±0.01	-0.01±0.02	-0.01±0.02	0.00±0.01	-0.01±0.02	-0.03±0.02	0.00±0.02	0.00±0.02	-0.01±0.02
	500 nm	0.00±0.01	0.00±0.02	0.00±0.02	0.00±0.01	0.00±0.01	-0.01±0.02	0.00±0.01	0.00±0.02	0.00±0.02
	1020 nm	0.00±0.00	0.00±0.01	0.00±0.02	0.00±0.00	0.00±0.01	-0.01±0.01	0.00±0.00	0.00±0.01	0.00±0.02
SSA	340 nm	-0.01±0.05	0.01±0.02	0.00±0.01	0.01±0.08	0.01±0.04	0.01±0.01	0.01±0.05	0.01±0.03	0.00±0.01
	500 nm	-0.05±0.07	-0.02±0.05	0.00±0.02	-0.05±0.07	-0.01±0.04	0.00±0.01	-0.02±0.07	-0.01±0.05	0.00±0.01
	1020 nm	-0.11±0.07	-0.05±0.08	-0.01±0.03	-0.01±0.06	0.00±0.04	0.00±0.02	-0.10±0.08	-0.06±0.12	-0.03±0.07
AAOT	340 nm	0.00±0.01	0.00±0.01	-0.01±0.01	0.00±0.01	-0.01±0.01	-0.02±0.02	0.00±0.01	0.00±0.01	-0.01±0.02
	500 nm	0.00±0.01	0.01±0.01	0.00±0.02	0.00±0.01	0.00±0.01	0.00±0.02	0.00±0.00	0.00±0.01	0.00±0.01
	1020 nm	0.00±0.00	0.00±0.01	0.00±0.01	0.00±0.00	0.00±0.01	0.00±0.02	0.00±0.00	0.00±0.01	0.01±0.02
RR	340 nm	0.02±0.05	0.04±0.02	0.04±0.01	-0.07±0.06	-0.05±0.05	-0.03±0.02	-0.06±0.04	-0.04±0.02	-0.03±0.01
	500 nm	0.04±0.06	0.03±0.03	0.03±0.01	-0.02±0.06	-0.01±0.05	-0.01±0.02	-0.02±0.04	-0.02±0.02	-0.02±0.01
	1020 nm	0.06±0.04	0.03±0.05	0.01±0.02	0.00±0.03	0.01±0.03	0.02±0.03	0.00±0.03	-0.02±0.03	-0.02±0.01
RI [%]	340 nm	77±250	-12±86	-10±30	37±111	-4±51	-8±12	-18±98	-23±52	-13±16
	500 nm	236±331	95±202	15±53	99±112	28±64	4±14	34±121	16±91	-6±23
	1020 nm	397±281	181±283	31±94	36±78	7±45	3±15	97±81	63±115	21±65

Table 6.7: As described in Table 6.5, but for SK2R.

		Water-soluble			Dust			Biomass burning		
	AOT500	0.05	0.2	1.0	0.05	0.2	1.0	0.05	0.2	1.0
AOT	340 nm	0.01±0.01	0.00±0.01	0.00±0.02	0.00±0.01	0.00±0.01	0.00±0.02	0.00±0.01	0.00±0.01	0.00±0.02
	500 nm	0.00±0.01	0.00±0.01	0.00±0.01	0.00±0.01	0.00±0.01	0.00±0.02	0.00±0.01	0.00±0.01	0.00±0.01
	1020 nm	0.00±0.00	0.00±0.01	0.00±0.01	0.00±0.00	0.00±0.01	0.00±0.01	0.00±0.01	0.01±0.01	0.01±0.01
SSA	340 nm	-0.03±0.06	-0.01±0.02	0.00±0.01	-0.01±0.07	0.00±0.03	0.00±0.01	-0.01±0.06	0.00±0.02	0.00±0.01
	500 nm	-0.03±0.06	-0.01±0.02	0.00±0.01	-0.01±0.06	0.00±0.03	0.00±0.01	-0.03±0.07	-0.01±0.03	0.00±0.01
	1020 nm	-0.05±0.10	-0.02±0.06	0.00±0.03	0.00±0.03	0.00±0.02	0.00±0.01	-0.18±0.21	-0.08±0.12	-0.02±0.04
AAOT	340 nm	0.00±0.01	0.00±0.01	0.00±0.01	0.00±0.01	0.00±0.01	-0.01±0.02	0.00±0.01	0.00±0.01	0.00±0.01
	500 nm	0.00±0.00	0.00±0.01	0.00±0.01	0.00±0.00	0.00±0.01	0.00±0.01	0.00±0.00	0.00±0.01	0.00±0.01
	1020 nm	0.00±0.00	0.00±0.01	0.00±0.01	0.00±0.00	0.00±0.00	0.00±0.01	0.00±0.01	0.01±0.01	0.01±0.01
RR	340 nm	0.04±0.07	0.02±0.06	0.01±0.06	-0.04±0.09	-0.03±0.07	-0.02±0.06	-0.03±0.09	-0.01±0.07	-0.01±0.06
	500 nm	0.02±0.04	0.01±0.04	0.00±0.03	-0.03±0.06	-0.02±0.04	-0.01±0.03	-0.02±0.06	-0.01±0.04	-0.01±0.04
	1020 nm	0.02±0.03	0.01±0.02	0.00±0.02	-0.01±0.03	-0.01±0.02	0.00±0.02	-0.01±0.05	-0.01±0.04	-0.01±0.03
RI [%]	340 nm	165±313	29±81	4±26	40±125	-2±36	-5±17	19±122	-4±46	-4±16
	500 nm	130±306	23±73	6±31	20±75	-2±28	-2±15	37±120	10±48	0±20
	1020 nm	192±478	74±187	11±77	0±27	-4±20	-2±18	322±473	106±182	18±43

6.4.2. Study of the polarization effect on the sky-radiometer data analysis

Figure 6.14 shows the distribution of the residuals for the DUDB-P estimated using the SK2R and the SKYMAP version 2.0 with IPOL4 (SK2P). Because SK2R uses the scalar RTM for the analysis, the residuals are larger than that of the SK2P, especially at a low aerosol optical thickness because the polarization strongly affects $\tilde{R}$ in the near UV wavelengths under the thin atmosphere by Rayleigh scattering, as discussed in Chapter 4. In the case of the SK2R,

to reconstruct the normalized radiance including the polarization effect ($\tilde{R}_{\mathrm{vector}}$) using the scalar RTM ($\tilde{R}_{\mathrm{scalar}} \equiv \tilde{R}_{\mathrm{vector}} - \tilde{R}_{\mathrm{pol}}$), the fine mode of the SDF is overestimated and to be small dispersion (Fig. 6.15). This is because $\tilde{R}$ in the near UV wavelengths are more affected than that in the longer wavelength and $\tilde{R}_{\mathrm{pol}}$ in the single scattering approximation is given by Eqs. (2.3) and (6.8b) as:

$$\tilde{R}_{\mathrm{pol}}(\boldsymbol{\Omega}, \boldsymbol{\Omega}'; \lambda) \approx \mathbf{L}(\pi - \chi_1) \left[\sum_k \Delta_{C_k} \mathbf{K}(\Theta, \lambda, m_{\mathrm{Re}}, m_{\mathrm{Im}}, r_k) \right] \mathbf{L}(-\chi_2), \tag{6.37}$$

where Δ_{C_k} is the value overestimated by using the SK2R. Increasing the aerosol optical thickness (*e.g.*, AOT500 = 1.0), there is no significant difference in the retrieved SDF between SK2R and SK2P because the polarization effect becomes weak, as shown in Figs. 1.1 and 6.9.

Figure 6.16 shows the distribution of the residuals for the DUDB-P estimated using the V42, V50, and SK2R. The residuals are larger than that for the DUDB-R (Fig. 6.10), as above discussion. Because the SKYRAD.pack series (V42 and V50) can not compute the sky radiance, including the polarization effect, we compared the results between DUDB-R and DUDB-P. The impact on the SDF for the V42 is similar to that for SK2R shown in Fig. 6.17-19, except mode widths (s_1 and s_2). This is because η values. Fig. 6.19 shows the results using the SK2R with $\eta \approx 0.863$ (or $s = 0.4$). The mode widths of the SDF are to be large. In contrast, the SDF for the V50 has no significant impact between the DUDB-R and DUDB-P because *a priori* values strongly work at low AOT500, as discussed in the previous section. Tables 6.8-10 summarize the performance for the DUDB-P. There are no significant residuals in the aerosol optical properties compared to the results for the DUDB-R because of low sensitivity. This result suggests that the SKYMAP version 2.0 with the RpSTAR/P^n-IMS is useful for estimating the accurate aerosol optical and microphysical properties from the sky-radiometer observation.

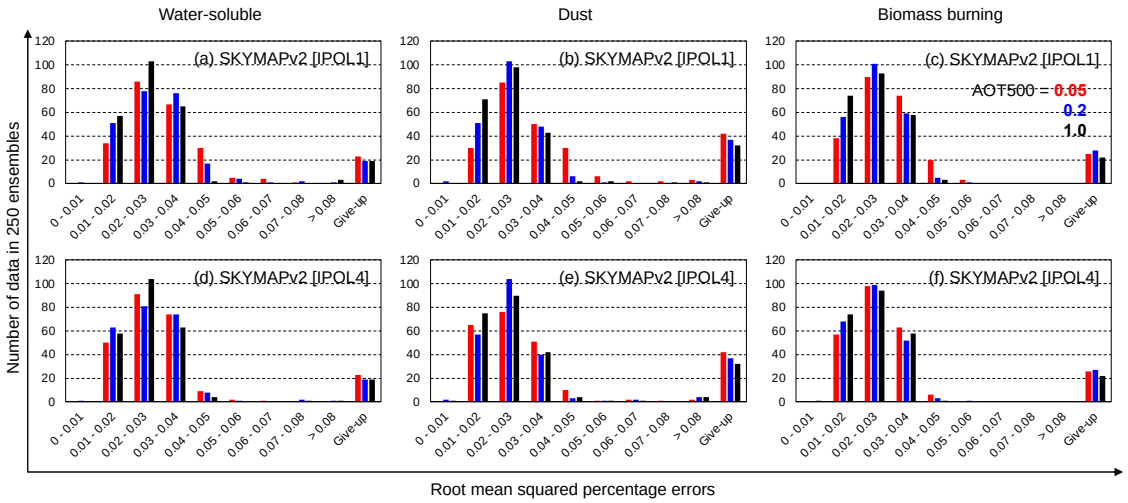

Figure 6.14: Histogram of the root mean squared percentage errors of the measurement vectors. The result of DUDB-R with (a-c) SK2R and (d-f) SK2P. Red, blue, and black show the results at AOT500 of 0.05, 0.2, and 1.0, respectively.

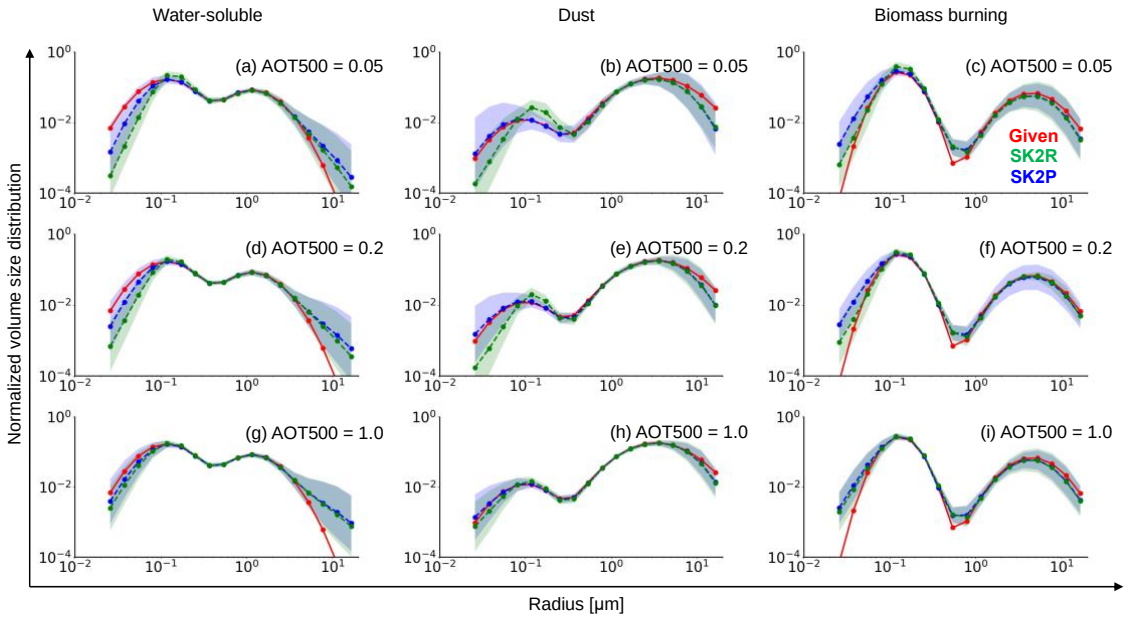

Figure 6.15: SDF of the DUDB-P estimated with the SKYMAP version 2 with IPOL1 (SK2R; Green) and IPOL4 (SK2P; Blue) at AOT500 of (a-c) 0.05, (d-f) 0.2, and (g-i) 1.0. Red lines are the "true" value. Other lines and fills are, respectively, means and standard deviations of the ensembles.

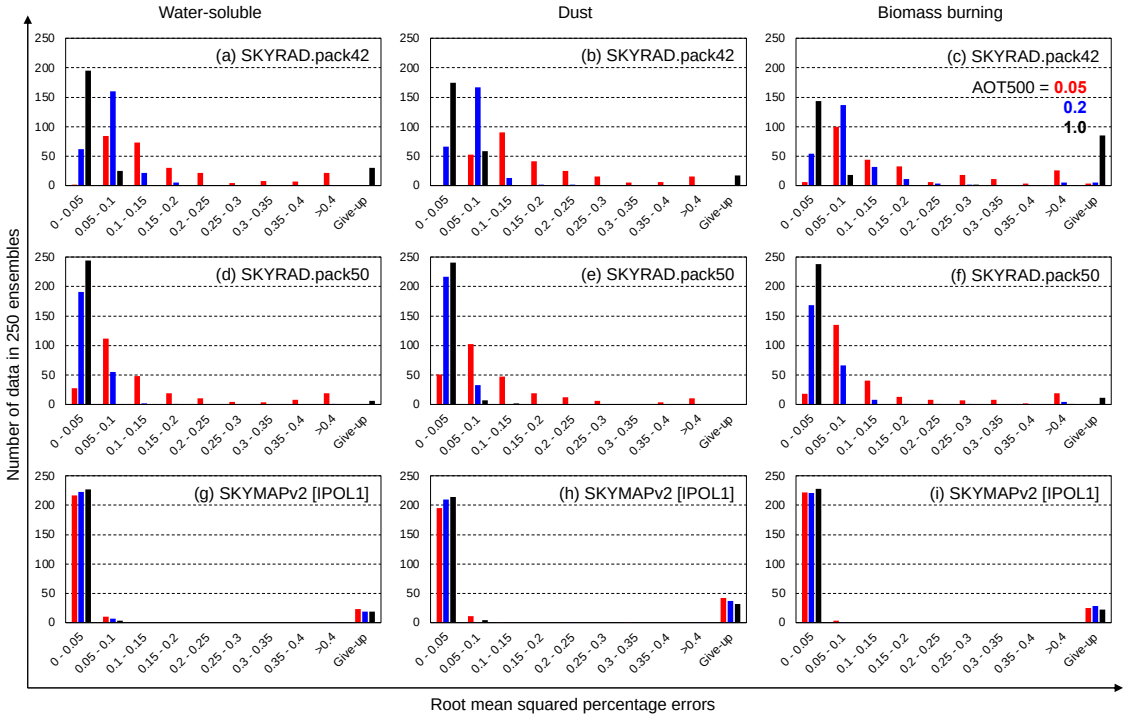

Figure 6.16: As described in Fig. 6.10, but for DUDB-P.

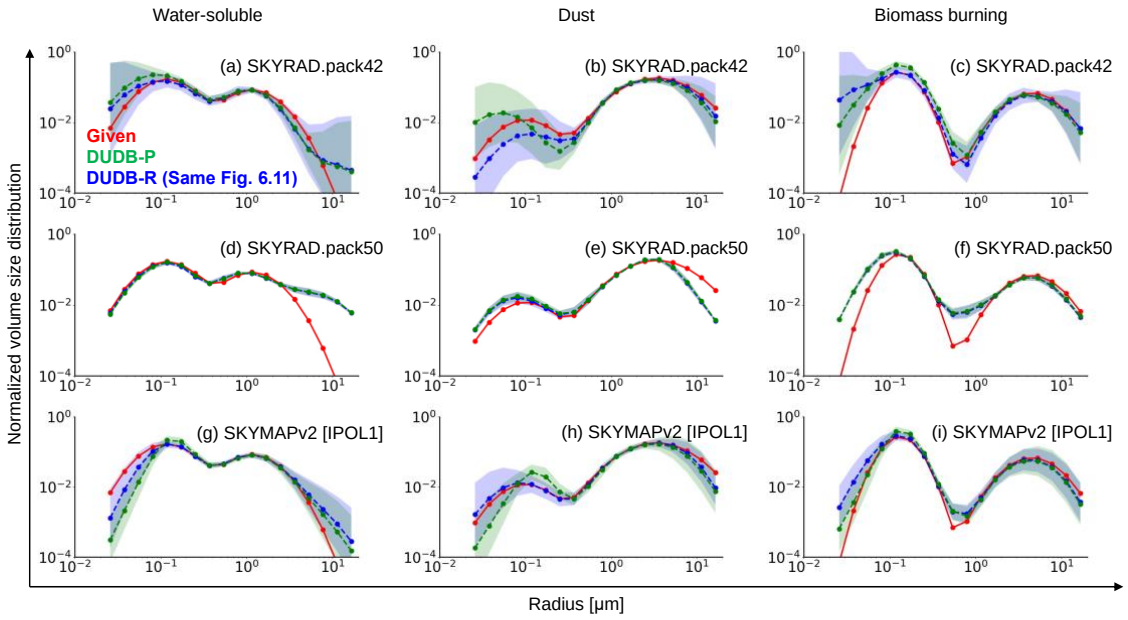

Figure 6.17: SDF of the DUDB-P (green) and DUDB-R (blue) at AOT500 of 0.05 with (a-c) V42, (d-f) V50, and (g-i) SK2R. Red lines are the "true" value. Other lines and fills are, respectively, means and standard deviations of the ensembles.

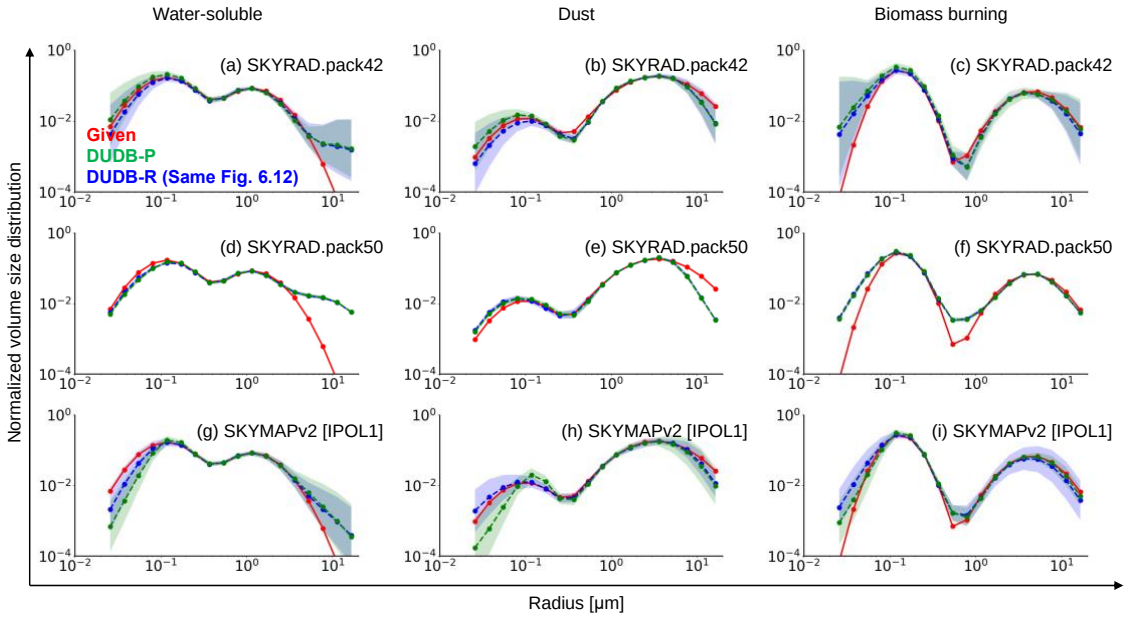

Figure 6.18: As described in Fig. 6.17, but at AOT500 of 0.2.

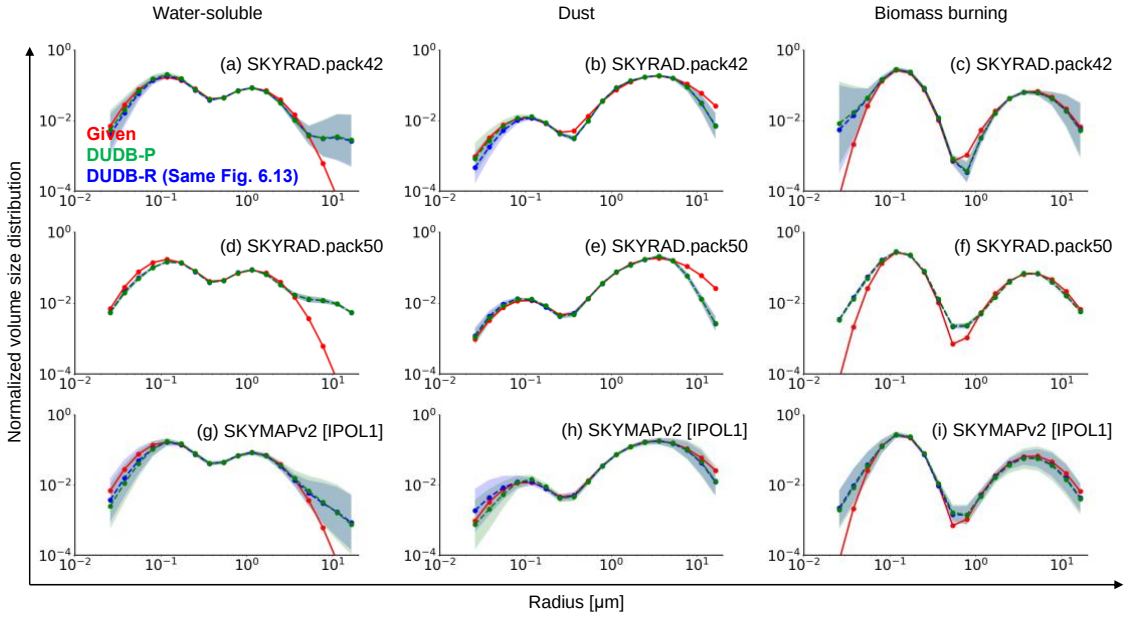

Figure 6.18: As described in Fig. 6.17, but at AOT500 of 1.0.

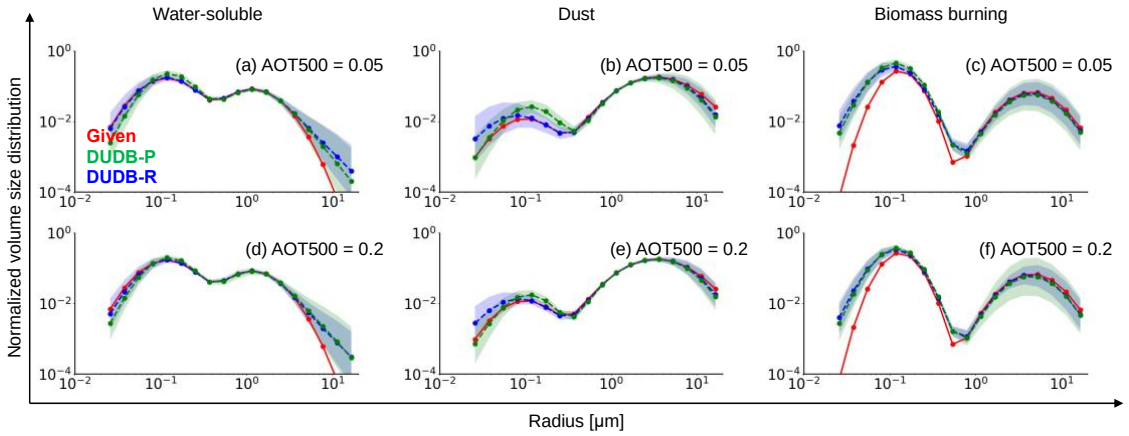

Figure 6.19: SDF of the DUDB-P (green) and DUDB-R (blue) with the SK2R with $\eta \approx 0.863$ (or $s = 0.4$) at AOT500 of (a-c) 0.05, and (d-f) 0.2. Red lines are the "true" value. Other lines and fills are, respectively, means and standard deviations of the ensembles.

Table 6.8: As described in Table 6.5, but for the DUDB-P.

		Water-soluble			Dust			Biomass burning		
	AOT500	0.05	0.2	1.0	0.05	0.2	1.0	0.05	0.2	1.0
AOT	340 nm	0.01±0.02	0.00±0.01	0.00±0.02	0.00±0.01	0.00±0.01	-0.02±0.02	0.01±0.01	0.00±0.02	-0.01±0.03
	500 nm	0.00±0.01	0.00±0.01	0.00±0.01	0.00±0.01	0.00±0.01	-0.02±0.01	0.00±0.01	0.00±0.02	0.00±0.02
	1020 nm	0.01±0.01	0.01±0.01	0.01±0.01	0.00±0.00	0.00±0.01	-0.01±0.01	0.00±0.00	0.01±0.01	0.00±0.02
SSA	340 nm	-0.01±0.09	0.01±0.03	0.00±0.01	0.10±0.13	0.03±0.06	0.00±0.01	0.00±0.09	0.02±0.04	0.00±0.01
	500 nm	-0.11±0.13	-0.04±0.08	0.00±0.02	-0.01±0.16	-0.01±0.07	0.00±0.01	-0.09±0.11	-0.05±0.08	-0.01±0.02
	1020 nm	-0.17±0.21	-0.08±0.12	-0.02±0.05	0.01±0.08	0.00±0.04	0.00±0.01	-0.17±0.20	-0.08±0.16	0.00±0.09
AAOT	340 nm	0.00±0.01	0.00±0.01	0.00±0.02	-0.01±0.01	-0.01±0.02	-0.01±0.01	0.00±0.01	-0.01±0.02	0.00±0.02
	500 nm	0.01±0.01	0.01±0.02	0.00±0.02	0.00±0.01	0.00±0.01	-0.01±0.01	0.01±0.01	0.01±0.02	0.01±0.03
	1020 nm	0.01±0.01	0.01±0.01	0.01±0.02	0.00±0.00	0.00±0.01	0.00±0.01	0.00±0.00	0.01±0.01	0.00±0.02
RR	340 nm	-0.06±0.05	-0.05±0.05	-0.03±0.05	-0.09±0.05	-0.06±0.04	-0.03±0.03	-0.15±0.06	-0.09±0.07	-0.04±0.05
	500 nm	-0.06±0.04	-0.04±0.04	-0.02±0.04	-0.11±0.04	-0.06±0.03	-0.03±0.02	-0.15±0.06	-0.07±0.07	-0.03±0.04
	1020 nm	-0.03±0.03	-0.02±0.02	-0.01±0.02	-0.02±0.02	-0.02±0.02	-0.02±0.02	-0.15±0.05	-0.07±0.06	-0.03±0.03
RI [%]	340 nm	22±255	-24±110	-5±33	-35±125	-11±83	-5±11	-33±113	-45±61	-17±21
	500 nm	295±352	131±246	7±63	50±148	17±86	-5±9	61±127	44±110	-7±41
	1020 nm	312±378	223±326	58±149	2±72	0±33	0±13	69±120	46±124	-8±78

Table 6.9: As described in Table 6.6, but for the DUDB-P.

		Water-soluble			Dust			Biomass burning		
	AOT500	0.05	0.2	1.0	0.05	0.2	1.0	0.05	0.2	1.0
AOT	340 nm	0.00±0.01	-0.01±0.02	-0.01±0.02	0.00±0.01	-0.01±0.02	-0.03±0.02	0.00±0.02	-0.01±0.02	-0.01±0.02
	500 nm	0.00±0.01	0.00±0.02	0.00±0.02	0.00±0.01	0.00±0.01	-0.01±0.02	0.00±0.01	0.00±0.02	0.00±0.02
	1020 nm	0.00±0.00	0.00±0.01	0.01±0.02	0.00±0.00	0.00±0.01	-0.01±0.02	0.00±0.00	0.00±0.01	0.00±0.02
SSA	340 nm	0.02±0.03	0.01±0.02	0.01±0.01	0.10±0.08	0.03±0.04	0.01±0.01	0.03±0.04	0.02±0.03	0.00±0.01
	500 nm	-0.04±0.07	-0.01±0.05	0.00±0.01	-0.04±0.07	-0.02±0.04	0.00±0.01	-0.02±0.07	-0.02±0.05	0.00±0.01
	1020 nm	-0.12±0.07	-0.05±0.08	-0.01±0.03	-0.02±0.06	0.01±0.03	0.00±0.02	-0.12±0.08	-0.05±0.12	-0.01±0.07
AAOT	340 nm	0.00±0.00	0.00±0.01	-0.01±0.01	-0.01±0.01	-0.01±0.01	-0.02±0.02	0.00±0.00	-0.01±0.01	-0.01±0.02
	500 nm	0.00±0.01	0.00±0.01	0.00±0.02	0.00±0.01	0.00±0.01	0.00±0.02	0.00±0.00	0.00±0.01	0.00±0.01
	1020 nm	0.00±0.00	0.01±0.01	0.01±0.01	0.00±0.00	0.00±0.01	0.00±0.02	0.00±0.00	0.00±0.01	0.00±0.02
RR	340 nm	0.01±0.05	0.03±0.02	0.04±0.02	-0.08±0.06	-0.06±0.04	-0.04±0.02	-0.07±0.04	-0.06±0.02	-0.03±0.01
	500 nm	0.03±0.05	0.01±0.03	0.02±0.01	-0.03±0.06	-0.03±0.06	-0.02±0.02	-0.02±0.04	-0.03±0.02	-0.02±0.01
	1020 nm	0.06±0.05	0.02±0.05	0.01±0.02	0.00±0.03	0.00±0.03	0.01±0.03	-0.01±0.03	-0.04±0.03	-0.03±0.01
RI [%]	340 nm	-0.43±1.37	-0.28±0.98	-0.13±0.30	-0.37±0.88	-0.16±0.51	-0.09±0.13	-0.67±0.69	-0.41±0.52	-0.13±0.15
	500 nm	1.91±3.14	0.75±1.85	0.21±0.51	0.94±1.13	0.37±0.65	0.04±0.14	0.36±1.19	0.22±0.90	-0.06±0.22
	1020 nm	4.39±2.65	2.00±2.94	0.49±0.97	0.43±0.84	0.01±0.32	0.03±0.18	1.07±0.75	0.59±1.14	0.08±0.62

Table 6.10: As described in Table 6.7, but for the DUDB-P.

		Water-soluble			Dust			Biomass burning		
	AOT500	0.05	0.2	1.0	0.05	0.2	1.0	0.05	0.2	1.0
AOT	340 nm	0.02±0.01	0.01±0.02	0.00±0.02	0.02±0.02	0.01±0.02	0.00±0.02	0.02±0.02	0.01±0.01	0.00±0.02
	500 nm	0.01±0.01	0.00±0.01	0.00±0.01	0.01±0.01	0.01±0.01	0.00±0.01	0.01±0.01	0.00±0.01	0.00±0.01
	1020 nm	0.00±0.00	0.00±0.01	0.00±0.01	0.00±0.00	0.00±0.01	0.00±0.01	0.00±0.01	0.01±0.01	0.00±0.01
SSA	340 nm	-0.07±0.09	-0.01±0.03	0.00±0.01	-0.06±0.10	-0.01±0.04	0.00±0.01	-0.05±0.09	-0.01±0.03	0.00±0.01
	500 nm	-0.06±0.09	-0.01±0.02	0.00±0.01	-0.07±0.07	-0.02±0.03	0.00±0.01	-0.06±0.09	-0.01±0.03	0.00±0.01
	1020 nm	-0.02±0.07	-0.01±0.05	-0.01±0.02	-0.01±0.04	0.01±0.02	0.00±0.01	-0.12±0.19	-0.07±0.12	-0.01±0.04
AAOT	340 nm	0.01±0.01	0.01±0.01	0.00±0.01	0.01±0.01	0.01±0.01	0.00±0.02	0.01±0.01	0.00±0.01	0.00±0.02
	500 nm	0.00±0.01	0.00±0.01	0.00±0.01	0.01±0.01	0.01±0.01	0.00±0.01	0.00±0.01	0.00±0.01	0.00±0.01
	1020 nm	0.00±0.00	0.00±0.01	0.00±0.01	0.00±0.00	0.00±0.00	0.00±0.01	0.00±0.01	0.01±0.01	0.00±0.01
RR	340 nm	0.03±0.07	0.00±0.05	0.01±0.06	-0.05±0.09	-0.07±0.07	-0.04±0.06	-0.06±0.08	-0.04±0.06	-0.02±0.06
	500 nm	-0.02±0.05	-0.01±0.03	-0.01±0.03	-0.09±0.07	-0.06±0.05	-0.03±0.04	-0.08±0.05	-0.04±0.04	-0.02±0.04
	1020 nm	-0.02±0.04	-0.01±0.02	0.00±0.02	-0.04±0.03	-0.02±0.02	-0.01±0.03	-0.07±0.05	-0.03±0.03	-0.02±0.03
RI [%]	340 nm	452±603	73±126	9±30	333±522	35±74	-2±16	130±247	10±59	-5±17
	500 nm	298±453	30±85	12±31	167±183	28±39	2±14	91±186	15±58	-1±23
	1020 nm	76±201	39±177	17±64	15±44	-7±23	-3±15	169±357	98±215	8±44

6.5. PWV estimation with the on-site self-calibration method

Using $\tilde{R}$ at 940 nm in the principal plane of the sky-radiometer measurement is unsuitable for PWV estimation because the aerosol vertical profile is unknown. In this study, we try to estimate PWV using angular distributions of $\tilde{R}$, which does not require the calibration constant of the sky-radiometer. Section 6.5.1 shows the concept of the PWV estimation using angular distributions, and then Section 6.5.2 conducted the sensitivity tests. Finally, Section 6.5.3 evaluated the performance using actual observation data. This section is primary based on the paper of Momoi et al. [2020; 2022b]. The filter response function at 940 nm was measured at the time of factory shipment.

6.5.1. Concept of Momoi et al. [2020]

The PWV estimation procedure consists of three steps described in Section 6.2.4. First, aerosol optical and microphysical properties are estimated from $\tilde{T}$ and the angular distribution of $\tilde{R}$ at aerosol channels (step 3 in Fig. 6.7). Second, aerosol optical properties at the water vapor channel are interpolated from those at aerosol channels. Then, PWV is estimated from the angular distribution of $\tilde{R}$ at the water vapor channel (step 4 in Fig. 6.7). Third, the calibration constant at the water vapor channel is estimated from PWV and the aerosol optical properties (step 5 in Fig. 6.7).

6.5.2. Sensitivity tests

This section is primary based on the paper of Momoi et al. [2020] using the SN-CKD method. Although the SN-CKD method is unsuitable for narrow-band computation discussed in Chapter 5 and causes residual errors in $\tilde{T}$ and $\tilde{R}$, it does not change the PWV dependency on $\tilde{R}$. Thus, in this section, we discuss the method of Momoi et al. [2020] by their results.

Sensitivity tests using simulated data were conducted to evaluate SKYMAP procedures steps 3 and 4 in Fig. 6.7. The simulation was conducted using the two aerosol types described in Table 5.8. The sensitivity test was conducted with sky radiances in the almucantar plane for the wavelengths of 340, 380, 400, 500, 675, 870, 940, and 1020 nm; AOTs of 0.02, 0.06, and 0.20 at 940 nm; PWV of 0.0 (0.5) 5.0 cm; and SZA of 30°, 50°, and 70°.

Figure 6.20 illustrates the retrieval results from the simulated data for the continental average aerosol with AOTs of 0.02, 0.06, and 0.20 at 940 nm. The estimation of the PWV corresponded with their input values (“true” values in Fig. 6.20) when the input of PWV was <2 cm. This is seen regardless of the magnitude of the AOT. When the input of PWV was >2 cm, the volume size distribution, scattering and absorption optical thickness were estimated well, but PWV is underestimated. When PWV was >2 cm, the angular distribution of $\tilde{R}$ is

insensitive to PWV (Fig. 5.7). Figure 6.21 illustrates the estimation results from the simulated data for the transported dust aerosol with AOTs of 0.02, 0.06 and 0.20 at 940 nm. The scattering and absorption optical thicknesses are estimated well. The volume size distribution of fine mode is slightly overestimated. The estimation errors of PWV increase with increasing AOT because the near-infrared wavelength is strongly affected by the estimation of coarse mode particles.

Sensitivity tests using the simulated data with bias errors are also conducted to investigate uncertainty in the SKYMAP-derived PWV. The bias errors are ± 5% and ± 10% for $\tilde{R}$. The value of 5% is given for the following reasons. The SVA bias errors of the diffuse radiances for the sky-radiometer observations were estimated to be less than 5% (Uchiyama et al. [2018b]). According to Dubovik et al. [2000] and Sinyuk et al. [2020], the uncertainty of the diffuse radiances for the AERONET measurements is ± 5%. Figures 6.22 and 6.23 show the results from the simulated data for the continental average and transported dust aerosols with AOTs of 0.02, 0.06 and 0.20 at 940 nm. PWV is overestimated when – 5% bias was applied to $\tilde{R}$. This corresponds to the relationship between $\tilde{R}$ and PWV, where $\tilde{R}$ decreases with increasing PWV (Section 5.2). The bias errors strongly affect the estimation of PWV at high PWV (> 2 cm), because the sensitivity of high PWV is lower than that of low PWV. The estimation error of PWV increases with increasing bias errors. The estimation error of PWV due to ± 5% and ± 10% errors for $\tilde{R}$ is within 10% for PWV < 2 cm and up to 200% for PWV > 2 cm.

When the input of PWV is < 2 cm, the PWV is estimated very well, within an error of 10% regardless of the AOT or aerosol type. This is also observed when the bias errors are added for $\tilde{R}$. The scattering and absorption parts of the AOT are also estimated very well within ± 0.01 in all conditions. Present sensitivity tests suggest the design of a sky-radiometer calibration program as follows: to determine the calibration constant of the water vapor channel in dry days/seasons with PWV <2 cm and to obtain PWV from direct solar irradiance data throughout the year, as illustrated in Fig. 6.24.

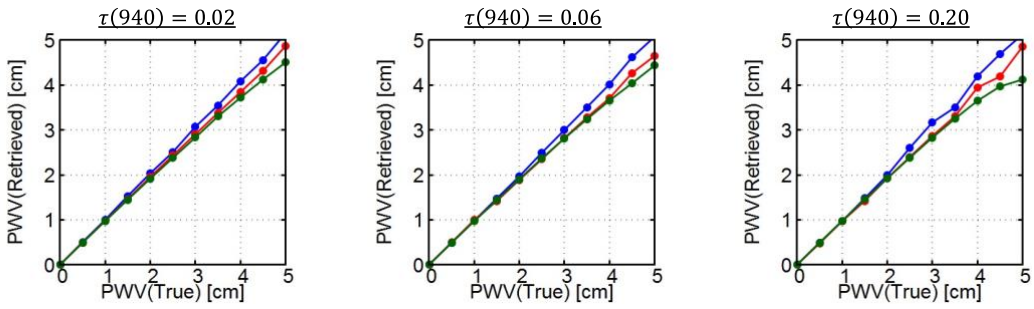

Figure 6.20: Comparison results of the "true" and estimation values of PWV from simulated data for continental average aerosol. Blue, red, and green lines are the estimation results at SZA = 30°, 50°, and 70°, respectively. The black line is the "true" value.

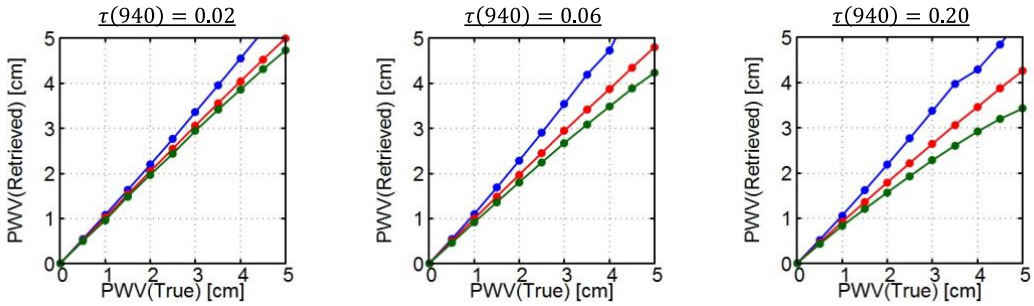

Figure 6.21: As described in Fig. 6.20, but for transported dust aerosol.

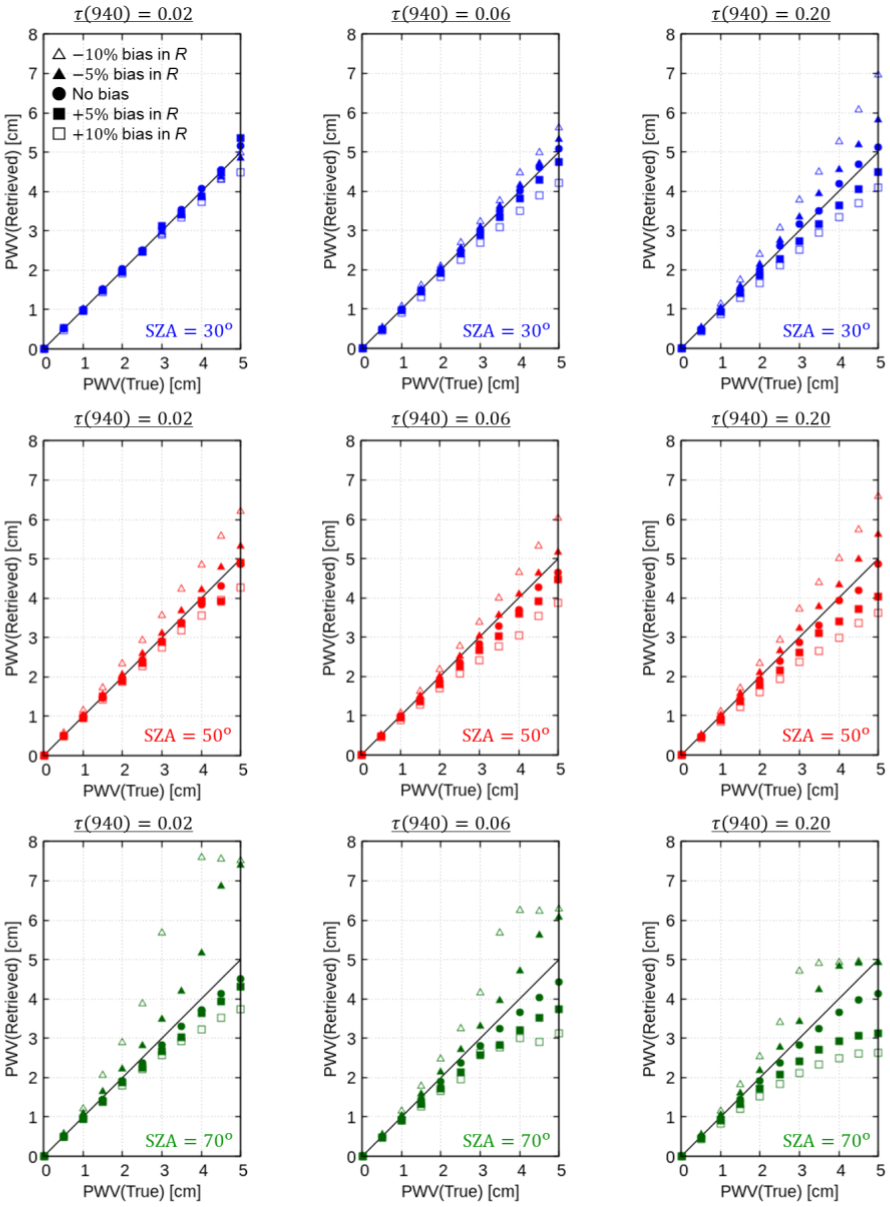

Figure 6.22: Comparison of the "true" and retrieval values of PWV from simulated data for continental average aerosol with bias errors. The top, middle, and bottom rows are the retrieval results at SZA = 30°, 50°, and 70°, respectively. Closed circles are the results with no bias errors. Closed squares and closed triangles are the results with bias errors of plus and minus 5% in *R*, respectively. Open squares and open triangles are the results with bias errors of plus and minus 10% in *R*, respectively.

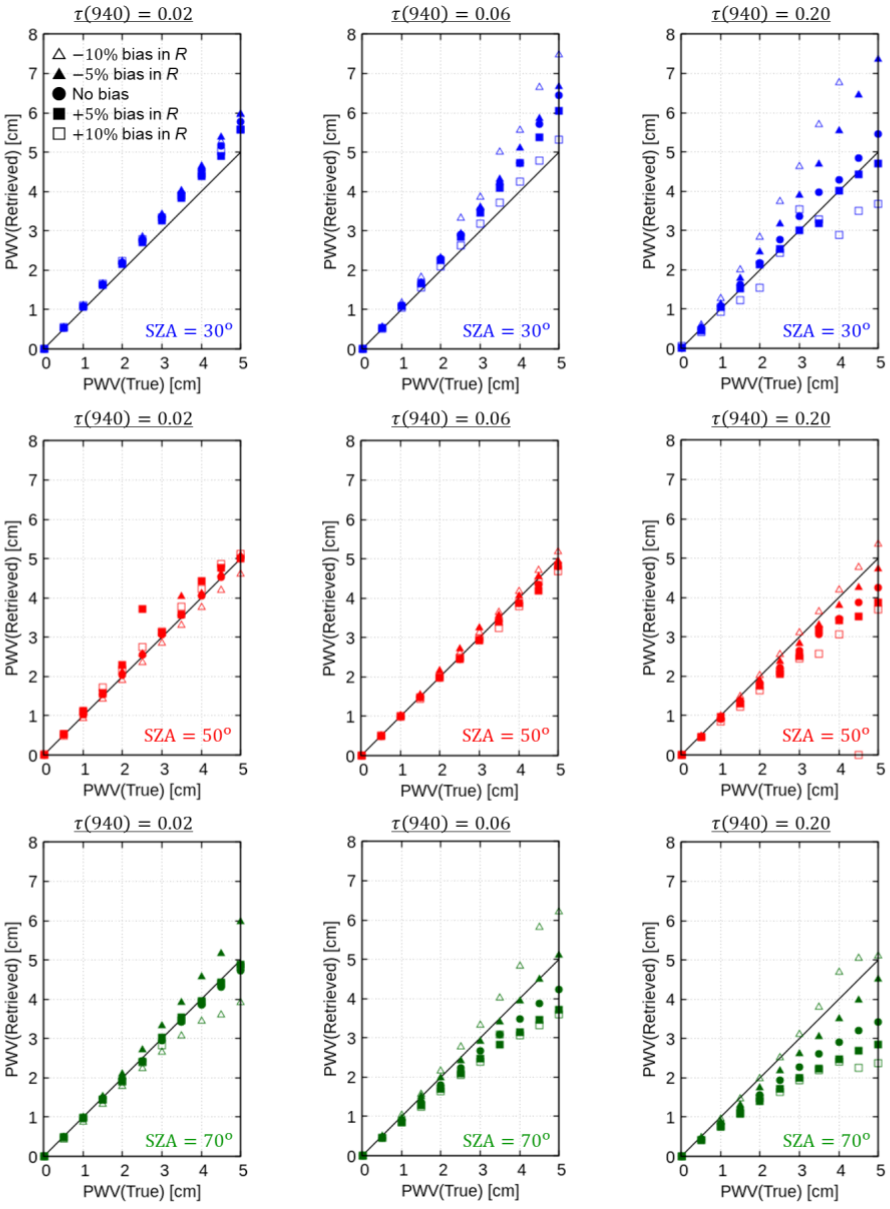

Figure 6.23: As described in Fig. 6.22, but for transported dust aerosol.

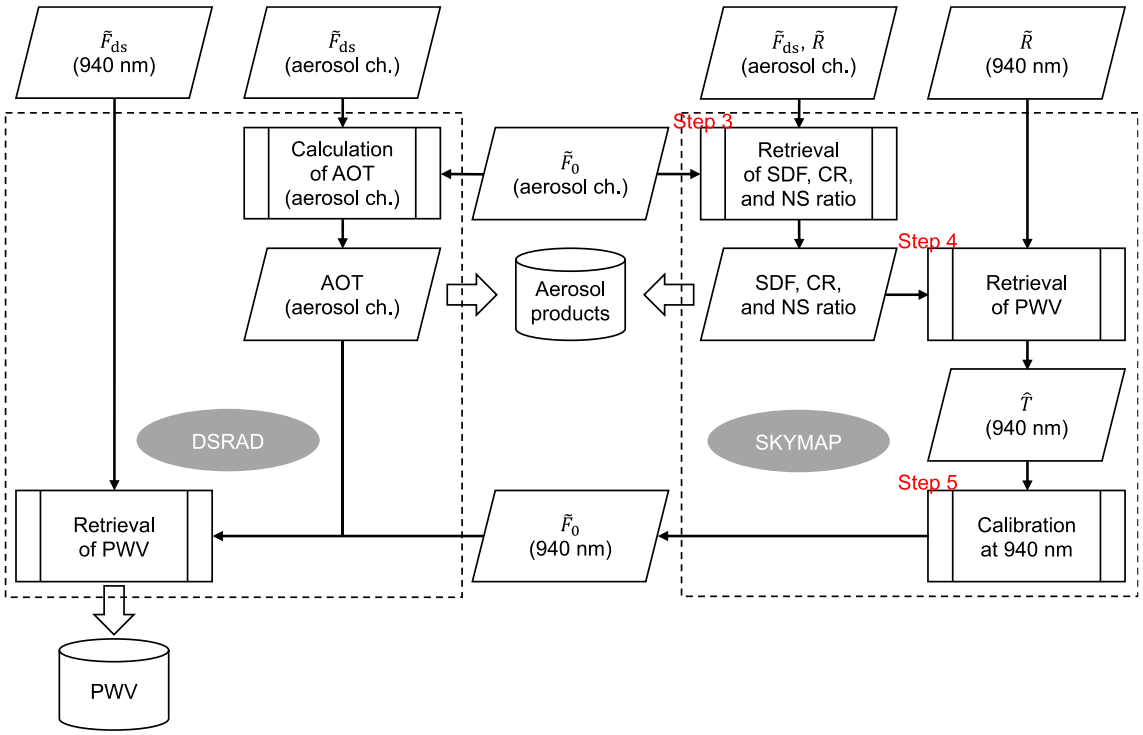

Figure 6.24: Diagram of the on-site self-calibration method (SKYMAP steps 3-5 in Fig. 6.7) and retrieval of PWV from direct solar irradiances (DSRAD).

6.5.3. Application to actual observation data

Momoi et al. [2020] applied SKYMAP and DSRAD to actual SKYNET sky-radiometer observation data and discussed those capabilities. We used the sky-radiometer model POM-02 (S/N PS2501417) data at Chiba University (35.63°N, 140.10°E; Figs. 6.25 and 6.26) in 2017. PWV was also obtained by a Radiometrix MP-1500 microwave radiometer (MWR) at the same location. The MWR measured the zenith brightness temperature in the 22-30 GHz region at 1-min temporal resolution and estimated PWV_{MWR} using default software. In the SKYMAP and DSRAD, the aerosol optical properties were estimated from 340, 380, 400, 500, 675, 870, 1020 nm, and the water vapor absorption was calculated using the SN-CKD with the vertical structure of temperature, pressure, and water vapor of the NCEP reanalysis 1 data. They calibrated the aerosol channels of the sky-radiometer by the IL method with SKYRAD.pack version 4.2 (Nakajima et al. [1996]; Campanelli et al. [2004; 2007]). Then, they evaluated the PWV derived with their procedure using the SN-CKD (hereafter PWV_{SNCKD}) by comparing it with the PWV_{MWR}. Figure 6.27 shows comparisons of PWV_{SNCKD} using monthly and annual mean calibration constants and PWV_{MWR}. PWV_{SNCKD} using monthly mean calibration constants agreed well (correlation coefficient $\gamma = 0.961$ and

slope = 0.964) with those of the MWR (Fig. 6.27b). PWV_{SNCKD} using the annual mean calibration constant agreed with PWV_{MWR} (Fig. 6.27c). The error of $PWV_{DSRAD+SKYMAP}$ was – 0.041 < bias < 0.024 cm and RMSE < 0.212 cm for low PWV (<3 cm) and bias < – 0.356 cm and RMSE > 0.465 cm for high PWV (Table 6.11). PWV_{SNCKD} using the annual mean calibration constant was 12% smaller than PWV_{MWR} (Table 6.12). Momoi et al. [2020] discussed the reason for the underestimation of PWV_{SNCKD} and reached two factors. The first is the estimation of PWV by the annual mean calibration constant for the water vapor channel. The calibration constant is subject to aging and undergoes seasonal variation due to temperature dependency (Uchiyama et al. [2018a]). Thus, it is possible to underestimate the calibration constant in the wet season. Second, uncertainty regarding the AOT affected PWV estimation. Figure 6.28 depicts the differences in PWV and AOTs at 675, 870, and 1020 nm between the DSRAD and the AERONET direct sun algorithm version 3 (Giles et al. [2019]). In the periods from January to May and from October to November, the differences in PWV and AOTs were less than 0.1 cm and 0.015, respectively. However, the difference in PWV was greater than 0.1 cm from July to September. This corresponds to the difference in AOTs at 675, 870, and 1020 nm from July to September, which indicates that the overestimation of AOT overestimated the transmittance of water vapor. This led to the underestimation of PWV_{SNCKD} using the annual mean calibration constant when PWV was > 3 cm. According to Section 6.3.4, + 0.03 error for the AOT at 940 nm resulted in – 0.214 cm error for PWV.

As discussed in Chapter 5, in addition to the above-discussed reasons of Momoi et al. [2020], we noticed another reason from the gas absorption calculation with a low accurate CKD table (SN-CKD). It was confirmed by comparing PWV_{WVKCD} derived with the WV-CKD-2 method, PWV_{SNCKD}, and PWV_{MWR} in 2019. The aerosol optical properties were estimated from 400, 500, 675, 870, and 1020 nm, except 340 and 380 nm, for the sake of simplicity, because these data do not significantly affect the PWV retrieval. The calibration constants at the aerosol channels were determined by gXIL method (Section 6.2.4). By this improvement, AOTs were good agreement with AERONET retrievals within 0.01 (Fig. 6.29). In the case of the SKYMAP with WV-CKD-2, the annual mean $\tilde{F}_0$ at 940 nm was 2.079×10^{-4} A and 7.5% larger than that determined with the SN-CKD (1.933×10^{-4} A). Using $\tilde{F}_0$, the PWV was estimated using the DSRAD, as shown in Fig. 6.30. In Fig. 6.30a, PWV_{SNCKD} was still underestimated from PWV_{MWR}, even with the improvement of accuracy of the AOTs. Underestimation was significantly about – 0.3 cm in bias in July and August (Fig. 6.30c and 6.30e). This is similar to the previous study of Momoi et al. [2020] shown in Fig. 6.28. In contrast, PWV_{WVCKD} was good agreement with PWV_{MWR} (correlation coefficient γ = 0.995 and slope = 1.002; Fig. 6.30b), even in July and August (Fig. 6.30d). Therefore, the error in PWV with the SN-CKD came from the SN-CKD, not the uncertainty of the AOT.

This result suggests that the SKYMAP/DSRAD with the WV-CKD is useful for the estimation of the accurate PWV from the sky-radiometer observation.

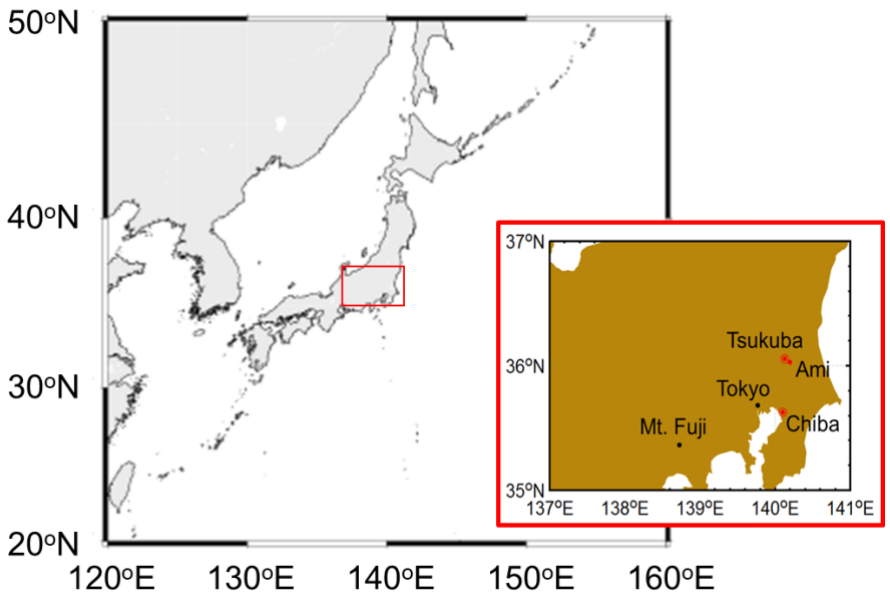

Figure 6.25: SKYNET Chiba site.

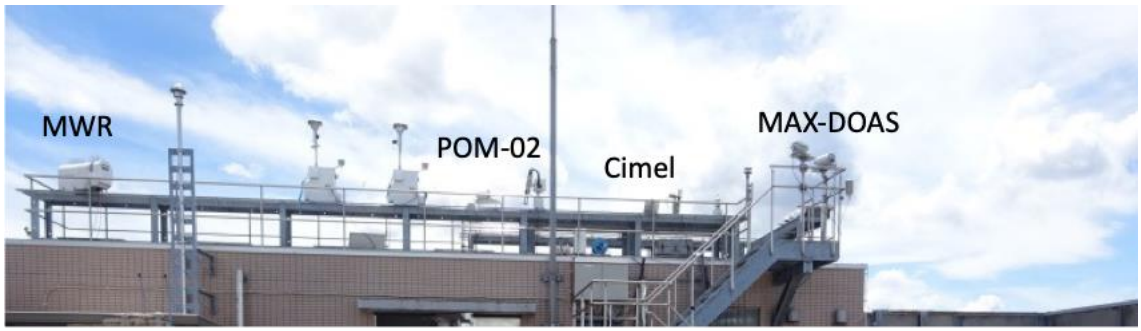

Figure 6.26: Rooftop of Chiba University (SKYNET Chiba site).

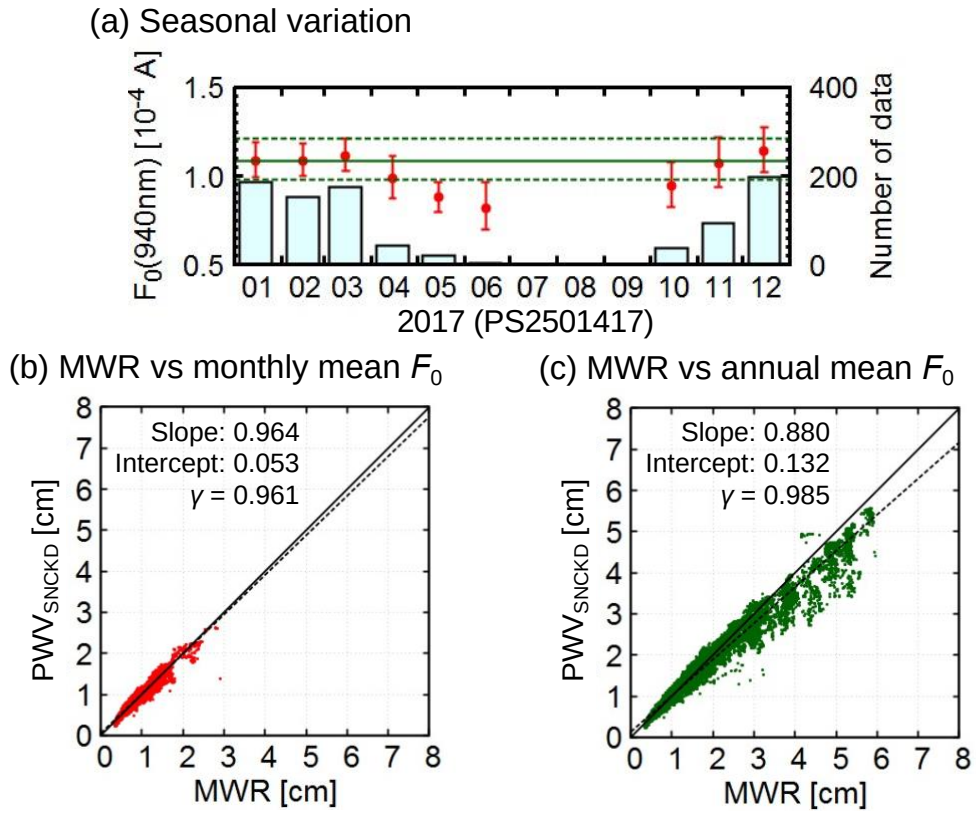

Figure 6.27: Application of SKYMAP/DSRAD to observational data from Chiba in 2017. (a) Seasonal variation in the calibration constant of the water vapor channel (red circles and error bars are monthly means and standard deviations, respectively; green solid and dotted lines are annual means and standard deviations, respectively; boxes indicate the number of data points). (b, c) Comparison of PWV between the MWR and the sky-radiometer with (b) the monthly mean F_0, and (c) the annual mean F_0.

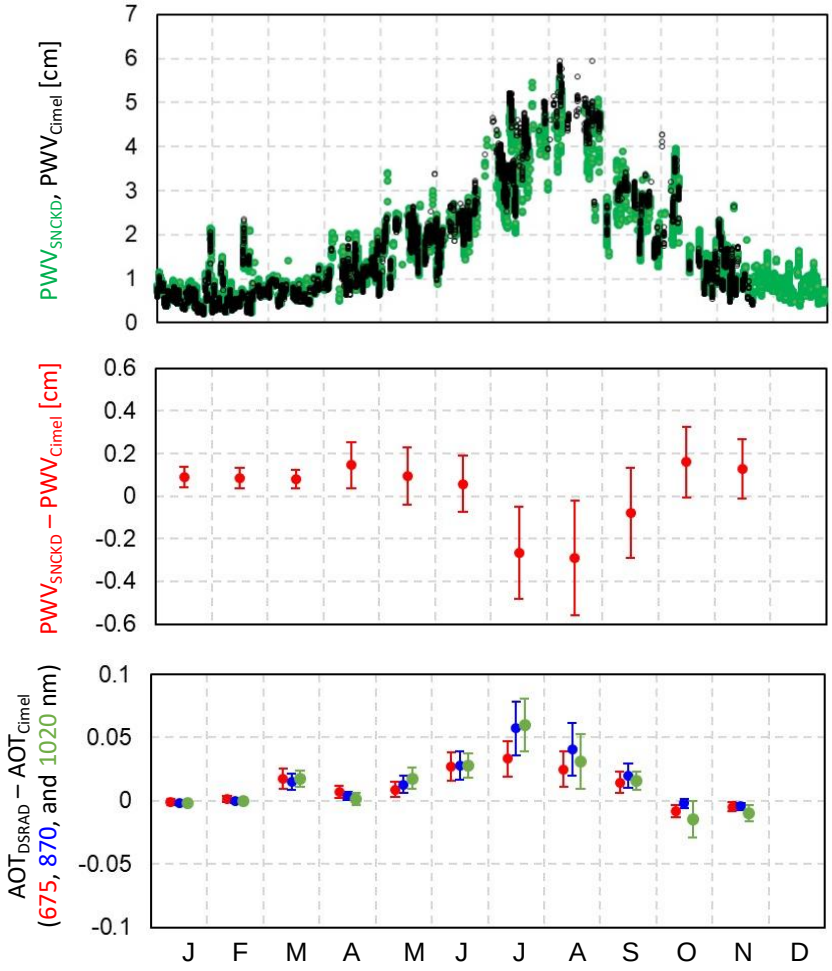

Figure 6.28: The top row shows the time series of PWV in 2017 at Chiba (green and black circles are PWV_{SNCKD} and PWV_{Cimel}, respectively). The middle row is the difference between PWV_{SNCKD} and PWV_{Cimel}. The bottom row is the difference in AOTs at 675 nm (red), 870 nm (blue), and 1020 nm (green) between the DSRAD with SN-CKD and the AERONET retrieval results. Circles and error bars in the middle and bottom rows are means and standard deviations, respectively.

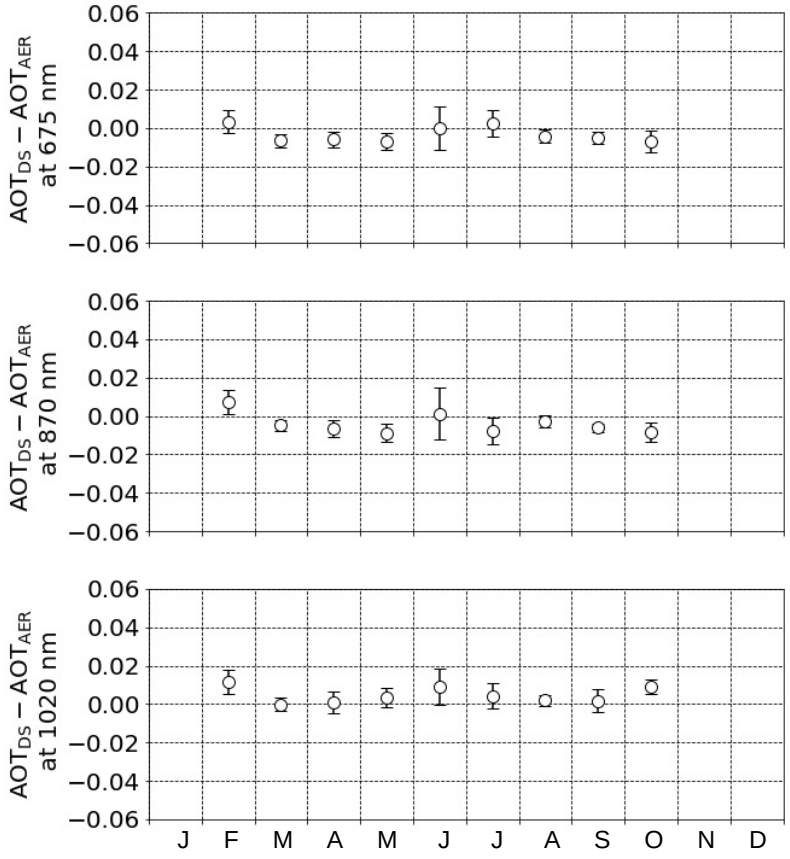

Figure 6.29: The difference in AOTs at 675 nm (top), 870 nm (middle), and 1020 nm (bottom) between the DSRAD calibrated by gXIL method and the AERONET retrieval results. Circles and error bars are means and standard deviations, respectively.

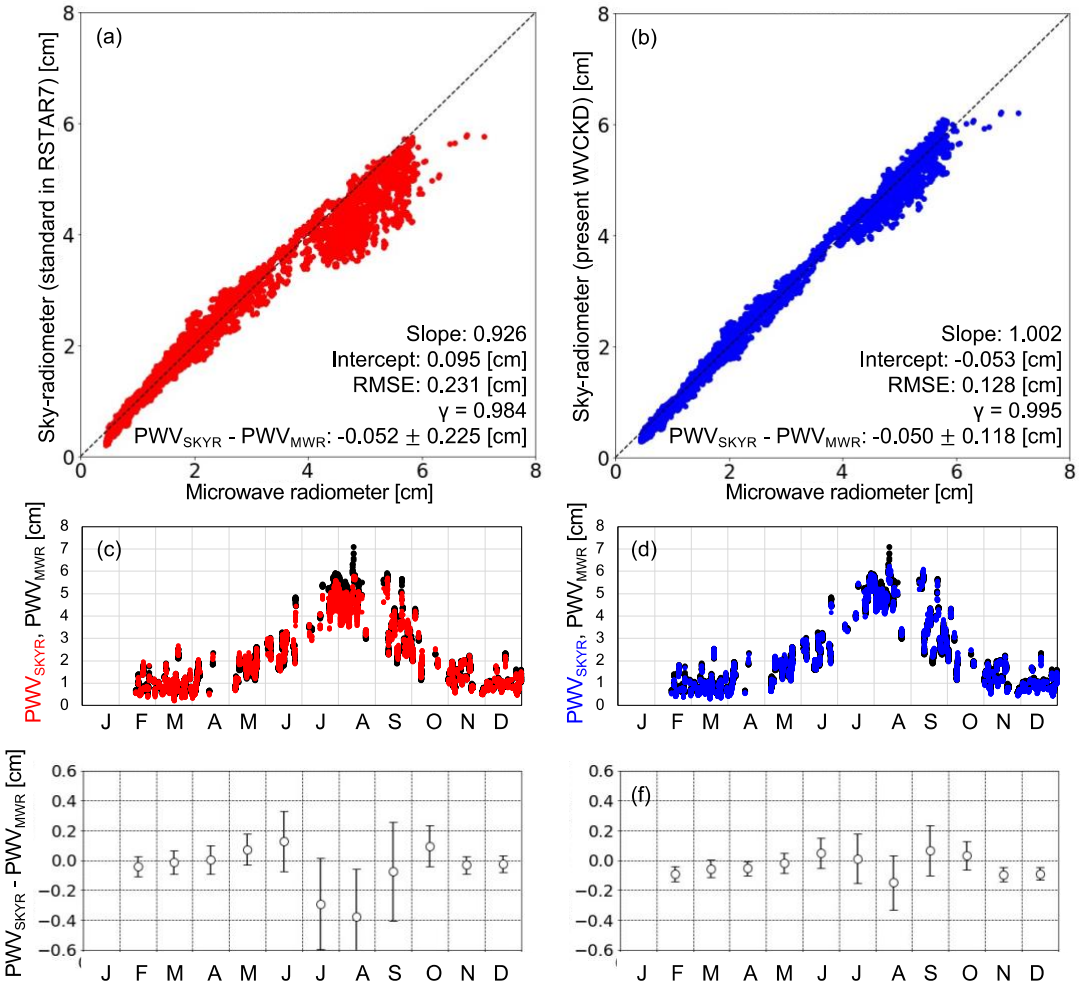

Figure 6.30: The top row shows comparison of PWV between the MWR and the sky-radiometer with (a) the SN-CKD and (b) the WV-CKD-2. The middle row shows the time series of PWV in 2017 at Chiba (red, blue and black circles are PWV_{SNCKD}, PWV_{WVCKD} and PWV_{Cimel}, respectively). The bottom row is the difference between (e) PWV_{SNCKD} and PWV_{Cimel}, (f) PWV_{WVCKD} and PWV_{Cimel}

Table 6.11: Difference in PWV between DSRAD with the annual mean calibration constants and other instruments.

	PWV_{MWR}				
	0 – 1 cm	1 – 2 cm	2 – 3 cm	3 – 4 cm	> 4 cm
	Bias [cm] (RMSE [cm])	Bias [cm] (RMSE [cm])	Bias [cm] (RMSE [cm])	Bias [cm] (RMSE [cm])	Bias [cm] (RMSE [cm])
PWV (SN-CKD)					
vs MWR (2017) (Momoi et al. [2020])	0.017 (0.066)	0.024 (0.153)	-0.041 (0.212)	-0.356 (0.465)	-0.594 (0.722)
vs MWR (2019)	-0.029 (-0.064)	0.066 (0.134)	0.085 (0.189)	0.004 (0.214)	-0.341 (0.467)
PWV (WV-CKD)					
vs MWR (2019)	-0.077 (0.089)	-0.027 (0.093)	0.033 (0.120)	0.065 (0.121)	-0.080 (0.215)

Bias: $PWV_{DSRAD} - PWV_{Other}$

Table 6.12: Comparison of PWV between DSRAD and MWR.

	Slope C_1	Intercept C_2 [cm]	γ	RMSE [cm]
PWV derived by SN-CKD				
Monthly mean F_0 vs MWR (2017)	0.964	0.053	0.961	0.091
Annual mean F_0 vs MWR (2017)	0.880	0.132	0.985	0.231
Annual mean F_0 vs MWR (2019)	0.926	0.095	0.984	0.231
PWV derived by WV-CKD				
Annual mean F_0 vs MWR (2019)	1.002	-0.053	0.995	0.128

C_1, C_2: $PWV_{DSRAD} = C_1 \times PWV_{MWR} + C_2$
Bias: $PWV_{DSRAD} - PWV_{MWR}$

6.6. Conclusions

We investigated the impact of this studies in Chapter 4-5 on the analysis from the ground-based angular-scanning radiometer observation data. To study, we developed new programs named SKYMAP and DSRAD using the methods developed in previous chapters for the sky-radiometer data analysis, which is deployed in the SKYNET all over the world.

We studied the impact of the polarization effect on aerosol estimation through numerical tests. By comparing the results between SKYMAP with the scalar and vector modes, the residual errors in the retrieval sky radiances with the scalar mode are larger than that with the vector mode, especially at a low AOT. This is because the polarization strongly affects angular distribution in the near UV wavelengths under the thin atmosphere by Rayleigh scattering, as discussed in Chapter 4. This causes an overestimation of the fine mode of the SDF and to be small dispersion. As the AOT increases, the polarization effects become weak. Thus, there is no significant difference between the scalar and vector modes when large AOT. It was found that using a vector RTM is important for estimating aerosol properties from sky-radiometer observations, including ultraviolet wavelengths under the thin atmosphere.

We developed a new on-site self-calibration method, SKYMAP, to retrieve PWV from sky-radiometer data at the water vapor channel. This method first retrieves PWV from the normalized angular distribution without the calibration constant. Then the calibration constant is retrieved from the obtained PWV. Once the calibration constant is determined, PWV can be estimated from direct solar irradiance. Our DSRAD algorithm retrieves PWV from direct solar irradiance. This method does not require adjustment parameters used in the empirical methods of previous studies (*e.g.*, Holben et al. [1998]; Uchiyama et al. [2014]; Campanelli et al. [2014; 2018]). Instead, the filter response function and the vertical profiles of water vapor, temperature, and pressure are required as input parameters. Thus, our physics-based algorithm has the potential to be applied to sky-radiometers all over the world. This is the greatest advantage of the DSRAD algorithm. Sensitivity tests using simulated data from sky-radiometer measurements showed that the SKYMAP algorithm retrieved PWV within an error of 10% for cases when PWV was <2 cm. Larger retrieval errors occurred in the cases when PWV was >2 cm since the normalized angular distribution became less sensitive to PWV. Therefore, the SKYMAP algorithm can be applied only to dry conditions. Finally, we applied the SKYMAP and DSRAD algorithms (Momoi et al. [2020]) to the actual SKYNET observations (Chiba, Japan) and compared them with the microwave radiometer. The PWV derived with the WV-CKD is in better agreement (correlation coefficient $\gamma = 0.995$ and slope = 1.002) than that derived with the SN-CKD (correlation coefficient $\gamma = 0.984$ and slope = 0.926) used in Momoi et al. [2020]. Therefore, applying the WV-CKD to the actual data

analysis found that using an accurate CKD table is essential for estimating PWV from sky-radiometer observations. These results also show that our new on-site self-calibration method (SKYMAP) is practical. In future work, we plan to compare our method with others in the SKYNET framework (Uchiyama et al. [2014]; Campanelli et al. [2014]).

References

[1] Boi, P., G. Tonna, G. Dalu, T. Nakajima, B. Olivieri, A. Pompei, M. Campanelli, and R. Rao, 1999: Calibration and data elaboration procedure for sky irradiance measurements, *Appl. Opt.*, **38**, 6, 896-907

[2] Bruegge, C. J., J. E. Conel, R. O. Green, J. S. Margolis, R. G. Holm, and G. Roon, 1992: Water vapor column abundance retrievals during FIFE, J. Geophys. Res., 97, 18759-18768

[3] Campanelli, M., Nakajima, T., and Olivieri, B.: Determination of the solar calibration constant for a sun-sky radiometer: proposal of an in-situ procedure, Appl. Opt., 43, 651-659, 2004

[4] Campanelli, M., Estellés, V., Tomasi, C., Nakajima, T., Malvestuto, V., and Martínez-Lozano, J. A.: Application of the SKYRAD Improved Langley plot method for the in situ calibration of CIMEL Sun-sky photometers, Appl. Opt., 46, 2688-2702, 2007

[5] Campanelli, M., T. Nakajima, P. Khatri, T. Takamura, A. Uchiyama, V. Estelles, G. L. Liberti, and V. Malvestuto, 2014: Retrieval of characteristic parameters for water vapour transmittance in the development of ground-based sun-sky radiometric measurements of columnar water vapour, Atmos. Meas. Tech., 7, 1075-1087

[6] Campanelli, M., A. Mascitelli, P. Sanò, H. Diémoz, V. Estellés, S. Federico, A. M. Iannarelli, F. Fratarcangeli, A. Mazzoni, E. Realini, M. Crespi, O. Bock, J. A. Martínez-Lozano, and S. Dietrich, 2018: Precipitable water vapour content from ESR/SKYNET sun–sky radiometers: validation against GNSS/GPS and AERONET over three different sites in Europe, Atmos. Meas. Tech., 11, 81-94

[7] Coddington, O. M., Richard, E. C., Harber, D., Pilewskie, P., Woods, T. N., Chance, K., et al., 2021: The TSIS-1 Hybrid Solar Reference Spectrum. Geophysical Research Letters, 48, e2020GL091709. https://doi.org/10.1029/2020GL091709

[8] Dubovik, O., Smirnov, A., Holben, B. N., King, M. D., Kaufman, Y. J., Eck, T. F., and Slutsker, I.: Accuracy assessments of aerosol optical properties retrieved from Aerosol Robotic Network (AERONET) Sun and sky radiance measurements, J. Geophys. Res., 105, 9791–9806, 2000

[9] Dubovik, O. and M. D. King, 2000: A flexible inversion algorithm for retrieval of aerosol optical properties from sun and sky radiance measurements, *J. Geophys. Res.*, **105**, 20673–20696

[10] Dubovik, O., Sinyuk, A., Lapyonok, T., Holben, B. N., Mishchenko, M., Yang, P., Eck, T. F., Volte, H., Muñoz, O., Veihelmann, B., van der Zande, W. J., Leon, J.-F., Sorokin, M., and Slutsker, I.: Application of spheroid models to account for aerosol particle nonsphericity in remote sensing of desert dust, J. Geophys. Res., 111, D11208,

doi:10.1029/2005JD006619, 2006

[11] Estellés, V., M. Campanelli, M. P. Utrillas, F. Expósito, and J. A. Martínez-Lozano, 2012: Comparison of AERONET and SKYRAD4.2 inversion products retrieved from a Cimel CE318 sunphotometer, *Atmos. Meas. Tech.*, **5**, 569-579, doi:10.5194/amt-5-569-2012

[12] Fröhlich, C. and Shaw, G. E., 1980: New determination of Rayleigh scattering in the terrestrial atmosphere, *Appl. Opt.*, **19**, 1.773– 1.775

[13] Fu, Q., and K. N. Liou, 1992: On the correlated k-distribution method for radiative transfer in nonhomogeneous atmospheres, *J. Atmos. Sci.*, **49**, 2139–2156.

[14] Giles, D. M., Sinyuk, A., Sorokin, M. G., Schafer, J. S., Smirnov, A., Slutsker, I., Eck, T. F., Holben, B. N., Lewis, J. R., Campbell, J. R., Welton, E. J., Korkin, S. V., and Lyapustin, A. I.: Advancements in the Aerosol Robotic Network (AERONET) Version 3 database – automated near-real-time quality control algorithm with improved cloud screening for Sun photometer aerosol optical depth (AOD) measurements, Atmos. Meas. Tech., 12, 169-209, https://doi.org/10.5194/amt-12-169-2019, 2019

[15] Gueymard, C. A., 2001: Parameterized transmittance model for direct beam and circumsolar spectral irradiance, *Solar Energy*, **71**, 325-346

[16] Hashimoto, M., Nakajima, T., Dubovik, O., Campanelli, M., Che, H., Khatri, P., Takamura, T., and Pandithurai, G.: Development of a new data-processing method for SKYNET sky radiometer observations, *Atmos. Meas. Tech.*, **5**, 2723-2737, 2012

[17] Holben, B. N., T. F. Eck, I. Slutsker, D. Tanré, J. P. Buis, A. Setzer, E. Vermote, J. A. Reagan, Y. J. Kaufman, T. Nakajima, F. Lavenu, I. Jankowiak and A. Smirnov, 1998: AERONET-A federated instrument network and data archive for aerosol characterization, *Remote Sens. Environ.*, **66**, 1-16

[18] Irie, H., H. M. S. Hoque, A. Damiani, H. Okamoto, A. M. Fatmi, P. Khatri, T. Takamura, and T. Jarupongsakul, 2019: Simultaneous observations by sky radiometer and MAX-DOAS for characterization of biomass burning plumes in central Thailand in January-April 2016, *Atmos. Meas. Tech.*, **12**, 599-606, https://doi.org/10.5194/amt-12-599-2019.

[19] Kobayashi, E., Uchiyama, A., Yamazaki, A., and Matsuse, K.: Application of the Statistical Optimization Method to the Inversion Algorithm for Analyzing Aerosol Optical Properties from Sun and Sky Radiance Measurements, J. Meteor. Soc. Japan, 84, 1047-1062, 2006

[20] Kobayashi, E., Uchiyama, A., Yamazaki, A., and Kudo, R.: Retrieval of aerosol optical properties based on the spheroid model, J. Meteorol. Soc. Jpn., 88, 847–856, 2010

[21] Kudo, R., T. Nishizawa, and T. Aoyagi, 2016: Vertical profiles of aerosol optical properties and the solar heating rate estimated by combining sky radiometer and lidar measurements, *Atmos. Meas. Tech.*, **9**, 3223–3243, doi:10.5194/amt-9-3223-2016

[22] Kudo, R., H. Diémoz, V. Estellé, M. Campanelli, M. Momoi, F. Marenco, C. Ryder, O. Ijima, A. Uchiyama, K. Nakashima, A. Yamazaki, R. Nagawasa, N. Ohkawara, and H. Ishida, 2021: Optimal use of the Prede POM sky radiometer for aerosol, water vapor, and ozone retrievals, *Atmos. Meas. Tech.*, **14**, 3395-3426, https://doi.org/10.5194/amt-14-3395-2021

[23] Lacis, A. A., and V. A. Oinas, 1991: Description if the correlated k-distribution method for modeling nongray gaseous absorption, thermal emission, and multiple scattering in vertically inhomogeneous atmospheres, *J. Geophys. Res.*, **96**, 9027–9063.

[24] Momoi, M., R. Kudo, K. Aoki, T. Mori, K. Miura, H. Okamoto, H. Irie, Y. Shoji, A. Uchiyama, O. Ijima, M. Takano, and T. Nakajima, Development of on-site self-calibration and retrieval methods for sky-radiometer observations of precipitable water vapor, Atmos. Meas. Tech., 13, 2635–2658, https://doi.org/10.5194/amt-13-2635-2020, 2020.

[25] Momoi, M., H. Irie, T. Nakajima, and M. Sekiguchi, Efficient calculation of radiative intensity including the polarization effect in moderately thick atmospheres using a truncation approximation, J. Quant. Spectrosc. Radiat. Transfer, 277, 107976, https://doi.org/10.1016/j.jqsrt.2021.107976, 2022a.

[26] Momoi, M., H. Irie, M. Sekiguchi, T. Nakajima, H. Takenaka, K. Miura, and K. Aoki, Rapid, accurate computation of narrow-band sky radiance in the 940 nm gas absorption region using the correlated *k*-distribution method for sun-photometer observations, Prog. Earth Planet. Sci., 9, 10, https://doi.org/10.1186/s40645-022-00467-6, 2022b.

[27] Nagasawa, K. 1999: Computations of Sunrise and Sunset, Chijin-Shoin (in Japanese)

[28] Nakajima, T., and M. Tanaka, 1986: Matrix formulations for the transfer of solar radiation in a plane-parallel scattering atmosphere. J. Quant. Spectrosc. Radiat. Transfer, 35, 13–21

[29] Nakajima, T., and M. Tanaka, 1988: Algorithms for radiative intensity calculations in moderately thick atmospheres using a truncation approximation. J. Quant. Spectrosc. Radiat. Transfer, 40, 51–69

[30] Nakajima, T., M. Tanaka, M. Yamano, M. Shiobara, K. Arao, and Y. Nakanishi, 1989: Aerosol Optical Characteristics in the Yellow Sand Events Observed in May, 1982 at Nagasaki-Part II Models, J. Meteorol. Soc. Japan, 67, 279-291, https://doi.org/10.2151/jmsj1965.67.2_279

[31] Nakajima, T., Tonna, G., Rao, R., Boi, P., Kaufman, Y., and Holben, B.: Use of Sky brightness measurements from ground for remote sensing of particulate polydispersions, Appl. Opt., 35, 2672-2686, 1996

[32] Nakajima, T., M. Tanaka, M. Yamano, M. Shiobara, K. Arao, and Y. Nakanishi, 1989:

Aerosol Optical Characteristics in the Yellow Sand Events Observed in May, 1982 at Nagasaki-Part II Models, J. Meteorol. Soc. Japan, 67, 279-291, https://doi.org/10.2151/jmsj1965.67.2_279

[33] Nakajima, T., M. Campanelli, H. Che, V. Estellés, H. Irie, S. Kim, J. Kim, D. Liu, T. Nishizawa, G. Pandithurai, V. K. Soni, B. Thana, N. Tugjsurn, K. Aoki, S. Go, M. Hashimoto, A. Higurashi, S. Kazadzis, P. Khatri, N. Kouremeti, R. Kudo, F. Marenco, M. Momoi, S.S. Ningombam, C. L. Royder, A. Uchiyama, and A. Yamazaki, 2020: An overview of and issues with sky radiometer technology and SKYNET, *Atmos. Meas. Tech.*, **13**, 4195-4218, https://doi.org/10.5194/amt-13-4195-2020.

[34] Ogawa, H., M. Tanaka, and T. Nakajima, 1989: A Simple Expression for the Additional Sky Radiance Produced by Polarization Effects, *J. Meteorol. Soc. Jpn.*, **67** (5), 877–888.

[35] Ota, Y., A. Higurashi, T. Nakajima, and T. Yokota, 2010: Matrix formulations of radiative transfer including the polarization effect in a coupled atmosphere–ocean system. *J. Quant. Spectrosc. Radiat. Transfer*, **111**, 878–894

[36] Sekiguchi, M., and T. Nakajima, 2008: A k-distribution- based radiation code and its computational optimization for an atmospheric general circulation model, J. Quant. Spectrosc. Radiat. Transfer, 109, 2779 –2793

[37] Sinyuk, A., B. N. Holben, T. F. Eck, D. M. Giles, I. Slutsker, S. Korkin, J. S. Schafer, A. Smirnov, M. Sorokin, and A. Lyapustin, 2020: The AERONET Version 3 aerosol retrieval algorithm, associated uncertainties and comparisons to Version 2, *Atmos. Meas. Tech.*, **13**, 3375–3411, https://doi.org/10.5194/amt-13-3375-2020.

[38] Smirnov, A., B. N. Holben, T. F. Eck, O. Dubovik, and I. Slutsker, 2000: Cloud-Screening and Quality Control Algorithms for the AERONET Database, *Remote Sens. Environ.*, **73**, 337-349

[39] Thuillier, G., M. Hersé, D. Labs, T. Foujols, W. Peetermans, D. Gillotay, P.C. Simon & H. Mandel, 2003: The Solar Spectral Irradiance from 200 to 2400 nm as Measured by the SOLSPEC Spectrometer from the Atlas and Eureca Missions, *Solar Physics*, **214**, 1–22, https://doi.org/10.1023/A:1024048429145

[40] Uchiyama, A., Yamazaki, A., and Kudo, R., 2014: Column Water Vapor Retrievals from Sky Radiometer (POM-02) 940 nm Data, J. Meteorol. Soc. Jpn., 92A, 195–203

[41] Uchiyama A., Matsunaga, T., and Yamazaki, A., 2018a: The instrument constant of sky radiometers (POM-02) – Part 1: Calibration constant, Atmos. Meas. Tech., 11, 5363-5388

[42] Uchiyama A., T. Matsunaga, and A. Yamazaki, 2018b: The instrument constant of sky radiometers (POM-02) – Part 2: Solid view angle, *Atmos. Meas. Tech.*, **11**, 5389-5402

Concluding remarks

In this study, we developed the fast radiative transfer model with keeping accuracy for the analysis of the ground-based angular-scanning radiometer observations in two topics: (1) development of an efficient computation method (P^n-IMS) of the sky radiances, including the polarization effects, and (2) a survey of the information about aerosol and water vapor in the water vapor absorption region of 940 nm with development of the look-up table of the *k*-distribution (WV-CKD).

In the former study, we developed a novel calculation method for polarized radiation. The P^1- and P^2-IMS methods are extended versions of the TMS and IMS methods in Nakajima and Tanaka [1988] formulated in the scalar approximation of the radiation field. We extended these methods to include the polarization effect based on the vector radiative transfer theory. We also developed any *n*-th order scattering correction. A series of numerical tests indicated that the P^1-IMS method is accurate enough to reconstruct the Stokes parameters within 0.2%, except for total radiance. The total radiance in the solar aureole region requires a higher order scattering correction by the P^2- and P^3-IMS methods. Numerical tests indicated that the P^3-IMS method can reconstruct sky radiance, including aureole region, within 1% with a low hemispheric quadrature stream $N = 10$ in the 340-1020 nm spectral region in a moderately thick atmosphere such as an aerosol optical thickness at 500 nm of 1. Thus, the P^3-IMS method is more efficient than the P^1-IMS method, which requires $N > 20$. We examined the numerical tests to evaluate the impact of the polarization effect on the aerosol estimation from the sky-radiometer observations. The numerical tests indicate that the polarization effect causes overestimating the fine mode particles of the volume size distribution at the low aerosol optical thickness. In addition to the downward radiance, the P^1-IMS is applicable to the upward radiance (*i.e.*, satellite observation).

The latter study investigated information contents on the sky radiance at 940 nm, one of the water vapor absorption regions in the near-infrared wavelength. To rapidly compute the narrow-band sky radiance at 940 nm, we developed the WV-CKD with keeping accuracy (<0.3%). Numerical tests indicate that the sky radiance in the almucantar plane is affected by PWV. On the other hand, that in the principal plane is affected by aerosol vertical profile and PWV. We developed the procedure to obtain PWV from the sky-radiometer observation of the almucantar plane without pre/post calibrations based on these surveys. We applied to the actual SKYNET observations and compared the PWV with the microwave radiometer. Then it is suggested that the PWV derived from the sky-radiometer is in good agreement with MWR. These results also show that our new on-site self-calibration method (SKYMAP) is practical.

Through this study, we found some future works: (1) to compare P^n-IMS methods with others (*e.g.*, Hioki et al. [2016] and Waquet and Herman [2019]), (2) to optimize the correction methods (P^n-IMS) by forward scattering energy, (3) to apply our present methods to forward scattering phenomena other than aerosol cases, that produce an intense polarization, such as polarization field simulation of 22^o halo of ice crystals and forward scattering of reflected direct solar radiation from the ocean surface, (4) to use polarized radiances measured by angular-scanning radiometer through the development of new retrieval method to obtain further information about aerosols (*e.g.*, particle shape (Dubovik et al. [2019])), (5) to compare our method with others in the SKYNET framework (Uchiyama et al. [2014]; Campanelli et al. [2014]), and (6) to use sky radiances in the gas absorption regions, such as 760 (oxygen) and 940 (water vapor) nm, in the principal plane to obtain further information about aerosols (*e.g.*, vertical profile (Chapter 5)).

Publications and Presentations

Publications

(1) Momoi, M., R. Kudo, K. Aoki, T. Mori, K. Miura, H. Okamoto, H. Irie, Y. Shoji, A. Uchiyama, O. Ijima, M. Takano, and T. Nakajima, Development of on-site self-calibration and retrieval methods for sky-radiometer observations of precipitable water vapor, Atmos. Meas. Tech., 13, 2635–2658, https://doi.org/10.5194/amt-13-2635-2020, 2020.

(2) Momoi, M., H. Irie, T. Nakajima, and M. Sekiguchi, Efficient calculation of radiative intensity including the polarization effect in moderately thick atmospheres using a truncation approximation, J. Quant. Spectrosc. Radiat. Transfer, 277, 107976, 1-15 https://doi.org/10.1016/j.jqsrt.2021.107976, 2022a.

(3) Momoi, M., H. Irie, M. Sekiguchi, T. Nakajima, H. Takenaka, K. Miura, and K. Aoki, Rapid, accurate computation of narrow-band sky radiance in the 940 nm gas absorption region using the correlated *k*-distribution method for sun-photometer observation, Prog. Earth Planet. Sci., 9, 10, 1-22, https://doi.org/10.1186/s40645-022-00467-6, 2022b.

Selected Presentations

International conference

(1) Momoi, M., M. Anzai, K. Miura, T. Mori, K. Aoki, and R. Kikuchi, Cloud screening method using direct solar irradiances of the sky-radiometer, Asia Aerosol Conference 2019, City University of Hong Kong (Hong Kong), May 27-30, 2019 (poster).

(2) Momoi, M., R. Kudo, K. Miura, A. Damiani, H.M.S. Hoque, H. Irie, and H. Okamoto, Development of an algorithm retrieving near-surface fine mode aerosol information from simultaneous sky-radiometer and MAX-DOAS observations, Japan, 2019 AGU Fall Meeting, Moscone center (San Francisco), December 9-13, 2019 (poster).

(3) Momoi, M., H. Irie, T. Nakajima, and M. Sekiguchi, PSTAR/P^n-IMS: Efficient calculation of sky radiative intensity including the polarization effect in moderately thick atmospheres using a truncation approximation, 6th International SKYNET Workshop, online hosted by Chiba University, November 9-11, 2021 (oral).

(4) Momoi, M., H. Irie, M. Sekiguchi, T. Nakajima, and H. Takenaka, RSTAR/WV-CKD: Development of the look-up table of the k-distribution in the gas absorption region around 940 nm for the sky-radiometer data analysis, 6th International SKYNET Workshop, online hosted by Chiba University, November 9-11, 2021 (poster)

Domestic conference

(1) 桃井裕広、工藤玲、三浦和彦、入江仁士、スカイラジオメータと MAX-DOAS の複合観測による対流圏下部の PM2.5 濃度のリモートセンシング観測、日本気象学会 2019 年度秋季大会、福岡県北九州市、2019 年 10 月 28 日―10 月 31 日 (oral).

Acknowledgments

I am happy and grateful to conduct my doctoral studies at the Center for Environmental Remote Sensing (CEReS) at Chiba University. I want to thank Dr. Hitoshi Irie for being my thesis supervisor. I am also thankful to him for giving me a lot of chances to attend the international conferences, which has helped me acquire a lot of knowledge. I want to thank Dr. Alessandro Damiani for his magnificent support. I still remember being encouraged by him at the AGU fall meeting that I attended for the first time alone before enrollment. I would also like to appreciate the assistance of Mr. Hiroshi Okamoto and Ms. Yasuyo Kumakawa.

In the scientific aspect, I am grateful to the OpenCLASTR project and its contributors for allowing us to use a lot of resources, especially the STAR series and SKYRAD.pack. Mainly, I could not complete the doctoral program without the dedicated support of Dr. Teruyuki Nakajima and Dr. Miho Sekiguchi. I am also thankful to the SKYNET community for continuously accumulating observational data over decades. I am also grateful to Dr. Kazuma Aoki, Dr. Hossain Mohammed Syedul Hoque, Dr. Rei Kudo, Dr. Kazuhiko Miura, and Dr. Hideaki Takenaka for their technical contributions. I am grateful to the examiners (Dr. Kazuhito Ichii, Dr. Josaphat Tetuko Sri Sumantyo, Dr. Hiroaki Kuze, and Dr. Naoko Saitoh) for giving me great suggestions.

Through my doctoral course, I learned many things, *e.g.*, writing/reviewing scientific papers and presentations in addition to expert knowledge from the people involved with me. I want to thank all colleagues & CEReS members.

Lastly, I would like to thank my parents for supporting me in many aspects.